High-temperature giant piezoresistivity of microstructured SiOC-based strain gauges

Zur Erlangung des akademischen Grades Doktor-Ingenieurwissenschaften (Dr. -Ing.)
Genehmigte kumulative Dissertation von M.Sc. Emmanuel Ricohermoso III

Erstgutachter: PD Dr. Emanuel Ionescu
Zweitgutachter: Prof. Dr. Anke Weidenkaff

TU Darmstadt, FB 11 – Material- und Geowissenschaften
Fachgebiet Disperse Feststoffe

2022 - Darmstadt

High-temperature giant piezoresistivity of microstructured SiOC strain gauge

vom Fachbereich Material- und Geowissenschaften
der Technische Universität Darmstadt
im Fachgebiet Disperse Feststoffe

zur Erlangung des akademischen Grades
Doktor der Ingenieurwissenschaften
(Dr.-Ing.)

Genehmigte kumulative Dissertation
von
M.Sc. Emmanuel Ricohermoso III
aus Oriental Mindoro, Philippines

1. Gutachter: Dr. Emanuel Ionescu
2. Gutachter: Prof. Dr. Anke Weidenkaff

Tag der Einreichung: 26.07.2022
Tag der Prüfung: 23.09.2022

Veröffentlicht unter CC BY-SA 4.0 International
Darmstadt – D 17

Declaration of Authorship

I hereby declare that the thesis submitted is my own unaided work. All direct or indirect sources used are acknowledged as references.
I am aware that the thesis in digital form can be examined for the use of unauthorized aid and in order to determine whether the thesis as a whole or parts incorporated in it may be deemed as plagiarism. For the comparison of my work with existing sources I agree that it shall be entered in a database where it shall also remain after examination, to enable comparison with future theses submitted. Further rights of reproduction and usage, however, are not granted here.
This thesis was not previously presented to another examination board and has not been published.

Ehrenwörtliche Erklärung

Ich erkläre hiermit ehrenwörtlich, dass ich die vorliegende Arbeit selbständig angefertigt habe. Die aus fremden Quellen direkt und indirekt übernommenen Gedanken sind als solche kenntlich gemacht.
Ich weiß, dass die Arbeit in digitalisierter Form daraufhin überprüft werden kann, ob unerlaubte Hilfsmittel verwendet wurden und ob es sich – insgesamt oder in Teilen – um ein Plagiat handelt. Zum Vergleich meiner Arbeit mit existierenden Quellen darf sie in eine Datenbank eingestellt werden und nach der Überprüfung zum Vergleich mit künftig eingehenden Arbeiten dort verbleiben. Weitere Vervielfältigungs- und Verwertungsrechte werden dadurch nicht eingeräumt.
Die Arbeit wurde weder einer anderen Prüfungsbehörde vorgelegt noch veröffentlicht.

Darmstadt, den 26.07.2022.

(Emmanuel Ricohermoso III)

The present cumulative dissertation summarizes the essential scientific findings reported to the scientific community in the following peer-reviewed articles. Article reprints [1] – [6] are enclosed in the Chapter *Publications* at the end of this work.

[1] Ricohermoso E, Rosenburg F, Klug F, Nicoloso N, Schlaak HF, Riedel R, et al. Piezoresistive carbon-containing ceramic nanocomposites – A review. Open Ceramics. 2021 Mar 1;5:100057.

[2] Ricohermoso E, Klug F, Schlaak H, Riedel R, Ionescu E. Electrically conductive silicon oxycarbide thin films prepared from preceramic polymers. International Journal of Applied Ceramic Technology. 2021 May 17;19(1):149–64.

[3] Ricohermoso E, Klug F, Schlaak H, Riedel R, Ionescu E. Compressive thermal stress and microstructure-driven charge carrier transport in silicon oxycarbide thin films. Journal of the European Ceramic Society. 2021 Oktober;41(13):6377–84.

[4] Ricohermoso E, Klug F, Schlaak H, Riedel R, Ionescu E. Microstrain-range giant piezoresistivity of silicon oxycarbide thin films under mechanical cyclic loads. Materials & Design. 2022 Jan 1;213:110323.

[5] Ricohermoso E, Vallet M, Haripre E, Solano-Arana S, Riedel R, Ionescu E. Hierarchical microstructure growth in a precursor-derived SiOC thin film prepared on silicon substrate. International Journal of Applied Ceramic Technology. *Accepted 22 July 2022.*

Acknowledgments

This manuscript is made possible through the generous support of my supervisor, PD Dr. Emanuel Ionescu. I am of great honor to have the chance to work with him and be under his guidance all throughout the course of my doctorate. I will forever be appreciative for the knowledge he imparted on me, both technical and life lessons.

I would also like to express my gratitude to Prof. Ralf Riedel for giving me the opportunity to work at Dispersive Solids group and entrusting me this project. His guidance and encouragement kept me motivated to finish my work on time.

I am thankful to Prof. Anke Weidenkaff for agreeing to be my second supervisor and for her valuable time and feedbacks.

I would like to extend my gratitude to all my research partners, Dr. Florian Klug, Ms. Susana Solano-Arana, Ms. Claudia Fasel, Dr. Maxime Vallet, Dr. Eva Haripre, Mr. Vivien Lefranc, and the Materials Science workshop team, for all the assistance they gave to finish the necessary experimental works for this thesis. It is a collaborative effort of these people that helped me progress with an ease.

My PhD journey will not be as enjoyable as it is without my colleagues from Disperse Feststoffe. Most of my time was shifted into digital space and in a controlled in-person interaction due to pandemic, yet we managed to sustain a fostering environment. I am appreciative for all the time spent with you all, may it be in and out of the workplace. Special thanks to Ying, Alex, Jan, and Sefa for keeping my spirit up on those dark moments. I am thankful to Antoine for all the encouragement in finalizing this manuscript.

I am very pleased for my friends, Jethro, PJ, Lady, Nestor, Yntet, Leonard, Philip, CJ for being a good support system here in Europe. You definitely brough home away from home.

Lubos akong nagpapasalamat sa aking pamilya sa Pilipinas sa kanilang patuloy na pagsuporta, at sa lahat nang mga panalangin upang aking matapos at mapagtagumpayan ang aking mga hangarin.

This work is also dedicated in memoriam of Prof. Helmut Schlaak.

Abstract

The foundation of this work is laid out based on the efficiency of silicon oxycarbide (SiOC) as a functional material for piezoresistive device applications. The realization of a cost-efficient strain gauge which can operate at elevated temperature serves as the foremost objective of this work. This goal is fathomed based on prevailing knowledge regarding the high piezoresistivity of SiOC at the range of 10 - 10^2 coupled with commendable properties such as electrical conductivity, good thermal resistance, and an excellent coating material for hostile environment. An optimized process of spin coating is used to deposit ~500 nm SiOC film onto the 100-mm diameter silicon substrate with a silica layer of 500 nm. The deposition process is screened with a Taguchi design of experiment resulting into a replicable and controlled process with a crack-free and homogenous coating. An in-house piezoresistivity test setup was fabricated with considerations of minimizing the electrical contact resistances, capability to perform mechanical cyclic loads, and the ability to operate at elevated temperature until 700 °C. After the annealing process, the SiOC film manifested round-shaped segregations which were identified as carbon-rich and oxygen-depleted, evenly dispersed in an oxygen-rich matrix. Deeper investigation of the segregated area revealed 2-level hierarchical microstructure of sp^2-hybridized carbon, Si_3N_4 and SiC. On the other hand, Raman analysis confirmed presence of sp^2-hybridized carbon not just on the segregated area but also on the matrix distinctive by the difference of crystal sizes. Larger domains of carbon including tortuosity (L_{eq}) are present on the segregation than on the matrix of the film. Kinetics study showed that the segregations area results of free carbon diffusion through the silica layer with an activation energy equal to 3.05 eV.

Platinum electrodes are printed on the surface of the SiOC film via photolithography for the PZR tests. The fabricated strain gauge prototypes have high sensitivity with gauge factors (GF) in the range of 2000 – 5000 tested at 25 – 400 °C. At 500 – 700 °C, the behavior of the material shifted from semiconducting to conducting decreasing its resistance to 11 Ω, and GF of 200. This GF is still comparably larger than commercial metal- and silicon-based strain gauges. The difference of mechanical cyclic loads applied on the prototypes influenced the degree of response' hysteresis and the linearity of the strain range. In both cases, tests under compressive load showed superiority over tensile tests. Through these results, this study provides a working strain gauge prototype based on SiOC thin film with high sensitivity, reproducibility, and robustness. The giant piezoresistivity of the fabricated strain gauge at an elevated temperature, until 700 °C, surpasses the known application of the current commercial strain gauges. Furthermore, the perceived shift on electrical behavior of the material at 460 °C broadens its applications to current-limiting devices and temperature sensors.

Abstract

Die vorliegende Arbeit untersucht eingehend die Effizienz von Silizium-Oxycarbid (SiOC) als piezoresistives Material für den Einsatz in Dehnungsmesswandler oder Drucksensoren. Die Realisierung eines kosteneffizienten Dehnungsmessstreifens, der bei erhöhter Temperatur arbeiten kann, dient als oberstes Ziel dieser Arbeit. Dieses Ziel wird auf der Grundlage der sehr hohen intrinsischen Piezoresistivität von SiOC (Gauge-Faktor im Bereich von 10 - 10^2) in Verbindung mit ausgezeichneten Eigenschaften wie elektrischer Leitfähigkeit, guter Wärmebeständigkeit und einer sehr guten Eignung als Beschichtungsmaterial für harsche Umgebungsbedingungen (z.B. hohe Temperaturen, korrosive Atmosphäre) ergründet. Ein optimierter Prozess der Schleuderbeschichtung wird verwendet, um einen ~500 nm dicken SiOC-Film auf ein passivierten Siliziumsubstrat mit einem Durchmesser von 100 mm aufzubringen. Der Abscheidungsprozess wird mit einem Taguchi-Experimentdesign überprüft, was zu einem reproduzierbaren und kontrollierten Prozess mit einer rissfreien und homogenen Beschichtung führt. Ein hauseigener Piezoresistivitäts-Testaufbau wird unter Berücksichtigung der Minimierung der elektrischen Kontaktwiderstände, der Fähigkeit zur Durchführung mechanischer zyklischer Belastungen und der Fähigkeit zum Betrieb bei erhöhter Temperatur bis 700 °C hergestellt. Nach dem Pyrolyseprozess bei 1400 °C weist der SiOC-Film rundliche Segregationen auf, die als kohlenstoffreich und sauerstoffarm identifiziert werden und gleichmäßig in einer SiOC-basierten Matrix verteilt sind. Eine genauere Untersuchung des segregierten Bereichs ergibt eine zweistufige hierarchische Mikrostruktur aus sp2-hybridisiertem Kohlenstoff, Si3N4 und SiC. Andererseits bestätigt die Raman-Analyse das Vorhandensein von sp2-hybridisiertem Kohlenstoff nicht nur im segregierten Bereich, sondern auch in der Matrix, die sich durch die unterschiedlichen Kristallgrößen auszeichnet. Kohlenstoffbereiche einschließlich Tortuosität (Leq) sind im segregierten Bereich größer als in der Matrix des Films. Eine Kinetikstudie zeigt, dass die Größe der Ausscheidungen das Ergebnis der freien Kohlenstoffdiffusion durch die Siliziumdioxidschicht bei einer Aktivierungsenergie von 3,05 eV ist. Für die PZR-Tests werden Platin-Elektroden mittels Fotolithografie auf die Oberfläche des SiOC-Films gedruckt. Die hergestellten-Prototypen haben eine hohe Empfindlichkeit mit Gauge Factor (GF) im Bereich von 2000 - 5000, die bei 25 - 400 °C getestet werden. Bei 500 - 700 °C verändert sich das Verhalten des Materials von halbleitend zu leitend, wodurch der Widerstand auf 11 W und der GF auf 200 sinkt. Dieser GF ist immer noch vergleichsweise größer als bei handelsüblichen Dehnungsmessstreifen auf Metall- und Siliziumbasis. Die unterschiedlichen mechanischen zyklischen Belastungen, denen die Prototypen ausgesetzt werden, beeinflussen den Grad der Reaktionshysterese und die Linearität

des Dehnungsbereichs. In beiden Fällen erweisen sich die Tests unter Druckbelastung gegenüber den Dehnungsversuchen als überlegen. Mit diesen Ergebnissen liefert die vorliegende Arbeit einen funktionierenden Dehnungsmessstreifen-Prototyp auf der Basis eines SiOC-basierten Dünnfilms mit hoher Empfindlichkeit, Reproduzierbarkeit und Robustheit. Die sehr hohe Empfindlichkeit des hergestellten Dehnungsmessstreifens bei erhöhter Temperatur (bis 700 °C) übertrifft die bekannte Anwendung der aktuellen kommerziellen Dehnungsmessstreifen. Darüber hinaus ermöglicht die beobachtete Veränderung des elektrischen Verhaltens des Materials bei 460 °C einen Einsatz als Strombegrenzer und Temperatursensor.

Table of Contents

Declaration of Authorship v
Acknowledgments vii
Abstract viii
Abstract ix
Table of Contents 1
1. .... Statement of the Problem 2
2. .... Background of the study 4
2.1. History of piezoresistivity 4
2.2. State of the art of piezoresistivity on ceramic materials 4
2.2.1. Piezoresistive effect in carbon-containing semiconductors 5
2.2.2. Piezoresistive effect in carbon-containing ceramic nanocomposites 6
2.3. Piezoresistivity in SiOC system 6
2.3.1. Morphology and Composition 7
2.3.2. Conduction mechanism 8
2.4. Piezoresistivity and MEMS technology 11
2.4.1. Fundamentals 11
2.4.2. Devices, Methods, and Applications 12
2.4.3. Device design, challenges, and tradeoffs 17
2.5. Research Framework 19
2.5.1. Design of Experiment 19
2.5.2. Statistical Approaches 20
3. .... Results and Discussion 21
3.1. Thin film deposition optimization 21
3.2. Thin film chracterization 22
3.2.1. Morphology and composition 22
3.2.2. Electrical property and conduction mechanism 29
3.3. Piezoresistivity Test 32
3.3.1. Thermal coefficient of resistance 32
3.3.2. Degree of hysteresis 34
3.3.3. Gauge Factor 36
4. .... Implications, Conclusion, and Outlook 41
5. .... References 44
I...... List of Abbreviations 56
II..... List of Symbols 58
III.... List of Figures 60
IV.... List of Tables 62
V..... Cumulative Part of the Thesis 63
VI.... Curriculum Vitae 65

1. Statement of the Problem

Thin film technology is at the developmental lead of solid-state electronics with more than 20,000 publications in recent years dedicated on the emerging demand for device miniaturization [1]. Such demands operate as a driving force of curiosity, both in the academic and industrial fields, to study the behavior of two-dimensional solids including metals, ceramics, and semiconductors. Known as one of the first microelectromechanical systems (MEMS) devices, piezoresistivity-based sensing devices offer a diverse range of applications such as force, pressure, accelerometers, and inertial sensors which are recognized but not restricted to the fields of automotive, ventilation, and air conditioning, and recently for healthcare dealing with wearable devices for health monitoring [2–6]. The precision and conciseness of instrumentation of piezoresistive sensors contributes as a main factor for its share on the MEMS sensors market today. In a 2019 market survey, a 12.6% compound annual growth rate of market share is expected of piezoelectric and piezoresistive devices which translates to a projection of US$ 48.5 billion in 2024 [7,8].

At the moment, the commercial piezoresistive sensors are dominated by metal and silicon-based strain gauges. The gauge factor (GF) of metal strain gauges is about 2 [9] at room temperature while silicon-based strain gauges showed more superior performance with GF equal to 150 [10] and a regulated performance at temperature below 250 °C. In spite of the long period of existence of metal and silicon-based strain gauges on the market, both missed the mark of being a formative element for high-temperature strain measurement due to its nonlinear response at high-temperatures which has restricted its applications in the development of turbines, motors, generators, or air-breathing engines [11–13]. The electrical resistance of strain gauges varies not only with strain but also with temperature which is currently compensated by using auxiliary devices which alters the configuration of the device, or via simulations. In practice, Wheatstone bridge either quarter-, half-, or full-, is the best method in place which uses two identical strain gauges mounted on the test material at the same temperature [14]. Alternatively, mathematical equations are used to control the digital architecture of the device with the use of analog to digital converters [15].

Going through the process chain of strain gauge development, material selection is a critical segment in designing the high-temperature capability of the device. In this work, a particular interest is given on silicon oxycarbide (SiOC), a polymer-derived ceramic, which has shown good thermal resistance, abrasive resistance, electrical conductivity, piezoresistive behavior, and have been a promising coating material to be used in hostile environments such as high temperatures, moisture, and corrosive atmosphere [16–19]. The work of Rosenburg in 2018

established the GF of this material to be equal to 45 for a monolithic sample. Heretofore, published works extensively engrossed on synthesis routes, methods of characterization, and discovery of new types of polymer-derived ceramics (PDCs) [16,19]. Such breakthroughs catapulted PDCs to great advancement although most of these studies are done on powders, fibers, and monolithic samples, whereas comparatively scarce are managed on thick and thin-film samples. This work is handled systematically with classified checkpoints to monitor the progress of the study. Three main sections are defined and chronologically studied and published which includes:

i. *Thin film deposition.* This work is cautiously designed to integrate the prevailing expertise on piezoresistive behavior of SiOC and mark an effective transfer of knowledge from monolithic to thin film sample. A design of experiment is prepared to optimize the deposition of thin film guided with statistical analysis all through the course.
ii. *Thin film characterization.* Corroborative methods are employed to grasp of comprehensive understanding of the SiOC film which unveils the microstructure and composition the material. Carbon diffusivity to the silica layer of the silicon substrate is also made to apprehend the relation of structural changes between the interfaces. Investigation of the electrical properties of the SiOC film focused on its charge carriers are also studied and correlated to the piezoresistive behavior of the material.
iii. *Strain gauge design and investigation.* Finally, a strain gauge prototype is prepared and examined under mechanical cyclic loads, tensile and compressive from 25 – 700 °C. Other design considerations such temperature coefficient of resistance, sensitivity, and degree of response' hysteresis is also taken into consideration.

Fundamentally, this work delivers a fully-realized strain gauge prototype based on SiOC thin film with high sensitivity and an operational temperature until 700 °C.

2. Background of the study

2.1. History of piezoresistivity

The discovery of piezoresistivity happened in the late nineteenth century (1856) by William Thomson better known as Lord Kelvin [20]. Using a modified Wheatstone bridge configuration, Lord Kelvin stretched similar-length copper and iron rods parallel to each other with weight and recorded the resistance change. Given the precision of the Wheatstone setup that he used, he postulated that the effect is due to the variation of the conductivities of the two samples considering that both rods have analogous elongation. Following the work of Lord Kelvin, H. Tomlinson performed a critical investigation of the effect of strain-induced change in resistance of several metals [21,22]. This process has been extended and refined toward polycrystalline and amorphous conductors [23–25]. In 1930, Rolnick studied the resistance of different metallic wires upon vibrational loads [26]. Almost 80 years after the first discovery, the term piezoresistance describing the correlation between the relative change in the resistance of a material and the applied stress was coined by Cookson in 1935 [27]. The etymology of the term "piezo" is rooted in the Greek term "piezein" which means to press. The piezoresistive effect was studied on semiconducting materials by Bardeen and Shockley in 1950 when a large change in conductivity in a single-crystal semiconductor element like silicon, germanium, and tellurium was linked to the change in the intrinsic conductivity and resistance of a p-n junction upon applying pressure [28]. In 1954, Smith confirmed this idea and demonstrated a change of resistivity occurring in silicon and germanium (both p- and n-type) upon application of uniaxial tension. These results were described in terms of a pressure coefficient of resistivity and two shear coefficients [29]. In 1956, Morin was able to demonstrate the temperature dependence of the piezoresistance of silicon and germanium [30], and a year later, the first silicon-based strain gauge was made by Mason and Thurston [31], which opened up the production of piezoresistive sensors in the market.

2.2. State of the art of piezoresistivity on ceramic materials

This section and its subsections have been published in:

[1] Ricohermoso, E.; Rosenburg, F.; Klug, F.; Nicoloso, N.; Schlaak, H.F.; Riedel, R.; Ionescu, E. **Piezoresistive Carbon-Containing Ceramic Nanocomposites – A Review.** *Open Ceramics* **2021**, *5*, 100057, doi:10.1016/j.oceram.2021.100057.

2.2.1. Piezoresistive effect in carbon-containing semiconductors

Piezoresistivity on semiconducting materials are mostly based on one-dimensional descriptions of electron and hole transport in crystalline structures under strain. The first discovery of Smith was based on the shifts on the bandgap energies [29]. Tufte and Stelzer were able to demonstrate in a study published in 1963 the piezoresistive properties of n- and p-type layers formed by the diffusion of impurities into silicon [32]. The mobilities and effective masses of the charge carriers are significantly different from one another and fluctuate under strain. The magnitude and signs of the piezoresistive coefficient were found to be associated with several factors including crystallographic directions, impurity concentration, temperature, and stress applied to the material. Several studies supported this relationship of carrier characteristics and strain [31,33–35]. The Herring's Many-Valley model proposed the symmetrical valleys along the <100> direction wherein in their basic state, the centerline of a constant energy ellipsoid with the minimum energy level is occupied by valence electrons [35]. The mobility of the electrons is at its highest perpendicular to the long axis of the ellipsoid. Asymmetrical dilation of the ellipsoid during external stress application causes in an anisotropic change of the charge mobility which is proportional to the applied stress.

For most piezoresistors, two arrangements between strain and resistance change are of interest resulting in a longitudinal and transversal piezoresistive effect. The longitudinal effect describes the change of the resistance parallel to the applied strain, while the second transverse effect describes the change to a perpendicular applied strain. The effective values for the longitudinal piezoresistive coefficient π_l and the transverse piezoresistive coefficient π_t can be calculated from the coefficients π_{ij}. For anisotropic materials such as doped silicon π_l and π_t strongly depend on the crystal orientation of the resistor as the mobility of the charge carrier is anisotropic upon the strain. For lightly doped silicon (p- or n-type < 1018 cm^{-3}) relatively high piezoresistive coefficients are obtained compared to higher doping concentrations. Regardless higher dopant concentrations are used more often as the temperature effect on resistance and sensitivity is much lower. In general, piezoresistors with larger sizes give better sensitivity and lower noise values. Commercially available microsystem devices are usually based on silicon and germanium and their alloys. In 1989, the piezoresistive effect on polycrystalline silicon showed that the conductivity change of the material due to stress is a result of the shifting of relative sub-bands and the carrier transfers [36]. The study also confirmed the theory of the difference in longitudinal and transverse strain measurements caused by the anisotropy of piezoresistance in silicon.

2.2.2. Piezoresistive effect in carbon-containing ceramic nanocomposites

An inorganic composite is a solid material consisting of at least two inorganic material phases. If one dimension of the embedded material phase is on a nano-dimensional scale, the composite can be considered as nanocomposite [37]. Besides the different features of each component, their distribution and geometry play a certain role in defining the resulting properties of the new composite.

There are two methods of functionalization which are considered in this work. In the first method, the carbon phase is mechanically mixed into the ceramic composite by using dispersing agents to prevent agglomeration. The second method refers to the polymer-derived ceramic route [19,38–41]. Here, the carbon phase is generated in-situ during the polymer to ceramic transformation. In the following section, we look at differently prepared piezoresistive nanocomposites, with a nano-dimensional carbon phase embedded into an insulating ceramic bulk matrix.

2.3. Piezoresistivity in SiOC system

Since the first reported synthesis route of PDC by Fritz and Raabe in 1956 [42], when monomeric organosilicon compounds were transformed to SiC through a thermal process at low-temperature conditions, numerous processes, and applications for PDC have been explored due to their excellent homogeneity as well as stability at high temperatures and in harsh environments. Silicon oxycarbide (SiOC), a type of PDC mostly derived from polysiloxanes, is of interest because of its wide array of outstanding properties including Li-storage capacity [43–45], thermal shock resistance [46], high resistance to crystallization, and low creep rates up to very high temperatures [47–49], gas sensing behavior [50,51], and piezoresistivity [16,52–54]. In this section, the conduction mechanism in SiOC system will be highlighted which is fundamental to understanding the piezoresistive property of SiOC.

2.3.1. Morphology and Composition

Silicon oxycarbide (SiOC) is a PDC type in pursual of a corner-sharing tetrahedra structure of SiO_4-xCx (x = 0 – 4) [55] and can be described as a glassy network of vitreous silica glasses, with oxygen being partly replaced by carbon. Generally, SiOC/C glasses can be prepared from networks of Si-R bonds (R = H, CH_3, CH_2CH_3, C_6H_5, ...) which can be produced from precursor containing organosiloxanes via the PDC route or the sol-gel process. In this study, majority of the work is focused on two preceramic polymers with free carbon weight percentages below the percolation threshold of SiOC pyrolyzed at 1400 °C, ~20 wt.% [56–58], namely MK PMS and SPR as illustrated in Figure 2.3-1.

SPR - 212

MK PMS

Figure 2.3-1. Molecular structural units of preceramic polymers used in this work.
MK PMS contains ~11 wt.% free carbon when pyrolyzed at 1100 °C while SPR 212 contains ~17 wt.% free carbon. For naming convention, samples obtained using MK PMS are called C11 and C17 for SPR 212 samples.

Multiple studies using different characterization methods including IR spectroscopy, Raman spectroscopy, XRD, NMR analysis, TGA/MS, and TEM have been conducted to elucidate the structural transformation of preceramic polysiloxanes into SiOC at different thermal treatment stages [19,40,41,52,55–57,59–66]. Precursors lead to different microstructures and rearrangements depending on the process temperature. Initially, the polysiloxane can be crosslinked via hydrosilation, free-radical initiation, or condensation, which can be assisted with catalysts such as peroxides and metal acetylacetonates. Polymer-to-ceramic conversion of the crosslinked polysiloxane initiates at 400 – 600 °C propelled by the evolution of hydrocarbons mainly CH_4 [60,67–69]. Pyrolysis temperature (T_P) at 600 – 1100 °C results in continuous cleavage of the Si-O, Si-C, and C-H bonds producing free carbons with an onset at 800 °C in an amorphous silicon oxycarbide ceramic phase [70,71]. It has been identified that in the SiOC system, the free carbon phase is always the first one to segregate at 500 °C - 800 °C in the form of polycyclic aromatic hydrocarbons (PAHs). As the heat-treatment temperature increases, these aromatics tend to stack up forming carbon-based basic structural units (BSU) consisting of at least 2 layers with ca. 1 nm lateral extension [41,72]. At 1000 °C – 1200 °C, the aromatic CH groups are unstable leading to hydrogen removal as gaseous H_2 from broken C-H bonds leaving neighboring BSU to form edge-to-edge linkages. This leads to clusters of graphene-like carbon with an increased degree of ordering. Thermal treatment at 1300 °C promotes the crystallization of the SiC phase parting the SiO_2 as the matrix of the material [73]. Bois *et al*, explained with the use of solid-state

^{29}Si MAS NMR, that the glassy network of the SiOC continuously evolves in the temperature range of 1200 – 1600 °C [74] with the phases separating into SiO_3C, SiO_2C_2, and the disappearance of the $SiOC_3$ tetrahedra structure. Above 1400°C, free carbon graphitization is highly favored followed by nucleation of SiC nanometric crystal phases [75]. The SiC phases are associated with the BSUs serving as nuclei which promote stacking of alternate Si and C atom layers. At 1500 °C, the evolution of β-SiC and an sp^2 -hybridized segregated carbon phase has been confirmed by XRD analysis [76,77]. Additional heat-treatment above 1700 °C results in the ordering of crystallites forming misaligned graphene sheets stacked in a turbostratic manner [78,79].

2.3.2. Conduction mechanism

Several studies on SiOC ceramics showed conductive behavior having conductivity values ranging from 10^{-3} to 10 S/cm at room-temperature conditions [56,79,80]. In 1935, Bruggeman's symmetric and asymmetric effect medium theory (EMT) was first used to predict the electrical properties of composite materials [81]. In both cases, symmetric and asymmetric, modelling the conduction mechanism of nanocomposites is limited by several factors; (1) Asymmetric model is commonly used for dispersions such as oils and foams and does not allow percolation, (2) Symmetric model is a volume-weighted approximation of ellipsoids ignoring the fractal and long-range correlations of the filler materials, (3) Both models are reduced on 2-dimensional percolation [82].

Considering the nonlinear behavior of composite materials in the insulator-conductor zone, the bond percolation theory (PT) was formulated to describe this electrical conductivity phenomenological change [83]. Bond percolation theory describes randomly-oriented interconnected clusters forming a continuous network to predict certain properties such as thermal conductivity, electrical resistivity/ conductivity, and diffusion constants [83–87]. In this model, highly conductive fillers of concentration Φ_C are added to an insulating matrix forming a continuous path until it approaches the critical concentration, Φ_{Crit}, or the percolation threshold. Once the threshold is reached, an abrupt change in conductivity is recorded and the overall conductivity of the composite can be expressed using Equation 2.3-1.

$$\sigma_C = \sigma_0 * (\Phi_C - \Phi_{crit})^t \quad \text{Equation 2.3-1}$$

where σ_0 is a proportionality constant, σ_C is the conductivity of the composite, and t is the critical exponent. The critical exponent t is known to be dependent on the dimensions of the lattice and was calculated to $t \approx 2.0$ in the three-dimensional state [88–92]. As explained by Balberg, the t value can have high values up to 6.0 depending on the variations of the tunneling distance involve in the tunneling-percolation mechanism [93,94]. In context, the electrical conductivity of

the SiOC follows the bond percolation theory wherein it is dependent on the amount of randomly distributed conductive particles (graphitic carbon and SiC) forming a continuous network of conductive paths [83,84,95]. The dependence showed attribution to the nature of the percolating system which is reliant on the aspect ratio of the free carbon phase [87].

Rosenburg *et* al showed the logarithmic dependence of the SiOC conductivity from the content of segregated carbon of the sample as shown in Figure 2.3-2C [56]. At 1600 °C, the SiOC sample with 6 vol% free carbon phases exhibited a *t*-value equal to 4.3, comparable to the *t*-value of a well-known fine dispersed composite, RuO_2/silica.

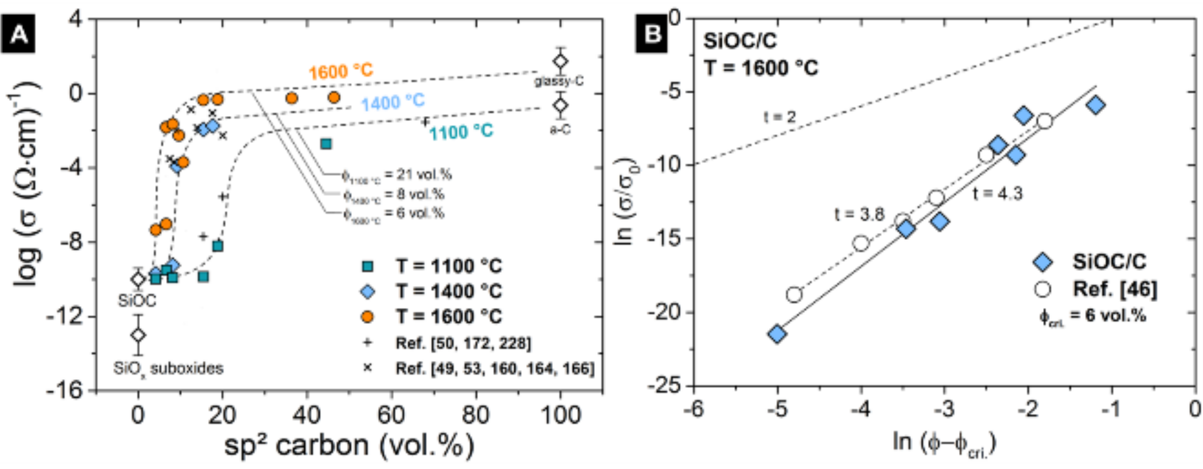

Figure 2.3-2. Effect of heat-treatment temperature on the RT-conductivity of C-11 and C-17 samples. A) Logarithmic room-temperature conductivity of SiOC vs free carbon concentrations. B) derivation of critical exponent (*t*) as a function of conductivity vs free carbon concentration.

In 2000, Cordelair *et al* used the General Effective Media (GEM) Theory [96] to explain the electrical conduction mechanism of SiOC ceramic derived from polysiloxane which combines the EMT and PT models [97]. In this case, the free carbon phase concentration is above the percolation threshold which results to direct transportation of charge carriers, illustrated in Figure 2.3-3a. In this model, the percolation threshold was found to have a high dependency on the morphology of the particles namely the size and shape (aspect ratio). The formation of a ribbon-like shape of free carbon which has a high aspect ratio was found to be beneficial to lower the percolation threshold of a PDC system.

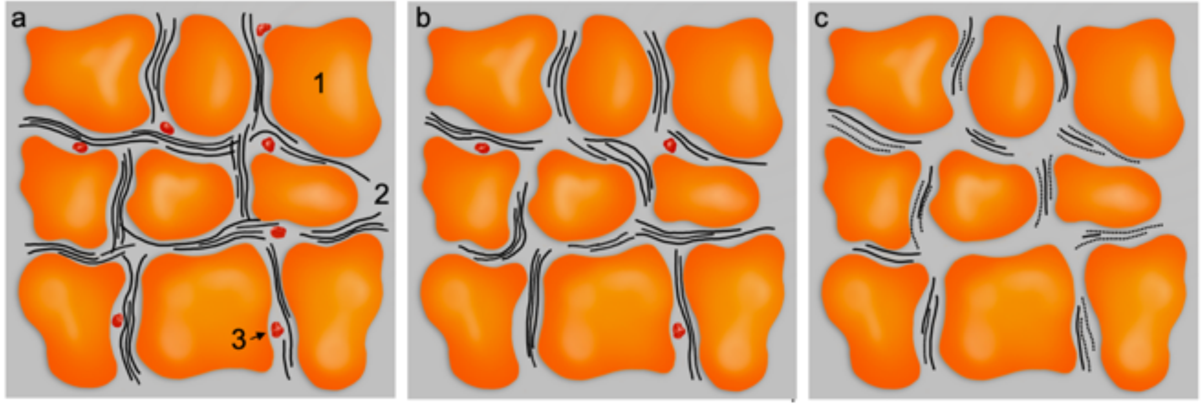

Figure 2.3-3. Models for the microstructure of PDCs in different conducting regimes [97]. (1), (2), and (3) are Si-based nanodomains, free carbon ribbons, and SiC nanoparticles, respectively.

In the second model, Figure 2.3-3b, the concentration of the free carbon phase is lower than the percolation threshold but is high enough to have tunneling conduction between the neighboring free carbon clusters [98,99]. In this state, the clusters or the ribbons are not interconnected but keeps a small distance between their neighboring cluster. This conduction mechanism is called the tunneling-percolation regime. In Figure 2.3-3c, the concentration of the free carbon phase is even lower than the tunneling-percolation regime. In this conduction mechanism named as the semiconducting regime, the semiconducting behavior of the PDC plays a major role wherein the conducting mechanism follows the hopping process of the charge carriers between the interconnected cages of carbon as described in Figure 2.3-3.

Correlating the microstructure discussion on page 7, conductivity of the material can be divided into three temperature regimes. In the first regime between 1000 and 1300 °C, the material is still amorphous state and displays a semiconducting behavior with a $T^{-1/4}$ dependence of σ_{dc} [100]. The semiconducting regime can be explained by the Variable-range Hopping (VRH) mechanism and can be differed into two rubrics depending on the T_P [101,102]. For PDCs pyrolyzed below 1200 °C, and $kT << E_{gap}$, the direct current (dc) – conductivity (σ_{dc}) obeys Mott's based on Equation 2.3-2 (k is the Boltzmann constant, T is the Temperature, E_{gap} is the energy gap between the Fermi level and conduction band) [97,103–105]. The enhancement of the sp^2/sp^3- ratio of the carbon atoms as temperature rises also increases the conductivity of the sample. In the second regime, T_p=1300–1600 °C, the existence of nanocrystalline SiC particles arise are responsible for the increase of σ_{dc} by the formation of percolation paths throughout the sample. PDCs annealed at a temperature above 1200 °C are more crystalline and behave under the condition of $kT >> E_{gap}$. At this temperature Arrhenius behavior is shown following Equation 2.3-3 wherein ΔE is the activation energy [100,104]. Finally, beyond T_p=1600 °C, when the samples are completely crystalline, the electric conductivity is highly dependent on the amount of SiC

$$\sigma_{dc} = \sigma_0 \exp\left[-\left(\frac{T_0}{T}\right)^{\frac{1}{4}}\right] \quad \text{Equation 2.3-2}$$

$$\sigma_{dc} = \sigma_0 \exp\left[-\frac{\Delta E}{kT}\right] \quad \text{Equation 2.3-3}$$

2.4. Piezoresistivity and MEMS technology

Since the first reported silicon strain gauge of Mason and Thurston in 1957, semiconductor strain gauges have been widely explored due to their room-temperature sensitivity being more than fifty times larger than metal strain gauges, 150: 2 [9,10,106,107]. In the late 1950s, the companies Kulite-Bytex and Microsystems introduced commercial metal-diaphragm pressure sensors [108]. Their design used four semiconductor-based strain gauges attached to a metallic diaphragm, two of which are epoxy-bonded and in tension at the diaphragm center while the other two are attached on the edge. This setup followed the Wheatstone bridge with four active arms allowing a better sensitivity, and first-order temperature compensation. Despite the proper correction method, the device had relatively low performance due to the mismatch between the thermal expansion coefficients of the silicon strain gauge and the metal diaphragm and the relatively poor stress transmission characteristics of the metal-epoxy-silicon interface, which caused creep and hysteresis.

Several advancements in strain gauges followed in the succeeding years. In 1962, Tufte *et al* used dopant infusion to create an integrated silicon pressure sensor within the diaphragm [32,109]. This technology eliminated the use of epoxy and substituted metal diaphragm with single-crystal silicon. In the late 1960s and early 1970s applied three microfabrication techniques; anisotropic chemical etching of silicon, ion implantation, and anodic bonding, were developed. These techniques played a major role in improving the performance of microfabricated pressure sensors. Anisotropic etching and anodic bonding allowed batch fabrication of pressure sensors, reducing the cost of the production. In addition, these technologies enabled miniaturization, increased sensitivity, and precise placement and dose of the piezoresistors. From the 1980s to the present, continued improvements in fabrication technologies, such as photolithography, dopant diffusion, wafer bonding, and thin film deposition, have allowed further size reduction, increase in sensitivity, higher yield, and better performance of the piezoresistors.

2.4.1. Fundamentals

A material's piezoresistivity can be quantified using the gauge factor (GF) which is defined as the ratio of the relative change in resistance ($\Delta R/R$) when the resistor is subjected to a strain, ε, and is expressed by the relation

$$GF = \frac{\Delta R/R}{\varepsilon}$$ Equation 2.4-1

A homogenous structure has an electrical resistance (R) as a function of its dimensions and resistivity (ρ). For a rectangular resistor of length L, width W, thickness H, and the resistivity is expressed by the relation in Equation 2.3-2. When the resistor is strained, Equation 2.4-3 gives the relation of the relative change in resistance ($\Delta R/R$) where ΔL, ΔW, ΔH and $\Delta\rho$ are the changes in the respective parameters due to the applied strain.

$$R = \frac{\rho L}{WH}$$ Equation 2.4-2

$$\frac{\Delta R}{R} = \frac{\Delta L}{L} - \frac{\Delta W}{W} = \frac{\Delta H}{H} + \frac{\Delta \rho}{\rho}$$ Equation 2.4-3

$$\frac{\Delta W}{W} = \frac{\Delta H}{H} = -\nu \frac{\Delta L}{L}$$ Equation 2.4-4

If the resistor is under tension, the cross-sectional area reduces in comparison to the longitudinal strain defined by its Poisson's ratio, ν. The relative change in resistance is then expressed as,

$$\frac{\Delta R}{R} = (1 + 2\nu)\varepsilon + \frac{\Delta \rho}{\rho}$$ Equation 2.4-5

The relation then captures both the change in resistance due to both the geometric effects $(1 + 2\nu)$ and the fractional change in resistivity ($\Delta\rho/\rho$) of the material with strain [26]. In metallic strain gauges, the GF is mainly because of geometry at approximately 1.4- 2.0, while the change in resistivity is too minimal in the order of 0.3. This effect is in reverse for silicon wherein the fractional change in resistivity is in order of 50 – 100 times larger than the geometric term.

2.4.2. Devices, Methods, and Applications

Depending on the materials and fabrication technologies, different piezoresistive strain gauges are available on the market. Common and commercially available strain gauges can be divided into the following two categories depending on the material used (metal, non-metals, and semiconductors), or the process used to fabricate the device (thin film, and thick film).

Metal strain gauges have a large market share, as they show a simple structure, and are inexpensive to manufacture. Metal strain gauges are usually in the form of strips, foils, or nanowires. Transducers are normally in the form of metallic strips typically arranged in a layered composite of metal and polymer films. In metal, as described before, the gauge factor is a result of the change in geometry when stretched and resistivity plays a minor role. In order to increase the usable geometry, etching, or laser processes in meandering form patterned thin metal foils. Protective layers of polymer material ensure better handling and application to the measuring surface. Due to the high conductivity of metals, the resistors are normally in the

range of 120 Ω, 350, Ω, or 1 kΩ and are designed to have a low cross-sensitivity of less than 0.1%. The temperature of operation of such devices can reach about 130 °C with the strain limit of ca. 40 x 10^3 με, while longitudinal and transverse GF is about two and zero, respectively [4]. For applications that require close contact with the strained body, metallic foils are more suitable as these are directly bonded to the body. Because of its particular geometry, the piezoresistors are mounted with the grid parallel to the direction of the dominant strain "longitudinal strain" although the massive body may also experience a secondary "transverse strain", in the orthogonal direction; this, however, is totally neglected because of the null *GF* [4]. In recent years, metallic nanowires, specifically gold and silver, have also been used for the design of piezoresistive sensors for flexible and wearable electronic skin applications [12,110–113]. Due to high conductivity, 63 x 10^4 S/m for silver and 45.2 x 10^4 S/m for gold, the sensing operation only requires a small amount of power consumption. However, both materials have a drawback of having an expensive fabrication process. As an alternative, copper nanowires with conductivity of 59.6 x 10^4 S/m, are comparable with that of gold and silver but are relatively cheaper to make. Nevertheless, copper nanowires have shortcomings due to thermal oxidation and chemical corrosion in harsh conditions leading to loss of conductivity over certain period of time [114].

Due to their high piezoresistivity relative to metallic-based strain gauges, semiconductors form the basis for the most sensitive elements. In comparison, the change in resistance caused by the change in geometry is negligible. Silicon sensor elements exhibit gauge factors two orders of magnitudes higher, up to a maximum of 200, and can reach negative values as well [115]. In terms of fabrication, they belong to two groups, homogeneous and inhomogeneous silicon elements. The production of homogeneous elements involves photolithography and etching methods of uniformly doped silicon. The application is similar to classical metal strain gauges by gluing on. Inhomogeneous elements are made of boron diffusion or ion implantation on silicon substrates that form p-n junctions. This allows integrated and miniaturized sensors with high base resistances of several kΩ for low power applications. However, all silicon-based sensors have a high-temperature dependence, which must be compensated during operation. Further, the low bandgap of 1.12 eV limits the application range of silicon to 200 °C [116,117]. With special designs and single crystalline silicon, a maximum of 400 °C is possible, where the mechanical limit occurs through plastic deformation upon loading. This encourages the use of other materials or semiconductors with higher band gaps and electromechanical stability [118].

Robotics, particularly the field of tactile and flexible sensors focuses on conductive polymers through incorporation of conductive fillers such as carbon fibers and powders which has the advantages of producing lightweight, sturdy, and robust designs. However, such strain gauges

are known to suffer from non-linear responses and high degree of hysteresis commonly originating from weak interactions between the conductive particle and the polymer matrix [110,119]. Several polymers have been adopted for nonmetal strain gauge applications for instance flexible epoxy, polymethyl methacrylate (PMMA), polypropylene (PP), polycarbonate (PC), polyelectrolytes (PE), polydimethylsiloxane (PDMS), and polyvinyl alcohol (PVA) [119–125]. Fillers used in synthesis of conductive polymers are mostly based on different allotropes of carbon such as carbon nanotubes (CNT), nanowires, and graphene due to their mechanical and thermal stability coupled with excellent electrical properties [122,123,126–129].

In 2012, Qiu *et al* developed a biomimetic graphene-based monolith with inherent mechanical property owing to the internal honeycomb structure of the material [130]. Such flexible polymer sensors posed promising characteristics for detecting subtle vibrations with high sensitivity making them suitable as wearable devices for artificial intelligence and health care systems [131–134]. Chen *et al* fabricated a device inspired by a fingertip with piezoresistive pressure detection by embedding the nanoscale CNTs into layers of PDMS mimicking the structure of the fingerprint and the epidermis [135]. In contrast with conventional strain sensors, (i.e., metallic and semiconductor) conductive polymer composites can operate on a nanoscale as both multidirectional and multifunctional high–resolution sensors.

The piezoresistive property of the conductive polymer composites is associated with concentration and the type of filler that is added to the polymer matrix which follows the percolation theory as the conduction mode as discussed in Section 2.3.2. The preparation method is the process of mixing the fillers and the polymer with or without the aid of detergents. Despite the simplicity of the process as compared to metals and semiconductor strain gauges, attaining homogenous distribution of the filler to matrix draws a great challenge to the system [136]. Additionally, the filler to polymer ratio determines the deformability and the conductivity of the composite in inverse relation. Aiming for high conductivity reduces the stretchability of the composite due to high filler content which restricts the field of application of the device as far as stretchable electronics is concerned [137,138].

Another approach is the production of thick film piezoresistors (TFR) with a spread application for hybrid microcircuits. A widely used production method is screen printing and sintering of ceramic materials loaded with functional oxides such as Ruthenium (IV). Strain gauges fabricated in the thick film use organic fluid suspension made with submicron conductive particles and glass grains also called resistive inks. The suspension is deposited on a ceramic substrate (an alumina film 250 – 500 µm in thickness) via screen printing and then dried to remove the volatile components of the paste. Subsequently, it is fired above the glass transition temperature for about 10 minutes leaving the conductive phase embedded in the glass matrix

[139,140]. Current fabrication substitutes include printing of resistors using an inkjet or aerosol processes. Although the average gauge factor is slightly higher with an average of 8-12, sensors based on this principle are not suitable for ultra-high temperatures at present [139,141].

Finally, thin-film systems have shown a great impact on the advancement of strain gauges in recent years. With appropriate substrates, platinum-based strain gauges reach maximum operating temperatures of up to 1000 °C via vapor phase deposition of the thin film [142]. Thin film technology has grown into major research area in recent years encompassing numerous applications including electronics, biosystems, and optical communications. The majority of its applications focus on semiconductor industry with the continuous demand for thin-film transistors, MEMS, large-area displays, and even magnetic data storage [15].

A variety of thin-film depositions processes are currently available and are based on both chemical and physical processes. Chemical vapor deposition (CVD) and physical vapor deposition (PVD) techniques based on liquid and gas-phase chemical processes, glow discharge, and evaporation methods, are routinely used to synthesize thin films but such processes are rather expensive and complex to handle [143,144]. An alternative to these processes is the sol-gel route which is cost-effective and enables the synthesis of materials with complex compositions. The sol-gel method is one of the key technologies in synthesizing multielement epitaxial oxides, carbides, and nitrides films [145–147]. In this work, sol-gel method is also used to deposit oxycarbide film on a silicon substrate.

The spin coating method is common technique utilized to prepare thin films from sol-gel or polymer solutions in a wide variety of industries and technology sectors for silicon wafer coatings due to its simplicity, readiness, and high reproducibility. The use of the spin coating process in nanotechnology has been prevalent, especially for semiconductor applications that require thin films with high uniformity. The thickness of the film depends on several factors such as rotational forces, precursor viscosity, and the adhesion of the solution with the substrate [148,149]. As illustrated in Figure 2.4-1, there are four distinct stages of the spin coating process that are reported to be crucial for homogeneity of the films [150–152].

The first stage of the spin coating process is the deposition of fluid onto the substrate which can be divided into two modes: static and dynamic deposition. The dispense stage normally provides considerable amount of excess solution compared to the required amount in the final coating thickness. Dynamic dispense is the process of dispensing while the substrate turns at low speed, normally at an onset speed of 500 rpm. The dynamic mode uses less resin as it spreads the fluid over the substrate while spinning. In case of substrate or fluid having poor wettability, dynamic mode is advantageous to eliminate the formation of voids. When using fluid with high viscosity, or larger area of substrate, static method of deposition can be more beneficial. In this method,

a small puddle of the solution is deposited on or near the center of the substrate before spinning. Commonly, the amount of fluid can range from 1 to 10 mL depending on the viscosity of the fluid and the size of the substrate to be coated.

Generally, when spin speed is above 1000 rpm, a dynamic dispense is the preferred mode unless special circumstances or difficulties arise. In doing so, several considerations must be followed to get a high-quality and consistent thin film:

i. It is important that the substrate should have reached its desired rotational speed before dispensing the fluid.
ii. The ink should be deposited as close as possible to the middle of the substrate to prevent formation of gap in the center.
iii. The ink should be deposited in one quick and smooth action to prevent multiple coats.
iv. There should not be any bubbles blown onto the surface from the pipette and the tip should never touch the rotating substrate

As spin speeds decrease below 1000 rpm or with very viscous solutions it becomes increasingly difficult to get a high-quality film. A dynamic dispense can be achieved at speeds all the way down to around 500 rpm. However, it becomes more difficult to get complete substrate coverage and so more ink is required as such, the cut-off point can be around 700 rpm, below which the static dispense spin coating method starts to give better film quality.

When using a static dispense it is usual to coat the entire substrate (or at least all the active part of the substrate) before starting the spin coating. However, this is itself can cause several issues. The first is that unless the substrate surface gives particularly good wetting for the ink (i.e. the ink likes to spread out across the surface) then it is usually necessary to use the pipette tip to "pull" the ink across the surface. However, it is of course very important for the pipette tip never to touch the surface of the substrate in the active areas as this can change the surface properties and/or damage any other layer present.

By carefully placing the pipette tip close to the surface such that it touches the edge of the ink droplet, it is possible to move the ink around the surface without touching it. Alternatively, if the edges of the substrate are not critical then the pipette tip can be moved around the edge of the substrate to pull the meniscus around. A third alternative is adding enough ink until the substrate is fully covered.

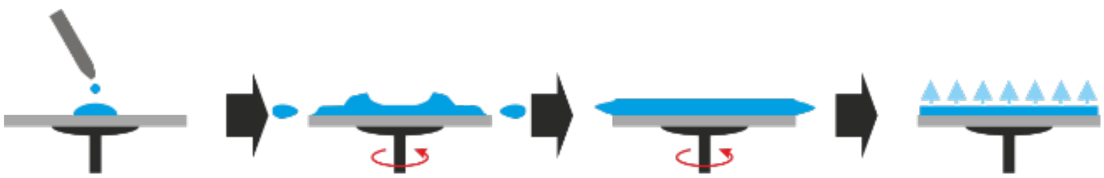

Figure 2.4-1. Illustration of the four stages of the spin coating process.

A) Stage 1: Deposition of solution. B) Stage 2: Spin-up. C) Stage 3: Spin-off. D) Stage 4: Evaporation of solvent.

The second stage is when the substrate is accelerated up to its final desired rotation speed. This stage is usually characterized by aggressive fluid expulsion from the substrate surface by the rotational motion. The third stage is when the substrate is spinning at a constant rate and fluid viscous forces dominate fluid thinning behavior. This stage is characterized by gradual fluid thinning. Fluid thinning is generally quite uniform, though with solutions containing volatile solvents; it is often possible to see interference colors "spinning off" and doing so progressively more slowly as the coating thickness is reduced. Edge effects are often seen because the fluid flows uniformly outward but must form droplets at the edge to be flung off. Thus, depending on the surface tension, viscosity, rotation rate, etc., there may be a small bead of coating thickness difference around the rim of the final film. The fourth stage is when the substrate is spinning at a constant rate and solvent evaporation dominates the coating thinning behavior. As the prior stage advances, the fluid thickness reaches a point where the viscosity effects yield only rather minor net fluid flow. At this point, the evaporation of any volatile solvent species will become the dominant process occurring in the coating. In fact, at this point, the coating effectively "gels" because as these solvents are removed the viscosity of the remaining solution will likely rise.

2.4.3. Device design, challenges, and tradeoffs

Since the discovery of piezoresistance, strain gauges have been designed and analyzed by industry practitioners and academic researchers for diverse applications. Nevertheless, the fundamental tradeoff of piezoresistive-based sensors still lies between the noise and sensitivity of the device. In practice, the device geometry together with the fabrication process must be taken care of simultaneously to reduce the noise while keeping high sensitivity dictated by its gauge factor. Generally, larger dimensions allow better sensitivity and larger piezoresistor size which lowers noise and improves heat dissipation. The noise integrated over the measurement or application frequency band sets the resolution, reported by converting voltage output to the measurement using the sensitivity calibration. Calibration methods vary from device to device but should be accomplished over the temperature range, dynamic range, and bandwidth appropriate to the application.

Except for simple strain measurements, strain gauges are integrated as parts in sensors for physical quantities such as force, torque, and pressure. The fundamental design of all sensors consists of a deformation body, the measuring element, leads, and readout electronics. Force and torque transducers usually have large dimensions with metal strain gauges glued to deformation bodies. Pressure transducers are easier to miniaturize and appear as MEMS in

many devices. The production takes place in cleanroom processes on the wafer level. The most common deformation body for piezoresistive pressure sensors is a diaphragm as shown in Figure 2.4-2.

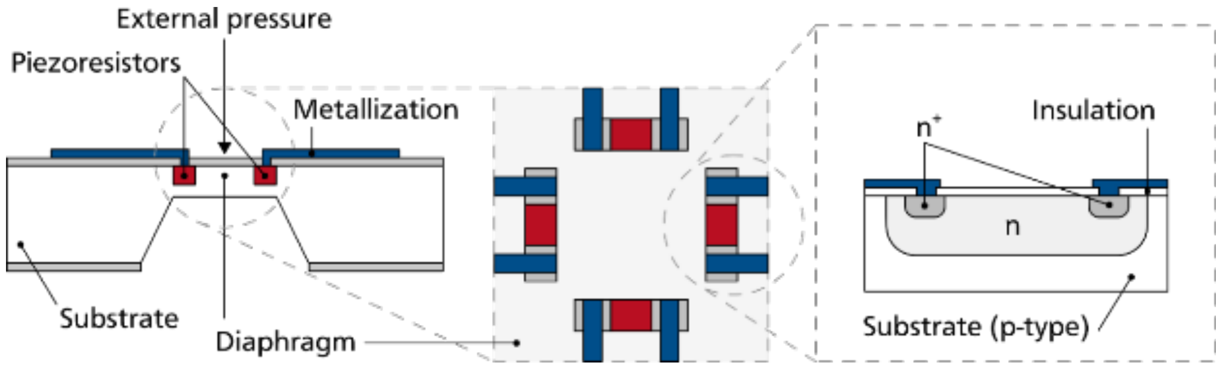

Figure 2.4-2. Typical diaphragm-based design of a piezoresistive pressure sensor illustrated for sensor elements made of p-n-junctions in silicon.

The sensor elements are positioned on the thin and elastic diaphragm so that they are exposed to strain when external pressure occurs. Therefore, the placement of the elements follows the locations of the highest stress. Simple sensors consist of a p- or n-doped silicon substrate with n- or p-doped regions that form the piezoresistive elements. Heavily doped n+ or p+ areas enable low impedance contacts. Metallization or bonding wires serve as electrical supply and signal lines for the sensor elements. Bridge circuits, usually in the form of Wheatstone bridges, evaluate the electrical resistance of these elements. This allows a highly precise acquisition of the accumulating resistances with simultaneous rejection of temperature-induced influences by the silicon. Due to their high sensitivity, high linearity, and simplicity in the evaluation by bridge circuits they are dominating in many industrial sectors. However, the only possibility for use in harsh environments is to shield these elements due to the temperature issues described above, which reduces accuracy while increasing complexity.

The most essential criteria for the design of the sensor are a high sensitivity significantly above a gauge factor of two, low interference from external influences such as temperature or humidity, and established manufacturing technologies to reduce costs. Therefore, the sensor material defines the main properties required for the device. In harsh environmental conditions, not only do the requirements for the functional material become higher, but other materials and the total number of components and processes also become decisive. In addition to temperature and chemical stability, the temperature dependence of the gauge factor should be as low as possible to enable accuracy at varying conditions. Moreover, not only thermal expansion coefficients of the materials must match, but also stable electrical lines and bonding techniques must be available. According to the current knowledge, this combination and the

limitation of suitable functional materials prevents the development of ultra-high temperature resistant sensors above 400-600 °C with high sensitivity comparable to silicon at the same time [118].

In addition to temperature stability, it is desired to use materials that exhibit a high gauge factor and a low-temperature coefficient of resistance (TCR), to minimize any temperature-induced impact on the sensor output characteristics. The TCR is the relative change in resistance per degree of temperature change. It is defined as:

$$R = R_0 [1 + TCR(T - T_0)] \quad \text{Equation 2.4-6}$$

$$TCR = \frac{(R - R_0)}{R_0(T - T_0)} \quad \text{Equation 2.4-7}$$

Where R is the material resistance at temperature T, R_0 is the material resistance at temperature T_0, usually 25 °C. For high-precision resistors, this specification is typically expressed in per °C, with reference to normal room temperature, typically 25 °C. For instance, Constantan and NiCR 80/20 alloys, which are commonly used strain gauges, have TCR values of 40 $°C^{-1}$ and 85 $°C^{-1}$ for bulk materials, respectively [153]. On the other hand, silicon, germanium, and amorphous carbon have TCR values of -0.075 $°C^{-1}$, -0.048 $°C^{-1}$, and -0.0005 $°C^{-1}$, respectively.

2.5. Research Framework

Statistics is needed when analyzing data of an already completed experimental work is probably one of the common misconceptions there is when conducting a research work. According to the book of Practical Statistics for Medical Research by Douglas Altman, "research design is arguably the most important aspect of the statistical contribution to both clinical and non-clinical research" [154]. In fact, only considering statistical issues at the final stage of research draws ambiguous lines leading for past mistakes in the project methodology unidentified and uncorrected.

2.5.1. Design of Experiment

Design of experiment has been used as a powerful tool introduced by R. A. Fischer in England in the 1920s to study the effect of multiple variables simultaneously [155]. It is a laborious approach that allows practitioners to make an explicit model of relationships among the variables in the system. This technique helps to make an informed decision at the early stage of research to arrive at a better solution in less time. Despite the advantages, DOE is more rigorous as compared to traditional experimental techniques such as trial-and error, and one-factor-at-a-time methods. It requires a huge number of experimental trials which can be time consuming and needs a lot of personnel or financial resources.

In the 1940s, Dr. Genichi Taguchi introduced a new method which is more user-friendly, and a standardized version of DOE. It is based on orthogonal array of experiments which gives much reduced variance for the experiment with optimum settings of control parameters. This method determines the robustness of the design by taking the prime permutation of design parameters from a minimum number of experiments hence ensuring the reproducibility of the results. The Taguchi method considers the means and the signal-to-noise (S/N) ratio of the results to reduce the variability of the design. The S/N ratio is the response tradeoff when setting the mean value to the desired level while keeping the variance low [156–158]. The S/N ratios are defined so that a maximum value of the ratio minimizes variability transmitted from the noise variables [156].

2.5.2. Statistical Approaches

A. Analysis of Variance

Analysis of variance (ANOVA) is a statistical tool pioneered by Sir Ronald Fischer to test the hypothesis that the means of two or more populations are equal [159]. The technique performs comparison of variances, thus the name “analysis of variance”, within the group and between the groups. In this way, the factors can be classified as a separate population with entirely different characteristics from the rest, or as a part of a bigger population with interdependent effect on each other. ANOVAs assess the importance of one or more factors by comparing the response variable means at the different factor levels. The null hypothesis states that all population means (factor level means) are equal while the alternative hypothesis states that at least one is different.

B. Process Capability Sixpack

The purpose of the process capability analysis involves assessing and quantifying variability before and after the product is released for production, analyzing the variability relative to product specifications, and improving the product design and manufacturing process to reduce the variability. Variation reduction is the key to product improvement and product consistency [160–162]. The process capability analysis is useful in determining how well the process will hold the tolerances set between the desired specifications. The analysis can also be useful in selecting or modifying the process during product design and development, selecting the process requirements for machines and equipment, and above all, reducing the variability in production processes.

3. Results and Discussion

3.1. Thin film deposition optimization

This section has been published on the reference mentioned below.

[2] Ricohermoso E, Klug F, Schlaak H, Riedel R, Ionescu E. Electrically conductive silicon oxycarbide thin films prepared from preceramic polymers. International Journal of Applied Ceramic Technology. 2021 May 17;19(1):149–64.

Thin film application of PDC has exhibited criticality on its thickness due to cracking and spallation. According to the work of Barroso et al, coating thickness of up to 10 μm is recommended to get a homogenous and crack-free PDC thin film [163]. In an attempt to get a filler-free coating, Günthner and Kraus showed PDC-based coating with a critical thickness of 1 μm [164,165]. To achieve thicker PDC-based coatings, the use of suitable fillers is required to compensate for the formation of cracks during shrinkage of the film [163]. The thickness of the film depends on several factors such as rotational forces, precursor viscosity, and the adhesion of the solution with the substrate [148,149]. In this work, the spin coating process is optimized with three main parameters in consideration namely 1st spin speed, acceleration, and 2nd spin speed. On the other hand, the deviations in solution concentration, working environment conditions, and user effect was considered being the noise factors. The Taguchi method is utilized to analyze the effect of the three factors. The DOE is comprised of 9 trials instead of 27 rivaled to a full-factorial design of the experiment. Considering these values, the S/N ratio of the results was calculated to minimize the response or using the "smaller-is-better" $(S/N)_S$ type. The desired factors resulted in an initial spin speed of 4000 rpm for 30 seconds then accelerated to a second spin speed of 8000 rpm for 30 seconds with an acceleration of 500 rpm/second.

As shown in Table 3.1-1, ANOVA at 95% confidence level revealed the initial spin speed as the main control factor responsible for the film thickness uniformity with a p-value of 0.027, F-statistic (df = 2) of 36.64. Given that the p-values of the second spin speed and the acceleration were both more than the alpha = 0.05, the null hypothesis was accepted stating the insignificance of both factors to the thickness homogeneity. Although statistically insignificant, it is imperative to look at the practical aspect of the experiment. Considering Figure 3.1-1, the significance of using the high initial spin speed has been highlighted by the decreasing number of cracks seen on the surface of the film, however, some cracks are still present on the sample spun at 4000 rpm. These cracks are then eliminated when the effect of the second spin speed

at 8000 rpm is taken into consideration. The film thickness measured with this set of the parameter is approximately 500 nm after the final heat-treatment process.

Table 3.1-1. Analysis of variance of the spin coating control factors with film thickness as the response factor.
The null hypothesis was rejected for initial spin speed having a p-value less than alpha (significance level) = 0.05. (DF = total degrees of freedom; Seq SS = sequential sum of squares; Adj SS = adjusted sum of squares; Adj MS = adjusted mean square of the error; F = variation between sample means; P = probability)

Parameter	DF	F-value	p-value
1st Spin Speed	2	36.64	0.027
Acceleration	2	0.05	0.956
2nd Spin Speed	2	3.34	0.230
Residual Error	2		
Total	8		

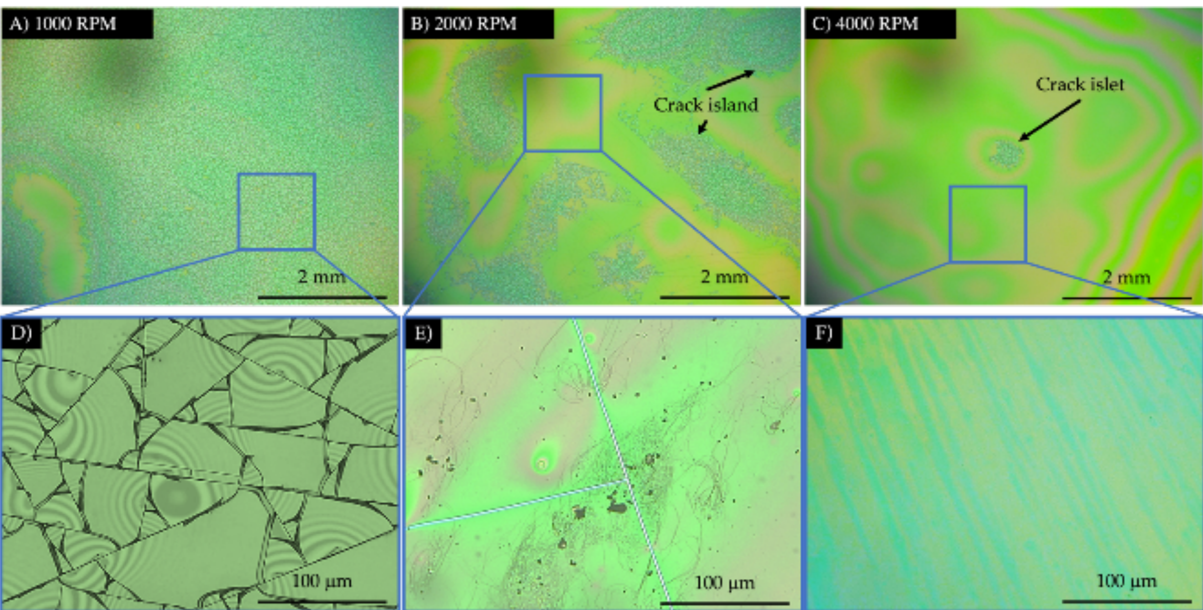

Figure 3.1-1. Optical microscopic images of the thin SiOC polymer film derived from SPR 212 after crosslinking at 250°C. Samples were spin coated at different initial spin speeds with the acceleration of 300 rpm per second, and a second spin speed of 8000 rpm.
(A) At the initial spin speed of 1000 rpm, almost the whole surface is crammed with micro-cracks. (B) Crack islands can be seen on the surface of samples spin coated at an initial speed of 2000 rpm which then decreased as the spin speed was changed to (C) 4000 rpm. (D–F) Magnified areas of images (A–C) highlighting the quality of the film surface.

3.2. Thin film chracterization

3.2.1. Morphology and composition

The content of this section has been partially published on the references listed below:

[2] Ricohermoso E, Klug F, Schlaak H, Riedel R, Ionescu E. Electrically conductive silicon oxycarbide thin films prepared from preceramic polymers. International Journal of Applied Ceramic Technology. 2021 May 17;19(1):149–64.
[3] Ricohermoso E, Klug F, Schlaak H, Riedel R, Ionescu E. Compressive thermal stress and microstructure-driven charge carrier transport in silicon oxycarbide thin films. Journal of the European Ceramic Society. 2021 Oktober;41(13):6377–84.
[5] Ricohermoso E, Vallet M, Haripre E, Solano-Arana S, Riedel R, Ionescu E. Hierarchical microstructure growth in a precursor-derived SiOC thin film prepared on silicon substrate. International Journal of Applied Ceramic Technology. *Accepted 22 July 2022.*

Several models have been proposed regarding the microstructure and composition of SiOC after thermal treatment, two of which are the models from Widgeon et al [55] and Saha *et al* [166]. In the proposed model of Widgeon et al, the structure of SiOC is described to follow a swiss-cheese morphology with a fractal backbone composed of SiC_nO_{4-n} where n denotes the fourfold coordination of Si to C and O, and the voids filled with sp^2-hybridized carbon. The SiC_nO_{4-n} is further characterized into two: (1) oxygen-rich SiC_nO_{4-n} on the interior of the fractal backbone, and (2) carbon-rich SiC_nO_{4-n} on the interface of the free carbon domains and the oxygen-rich SiC_nO_{4-n}. In the work of Saha et al, silica tetrahedra is described to be enclosed in a sp^2-hybridized carbon cage and bonds of SiC_nO_{4-n}. In Figure 3.2-1A, a clear indication of compositional differences is seen on the surface of the C17_1400_3h sample. On the backscattered SEM micrograph in Figure 3.2-1B coupled with EDS analysis, 5 areas were selected and the composition of each spectrum, in wt.%, is recorded as an inset. Spectrum 1 revealed that a high concentration of oxygen is on the matrix of the film while Spectra 2 – 5 are carbon-rich and oxygen-deficient. Interestingly, nitrogen is also present within the formed segregation which can originate from the annealing atmosphere.

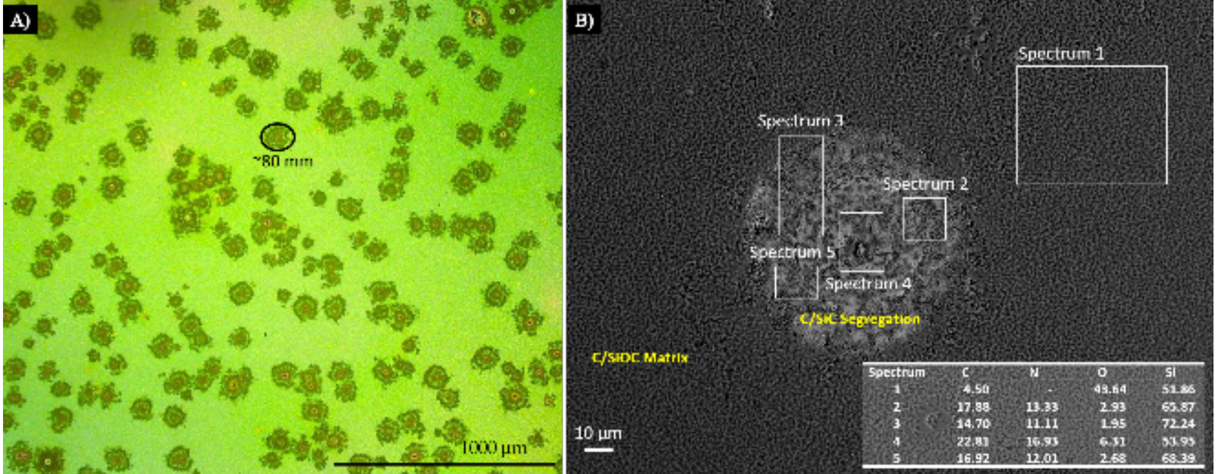

Figure 3.2-1. Morphology and composition of the segregation on the SiOC film surface.
A) Optical microscopic image of the C17-1400 film showing the presence of dispersed particles with ~80 µm in size. B) Backscattered SEM image displaying the color contrast (topographical difference) of the dispersed particle from the matrix of the C17-1400 sample. Five areas are marked where EDS spectra are taken. Results of which are reflected on the inset table.

Raman analysis has been identified as a suitable non-destructive characterization technique for carbon and carbon-based materials where every band of the spectrum corresponds to a specific vibrational frequency of a molecular bond. In particular, carbon materials are typically characterized by three major bands on the Raman spectrum namely the G-band, the D-band, and the 2D-band. Detailed work on these bands has been made to extract indications about the quality and microstructures including crystallinity and level of disorder revealed by the peak positions, peak shapes, and peak intensities [167–170]. Larouche et al expanded the work by considering the tortuosity of carbon domains within the material and defining a new parameter, L_{eq}, by multiplying the tortuosity ratio with the lateral crystal size, L_a [171]. The works of Cançado et al, on quantifying defects have been the basis of this study to calculate the defect density, n_D, and the distance between defects, L_D [167,168].

$$L_a = (2.4 \text{ x } 10^{-10})\lambda_L^4 \left(\frac{\mathrm{A_D}}{\mathrm{A_G}}\right)^{-1}$$ Equation 3.2-1

$$L_D^2 = 1.8 \, x \, 10^{-9} \lambda_L^4 \frac{A_G}{A_D}$$ Equation 3.2-2

$$n_D = \frac{2.4 \text{ x } 10^{22}}{\lambda_\mathrm{L}^4} \frac{\mathrm{A_D}}{\mathrm{A_G}}$$ Equation 3.2-3

$$L_{eq} = 77.0648 \frac{A_{2D}}{A_D}$$ Equation 3.2-4

Listed in Table 3.2-1 are graphitization indices calculated using Equations Equation 3.2-1 - Equation 3.2-4. Increasing the temperature and dwelling have shown to improve the ratio between the D- and G- bands which is further supported by the enlargement of the crystallite size as the temperature progress from 1100 °C to 1400 °C. In Table 3.2-1, calculations are made

separately between the matrix and the segregation. While the L_{eq} on the matrix decreases, a growth is perceived on the L_{eq} within the C-rich segregation.

Table 3.2-1. Graphitization indices of SiOC thin-film samples annealed at different temperatures and dwelling times. Indices were calculated using the Raman spectra using Equation 3.2-1 - Equation 3.2-4.

Sample	A_D	A_G	A_{2D}	A_D/A_G	L_a (nm)	L_D (nm)	n_D (x 10^{12} cm^{-3})	L_{eq} (nm)
Matrix: Oxygen-rich, carbon-deficient								
C17_1100_3h	70.58	8.13	-	8.68	1.93	3.91	2.98	-
C17_1200_3h	18.35	2.99	15.07	6.14	2.73	4.65	2.11	63.31
C17_1300_3h	41.30	6.25	16.29	6.61	2.53	4.48	2.27	30.40
C17_1400_1h	38.49	11.05	12.27	3.48	4.81	6.17	1.20	24.57
C17_1400_2h	33.64	12.67	7.76	2.65	6.31	7.07	0.91	17.78
C17_1400_3h	30.30	14.32	4.94	2.12	7.92	7.92	0.73	12.56
Segregation: Carbon-rich, oxygen-depleted								
C17_1300_3h	41.30	6.25	16.29	6.61	2.53	4.48	2.27	30.40
C17_1400_1h	30.76	8.51	8.45	3.62	4.63	6.06	1.24	21.17
C17_1400_2h	36.99	11.34	18.41	3.26	5.13	6.38	1.12	38.35
C17_1400_3h	18.30	15.21	18.22	1.20	13.93	10.50	4.14	76.74

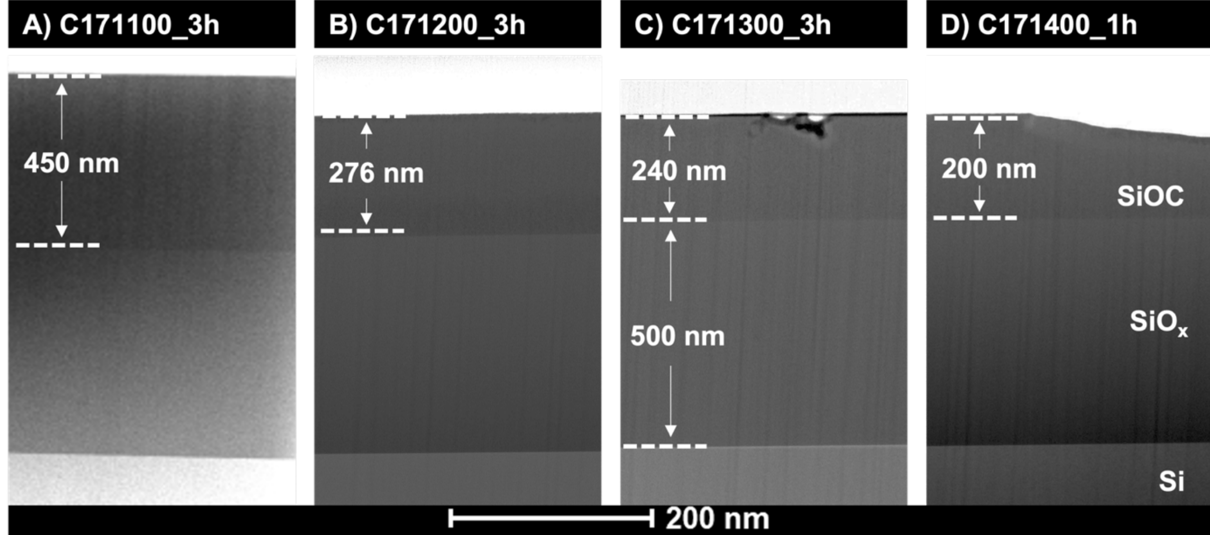

Figure 3.2-2. Cross-section of the matrices of SiOC film samples annealed at A) 1100 °C for 3h, B) 1200 °C for 3h, C) 1300 °C for 3h, and D) 1400 °C for 1h.

To further discriminate the components of the film, cross-sections of samples annealed at different temperatures and dwelling times are prepared and analyzed using FIB, and TEM coupled with EELS and EDS. An inverse proportionality of the film thickness with increasing temperature is evident with the film thickness decreasing from 450 nm to ~200 nm at 1100 °C to 1400 °C respectively. As shown in Figure 3.2-3, a depression is formed on the film wherein SiC started to grow supported by SAED Pattern 3. In SAED Pattern 1, the film manifested to remain in an amorphous state.

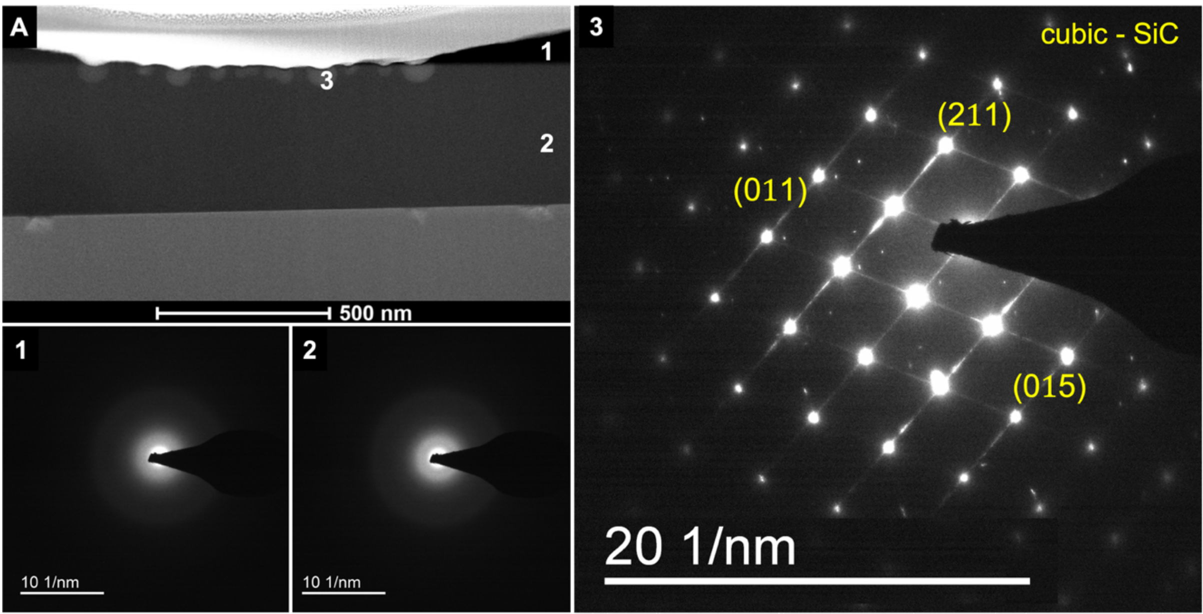

Figure 3.2-3. TEM image of C17_1400_1h sample with an evident thickness depletion with corresponding SAED patterns of (1) SiOC film, (2) SiO2 layer, and (3) stacking fault of SiC.

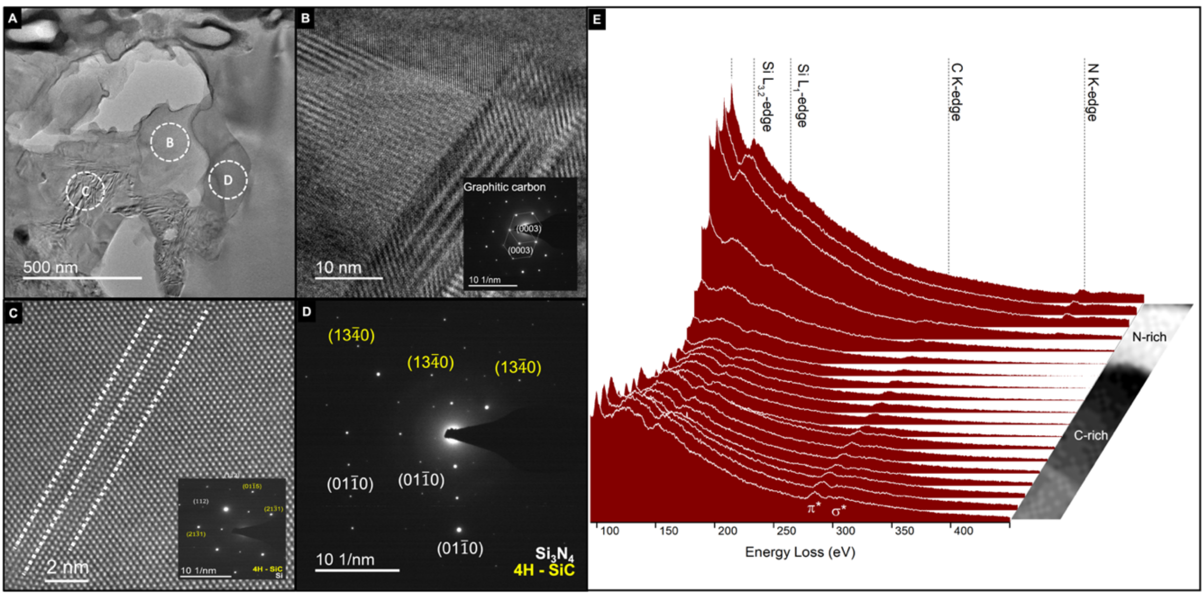

Figure 3.2-4. TEM image and SAED pattern of the A) carbon-rich area of the C17_1400_3h sample, B) 4H-SiC-rich region, C) Hexagonal Si_3N_4-rich region. D) EELS spectra of C17_1400_3h sample taken within the segregation region (C/SiC/N).

The EELS map in Figure 3.2-4 reveals the highly visible Si $L_{2,3}$ edge in all the spectra. This can be differed into the energy loss near edge structure (ELNES) at 120 eV with an onset at 104 eV, and the extended energy loss fine structure (EXELFS) at 150 eV superimposed with the L_1 edge [172–175]. The amorphous O-Si-C units within the region is responsible for the broadened peak at 120 eV with the effect of Si-O-Si bonds at the residual peak at 115 eV [173,175]. The absence of SiO_2 within the C-rich area of the segregation is confirmed by the lack of the sharp peak at 108 eV [172,174]. The mixture of sp^2 and sp^3 carbons are suggested by the broad π^* peaks at 285 eV which

diminishes towards the gray area of the map with the rise of the σ* peak ca. 300 eV [70,173,176,177]. The white region on the map exhibited peaks of N K-edge at 400 eV which supports the presence of Si_3N_4 within the segregation.

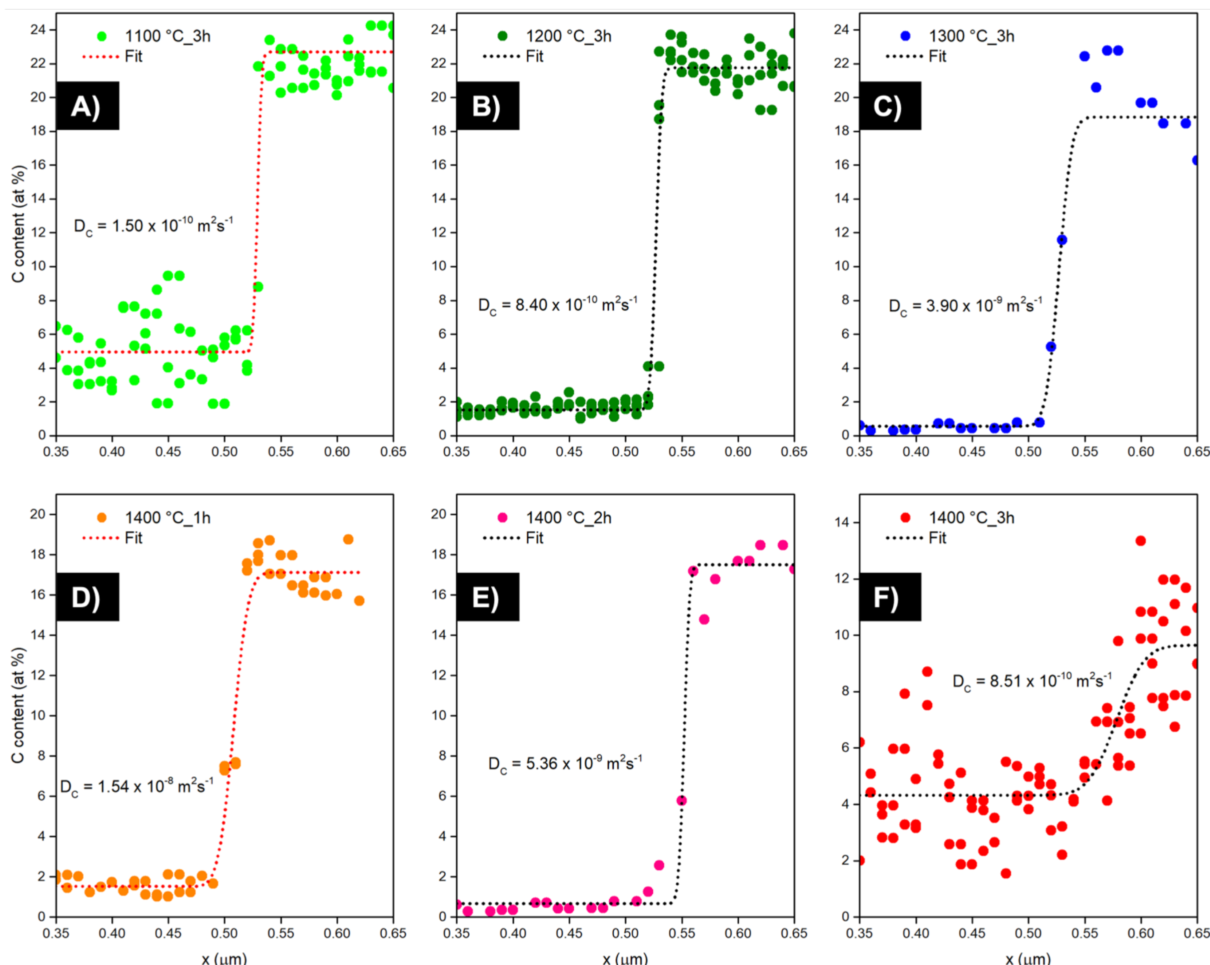

Figure 3.2-5. A-C) Diffusion coefficients of carbon obtained from EDS analysis of carbon profiles of SiOC thin film samples annealed at different temperatures, 1100 - 1300 °C, at 3h dwelling time. D-F) Carbon profiles of isothermally annealed samples at 1400 °C at different dwelling times, 1-3h.

Figure 3.2-5A-C displays the resulting carbon distribution after 3h of annealing at temperatures 1100 – 1300 °C wherein the carbon concentration on the SiOC layer is sustained at ~22 at%. In Figure 3.2-5D-F, isothermal annealing is performed at 1400 °C at different dwelling times, 1 – 3h. The resulting diffusion coefficients at the isothermally annealed samples exhibited an inverse proportionality with increasing dwelling time. The diffusion coefficient at 1400_3h sample is one magnitude lower than the other two samples annealed at 1400 °C. This can be attributed to the low carbon concentration gradient between the film and SiO_x layer which is a result of the growth of C-rich segregations which are more prominent after 3h of annealing at 1400 °C. To keep the carbon concentration at an akin level, the 1400_1h sample is used to compare the diffusion coefficients of carbon at different temperatures.

EDS profiles of the cross-sections presented in Figure 3.2-5 are extracted to determine the diffusivity of carbon between the SiOC thin film and the SiO_x layers depicted in Figure 3.2-2 Using the Fick's second law of diffusion, the carbon diffusion constant (D_C) is estimated using Equation 3.2-5, where c_{max} and c_{min} are the initial concentrations on the interface between the SiOC film and the SiO_x passivation layer, x_0 corresponds to the inflection point of the profile, and t is annealing dwell time.

$$y(x,t) = \frac{c_{max} + c_{min}}{2} + \frac{c_{max} - c_{min}}{2} \operatorname{erf}\left(\frac{x - x_0}{2\sqrt{D_C t}}\right) \qquad \text{Equation 3.2-5}$$

$$D_C = D_0 exp\left(-\frac{E_a}{RT}\right) \qquad \text{Equation 3.2-6}$$

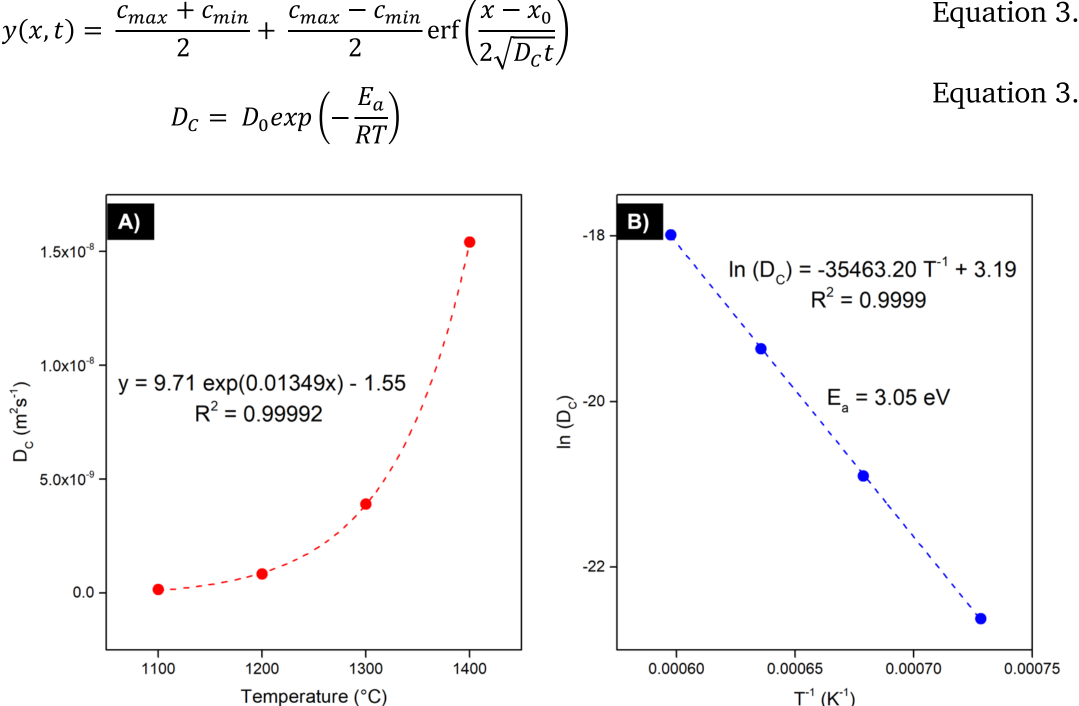

Figure 3.2-6. Diffusion coefficients of carbon obtained from EDS analysis of carbon profiles of SiOC thin film samples annealed at different isothermal temperatures, 1400 °C, for 1 - 3h.

Using the Arrhenius relation in Equation 3.2-6, wherein D_0 is the pre-exponential factor, E_a is the activation energy, and R is the gas constant (8.31 J mol^{-1} K^{-1}), an exponential relationship of the diffusivity with temperature is observed in Figure 3.2-6A. The natural logarithm of the calculated D_C is then plotted against the inverse of temperature to extract the activation energy of the diffusing species which is shown in Figure 3.2-6B. The activation energy is extracted from the slope of the line of the Arrhenius plot resulting in 3.05 eV with an excellent fit of 99.99%, and D_0 equal to 3.19. The calculated activation energy is analogous to the results of Shimoo et al [178], E_a^C = 3.74 eV, obtained from the reduction of SiO_2 with graphite leading to the formation of SiC and SiO as reduction products. In comparison, looking at the potential diffusivity of the three elements present on SiOC, the calculated E_a^C (3.05 eV) of carbon to silica is lower than the activation energy required to facilitate self-diffusion of Si to SiO_2 (E_a^{Si} = 4.56 eV) [178–180] but larger than the activation energy required to diffuse oxygen to silica (E_a^O = 2.54 eV) [114,181]. Increasing the annealing temperature also promotes free carbon segregation which also

increases the C/SiO_2 mixture ratio leading to a significant increase in the production of SiC. Consequently, with more time for annealing, the concentration of carbon left on the SiOC matrix diminishes slowing down the diffusivity of carbon which is evident in Figure 3.2-5D-F.

3.2.2. Electrical property and conduction mechanism

This section is published on the reference stated below.

[3] Ricohermoso E, Klug F, Schlaak H, Riedel R, Ionescu E. Compressive thermal stress and microstructure-driven charge carrier transport in silicon oxycarbide thin films. Journal of the European Ceramic Society. 2021 Oktober;41(13):6377–84.

The average thickness of the SiOC thin film obtained from profilometer measurement was approximately 500 nm. Using these profiles and the sheet resistance measured with the four-point probe, the conductivity of the film was calculated to be in the range of 5.27 to 8.79 S/cm which are 2-3 magnitudes larger than that of the electrical conductivities measured for monolithic samples with a similar chemical composition [56,97,182,183]. Using tunneling AFM (TUNA), a representative area of 95 x 60 μm^2 is scanned using a platinum-deposited cantilever tip collecting current measurements down to sub-picoampere range [184]. The resulting current map is presented in Figure 3.2-7 with the current ranging from 0.001 – 2 nA. In Figure 3.2-7A and B are focused areas of on the matrix and segregation respectively. TUNA is known to have higher current sensitivity than that of the conductive AFM mode which can measure currents down to sub-picoampere range through a highly resistive sample. In principle, the measurement depends on the tip geometry to define the lateral resolution. A bias voltage is applied between the conductive tip and the sample while scanning in contact mode generates topographic and current images [184]. With Figure 3.2-1B, a representative area of 95 x 60 μm^2 was used to map out the AFM-based conductivity of the sample C17-1400 and is presented in Figure 3.2-7. A range of 0.001 – 2 nA was detected forming regions within the map. The current map shown in Figure 3.2-7A, which corresponds to the matrix of C17-1400, indicates that these regions are of varying sizes, and are spaced from each other by approximately 2 µm. In Figure 3.2-7B, which represents the current map of a particle in C17-1400, these regions are denser and more interconnected with each other. Some sites, depicted in dark blue color, show current values above 200 nA with the highest value recorded at 454 nA.

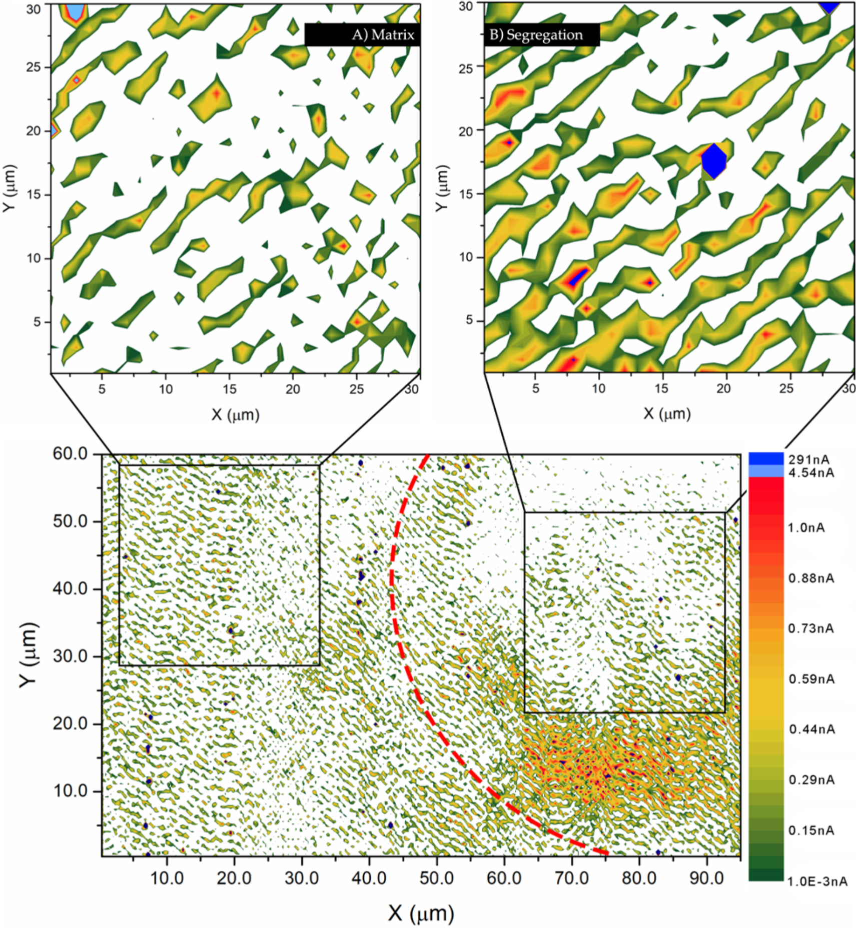

Figure 3.2-7. TUNA current map of the C17-1400 sample including both the matrix and a dispersed particle is shown in Image C. The red dotted line signifies the boundary of the particle from the matrix.
(A) Elongated regions with current values of 0.01 – 2 nA were observed on the C17-1400 matrix with ~2 µm spacing between each other. (B) Elongated regions observed within the dispersed particles are denser and more interconnected as compared to those observed within the matrix. In dark blue are specific areas on the particle with current values above 100 nA with the highest recorded at 454 nA. The current map was recorded with a 5 µm scan at a DC sample bias of 1 V.

In Table 3.2-2, the Hall coefficients (R_H) of the C/SiOC monolith and the thin-film are presented together with the measured charge densities (N) and carrier mobilities (μ_H) obtained using the Van der Pauw method. In both samples, the RH values are positive, indicating p-type behavior with holes as the main charge carrier of the system. With the SiOC film at 500 nm thickness, the carrier densities of both samples, monolith, and thin film, are of the same magnitude. Furthermore, the carrier mobility of the thin film is measured to be 2 magnitudes larger than that of the monolith.

Table 3.2-2. Hall coefficients, charge carrier densities, carrier mobilities, and conductivities of C/SiOC samples with 17 vol% C and heat-treated at 1400 °C.

Parameters	Unit of Measure	SiOC Monolith	SiOC Thin Film
Hall Coefficient (R_H)	$cm^3\ C^{-1}$	0.074	11.25
Carrier density (*N*)	cm^{-3}	6.22×10^{17}	5.55×10^{17}
Carrier mobility (μ_H)	$cm^2\ V^{-1}s^{-1}$	3.0	184.48
Conductivity (σ)	$S\ cm^{-1}$	0.32	16.40

Thus, the electrical conduction occurs in C17-1400 through both the matrix and the dispersed segregations. C17-1400 possesses a hierarchical microstructure which provides appropriate charge carrier transport: firstly, the carbon-enriched micro-sized particles are generated throughout the thin-film upon exposure to 1400 °C and exhibit enhanced electrical conductivity due to the relatively high graphitization degree of their sp^2-hybridized carbon; secondly, sp^2-hybridized carbon is present in the oxygen-rich matrix of C17-1400 and is responsible for the charge carrier transport between the large C-rich particles. Thus, the phase separation of sp^2-carbon, which typically occurs in polymer-derived ceramics at the nanometer scale, corroborates with the precipitation of large C-rich particles at the micro-scale and thus sustains charge carrier transport paths throughout the sample. Interestingly, the formation of the large carbon-enriched particles occurred to an extent that was sufficient to provide a large fraction of highly conductive particles in the SiOC based thin films while keeping an adequate amount of sp^2-hybridized carbon back in the matrix to sustain charge carrier transport between the large particles.

In this context, the electrical conductivity of SiOC follows the bond percolation theory, in which it depends on the amount of randomly distributed conductive particles (graphitic carbon and SiC) forming a continuous network of conductive paths [83,84,95]. The conduction regimes of percolative systems, namely insulating, percolative, and conducting, have been thoroughly discussed in our review manuscript [6]. In the percolative regime, the material can transition from insulator to conductor or vice versa. The sample used in this work contains 17 wt.% of free carbon domains, which is just under the known threshold of SiOC monolithic material, 20 vol. % [56,185]. The formation of SiC within the SiOC thin film increases the aspect ratio of the conductive particle, thus reducing the percolation threshold of the synthesized film, pushing it further into the conductive regime.

Taki et al explained that excess carbon induces shallow impurity levels in SiC, leading to lower activation energy and a 2-magnitude higher conductivity value [186,187]. Commonly, the resistance of a semiconductor decreases below the ionization of impurities at 0 °C. Beyond this temperature, the resistance of the material increases due to the effect of lattice scattering, which is more dominant than the thermal electron-hole generation [106,107].

The observed microstructure in the SiOC-based thin film samples is unique and has not been observed in monolithic silicon oxycarbide. Monolithic SiOC samples were shown to provide charge carrier transport through the formation of a percolative network of sp^2-hybridized carbon via segregation at nanoscale [188]. Whereas in SiOC-based thin films, the electrical conductivity is boosted by the additional in-situ formation of large particles possessing highly

graphitized carbon (see Figure 3.2-8). However, the reason for the formation of the large carbon-rich particles has not been elucidated.

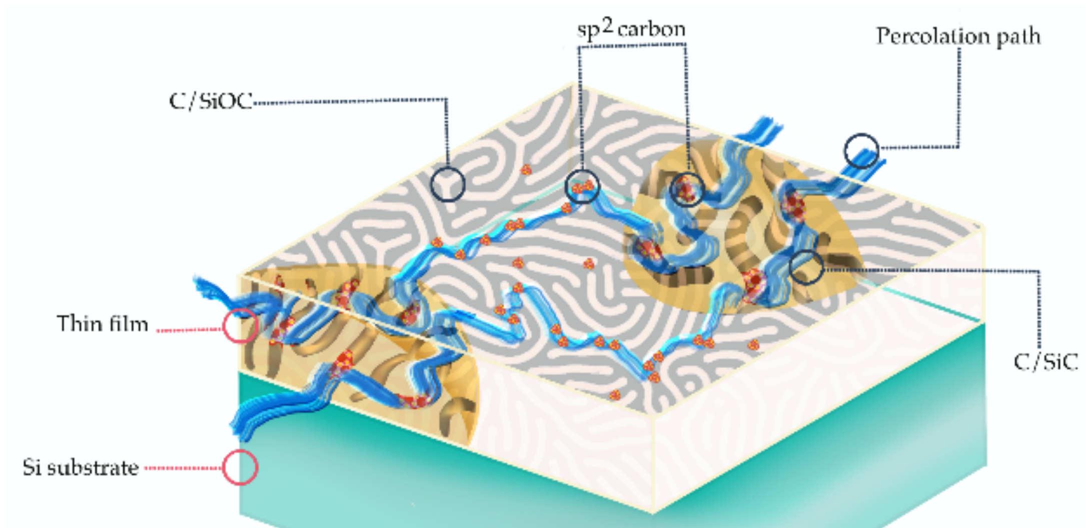

Figure 3.2-8. The proposed hierarchical microstructure of the prepared SiOC thin film.
The large particles containing highly graphitized carbon (represented by the red hexagonal structures). The matrix also contains sp^2-hybridized carbon (small hexagonal structures) and contributes to the charge carrier transport between the large particles. The blue lines represent percolation paths throughout the sample.

3.3. Piezoresistivity Test

This section is published in two parts, room-temperature, and high-temperature piezoresistive behavior of SiOC film, stated on the references below.

[4] Ricohermoso E, Klug F, Schlaak H, Riedel R, Ionescu E. Microstrain-range giant piezoresistivity of silicon oxycarbide thin films under mechanical cyclic loads. Mater Des. 2022 Jan 1;213:110323.

3.3.1. Thermal coefficient of resistance

In-situ measurement of resistance is performed in a temperature range of 25 – 700 °C at a constant heating rate of 12 °C/min with the room-temperature base resistance of the C17-1400-3h samples in the range of 60 - 90 Ω. Intervals of 100 °C is used to differentiate the temperature-dependence of the changes in resistance. The resistance of the SiOC film rises with a positive slope from room temperature until 400 °C before it started to decrease at 460 °C. This behavior is in accordance with the reported temperature-dependent electrical resistivity values of multicomponent materials of Si/SiC, SiO2, and SiC/C [189–193].

The unique phenomenon of the SiOC film ascribing a transition temperature at 460 °C is demonstrated by the temperature coefficient of resistance with notable reversibility replicated three times. This can be accounted to two causes:

i. *A characteristic of conductive systems in pursuit of the bond percolation theory*. Here, an abrupt change in resistance occurs upon heating, leading to the conversion of conductive material into an insulating material or vice versa at a narrow temperature range [194–196]. The difference in the thermal expansions between the conductive filler and the matrix is identified to be responsible for this mechanism. In this work, it is between the graphitic domains and the SiC, and the amorphous SiOC matrix. The thermal expansion can destroy or build the continuous conductive network within the composite and the temperature at which this occurs is called commutation temperature (T_{com}) [195].

ii. *Coexistence of electrons and holes on the system*. At room temperature, electrons and holes can coexist in the SiOC film used in this work, contributed by the presence of graphitic domains and supplementary electrons coming from the SiC. The increase in temperature leads to more vibrations causing more collisions between the lattice and the free electrons. Each collision drains out the energy of the electrons making the delocalized electrons unable to move, resulting in a decrease in the carrier drift velocity. As a result, the current flow decreases, which then increases the resistance of the material. Furthermore, increasing the temperature also promotes the minority holes coming from the H-point ($k_z = 0.5$). With the effect of the Dingle temperature ($T + x$) [197], x being the extra temperature reconciling the theoretical and experimental temperatures, the negatively charged centers tend to scatter holes more strongly than electrons [198,199]. Since the SiOC film behaves as a semiconducting material, it reaches a saturation temperature identified at 460 °C. Beyond this temperature, the electrons from the impurities are swamped by the intrinsic hole carriers of the SiOC film, triggering the resistance to decrease once more. The behavior of both carriers is temperature-dependent, wherein the effect of electrons carried by the SiC and graphitic domains increases with temperature, and is then overwhelmed by the intrinsic carrier after the critical temperature [200].

This property, despite not being the principal motivation for this work, broadens the likelihood of using the SiOC film for applications involving smart materials for current limiting devices and temperature sensors, such as thermistors. Listed in Table 3.3-1 is the calculated TCR of the SiOC film using Equation 2.4-7. Measurements from room temperature up to 460 °C showed a gradual increase in the resistance of the SiOC film resulting in a TCR of ca. 0.004 °C^{-1}. Whilst the temperature surpasses the threshold temperature, the SiOC film becomes conductive as a result of the decrease of the activation energy following the Arrhenius relationship [186]. Based on these values, the TCR of SiOC film behaves in two regimes. Below 460 °C, a positive TCR is observed signifying the increase of resistance with temperature. Above 460 °C, a negative TCR

is calculated which has a similar behavior to nonmetallic strain gauges. The TCR reflects the temperature dependence of the magnitude and direction of the resistivity of the material which is essential in deciding the approach necessary to compensate for the effect of temperature on the strain gauge. Due to the multicomponent nature of the film used in this work, i.e., Si, SiO_2, SiC, and C, TCR is declared per temperature range to explicitly define the applicability of the strain gauge prototype.

Table 3.3-1. Calculated temperature coefficient of resistance of the C17-1400 samples at temperature ranges between 25 °C to 700 °C.

Temperature Range (°C)	TCR (°C^{-1})	Standard Error
25 – 100	0.00139	3.98×10^{-6}
100 – 200	0.00202	5.41×10^{-6}
200 – 300	0.00304	7.56×10^{-6}
300 – 400	0.00404	5.93×10^{-6}
400 – 500	0.00410	7.47×10^{-6}
500 – 600	-0.01698	4.13×10^{-5}
600 – 700	-0.00914	9.78×10^{-5}

In comparison, TCR values of metal strain gauges are in the range of 10 – 10^3 °C^{-1} and can at least operate until 400 °C [201–203]. Platinum film on Al_2O_3 substrate, in particular, has a comparatively large TCR value of 2600 °C^{-1} at 400 °C [201]. Recent developments integrate ceramics in nanocomposites with refractory metals to minimize the TCR of the strain gauges which can operate until 1200 °C, upon considering, for instance, the use of conductive oxides and semiconducting ceramics such as indium-tin-oxide (ITO), gallium nitride (GaN), and titanium aluminum nitride (TIAlN) [204–207]. These ceramic strain gauges demonstrated TCR values that were 2 magnitudes lower than metal strain gauges. Remarkably, the near-zero TCR values calculated for the SiOC film in the present study are comparable to that of TiAlN (-1.75×10^{-4}) which can operate until 350 °C and is prepared using a target of 50% aluminum and 50% titanium alloy sputter-coated in a nitrogen atmosphere [206]. This result imposes a promising temperature self-compensation property of the SiOC film.

3.3.2. Degree of hysteresis

The accuracy of piezoresistive sensor devices is being limited by the hysteresis which in this work corresponds to the relative change in resistance (ΔR) during the strain loading and unloading cycles which do not overlap. The weak interactions between the conductive materials and the amorphous matrix has been pointed out as the source of hysteresis for piezoresistive sensors which mainly follows a percolating mechanism [110,119]. These effects cause slow recovery

of signal with relaxation time that can be more detrimental leading to a permanent change in the initial resistance or the resistance in the absence of pressure.

These results are further supported by Raman analysis data which discriminated the graphitization indices between the film matrix and the phase separation. This is reported in Table 3.2-1 indicating the large free carbon phases on the phase-segregated area as compared to the matrix of the film. The Leq, the average continuous graphene length including tortuosity [171], is 8 times larger on the dispersed segregation relative to the matrix of the film.

$$DH = \frac{|A_{Unloading} - A_{Loading}|}{A_{Loading}} \qquad \text{Equation 3.3-1}$$

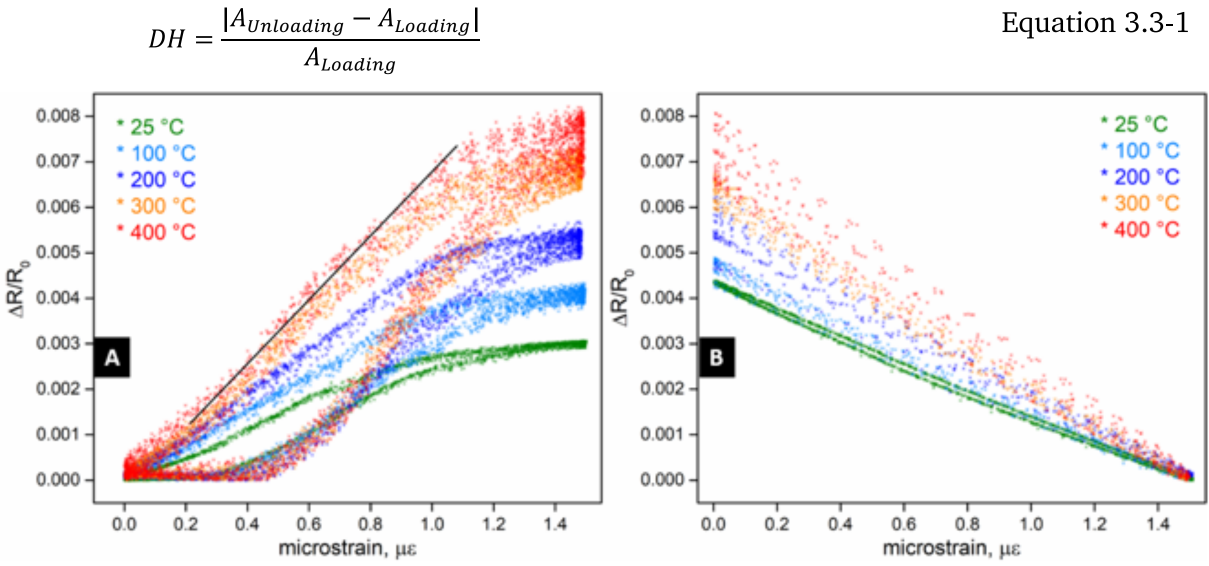

Figure 3.3-1. Relative changes in resistance as a function of microstrain at different temperatures. The gauge factor is derived from the slope of the strain versus $\Delta R/R_0$ after cycling loading in A) Tension and B) Compression.

Using Equation 3.3-1, the degree of hysteresis (DH) in Figure 3.3-1 is calculated, with $A_{Unloading}$ and $A_{Loading}$ representing the areas under the unloading and loading curves, respectively [208,209]. At room temperature, samples under tension revealed a DH value of ca. 15%, which is almost three times larger than that of samples under compression (DH ca. 5.6%). The DH revealed an increasing trend with temperature reaching ca. 30% and ca. 13% under tension and compression, respectively. The typical DH values for strain sensors are above 30 % according to the collected data of Oh et al [209]. The compressive test displayed better linearity with a larger microstrain range application of ca. 1.4, in contrast to 1.0 of the specimens in tension. The strain gauge elements produced in this work possess significantly lower DH values (especially when compression load is applied). The excellent response of the strain gauge from this work with high reversibility of their piezoresistive response which may make periodic calibrations less mandatory.

3.3.3. Gauge Factor

At room temperature, the fabricated strain gauge elements hold giant piezoresistivity. Higher sensitivity of the samples is measured under compression (GF ~ 5 x 10^3 ± 0.20746) than that measured upon tensile load (GF ~ 3 x 10^3 ± 0.38071). Laid out in Figure 3.3-2 is the resistance change of the strain gauge when a compressive cyclic load is applied at different temperatures ranging from 25 °C – 700 °C. Figure 3.3-2A displays that ΔR is increasing with temperature until 400 °C; beyond that, the resistance starts to decrease reaching ca. 11 Ω at 700 °C (Figure 3.3-2B). This response fits well with the behavior witnessed in the TCR calculation. This change in resistance is paramount to the trend of TCR values of the SiOC film as explained previously. The temperature dependence of strain gauges is an irrefutable concern that is pronounced to the community.

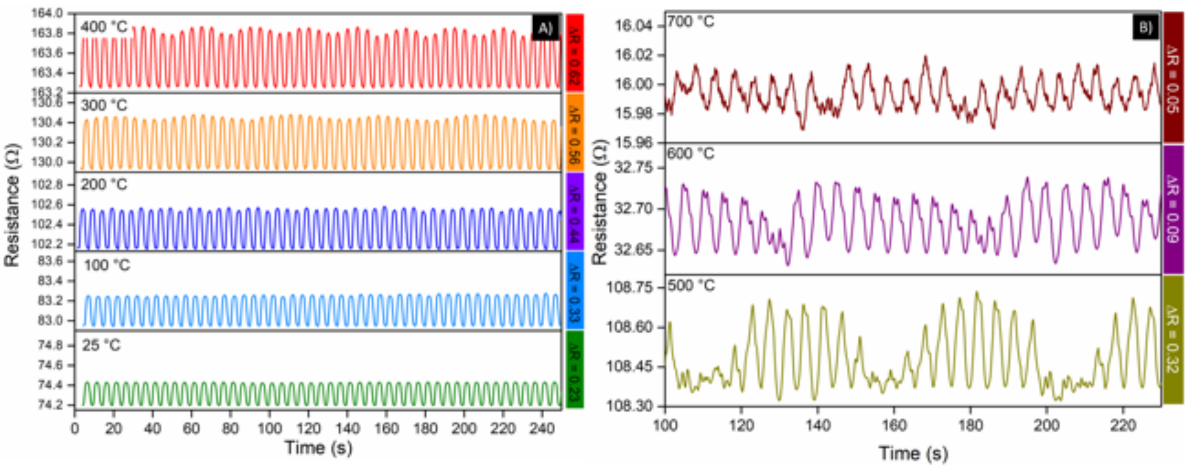

Figure 3.3-2. Resistance response of SiOC film under compressive cyclic load.
A) Representative data of the long-term exposure (4h) of SiOC strain gauge at compressive cyclic load 25 °C, 100 °C, 200 °C, 300 °C, and 400 °C. B) Calibrated data compensating the thermal output at 500 – 700 °C.

It is a common knowledge to use different methods to compensate the effect of temperature on strain gauges. Implementation of Wheatstone bridges configurations, computational methods, use of frequency amplifiers, and self-compensated strain gauges are some of the current practices of different manufacturers [210–213]. In particular, self-compensated strain gauges involve a sensing element with a TCR that can counteract the linear expansion of the measuring object due to temperature variations [204].

In Figure 3.3-3A, a representative performance of the SiOC-based strain gauge under compressive cyclic load at 400 °C runs continuously for 4 hours. An illustration of the film under compressive load is added as an inset on the figure. With three replicates on hand, the response of the device remained perpetual with ΔR ~0.62 Ω. As can be seen in Figure 3.3-3A, the SiOC-based strain gauge can regulate the effect of temperature on its own, credit to having a TCR with a near-zero value. In the 4h-experiment of continuous cycling, while running at high

temperature, the device showed a stable response after ~20 min of exposure time. The 20-minute stabilization time of the device can be accounted for 1) the time it takes for the chamber to reach the set temperature, and 2) the ~2 mm gap between the sample and the heating element. Due to this ability to regulate the effect of temperature, the device eliminates the requirement of having additional compensation procedures both for the physical and computational aspect of the measurement. Three points within the figure are identified to clearly demonstrate the self-regulating property of the device. The first point is the beginning of the measurement process wherein the steepest slopes are calculated. The second point at ~20 min represents the stabilization point, while the third point is the end of the 4-hr cycling process exhibiting a stable response.

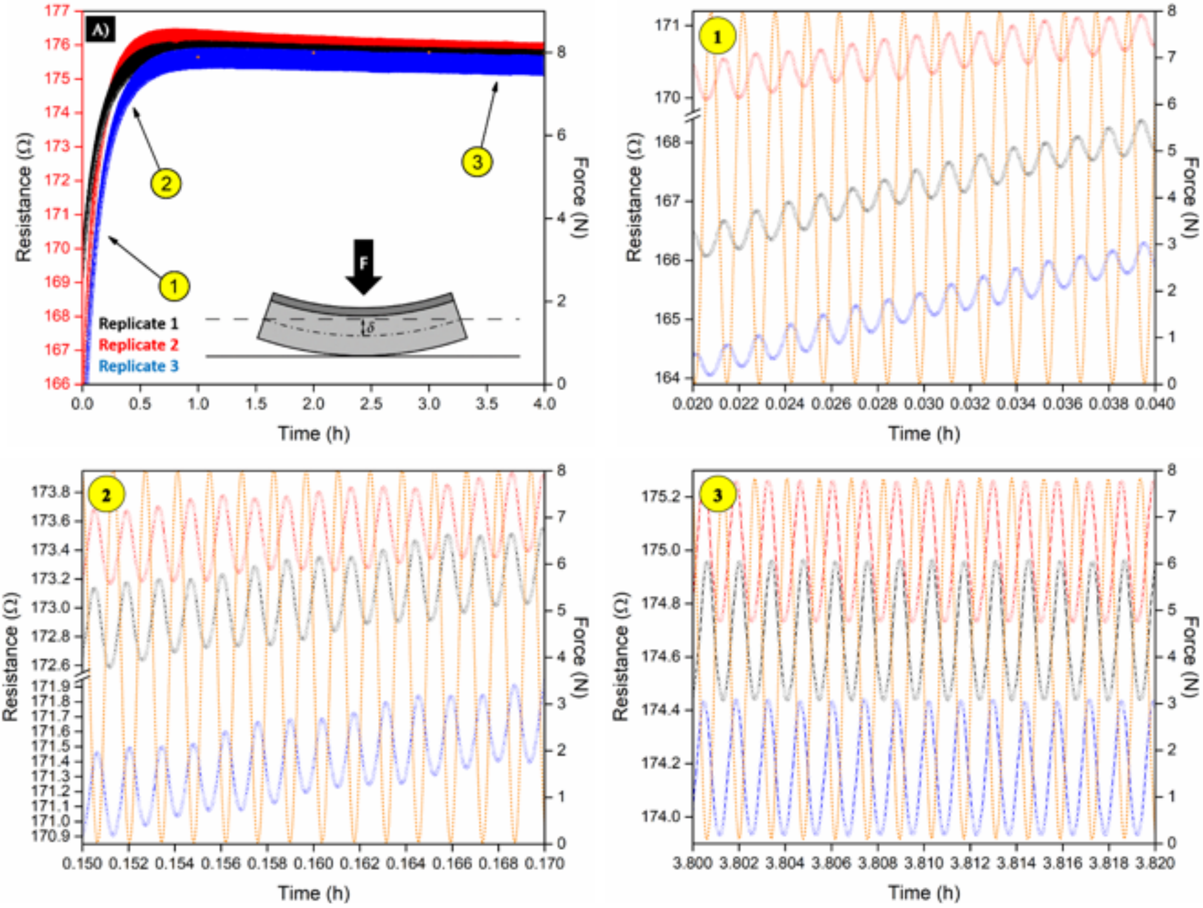

Figure 3.3-3. A) Replicability of resistance response of strain gauge under compressive cyclic load at 400 °C showing the thermal stability of the response after ~25 mins of cycling time.
Three sections are highlighted on the main graph to focus the self-regulating ability of the device namely 1) starting point of the mechanical cycle loading, 2) Transition point before the perceived stabilization, and 3) End point of the cyclic test. The corresponding force applied on the sensor is also added to visualize the inverse response of resistance vs the applied force. An illustration of the film under compressive stress is shown as an inset in Figure 3.3-3A.

The ageing study established a remarkable response wherein after 4 hours of continuous cyclic load application, the performance of the device does not deteriorate but rather improves. In Table 3.3-2, a general full factorial design with four replicates is implemented to analyze the effect of the temperature setting (on hold (isothermal) and during ramp (dynamic)),

temperature, and the type of loading (tensile and compressive) on the gauge factor of the samples. At 95% confidence level, analysis of variance (ANOVA) revealed the dependence of gauge factor on the temperature setting (p-value < 0, F = 138.88, df = 1) and temperature values (p-value < 0, F = 328.21, df = 4) only. Seemingly, the fabricated strain sensor can uphold to both compressive and tensile loads resulting to statistically insignificant gauge factors. This result broadens the design capability of the device which is not limited by its contacting orientation towards the test specimen. The F-value denotes the variance between the means of two populations and while the p-value is the probability of getting a result as extreme as the one that is determined experimentally [214,215].

Table 3.3-2. General full factorial design of experiment at 95% confidence level, $\alpha = 0.05$.

Factors	Levels					F-value	p-value
Temperature Setting	Hold	Ramp	-	-	-	138.88	< 0
Temperature	25	100	200	300	400	328.21	< 0
Load	Tensile	Compressive	-	-	-	3.77	0.057

Presented in Figure 3.3-4A is the box plot distribution of the gauge factor responses combined with the individual data points displayed on the left side of the box plots. The median of each group denoted by the centerlines are statistically insignificant. The square boxes representing the means exhibited a more skewed distribution for samples under the dynamic temperature setting with an increasing dispersion of data as temperature increases. In all the groups, zero outliers were found. In Figure 3.3-4B, the Pareto chart of the standardized effects of each sample with the reference line at 2.00 calculated with the standardized effect at 95% confidence level. The figure revealed the nonlinear regression of the responses with the 2-way interactions occurring between the temperature settings and the temperature values, and the 2-way interactions between the temperature values and the type of cyclic load applied to each sample. These interactions indicate that there are significant differences between these groups over time. In Figure 3.3-4C and D, the residuals are calculated by taking the difference between the experimental values and the regression values. It is then standardized by dividing the residuals by the corresponding standard deviations. Standardized residuals greater than 2 and less than -2 are considered unusual observations [215]. Ideally, the residuals should fall randomly on the centerline of the plot, which is the case in Figure 3.3-4C, except for four data points from the samples tested at 400 °C. In Figure 3.3-4D, a pattern can be distinguished for both sets of data points during ramp and while held at a specific temperature, meaning that the gauge factor has a nonlinear relationship with the temperature setting. This finding is congruent with the prolonged aging study which presented a more stable response after 4 hours of continuous

application of cyclic load. At a fixed temperature, the resistance response stabilizes and remains constant after 20 minutes of holding time.

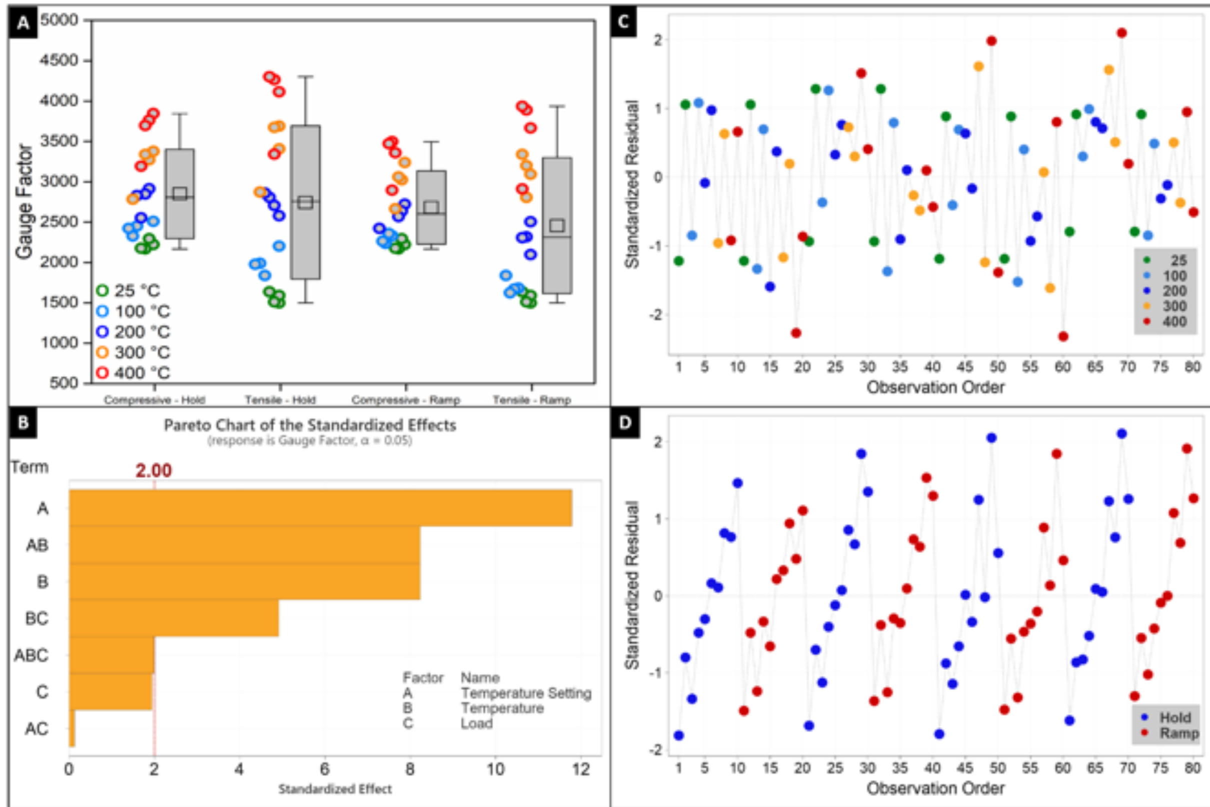

Figure 3.3-4. Aging study of sensor sensitivity at high temperature, maximum of 400 °C.
A) Box plot distribution of the gauge factor responses. Individual data points on the right reflect the number of replicates measured at a given temperature. B) Pareto chart of the main factors affecting the gauge factor of the samples. Standardized residual distribution of individual data points grouped by the significant factors C) Temperature and D) Temperature setting.

To identify the temperature coefficient of sensitivity (TCS) of the fabricated gauges, the GFs are plotted against the test temperature and is shown on Figure 3.3-5. The data taken from the dynamic temperature experiment are reflected to show the stability of the strain gauges' sensitivity to fluctuating temperatures.

In both tensile and compressive cyclic loads, the giant piezoresistivity of the strain gauges is calculated between 25 – 400 °C resulting in ca. 2000 – 5000 values. Ultimately, Figure 3.3-4 provides remarkable considerations for the SiOC-based strain gauge synthesized in this work:

i. The values of the gauge factor exhibited robustness to the temperature effect, regardless of the applied cyclic load, compressive or tensile, as well as of the temperature test condition, isothermal or dynamic.

ii. The linear dependence of the gauge factor on the temperature and the fact presented in (1) allows a predictable / highly reliable use of this material as a piezoresistive sensing component in devices.

iii. The strain gauges exhibited a giant piezoresistivity, GF > 500, from room temperature until 600 °C for both tensile and compressive cyclic loads. Acquired measurements until 400 °C demonstrated exceptionally high values above 2000.

iv. Based on the TCR trend in Section 3.3, the gauge factor declined above 400 °C, which is anticipated as the material starts to transition from semiconducting to non-conducting and vice versa at 460 °C, as explained beforehand. The giant piezoresistivity is maintained up to 600 °C.

v. The gauge factor measured at 700 °C is in the range of 20 – 200 which is comparable to the known gauge factors of metallic and silicon strain gauges, limited to 2 and 150, taken at room temperature [9,106,107]. This demonstrates the outstanding sensitivity of the strain gauges until 700 °C.

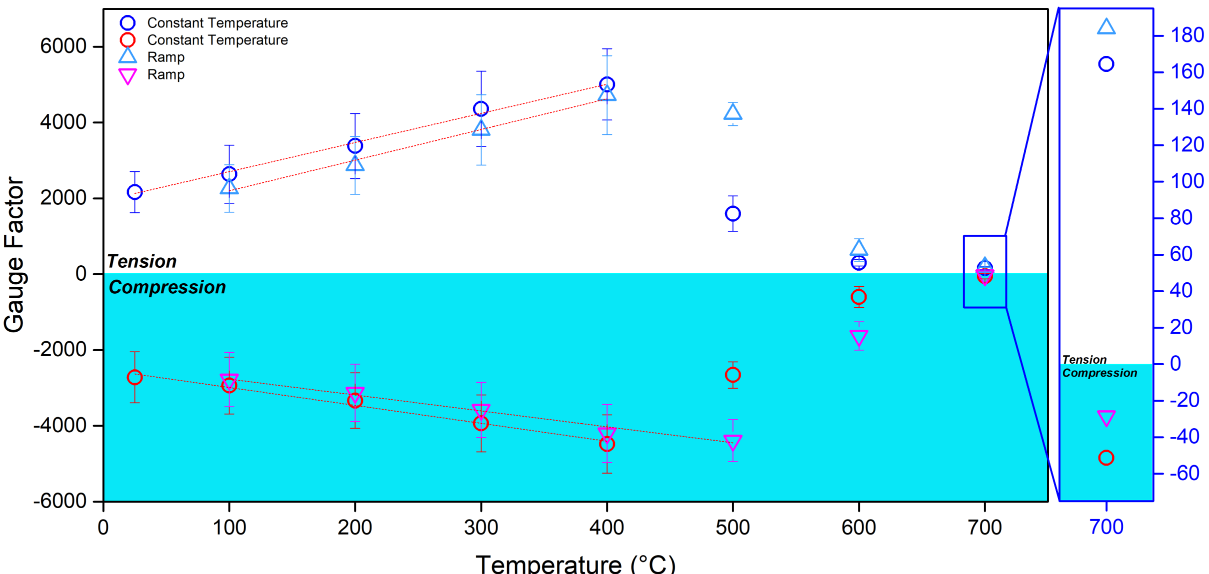

Figure 3.3-5. The temperature coefficient of sensitivity of SiOC film is measured at a temperature range of 25 – 700 °C.

4. Implications, Conclusion, and Outlook

This research aimed to provide a SiOC-based thin film strain gauge with high sensitivity that can operate at elevated temperature. Based on the quantitative analysis of results gathered from the experimental work, the fabricated prototypes possess giant piezoresistivity ($2000 < GF < 5000$) from room temperature until 400 °C, under compressive and tensile cyclic loads. The gauge factors manifested a declining slope at the range of 500 – 700 °C but is still comparably more sensitive than commercial metal- and silicon-based strain gauges.

The fabricated prototype followed a simple process framework involving spin coating followed by multistep thermal treatment of the SiOC thin film to facilitate the polymer-to-ceramic conversion. After the annealing process, two distinct regions are highly visible on the surface of the film which are identified as C/SiOC and C/SiC phases. The C/SiOC phase is the matrix of the film while the C/SiC phase is the carbon-rich and oxygen-depleted region manifested as round segregations dispersed evenly on the film. Graphitic indices of both phases are calculated based on the Raman peaks which ascertained the existence of graphitic domains on the system that is further confirmed by TEM and SAED images. The formation of the C-rich segregation is acknowledged to be a result of the diffusion of carbon through the silica layer on top of the silicon substrate used in this work. EELS spectroscopy confirmed these results showing the C K-edge dominated by the π* peak. TEM images coupled with SAED established the multicomponent nature of the segregation containing SiC, Si_3N_4, and graphitic carbons which is confirmatory of the 2-level hierarchical microstructure of the SiOC film on a silicon substrate. Through the kinetics study, the carbon diffusion coefficient showed a direct proportionality to increasing temperature and an Arrhenius relation leading to an activation energy of 3.05 eV. The effect of varying the structure going from bulk to thin film sample to improve the electrical transport mechanism in C/SiOC is established in this work. Hall measurement revealed p-type carriers as the main charge carrier of the system. The charge carrier concentration of both monolith and thin-film samples is found to be comparable while a significant increase in mobility, by 2 orders of magnitude, is realized for the SiOC thin film. The conductivity of the C/SiOC thin film, ca. 16 S cm^{-1}, is also 2 magnitudes higher as compared to monolithic samples and is supposed to rely on the improved charge carrier mobility as well as on the decreased percolation threshold due to the phase-separated morphology of the thin film. The present study indicates that the charge carrier transport in SiOC-based systems can be modulated not only by adjusting the chemical composition (i.e., carbon content) of SiOC but also by tailoring its morphology.

In relation to the multicomponent nature of the film, the TCR of the SiOC film exhibited a transition temperature at 460 °C wherein it shifts from semiconducting to conducting behavior and vice versa. This electrical behavioral shifts at 460 °C turns into new opportunities for the SiOC thin film to be used as current-limiting devices and temperature sensors such as thermistors. The fabricated strain gauges displayed better reversibility under compressive loads as compared to tensile loads. Even at high temperatures, the linearity of the response under compressive loads persists at 1.4 microstrains and 0.8 microstrains under tensile loads. Remarkably, the device performance improved as the loading time lengthens. The aging study conducted for 4h with 4 replicates displayed immense stability of the device and robustness of the SiOC-based strain gauge towards high-temperature fatigue. Most outstandingly, the SiOC-based strain gauge exhibited a self-regulating effect with temperature. After 20 minutes of holding time at a fixed temperature, the change in resistance remained constant with continuous cyclic load application. This result eliminates the need to perform temperature compensation on measurement setups, either by physical or digital methods.

The fabricated sensor prototype from this work can be used to challenge the current state of the art of self-sensing devices due to its simplistic and cost-efficient fabrication process with high reproducibility. Functionally, the prototype can operate at the microstrain with high sensitivity. Moreover, the thermal stability of the material used, SiOC, provides an opportunity for further applications which can be explored at elevated temperature, above 400 °C, higher than the current maximum temperature of commercial Si-based piezoresistive sensors.

The process capability of the prototype is also analyzed revealing a statistically stable process and good replicability. Though capability indices indicated the statistical stability of the process, the current approach can further be optimized for improvements that can be done in a more controlled environment. Future works can try to focus on the following items to further improve the strain gauge prototype:

i. The current film is filler-free that limits the thickness of the deposited film. This then becomes a critical consideration on the amount of power used for electrode deposition and the thickness thereof that it can hold before peeling off. Possibility of using carbon-based fillers can be an option to explore, or deposition of multiple layers of filler-free SiOC film deposition can also be a promising candidate.

ii. Hall measurements at high-temperature can be done to gain an insight on the effect of temperature on charge carrier transport mechanism of the film and how it affects the piezoresistive behavior of the SiOC-based strain gauge at elevated temperature.

iii. Detailed study on kinetics, in-situ, if possible, is recommended to deepen the knowledge on the formation of the C-rich segregation. Dedicated work on TEM and

EELS analyses is suggested to fully grasp the evolution of the components on the system.

iv. The ~20 min stabilization time of the long-time piezoresistive measurement is attributed to the test-up being exposed to varying external temperature. Although this simulates a real-life scenario, a fully-enclosed set-up wherein temperature can be controlled is ideal to have a better understanding of the PZR behavior dependence on temperature.

v. Also related to the PZR test setup, electrical contracts can be varied from either clamped or soldered system.

From this perspective, this PhD work has laid the groundwork for the development of an extremely promising strain gauge prototype worthy to challenge the status quo of the commercial strain gauges. Aside from the exceptional performance of the SiOC thin film strain gauges, the author finds it worth bearing in mind that this work pushes the boundary of the SiOC-based material to a more concrete application that can be picked up and improved for industrial applications.

5. References

1. Zeijl HW van. (Invited) Thin Film Technologies for Micro/Nano Systems; A Review. ECS Trans. 2014 Mar 26;61(3):191.
2. Barlian AA, Park WT, Mallon JR, Rastegar AJ, Pruitt BL. Review: Semiconductor Piezoresistance for Microsystems. Proc IEEE Inst Electr Electron Eng. 2009;97(3):513–52.
3. Nauman S. Piezoresistive Sensing Approaches for Structural Health Monitoring of Polymer Composites—A Review. Eng. 2021 Jun;2(2):197–226.
4. Fiorillo AS, Critello CD, Pullano SA. Theory, technology and applications of piezoresistive sensors: A review. Sensors and Actuators A: Physical. 2018 Oct;281:156–75.
5. Chung DDL. A critical review of piezoresistivity and its application in electrical-resistance-based strain sensing. J Mater Sci. 2020 Nov 1;55(32):15367–96.
6. Ricohermoso E, Rosenburg F, Klug F, Nicoloso N, Schlaak HF, Riedel R, et al. Piezoresistive carbon-containing ceramic nanocomposites – A review. Open Ceramics. 2021 Mar 1;5:100057.
7. Piezoelectric Material From Bulk to Thin Film – Comparison 2019 [Internet]. i-Micronews. [cited 2021 Mar 9]. Available from: https://www.i-micronews.com/products/piezoelectric-material-from-bulk-to-thin-film-comparison-2019/
8. Piezoelectric Devices: From Bulk to Thin-Film 2019 [Internet]. i-Micronews. [cited 2021 Mar 9]. Available from: https://www.i-micronews.com/products/piezoelectric-devices-from-bulk-to-thin-film-2019/
9. Bajpai P. Chapter 24 - Process Control. In: Bajpai P, editor. Biermann's Handbook of Pulp and Paper (Third Edition) [Internet]. Elsevier; 2018 [cited 2022 Feb 15]. p. 483–92. Available from: https://www.sciencedirect.com/science/article/pii/B9780128142387000246
10. Fraden J. Pressure Sensors. In: Fraden J, editor. Handbook of Modern Sensors: Physics, Designs, and Applications [Internet]. New York, NY: Springer; 2010 [cited 2022 Feb 15]. p. 375–97. Available from: https://doi.org/10.1007/978-1-4419-6466-3_10
11. Obitayo W, Liu T. A Review: Carbon Nanotube-Based Piezoresistive Strain Sensors. Journal of Sensors. 2012 Apr 17;2012:e652438.
12. Zhao Y, Liu Y, Li Y, Hao Q. Development and Application of Resistance Strain Force Sensors. Sensors (Basel). 2020 Oct 15;20(20):5826.
13. Arena M, Viscardi M. Strain State Detection in Composite Structures: Review and New Challenges. Journal of Composites Science. 2020 Jun;4(2):60.
14. Ştefănescu DM. Strain gauges and Wheatstone bridges — Basic instrumentation and new applications for electrical measurement of non-electrical quantities. In: Eighth International Multi-Conference on Systems, Signals Devices. 2011. p. 1–5.
15. Barlian AA, Park WT, Mallon JR, Rastegar AJ, Pruitt BL. Review: Semiconductor Piezoresistance for Microsystems. Proc IEEE Inst Electr Electron Eng. 2009;97(3):513–52.
16. Colombo P, Mera G, Riedel R, Sorarù GD. Polymer-Derived Ceramics: 40 Years of Research and Innovation in Advanced Ceramics. Journal of the American Ceramic Society. 2010;93(7):1805–37.
17. Lu K, Erb D. Polymer derived silicon oxycarbide-based coatings. International Materials Reviews. 2018 Apr 3;63(3):139–61.
18. Ionescu E, Mera G, Riedel R. Polymer-Derived Ceramics (PDCs): Materials Design towards Applications at Ultrahigh-Temperatures and in Extreme Environments [Internet]. MAX Phases and Ultra-High Temperature Ceramics for Extreme Environments. IGI Global;

2013 [cited 2021 Mar 24]. p. 203–45. Available from: www.igi-global.com/chapter/polymer-derived-ceramics-pdcs/80033
19. Riedel R, Mera G, Hauser R, Klonczynski A. Silicon-Based Polymer-Derived Ceramics: Synthesis Properties and Applications-A Review: Dedicated to Prof. Dr. Fritz Aldinger on the occasion of his 65th birthday. Nippon Seramikkusu Kyokai gakujutsu ronbunshi. 2006;114(1330):425–44.
20. XIX. On the electro-dynamic qualities of metals:—Effects of magnetization on the electric conductivity of nickel and of iron. Proc R Soc Lond. 1857 Dec 31;8:546–50.
21. Tomlinson H, Adams WG. II. On the increase in resistance to the passage of an electric current produced on wires by stretching. Proceedings of the Royal Society of London. 1877 Jan;25(171–178):451–3.
22. Tomlinson H. The influence of stress and strain on the action of physical forces. 1883 Dec 31 [cited 2020 Mar 3];174. Available from: https://royalsocietypublishing.org/doi/pdf/10.1098/rstl.1883.0001
23. Williams WE. LV. On the influence of stress on the electrical conductivity of metals. The London, Edinburgh, and Dublin Philosophical Magazine and Journal of Science. 1907 May;13(77):635–43.
24. Bridgman PW. General survey of the effects of pressure on the properties of matter. Proc Phys Soc. 1928 Oct;41(1):341–60.
25. Bridgman PW. The Effect of Homogeneous Mechanical Stress on the Electrical Resistance of Crystals. In: The Effect of Homogeneous Mechanical Stress on the Electrical Resistance of Crystals [Internet]. Harvard University Press; 2013 [cited 2022 Apr 19]. p. 2664–70. Available from: https://www.degruyter.com/document/doi/10.4159/harvard.9780674287785.c6/html
26. Rolnick H. Tension Coefficient of Resistance of Metals. Phys Rev. 1930 Aug 1;36(3):506–12.
27. Cookson JW. Theory of the Piezo-Resistive Effect. Phys Rev. 1935 Jan 15;47(2):194–5.
28. Bardeen J, Shockley W. Deformation Potentials and Mobilities in Non-Polar Crystals. Phys Rev. 1950 Oct 1;80(1):72–80.
29. Smith CS. Piezoresistance Effect in Germanium and Silicon. Phys Rev. 1954 Apr 1;94(1):42–9.
30. Morin FJ, Geballe TH, Herring C. Temperature Dependence of the Piezoresistance of High-Purity Silicon and Germanium. Phys Rev. 1957 Jan 15;105(2):525–39.
31. Mason WP, Thurston RN. Use of Piezoresistive Materials in the Measurement of Displacement, Force, and Torque. The Journal of the Acoustical Society of America. 1957 Oct;29(10):1096–101.
32. Tufte ON, Stelzer EL. Piezoresistive Properties of Silicon Diffused Layers. Journal of Applied Physics. 1963 Feb;34(2):313–8.
33. Pfann WG, Thurston RN. Semiconducting Stress Transducers Utilizing the Transverse and Shear Piezoresistance Effects. Journal of Applied Physics. 1961 Oct;32(10):2008–19.
34. Kanda Y. A graphical representation of the piezoresistance coefficients in silicon. IEEE Trans Electron Devices. 1982 Jan;29(1):64–70.
35. Herring C, Vogt E. Transport and Deformation-Potential Theory for Many-Valley Semiconductors with Anisotropic Scattering. Phys Rev. 1956 Feb 1;101(3):944–61.
36. French PJ, Evans AGR. Piezoresistance in polysilicon and its applications to strain gauges. Solid-State Electronics. 1989 Jan;32(1):1–10.
37. Camargo PHC, Satyanarayana KG, Wypych F. Nanocomposites: synthesis, structure, properties and new application opportunities. Mat Res. 2009 Mar;12(1):1–39.
38. Colombo P, Mera G, Riedel R, Sorarù GD. Polymer-Derived Ceramics: 40 Years of Research and Innovation in Advanced Ceramics. Journal of the American Ceramic Society. 2010 Jul 1;93(7):1805–37.

39. Fu S, Zhu M, Zhu Y. Organosilicon polymer-derived ceramics: An overview. J Adv Ceram. 2019 Dec 1;8(4):457–78.
40. Ionescu E, Mera G, Riedel R. Polymer-Derived Ceramics: Materials Design towards Applications at Ultrahigh-Temperatures and in Extreme Environments. In: Nanotechnology: Concepts, Methodologies, Tools, and Applications. IGI Global; p. 1108–39.
41. Mera G, Navrotsky A, Sen S, Kleebe HJ, Riedel R. Polymer-derived SiCN and SiOC ceramics – structure and energetics at the nanoscale. J Mater Chem A. 2013 Feb 26;1(12):3826–36.
42. Fritz G, Raabe B. Bildung siliciumorganischer Verbindungen. V. Die Thermische Zersetzung von Si(CH3)4 und Si(C2H5)4. Z Anorg Allg Chem. 1956 Jul;286(3–4):149–67.
43. Bhandavat R, Pei Z, Singh G. Polymer-derived ceramics as anode material for rechargeable Li-ion batteries: a review. Nanomaterials and Energy. 2012 Nov;1(6):324–37.
44. Wilson A, Reimers J, Fuller E, Dahn J. Lithium insertion in pyrolyzed siloxane polymers. Solid State Ionics. 1994 Dec 15;74(3–4):249–54.
45. Ahn D, Raj R. Cyclic stability and C-rate performance of amorphous silicon and carbon based anodes for electrochemical storage of lithium. Journal of Power Sources. 2011 Feb;196(4):2179–86.
46. Bergero L, Sglavo VM, Soraru GD. Processing and Thermal Shock Resistance of a Polymer-Derived MoSi2/SiCO Ceramic Composite. J American Ceramic Society. 2005 Nov;88(11):3222–5.
47. Iwamoto Y, Völger W, Kroke E, Riedel R, Saitou T, Matsunaga K. Crystallization Behavior of Amorphous Silicon Carbonitride Ceramics Derived from Organometallic Precursors. Journal of the American Ceramic Society. 2004 Dec 20;84(10):2170–8.
48. Qing Z, Zhou W, Xia W, Li H. Crystallization kinetics, sintering, microstructure, and properties of low temperature co-fired magnesium aluminum silicate glass-ceramic. Journal of Non-Crystalline Solids. 2018 Apr;486:14–8.
49. Harshe R, Balan C, Riedel R. Amorphous Si(Al)OC ceramic from polysiloxanes: bulk ceramic processing, crystallization behavior and applications. Journal of the European Ceramic Society. 2004 Jan;24(12):3471–82.
50. Karakuscu A, Ponzoni A, Aravind PR, Sberveglieri G, Soraru GD. Gas Sensing Behavior of Mesoporous SiOC Glasses. Journal of the American Ceramic Society. 2013;96(8):2366–9.
51. Yu Y, Liu Y, Zhang Z, Zhang J. Fabrication of high-fracture-strength and gas-tightness PDC films via PIP process for pressure sensor application. Journal of the American Ceramic Society [Internet]. [cited 2020 Mar 20];n/a(n/a). Available from: https://ceramics.onlinelibrary.wiley.com/doi/abs/10.1111/jace.17063
52. Ionescu E, Kleebe HJ, Riedel R. Silicon-containing polymer-derived ceramic nanocomposites (PDC-NCs): preparative approaches and properties. Chem Soc Rev. 2012 Jul 9;41(15):5032–52.
53. Roth F, Guillon O, Ionescu E, Nicoloso N, Schmerbauch C, Riedel R. Piezoresistive Ceramics for High-Temperature Force and Pressure Sensing. In: Sensors and Measuring Systems 2014; 17 ITG/GMA Symposium. 2014. p. 1–4.
54. Roth F, Schmerbauch C, Ionescu E, Nicoloso N, Guillon O, Riedel R. High-temperature piezoresistive C / SiOC sensors. Journal of Sensors and Sensor Systems. 2015 Mar 31;4(1):133–6.
55. Widgeon SJ, Sen S, Mera G, Ionescu E, Riedel R, Navrotsky A. 29Si and 13C Solid-State NMR Spectroscopic Study of Nanometer-Scale Structure and Mass Fractal Characteristics of Amorphous Polymer Derived Silicon Oxycarbide Ceramics. Chem Mater. 2010 Dec 14;22(23):6221–8.

56. Rosenburg F, Balke B, Nicoloso N, Riedel R, Ionescu E. Effect of the Content and Ordering of the sp2 Free Carbon Phase on the Charge Carrier Transport in Polymer-Derived Silicon Oxycarbides. Molecules. 2020 Jan;25(24):5919.
57. Felix Rosenburg, Emanuel Ionescu, Norbert Nicoloso, Ralf Riedel. High-Temperature Raman Spectroscopy of Nano-Crystalline Carbon in Silicon Oxycarbide. Materials. 2018 Jan 9;11(1):93.
58. Stabler C, Reitz A, Stein P, Albert B, Riedel R, Ionescu E. Thermal Properties of SiOC Glasses and Glass Ceramics at Elevated Temperatures. Materials (Basel). 2018 Feb 10;11(2).
59. Mera G, Gallei M, Bernard S, Ionescu E. Ceramic Nanocomposites from Tailor-Made Preceramic Polymers. Nanomaterials (Basel). 2015 Apr 1;5(2):468–540.
60. Babonneau F, Soraru GD, D'Andrea G, Dire S, Bois L. Silicon Oxycarbide Glasses from Sol-Gel Precursors. MRS Online Proceedings Library (OPL). 1992;271.
61. Kalfat R, Babonneau F, Gharbi N, Zarrouk H. 29 Si MAS NMR investigation of the pyrolysis process of cross-linked polysiloxanes prepared from polymethylhydrosiloxane. J Mater Chem. 1996 Jan 1;6(10):1673–8.
62. Trimmel G, Badheka R, Babonneau F, Latournerie J, Dempsey P. Solid State NMR and TG/MS Study on the Transformation of Methyl Groups During Pyrolysis of Preceramic Precursors to SiOC Glasses - ProQuest. Journal of Sol-Gel Science and Technology. 2003 Jan;26(1–3):279–83.
63. Weinmann M, Ionescu E, Riedel R, Aldinger F. Chapter 11.1.10 - Precursor-Derived Ceramics*. In: Somiya S, editor. Handbook of Advanced Ceramics (Second Edition). Oxford: Academic Press; 2013. p. 1025–101.
64. Roth F, Waleska P, Hess C, Ionescu E, Nicoloso N. UV Raman spectroscopy of segregated carbon in silicon oxycarbides. J Ceram Soc Japan. 2016;124(10):1042–5.
65. Colombo P, Mera G, Riedel R, Sorarù GD. Polymer-Derived Ceramics: 40 Years of Research and Innovation in Advanced Ceramics. Journal of the American Ceramic Society. 2010;93(7):1805–37.
66. Kleebe HJ, Turquat C, Sorarù GD. Phase Separation in an SiCO Glass Studied by Transmission Electron Microscopy and Electron Energy-Loss Spectroscopy. Journal of the American Ceramic Society. 2001 May;84(5):1073–80.
67. Chomel AD, Dempsey P, Latournerie J, Hourlier-Bahloul D, Jayasooriya UA. Gel to Glass Transformation of Methyltriethoxysilane: A Silicon Oxycarbide Glass Precursor Investigated Using Vibrational Spectroscopy. Chem Mater. 2005 Aug 1;17(17):4468–73.
68. Sorarù GD, D'Andrea G, Glisenti A. XPS characterization of gel-derived silicon oxycarbide glasses. Materials Letters. 1996 May 1;27(1):1–5.
69. Sorarù GD. Silicon oxycarbide glasses from gels: Code: H1. J Sol-Gel Sci Technol. 1994;2(1–3):843–8.
70. Giuliano G, Hans-Joachim K, D BY, Florence B. Evolution of C-rich SiOC ceramics Part II. Characterization by high lateral resolution techniques: electron energy-loss spectroscopy, high-resolution TEM and energy-filtered TEM. International Journal of Materials Research. 2006;97(6):710–20.
71. Sorarù GD, Modena S, Guadagnino E, Colombo P, Egan J, Pantano C. Chemical Durability of Silicon Oxycarbide Glasses. Journal of the American Ceramic Society. 2002;85(6):1529–36.
72. Monthioux M, Delverdier O. Thermal behavior of (organosilicon) polymer-derived ceramics. V: Main facts and trends. Journal of the European Ceramic Society. 1996 Jan 1;16(7):721–37.
73. Bois L, Maquet J, Babonneau F, Mutin H, Bahloul D. Structural Characterization of Sol-Gel Derived Oxycarbide Glasses. 1. Study of the Pyrolysis Process. Chem Mater. 1994 Jun;6(6):796–802.

74. Bois L, Maquet J, Babonneau F, Bahloul D. Structural Characterization of Sol-Gel Derived Oxycarbide Glasses. 2. Study of the Thermal Stability of the Silicon Oxycarbide Phase. Chem Mater. 1995 May;7(5):975–81.
75. Xu Y, Zangvil A, Lipowitz J, Rabe JA, Zank GA. Microstructure and Microchemistry of Polymer-Derived Crystalline SiC Fibers. Journal of the American Ceramic Society. 1993;76(12):3034–40.
76. Bréquel H, Parmentier J, Walter S, Badheka R, Trimmel G, Masse S, et al. Systematic Structural Characterization of the High-Temperature Behavior of Nearly Stoichiometric Silicon Oxycarbide Glasses. Chem Mater. 2004 Jun 1;16(13):2585–98.
77. Saha A, Raj R. Crystallization Maps for SiCO Amorphous Ceramics. J American Ceramic Society. 2007 Feb;90(2):578–83.
78. Schuepfer DB, Badaczewski F, Guerra-Castro JM, Hofmann DM, Heiliger C, Smarsly B, et al. Assessing the structural properties of graphitic and non-graphitic carbons by Raman spectroscopy. Carbon. 2020 May 1;161:359–72.
79. Rosenburg F, Ionescu E, Nicoloso N, Riedel R. High-Temperature Raman Spectroscopy of Nano-Crystalline Carbon in Silicon Oxycarbide. Materials. 2018 Jan;11(1):93.
80. Lu K, Erb D, Liu M. Thermal stability and electrical conductivity of carbon-enriched silicon oxycarbide. J Mater Chem C. 2016;4(9):1829–37.
81. Bruggeman D a. G. Berechnung verschiedener physikalischer Konstanten von heterogenen Substanzen. I. Dielektrizitätskonstanten und Leitfähigkeiten der Mischkörper aus isotropen Substanzen. Annalen der Physik. 1935;416(7):636–64.
82. Rozen J, Lopez R, Haglund RF, Feldman LC. Two-dimensional current percolation in nanocrystalline vanadiumdioxide films. Appl Phys Lett. 2006 Feb 20;88(8):081902.
83. Kirkpatrick S. Percolation and Conduction. Rev Mod Phys. 1973 Oct 1;45(4):574–88.
84. Broadbent SR, Hammersley JM. Percolation processes: I. Crystals and mazes. Math Proc Camb Phil Soc. 1957 Jul;53(3):629–41.
85. Saberi AA. Recent advances in percolation theory and its applications. Physics Reports. 2015 May 24;578:1–32.
86. Wang M, Gurunathan R, Imasato K, Geisendorfer NR, Jakus AE, Peng J, et al. A Percolation Model for Piezoresistivity in Conductor–Polymer Composites. Advanced Theory and Simulations. 2019;2(2):1800125.
87. Li J, Ma PC, Chow WS, To CK, Tang BZ, Kim JK. Correlations between Percolation Threshold, Dispersion State, and Aspect Ratio of Carbon Nanotubes. Advanced Functional Materials. 2007;17(16):3207–15.
88. Batrouni GG, Hansen A, Larson B. Current distribution in the three-dimensional random resistor network at the percolation threshold. Phys Rev E. 1996 Mar 1;53(3):2292–7.
89. Clerc JP, Podolskiy VA, Sarychev AK. Precise determination of the conductivity exponent of 3D percolation using exact numerical renormalization. Eur Phys J B. 2000 Jun 1;15(3):507–16.
90. Hunt A, Ewing R, Ghanbarian B. Percolation Theory for Flow in Porous Media. 3rd ed. Springer; 2014. 466 p.
91. Vionnet-Menot S, Grimaldi C, Maeder T, Strässler S, Ryser P. Tunneling-percolation origin of nonuniversality: Theory and experiments. Phys Rev B. 2005 Feb 16;71(6):064201.
92. Vionnet-Menot S, Grimaldi C, Maeder T, Ryser P, Strässler S. Study of electrical properties of piezoresistive pastes and determination of the electrical transport. Journal of the European Ceramic Society. 2005;25(12):2129–32.
93. Balberg I. Tunneling and nonuniversal conductivity in composite materials. Phys Rev Lett. 1987 Sep 21;59(12):1305–8.
94. Balberg I. Limits on the continuum-percolation transport exponents. Phys Rev B. 1998 Jun 1;57(21):13351–4.

95. Cordelair J, Greil P. Electrical conductivity measurements as a microprobe for structure transitions in polysiloxane derived Si–O–C ceramics. Journal of the European Ceramic Society. 2000 Nov 1;20(12):1947–57.
96. McLachlan DS, Blaszkiewicz M, Newnham RE. Electrical Resistivity of Composites. Journal of the American Ceramic Society. 1990;73(8):2187–203.
97. Cordelair J, Greil P. Electrical conductivity measurements as a microprobe for structure transitions in polysiloxane derived Si–O–C ceramics. Journal of the European Ceramic Society. 2000 Nov 1;20(12):1947–57.
98. Wang Y, Zhang L, Fan Y, Jiang D, An L. Stress-dependent piezoresistivity of tunneling-percolation systems. J Mater Sci. 2009 Jun;44(11):2814–9.
99. Wang Y, Zhang L, Xu W, Jiang T, Fan Y, Jiang D, et al. Effect of Thermal Initiator Concentration on the Electrical Behavior of Polymer-Derived Amorphous Silicon Carbonitrides. Journal of the American Ceramic Society. 2008;91(12):3971–5.
100. Haluschka C, Engel C, Riedel R. Silicon carbonitride ceramics derived from polysilazanes. Part 2: Investigation of electrical properties. Journal of the European Ceramic Society. 2000 Aug;20(9):1365–74.
101. Mott NF. Conduction in non-crystalline materials. The Philosophical Magazine: A Journal of Theoretical Experimental and Applied Physics. 1969 Apr 1;19(160):835–52.
102. Mott NF, Davis EA. Electronic Processes in Non-Crystalline Materials. 2nd ed. Oxford, New York: Oxford University Press; 1979. 608 p. (Oxford Classic Texts in the Physical Sciences).
103. Wang K, Li X, Ma B, Wang Y, Zhang L, An L. On electronic structure of polymer-derived amorphous silicon carbide ceramics. Appl Phys Lett. 2014 Jun 2;104(22):221902.
104. Trassl S, Puchinger M, Rössler E, Ziegler G. Electrical properties of amorphous SiCxNyHz-ceramics derived from polyvinylsilazane. Journal of the European Ceramic Society. 2003 Apr;23(5):781–9.
105. Heywang W. Einleitung. In: Heywang W, editor. Amorphe und polykristalline Halbleiter [Internet]. 1st ed. Berlin, Heidelberg: Springer; 1988 [cited 2022 Apr 20]. p. 15–20. Available from: https://doi.org/10.1007/978-3-662-09862-2_1
106. Norton P, Braggins T, Levinstein H. Impurity and Lattice Scattering Parameters as Determined from Hall and Mobility Analysis in n-Type Silicon. Phys Rev B. 1973 Dec 15;8(12):5632–53.
107. Shor JS, Goldstein D, Kurtz AD. Characterization of n-type beta -SiC as a piezoresistor. IEEE Transactions on Electron Devices. 1993 Jun;40(6):1093–9.
108. Neilsen HA. From locomotives to strain gages. Los Angeles: Vantage Press; 1985.
109. Tufte ON, Chapman PW, Long D. Silicon Diffused-Element Piezoresistive Diaphragms. Journal of Applied Physics. 1962 Nov;33(11):3322–7.
110. Amjadi M, Pichitpajongkit A, Lee S, Ryu S, Park I. Highly Stretchable and Sensitive Strain Sensor Based on Silver Nanowire–Elastomer Nanocomposite. ACS Nano. 2014 May 27;8(5):5154–63.
111. Zhou J, Gu Y, Fei P, Mai W, Gao Y, Yang R, et al. Flexible Piezotronic Strain Sensor. Nano Lett. 2008 Sep 10;8(9):3035–40.
112. Cruz S, Rocha LA, Viana JC. Piezo-resistive behaviour at high strain levels of PEDOT:PSS printed on a flexible polymeric substrate by a novel surface treatment. J Mater Sci: Mater Electron. 2017 Feb 1;28(3):2563–73.
113. Gong S, Schwalb W, Wang Y, Chen Y, Tang Y, Si J, et al. A wearable and highly sensitive pressure sensor with ultrathin gold nanowires. Nat Commun. 2014 Feb 4;5(1):3132.
114. di Ventra M, Pantelides ST. Oxygen stability, diffusion, and precipitation in SiC: Implications for thin-film oxidation. Journal of Elec Materi. 2000 Mar;29(3):353–8.
115. Beeby S, editor. MEMS mechanical sensors. Boston: Artech House; 2004. 269 p. (Artech House microelectromechanical system series).

116. Neudeck PG, Okojie RS, Liang-Yu Chen. High-temperature electronics - a role for wide bandgap semiconductors? Proceedings of the IEEE. 2002 Jun;90(6):1065–76.
117. Fahrner WR, Werner M, Job R. Sensors and smart electronics in harsh environment applications. Microsystem Technologies. 2001 Nov 1;7(4):138–44.
118. Ngo HD, Ehrmann O, Schneider-Ramelow M, Lang KD. Piezoresistive Pressure Sensors for Applications in Harsh Environments—A Roadmap. Modern Sensing Technologies. 2019;231–51.
119. Kim JS, Kim GW. Hysteresis Compensation of Piezoresistive Carbon Nanotube/Polydimethylsiloxane Composite-Based Force Sensors. Sensors. 2017 Feb;17(2):229.
120. Wang N, Xu Z, Zhan P, Dai K, Zheng G, Liu C, et al. A tunable strain sensor based on a carbon nanotubes/electrospun polyamide 6 conductive nanofibrous network embedded into poly(vinyl alcohol) with self-diagnosis capabilities. J Mater Chem C. 2017 May 11;5(18):4408–18.
121. Loh KJ, Lynch JP, Shim BS, Kotov NA. Tailoring piezoresistive sensitivity of multilayer carbon nanotube composite strain sensors.
122. Yin G, Hu N, Karube Y, Liu Y, Li Y, Fukunaga H. A carbon nanotube/polymer strain sensor with linear and anti-symmetric piezoresistivity: Journal of Composite Materials [Internet]. 2011 Apr 26 [cited 2020 Mar 3]; Available from: https://journals.sagepub.com/doi/10.1177/0021998310393296
123. Zhang W, Suhr J, Koratkar N. Carbon nanotube/polycarbonate composites as multifunctional strain sensors. J Nanosci Nanotechnol. 2006 Apr;6(4):960–4.
124. Pham GT, Park YB, Liang Z, Zhang C, Wang B. Processing and modeling of conductive thermoplastic/carbon nanotube films for strain sensing. Composites Part B: Engineering. 2008 Jan 1;39(1):209–16.
125. Kasgoz A, Akın D, Durmus A. Rheological and electrical properties of carbon black and carbon fiber filled cyclic olefin copolymer composites. Composites Part B: Engineering. 2014 Jun 1;62:113–20.
126. Hu C, Li Z, Wang Y, Gao J, Dai K, Zheng G, et al. Comparative assessment of the strain-sensing behaviors of polylactic acid nanocomposites: reduced graphene oxide or carbon nanotubes. J Mater Chem C. 2017 Mar 2;5(9):2318–28.
127. Yu S, Wang X, Xiang H, Zhu L, Tebyetekerwa M, Zhu M. Superior piezoresistive strain sensing behaviors of carbon nanotubes in one-dimensional polymer fiber structure. Carbon. 2018 Dec 1;140:1–9.
128. Alamusi, Hu N, Fukunaga H, Atobe S, Liu Y, Li J. Piezoresistive Strain Sensors Made from Carbon Nanotubes Based Polymer Nanocomposites. Sensors (Basel). 2011 Nov 11;11(11):10691–723.
129. Grow RJ, Wang Q, Cao J, Wang D, Dai H. Piezoresistance of carbon nanotubes on deformable thin-film membranes. Appl Phys Lett. 2005 Feb 28;86(9):093104.
130. Qiu L, Liu JZ, Chang SLY, Wu Y, Li D. Biomimetic superelastic graphene-based cellular monoliths. Nat Commun. 2012;3:1241.
131. Coskun MB, Qiu L, Arefin MdS, Neild A, Yuce M, Li D, et al. Detecting Subtle Vibrations Using Graphene-Based Cellular Elastomers. ACS Appl Mater Interfaces. 2017 Apr 5;9(13):11345–9.
132. Rinaldi A, Tamburrano A, Fortunato M, Sarto MS. A Flexible and Highly Sensitive Pressure Sensor Based on a PDMS Foam Coated with Graphene Nanoplatelets. Sensors. 2016 Dec;16(12):2148.
133. Ye X, Yuan Z, Tai H, Li W, Du X, Jiang Y. A wearable and highly sensitive strain sensor based on a polyethylenimine–rGO layered nanocomposite thin film. J Mater Chem C. 2017 Aug 10;5(31):7746–52.
134. Zang Y, Zhang F, Di C an, Zhu D. Advances of flexible pressure sensors toward artificial intelligence and health care applications. Mater Horiz. 2015 Feb 23;2(2):140–56.

135. Chen H, Miao L, Su Z, Song Y, Han M, Chen X, et al. Fingertip-inspired electronic skin based on triboelectric sliding sensing and porous piezoresistive pressure detection. Nano Energy. 2017 Aug 1;40.
136. Zhao P, Luo Y, Yang J, He D, Kong L, Zheng P, et al. Electrically conductive graphene-filled polymer composites with well organized three-dimensional microstructure. Materials Letters. 2014;121:74–7.
137. Wu X, Han Y, Zhang X, Lu C. Spirally Structured Conductive Composites for Highly Stretchable, Robust Conductors and Sensors. ACS Appl Mater Interfaces. 2017 Jul 12;9(27):23007–16.
138. Zhao S, Li J, Cao D, Gao Y, Huang W, Zhang G, et al. Percolation threshold-inspired design of hierarchical multiscale hybrid architectures based on carbon nanotubes and silver nanoparticles for stretchable and printable electronics. J Mater Chem C. 2016 Jul 7;4(27):6666–74.
139. Canali C, Malvasi D, Morten B, Prudenziati M, Taroni A. Strain Sensitivity in Thick-Film Resistors. IEEE Transactions on Components, Hybrids, and Manufacturing Technology. 1980 Sep;3(3):421–3.
140. Canali C, Malavasi D, Morten B, Prudenziati M, Taroni A. Piezoresistive effects in thick-film resistors. Journal of Applied Physics. 1980 Jun;51(6):3282–8.
141. Maeder T, Jacq C, Ryser P. Assessment of thick-film resistors for manufacturing piezoresistive sensors. Additional Conferences (Device Packaging, HiTEC, HiTEN, and CICMT). 2015 Sep 1;2015(CICMT):000213–23.
142. Miyakawa N, Legner W, Ziemann T, Telitschkin D, Fecht HJ, Friedberger A. MEMS-based microthruster with integrated platinum thin film resistance temperature detector (RTD), heater meander and thermal insulation for operation up to 1,000°C. Microsystem Technologies. 2012 Aug;18(7–8):1077–87.
143. A GD, Shah SI. Handbook of Thin Film Process Technology: Reactive Sputtering. Boca Raton: CRC Press; 2017. 90 p.
144. Tilli M, Motooka T, Airaksinen VM, Franssila S, Paulasto-Kröckel M, Lindroos V, editors. Chapter 6 - Thin Films on Silicon. In: Handbook of Silicon Based MEMS Materials and Technologies (Second Edition) [Internet]. Boston: William Andrew Publishing; 2015 [cited 2020 Dec 29]. p. 124–205. (Micro and Nano Technologies). Available from: http://www.sciencedirect.com/science/article/pii/B9780323299657000063
145. Alberti S, Jágerská J. Sol-Gel Thin Film Processing for Integrated Waveguide Sensors. Frontiers in Materials [Internet]. 2021 [cited 2022 Apr 25];8. Available from: https://www.frontiersin.org/article/10.3389/fmats.2021.629822
146. Bahuguna G, Mishra NK, Chaudhary P, Kumar A, Singh R. Thin Film Coating through Sol-Gel Technique. 2016;6:8.
147. Brinker CJ, Hurd AJ, Schunk PR, Frye GC, Ashley CS. Review of sol-gel thin film formation. Journal of Non-Crystalline Solids. 1992 Jan 1;147–148:424–36.
148. Mandoj F, Nardis S, Di Natale C, Paolesse R. Porphyrinoid Thin Films for Chemical Sensing. In: Wandelt K, editor. Encyclopedia of Interfacial Chemistry [Internet]. Oxford: Elsevier; 2018 [cited 2020 Dec 28]. p. 422–43. Available from: http://www.sciencedirect.com/science/article/pii/B9780124095472116774
149. Makhlouf ASH. 1 - Current and advanced coating technologies for industrial applications. In: Makhlouf ASH, Tiginyanu I, editors. Nanocoatings and Ultra-Thin Films [Internet]. Woodhead Publishing; 2011 [cited 2020 Dec 28]. p. 3–23. (Woodhead Publishing Series in Metals and Surface Engineering). Available from: http://www.sciencedirect.com/science/article/pii/B9781845698126500014
150. Bornside DE, Macosko CW, Scriven LE. MODELING OF SPIN COATING. Journal of Imaging Science and Technology. 1987 Aug 1;13(4):122–30.

151. Mouhamad Y, Mokarian-Tabari P, Clarke N, Jones R a. L, Geoghegan M. Dynamics of polymer film formation during spin coating. Journal of Applied Physics. 2014 Sep 28;116(12):123513.
152. Nghiem QD, Kim DP. Highly-resistant SiCBN films prepared by a simple spin-coating process with poly(borosilazane). Journal of Materials Chemistry. 2005;15(22):2188–92.
153. Klaas D, Ottermann R, Dencker F, Wurz MC. Development, Characterisation and High-Temperature Suitability of Thin-Film Strain Gauges Directly Deposited with a New Sputter Coating System. Sensors. 2020 Jan;20(11):3294.
154. Altman DG. Practical Statistics for Medical Research. CRC Press; 1990. 624 p.
155. Box JF. R. A. Fisher and the Design of Experiments, 1922-1926. The American Statistician. 1980;34(1):1–7.
156. Montgomery D. Design and Analysis of Experiments. Eight. John Wiley & Sons, Inc.; 2013. 757 p.
157. Mukerjee R, Wu CFJ, editors. Robust Parameter Design. In: A Modern Theory of Factorial Designs [Internet]. New York, NY: Springer; 2006 [cited 2020 Dec 28]. p. 197–210. (Springer Series in Statistics). Available from: https://doi.org/10.1007/0-387-37344-6_9
158. Roy RK. A primer on the Taguchi method [Internet]. Dearborn, MI: Society of Manufacturing Engineers; 2010 [cited 2021 Jan 20]. Available from: http://search.ebscohost.com/login.aspx?direct=true&scope=site&db=nlebk&db=nlabk&AN=860349
159. Fisher RA. Statistical Methods for Research Workers. In: Kotz S, Johnson NL, editors. Breakthroughs in Statistics: Methodology and Distribution [Internet]. New York, NY: Springer; 1992 [cited 2022 May 13]. p. 66–70. (Springer Series in Statistics). Available from: https://doi.org/10.1007/978-1-4612-4380-9_6
160. Henderson GR. Process Capability Analysis. In: Six Sigma Quality Improvement with Minitab [Internet]. Second. John Wiley & Sons, Ltd; 2011 [cited 2021 Aug 25]. p. 203–23. Available from: https://onlinelibrary.wiley.com/doi/abs/10.1002/9781119975328.ch6
161. Sahay A. PROCESS CAPABILITY ANALYSIS FOR SIX SIGMA. 2010;23.
162. Sambrani DVN. Process Capability–A Managers Tool for 6 Sigma Quality Advantage. Global Journals Inc (USA). 2016;16(3):9.
163. Barroso G, Li Q, Bordia RK, Motz G. Polymeric and ceramic silicon-based coatings – a review. J Mater Chem A. 2019 Jan 29;7(5):1936–63.
164. Günthner M, Kraus T, Krenkel W, Motz G, Dierdorf A, Decker D. Particle-Filled PHPS Silazane-Based Coatings on Steel. International Journal of Applied Ceramic Technology. 2009;6(3):373–80.
165. Kraus T, Günthner M, Krenkel W, Motz G. cBN particle filled SiCN precursor coatings. Advances in Applied Ceramics. 2009 Nov 1;108(8):476–82.
166. Saha A, Raj R, Williamson DL. A Model for the Nanodomains in Polymer-Derived SiCO. J American Ceramic Society. 2006 Apr 28;0(0):060428035142017-???
167. Cançado LG, Takai K, Enoki T, Endo M, Kim YA, Mizusaki H, et al. General equation for the determination of the crystallite size La of nanographite by Raman spectroscopy. Appl Phys Lett. 2006 Apr 17;88(16):163106.
168. Cançado LG, Jorio A, Ferreira EHM, Stavale F, Achete CA, Capaz RB, et al. Quantifying Defects in Graphene via Raman Spectroscopy at Different Excitation Energies. Nano Lett. 2011 Aug 10;11(8):3190–6.
169. Bokobza L, Bruneel JL, Couzi M. Raman Spectra of Carbon-Based Materials (from Graphite to Carbon Black) and of Some Silicone Composites. C. 2015 Dec;1(1):77–94.

170. Baranov AV, Bekhterev AN, Bobovich YaS, Petrov VI. Interpretation of certain characteristics in Raman spectra of graphite and glassy carbon. Optics and Spectroscopy. 1987 May 1;62:612–6.
171. Larouche N, Stansfield BL. Classifying nanostructured carbons using graphitic indices derived from Raman spectra. Carbon. 2010 Mar 1;48(3):620–9.
172. Wang YY, Chan SF, Jin Q, Zhuang K, Choi JK. A method of using Si L-edge for O/Si and N/Si quantitative ratio analysis by electron energy loss spectroscopy (EELS). Micron. 2021 Jul;146:103065.
173. Schneider R, Woltersdorf J, Lichtenberger O. Phase identification in composite materials by EELS fine-structure analysis. Journal of Microscopy. 1996 Jul;183(1):39–44.
174. Garvie L, Buseck P. Bonding in silicates: Investigation of the Si L2,3 edge by parallel electron energy-loss spectroscopy. 1999;
175. Pippel E, Lichtenberger O, Woltersdorf J. Identification of silicon oxycarbide bonding in Si-C-O-glasses by EELS. :2.
176. Edalati K, Daio T, Ikoma Y, Arita M, Horita Z. Graphite to diamond-like carbon phase transformation by high-pressure torsion. Applied Physics Letters. 2013 Jul 18;103(3):034108.
177. Ponsonnet L, Donnet C, Varlot K, Martin JM, Grill A, Patel V. EELS analysis of hydrogenated diamond-like carbon films. Thin Solid Films. 1998 Apr 29;319(1):97–100.
178. Shimoo T, Mizutaki F, Ando S, Kimura H. Kinetics of Reduction of Silica with Graphite. Journal of the Japan Institute of Metals. 1988;52(10):945–53.
179. Estreicher SK, Backlund DJ, Carbogno C, Scheffler M. Activation Energies for Diffusion of Defects in Silicon: The Role of the Exchange-Correlation Functional. Angew Chem Int Ed. 2011 Oct 17;50(43):10221–5.
180. Bracht H. Self- and foreign-atom diffusion in semiconductor isotope heterostructures. I. Continuum theoretical calculations. Phys Rev B. 2007 Jan 17;75(3):035210.
181. Gösele U, Tan TY. Oxygen diffusion and thermal donor formation in silicon. Appl Phys A. 1982 Jun 1;28(2):79–92.
182. Nguyen VL, Zanella C, Bettotti P, Sorarù GD. Electrical Conductivity of SiOCN Ceramics by the Powder-Solution-Composite Technique. Journal of the American Ceramic Society. 2014;97(8):2525–30.
183. Terauds K, Sanchez-Jimenez PE, Raj R, Vakifahmetoglu C, Colombo P. Giant piezoresistivity of polymer-derived ceramics at high temperatures. Journal of the European Ceramic Society. 2010 Aug 1;30(11):2203–7.
184. Li C, Minne S, Pittenger B, Mednick A. Simultaneous Electrical and Mechanical Property Mapping at the Nanoscale with PeakForce TUNA. Santa Barbara, CA, USA: Bruker Corporation; 2011 p. 12. (Application Note 132).
185. Rosenburg F. The state of carbon and the piezoresistive effect in silicon oxycarbide ceramics [Internet] [Ph.D. Thesis]. [Darmstadt]: Technische Universität; 2018 [cited 2020 Jun 28]. Available from: https://tuprints.ulb.tu-darmstadt.de/7517/
186. Taki Y, Kitiwan M, Katsui H, Goto T. Electrical and thermal properties of off-stoichiometric SiC prepared by spark plasma sintering. Journal of Asian Ceramic Societies. 2018 Jan 2;6(1):95–101.
187. Taki Y, Kitiwan M, Katsui H, Goto T. Electrical conductivity of C-SiC and Si-SiC prepared by spark plasma sintering. Materials Today: Proceedings. 2017 Jan 1;4(11, Part 1):11441–4.
188. Toma L, Kleebe HJ, Müller MM, Janssen E, Riedel R, Melz T, et al. Correlation Between Intrinsic Microstructure and Piezoresistivity in a SiOC Polymer-Derived Ceramic. Journal of the American Ceramic Society. 2012;95(3):1056–61.

189. Mallick D, Chakrabarti O, Bhattacharya D, Mukherjee M, Maiti HS, Majumdar R. Electrical conductivity of cellular Si/SiC ceramic composites prepared from plant precursors. Journal of Applied Physics. 2007 Feb;101(3):033707.
190. Srivastava JK, Prasad M, Wagner JB. Electrical Conductivity of Silicon Dioxide Thermally Grown on Silicon.
191. Agarwal AK. An overview of SiC power devices. In: 2010 International Conference on Power, Control and Embedded Systems. 2010. p. 1–4.
192. Agarwal A, Saddow S. Advances in Silicon Carbide Processing and Applications (Semiconductor Materials and Devices Series). Artech House, Inc.; 229 p.
193. North B, Gilchrist KE. Si Silicon: System Si-C. SiC: Natural Occurrence. Preparation and Manufacturing Chemistry. Special Forms. Manufacture. Electrochemical Properties. Chemical Reactions. Applications. Ternary and Higher Systems with Si and C. Springer Science & Business Media; 1981. 562 p.
194. Rybak A, Boiteux G, Melis F, Seytre G. Conductive polymer composites based on metallic nanofiller as smart materials for current limiting devices. Composites Science and Technology. 2010 Feb 1;70(2):410–6.
195. Yi XS, Shen L, Pan Y. Thermal volume expansion in polymeric PTC composites: a theoretical approach. Composites Science and Technology. 2001 May 1;61(7):949–56.
196. Bar H, Narkis M, Boiteux G. The electrical behavior of thermosetting polymer composites containing metal plated ceramic filler. Polymer Composites. 2005;26(1):12–9.
197. Shoenberg D, editor. The Dingle temperature. In: Magnetic Oscillations in Metals [Internet]. Cambridge: Cambridge University Press; 1984 [cited 2022 Apr 13]. p. 369–424. (Cambridge Monographs on Physics). Available from: https://www.cambridge.org/core/books/magnetic-oscillations-in-metals/dingle-temperature/8934DEB85470E2F4F95724CF8BD0D684
198. Cooper JD, Woore J, Young DA. Electronic Properties of Well Oriented Graphite. Nature. 1970 Feb;225(5234):721–2.
199. Schneider JM. ELECTRONIC PROPERTIES OF GRAPHITE. [Grenoble, France]: Université Joseph-Fourier - Grenoble I; 2010.
200. Zhuiykov S, editor. 1 - Electrons and holes in a semiconductor. In: Nanostructured Semiconductor Oxides for the Next Generation of Electronics and Functional Devices [Internet]. Woodhead Publishing; 2014 [cited 2022 Mar 18]. p. 1–49. Available from: https://www.sciencedirect.com/science/article/pii/B9781782422204500019
201. Fricke S, Friedberger A, Mueller G, Seidel H, Schmid U. Strain gauge factor and TCR of sputter deposited Pt thin films up to 850°C. In: 2008 IEEE SENSORS. 2008. p. 1532–5.
202. Kayser P, Godefroy JC, Leca L. High-temperature thin-film strain gauges. Sensors and Actuators A: Physical. 1993 Jun 1;37–38:328–32.
203. Rölke J. Nichrome Thin Film Technology and its Application. ElectroComponent Science and Technology. 1981;9(1):51–7.
204. Gregory OJ, Luo Q. A self-compensated ceramic strain gage for use at elevated temperatures. Sensors and Actuators A: Physical. 2001 Jan 5;88(3):234–40.
205. Gregory OJ, Chen X. A Low TCR Nanocomposite Strain Gage for High Temperature Aerospace Applications. In: 2007 IEEE SENSORS. 2007. p. 624–7.
206. Zarfl C, Schmid P, Balogh G, Schmid U. TiAlN Thin Films as High Temperature Strain Gauges. Procedia Engineering. 2014 Jan 1;87:136–9.
207. Tilak V, Jiang J, Batoni P, Knobloch A. GaN based high temperature strain gauges. J Mater Sci: Mater Electron. 2008 Feb 1;19(2):195–8.
208. Park K, Kim S, Lee H, Park I, Kim J. Low-hysteresis and low-interference soft tactile sensor using a conductive coated porous elastomer and a structure for interference reduction. Sensors and Actuators A: Physical. 2019 Aug 15;295:541–50.

209. Oh J, Kim JO, Kim Y, Choi HB, Yang JC, Lee S, et al. Highly Uniform and Low Hysteresis Piezoresistive Pressure Sensors Based on Chemical Grafting of Polypyrrole on Elastomer Template with Uniform Pore Size. Small. 2019;15(33):1901744.
210. Principles of Self-temperature-compensation Strain Gages (SELCOM Gages) | KYOWA [Internet]. 2019 [cited 2022 Mar 20]. Available from: https://www.kyowa-ei.com/eng/technical/notes/technical_note/selcom_gages.html
211. Cadence Systems Analysis. The Need for Temperature Compensation in a Strain Gauge [Internet]. 2019 [cited 2022 Mar 20]. Available from: https://resources.system-analysis.cadence.com/blog/msa2020-the-need-for-temperature-compensation-in-a-strain-gauge
212. Temperature Compensation of Strain Gauges [Internet]. HBM. 2021 [cited 2022 Mar 20]. Available from: https://www.hbm.com/en/6725/article-temperature-compensation-of-strain-gauges/
213. How Is Temperature Affecting Your Strain Measurement Accuracy? [Internet]. 2020 [cited 2022 Mar 20]. Available from: https://www.ni.com/de-de/innovations/white-papers/06/how-is-temperature-affecting-your-strain-measurement-accuracy-.html
214. Dean A, Voss D, Draguljić D. Confounding in General Factorial Experiments. In: Dean A, Voss D, Draguljić D, editors. Design and Analysis of Experiments [Internet]. Cham: Springer International Publishing; 2017 [cited 2021 May 29]. p. 473–93. (Springer Texts in Statistics). Available from: https://doi.org/10.1007/978-3-319-52250-0_14
215. Montgomery DC. Design and analysis of experiments. Eighth edition. Hoboken, NJ: John Wiley & Sons, Inc; 2013. 730 p.

I. List of Abbreviations

ANOVA	Analysis of Variance
BSU	Basic Structural Units
c-AFM	Conductive Atomic Force Microscope
C/SiOC	Carbon / Silicon oxycarbide (components)
CL	Statistical Confidence level (Upper and Lower)
df	Degrees of Freedom
DH	Degree of hysteresis
EDS	Energy Dispersive X-ray Spectroscopy
EELS	Electron Energy Loss Spectroscopy
EMT	Effect Medium Theory
FIB	Focused Ion Beam
GEM	General Effective Media Theory
GF	Gauge Factor
IR	Infrared Spectroscopy
MEMS	Microelectromechanical Systems
NMR	Nuclear Magnetic Resonance
PDC	Polymer-derived ceramics
PT	Percolation Theory
PZR	Piezoresistivity (setup)
SAED	Selected Area Diffraction
SEM	Scanning Electron Microscope
SiC	Silicon carbide

SiOC	Silicon oxycarbide
TCR	Temperature Coefficient of Resistance
TCS	Temperature Coefficient of Sensitivity
TGA/MS	Thermogravimetric Analysis / Mass Spectroscopy
TUNA	Tunneling Atomic Force Microscope
VRH	Variable-range Hopping
XRD	X-ray diffraction

II. List of Symbols

π_{ij}	Piezoresistive coefficients
T_P	Pyrolysis temperature
Φ_C	Conductive fillers concentration
Φ_{Crit}	Percolation threshold
σ_0	Proportionality Constant
σ_C	Electrical conductivity
t	Critical percolation exponent
k	Boltzmann constant
E_{gap}	Energy gap
R	Resistance
ε	Strain
ρ	resistivity
ν	Poisson's ratio
S/N	Signal-to-Noise ratio
p	p-value, probability
F	F-statistics, F-distribution, coined after Fischer
alpha	Statistical significance level
L_a	Lateral crystal size
L_D	Distance between defects
n_D	Defect density
L_{eq}	Carbon domain including tortuosity
A_D	Area under the curve of D-band

A_G	Area under the curve of G-band
A_{2D}	Area under the curve of 2D-band
λ_L	Laser wavelength
D_C	Diffusion coefficient
C_{max}, C_{min}	Initial concentrations at the interface of SiOC and SiO_x
E_a	Activation energy
R	Gas constant
R_H	Hall coefficient
N	Charge carrier density
μ_H	Charge carrier mobility
T_{com}	Commutation temperature
$A_{Unloading}$, $A_{Loading}$	Area under hysteresis curve

III. List of Figures

Figure 2.3-1. Molecular structural units of preceramic polymers used in this work. 7
Figure 2.3-2. Effect of heat-treatment temperature on the RT-conductivity of C-11 and C-17 samples. 9
Figure 2.3-3. Models for the microstructure of PDCs in different conducting regimes [97]. (1), (2), and (3) are Si-based nanodomains, free carbon ribbons, and SiC nanoparticles, respectively. 10
Figure 2.4-1. Illustration of the four stages of the spin coating process. 16
Figure 2.4-2. Typical diaphragm-based design of a piezoresistive pressure sensor illustrated for sensor elements made of p-n-junctions in silicon. 18
Figure 3.1-1. Optical microscopic images of the thin SiOC polymer film derived from SPR 212 after crosslinking at 250°C. Samples were spin coated at different initial spin speeds with the acceleration of 300 rpm per second, and a second spin speed of 8000 rpm. 22
Figure 3.2-1. Morphology and composition of the segregation on the SiOC film surface. 24
Figure 3.2-2. Cross-section of the matrices of SiOC film samples annealed at A) 1100 °C for 3h, B) 1200 °C for 3h, C) 1300 °C for 3h, and D) 1400 °C for 1h. 25
Figure 3.2-3. TEM image of C17_1400_1h sample with an evident thickness depletion with corresponding SAED patterns of (1) SiOC film, (2) SiO2 layer, and (3) stacking fault of SiC. 26
Figure 3.2-4. TEM image and SAED pattern of the A) carbon-rich area of the C17_1400_3h sample, B) 4H-SiC-rich region, C) Hexagonal Si_3N_4-rich region. D) EELS spectra of C17_1400_3h sample taken within the segregation region (C/SiC/N). 26
Figure 3.2-5. A-C) Diffusion coefficients of carbon obtained from EDS analysis of carbon profiles of SiOC thin film samples annealed at different temperatures, 1100 - 1300 °C, at 3h dwelling time. D-F) Carbon profiles of isothermally annealed samples at 1400 °C at different dwelling times, 1-3h. 27
Figure 3.2-6. Diffusion coefficients of carbon obtained from EDS analysis of carbon profiles of SiOC thin film samples annealed at different isothermal temperatures, 1400 °C, for 1 - 3h. 28
Figure 3.2-7. TUNA current map of the C17-1400 sample including both the matrix and a dispersed particle is shown in Image C. The red dotted line signifies the boundary of the particle from the matrix. 30
Figure 3.2-8. The proposed hierarchical microstructure of the prepared SiOC thin film. 32

Figure 3.3-1. Relative changes in resistance as a function of microstrain at different temperatures. 35

Figure 3.3-2. Resistance response of SiOC film under compressive cyclic load. 36

Figure 3.3-3. A) Replicability of resistance response of strain gauge under compressive cyclic load at 400 °C showing the thermal stability of the response after ~25 mins of cycling time. 37

Figure 3.3-4. Aging study of sensor sensitivity at high temperature, maximum of 400 °C. 39

Figure 3.3-5. The temperature coefficient of sensitivity of SiOC film is measured at a temperature range of 25 – 700 °C. 40

IV. List of Tables

Table 3.1-1. Analysis of variance of the spin coating control factors with film thickness as the response factor. 22
Table 3.2-1. Graphitization indices of SiOC thin-film samples annealed at different temperatures and dwelling times. Indices were calculated using the Raman spectra using Equation 3.2-1 - Equation 3.2-4. 25
Table 3.2-2. Hall coefficients, charge carrier densities, carrier mobilities, and conductivities of C/SiOC samples with 17 vol% C and heat-treated at 1400 °C. 30
Table 3.3-1. Calculated temperature coefficient of resistance of the C17-1400 samples at temperature ranges between 25 °C to 700 °C. 34
Table 3.3-2. General full factorial design of experiment at 95% confidence level, α = 0.05...38

V. Cumulative Part of the Thesis

Statement of Personal Contribution

The personal contribution of the author himself to the following research articles is listed.

[1] Ricohermoso E, Rosenburg F, Klug F, Nicoloso N, Schlaak HF, Riedel R, et al. Piezoresistive carbon-containing ceramic nanocomposites – A review. Open Ceramics. 2021 Mar 1;5:100057.

Most of the sections of this review article is written by me. Sections on fabrication process was co-written by Dr. Florian Klug, while data on carbon-containing concrete nanocomposites were collected by Dr. Felix Rosenburg. Revision and approval were performed by PD Dr. Emanuel Ionescu, Prof. Helmut Schlaak and Prof. Ralf Riedel.

[2] Ricohermoso E, Klug F, Schlaak H, Riedel R, Ionescu E. Electrically conductive silicon oxycarbide thin films prepared from preceramic polymers. International Journal of Applied Ceramic Technology. 2021 May 17;19(1):149–64.

The conceptualization and execution of the design of experiment for the optimization of thin film deposition were all performed by me with the assistance of Dr. Florian Klug. All the characterization made on the thin film were performed by me including the statistical analyses. This manuscript is written by me. Revision and approval were performed by PD Dr. Emanuel Ionescu, Prof. Helmut Schlaak and Prof. Ralf Riedel.

[3] Ricohermoso E, Klug F, Schlaak H, Riedel R, Ionescu E. Compressive thermal stress and microstructure-driven charge carrier transport in silicon oxycarbide thin films. Journal of the European Ceramic Society. 2021 Oktober;41(13):6377–84.

All experimental work was performed by me including the data analysis. The manuscript was written by me and revised by PD. Dr. Emanuel Ionescu and Prof. Ralf Riedel.

[4] Ricohermoso E, Klug F, Schlaak H, Riedel R, Ionescu E. Microstrain-range giant piezoresistivity of silicon oxycarbide thin films under mechanical cyclic loads. Materials & Design. 2022 Jan 1;213:110323.

The piezoresistive test setup used in this work was design by Dr. Florian Klug including the software for data recording. The sample preparations and assessment were conducted by me together with the statistical analysis for sample replicability and capability. The manuscript is written by me and revised by PD Dr. Emanuel Ionescu and Prof. Ralf Riedel.

[5] Ricohermoso E, Vallet M, Haripre E, Solano-Arana S, Riedel R, Ionescu E. Hierarchical microstructure growth in a precursor-derived SiOC thin film prepared on silicon substrate. International Journal of Applied Ceramic Technology. *Accepted 22 July 2022.*

This paper is a collaboration between Dispersive Solids in TU Darmstadt and the LMPS – CNRS in France. The FIB preparation, TEM, and EELS analyses were carried out by Dr. Maxime Vallet and Dr. Eva Haripre. The remaining experimental work were performed by me and Susana Solano-Arana. Data analyses were analyzed by me with corrections from Dr. Vallet for the TEM and EELS result. The diffusion coefficient calculation was done with the supervision of PD Dr. Emanuel Ionescu. The manuscript is written by me and revised and approved by Dr. Vallet, PD Dr. Emanuel Ionescu and Prof. Riedel.

VI. Curriculum Vitae

Personal Data

Name:	Emmanuel Ricohermoso III
Date of birth:	22 October 1991
Nationality:	Filipino

Education

Since October 2019	**Technische Universität Darmstadt** PhD candidate in Materials Science
09/2017 – 09/2019	**EIT RawMaterials Academy** Double-degree master's in Advanced Materials for Innovation and Sustainability (AMIS) **Technische Universität Darmstadt** Master of Science **Grenoble INP- Phelma** MS Materials Science and Engineering
06/2008 – 03/2013	**University of the Philippines** BS Materials Engineering
06/2004 – 04/2008	**Leuteboro National High School**
06/1998 – 04/2004	**Socorro Central School**

Open Ceramics 5 (2021) 100057

Contents lists available at ScienceDirect

Open Ceramics

journal homepage: www.editorialmanager.com/oceram

Piezoresistive carbon-containing ceramic nanocomposites – A review

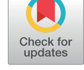

Emmanuel Ricohermoso III [a,**], Felix Rosenburg [a], Florian Klug [b], Norbert Nicoloso [a], Helmut F. Schlaak [b], Ralf Riedel [a], Emanuel Ionescu [a,*]

[a] Fachbereich Material- und Geowissenschaften, Technische Universität Darmstadt, Otto-Berndt-Str. 3, D-64287, Darmstadt, Germany
[b] Fachbereich Elektrotechnik und Informationstechnik, Technische Universität Darmstadt, Merckstr. 23, D-64283, Darmstadt, Germany

ARTICLE INFO

Keywords:
Piezoresistivity
Piezoresistive sensing
Ceramic nanocomposites
Polymer derived ceramics
Carbon-containing nanocomposites

ABSTRACT

The present review introduces a class of ceramic nanocomposites that contain carbon as disperse phases and exhibit piezoresistive behavior. After a brief introduction in which the piezoresistive effect is described and selected principles for the design of piezoresistive sensing devices are highlighted, various carbon-containing ceramic nanocomposites are presented and discussed in the light of their preparative access as well as their piezoresistive behavior. Emphasis is put on carbon-containing ceramic nanocomposites in which the dispersed carbon phase is generated in situ during a thermal treatment process, which allows tunable carbon contents and crystallinities, along with a highly homogeneous dispersion of the carbon phase in the ceramic matrix. The piezoresistive carbon-containing ceramic nanocomposites presented here are furthermore critically discussed within the context of their potential use as force/strain/pressure sensing materials for applications at ultrahigh temperatures and in hostile environments.

1. Introduction

1.1. Historical background of the piezoresistive effect

Piezoresistivity was discovered in the late nineteenth century (1856), when Lord Kelvin revealed through a tensile test on copper and iron rods that the change in electrical conductivity was different for both materials at the same amount of elongation [1]. He further mentioned that these differences were specific to individual material properties. The exact measurement of the change of resistance caused by tension along the length of the rods was carried out by H. Tomlinson soon after the findings of Lord Kelvin [2]. In 1930, Rolnick studied the resistance of different metallic wires upon vibrational loads [3]. In 1935, Cookson defined the term piezoresistance which describes the correlation between the relative change in the resistance of a material and the applied stress [4]. The term "piezo" is rooted in the Greek term "piezein" which means to press. A large change in conductivity in a single-crystal semiconductor element like silicon, germanium, and tellurium was discovered by Bardeen and Shockley in 1950, which are linked to the change in the intrinsic conductivity and resistance of a p-n junction upon applying pressure on it [5]. In 1954, this idea was confirmed by Smith, who demonstrated a change of resistivity occurring in silicon and germanium (both p- and n-type) when a uniaxial tension was applied. These results were described in terms of a pressure coefficient of resistivity and two shear coefficients [6]. In 1956, Morin was able to demonstrate the temperature dependence of the piezoresistance of silicon and germanium [7], and a year later, the first silicon-based strain gauge was made by Mason and Thurston [8], which opened up to the production of piezoresistive sensors in the market. A state of the art of piezoresistive strain gauges including the design challenges is given below in the present Review (see Section 1.3).

1.2. Principles of piezoresistive effect

1.2.1. A general principle of piezoresistive effect

Most of the metals own a small piezoresistive effect with GF (gauge factor) values of ca. 2, as the change in their resistance is only affected by geometrical effects (for instance GF for constantan alloy with 60% Cu and 40% Ni is 2.1). In the case of semiconducting materials, the piezoresistive effect originates from the intrinsic deformation of the energy bands as a result of the applied stress. This induces changes in their charge carrier mass and mobility and thus the resistivity of the material is changed. Consequently, semiconducting piezoresistive materials exhibit significantly higher gauge factors as compared to their metallic counterparts.

* Corresponding author.
** Corresponding author.
E-mail addresses: emmanuel_iii.ricohermoso@tu-darmstadt.de (E. Ricohermoso), emanuel.ionescu@tu-darmstadt.de (E. Ionescu).

https://doi.org/10.1016/j.oceram.2021.100057
Received 28 November 2020; Received in revised form 6 January 2021; Accepted 7 January 2021
Available online 13 January 2021
2666-5395/© 2021 The Author(s). Published by Elsevier Ltd on behalf of European Ceramic Society. This is an open access article under the CC BY-NC-ND license (http://creativecommons.org/licenses/by-nc-nd/4.0/).

The following table shows commonly used strain gauge materials and their corresponding GF values.

As mentioned above, the term piezoresistivity describes the fractional change of the resistance of a material that is exposed to mechanical stress. It is one of the most used transducer effects with a broad field of applications as pressure, force, and an inertial sensor.

Two contributions concerning the change in the resistance of materials upon mechanical load can be identified: The first contribution is a purely geometrical effect, $(1 + 2\nu)$, with ν as the material's Poisson's ratio, while the second part describes the piezoresistive response of the material $(\Delta\rho/\rho)$, ρ as the resistivity of the material [9]. Considering isotropic material and a linear elastic region described by Hooke's law, the change in the resistivity can be defined cf. $\frac{\Delta R}{R_0} = (1 + 2\nu)\varepsilon + \left(\frac{\Delta\rho}{\rho_0}\right)$, where $\frac{\Delta R}{R_0}$ is the fractional change in resistance to strain, ε. The gauge factor (GF), which describes the fractional change of the resistance with the applied strain is defined cf. $GF = \frac{\Delta R/R_0}{\varepsilon} = (1 + 2\nu) + \frac{\Delta\rho}{\varepsilon\Delta\rho_0}$ and is a standard measure of the sensitivity of strain-based sensors. Table 1 shows commonly used strain gauge materials and their corresponding GF values.

1.2.2. Piezoresistivity in semiconducting materials

The theory of piezoresistance on semiconducting materials are mostly based on one-dimensional descriptions of electron and hole transport in crystalline structures under strain. Shifts on the bandgap energies were the basis of the first discovery of Smith [6]. Tufte and Stelzer were able to demonstrate in a study published in 1963 the piezoresistive properties of n- and p-type layers formed by the diffusion of impurities into silicon [10]. The mobilities and effective masses of the charge carriers are significantly different from one another and fluctuate under strain. The magnitude and signs of the piezoresistive coefficient were found to be associated with several factors including crystallographic directions, impurity concentration, temperature, and stress applied to the material. Several studies supported this relationship of carrier characteristics and strain [8,11–13].

Three symmetrical valleys along the ⟨100⟩ direction were proposed under the Herring's Many-Valley model [13]. In this direction, in their basic state, the valence electrons occupy the minimum energy level of each valley along the centerline of a constant energy ellipsoid. Perpendicular to the long axis of the ellipsoid the mobility of the electrons is higher. When external stress is applied the ellipsoids are asymmetrically dilated or constricted resulting in an anisotropic change in charge mobility proportional to the applied stress. In n-type silicon, the asymmetric deformation of the ellipsoids results in a decrease of electron density along the [100]-axis while the density along [010] and [001] is increased. Hence the isotropy of the conductivity in the semiconductor is lost and the average electron mobility in the direction of the compression is about five times smaller than the transversal mobility [14].

Consequently, the magnitude of the piezoresistivity is dependent on the orientation of the crystal planes and the applied stress. To describe the direction-dependency of the piezoresistive effect the piezoresistive coefficients π_{ij} are introduced. Therefore, the electric field vector $\vec{E}$, and the current density vector $\vec{j}$ have to be linked by a 3-by-3 resistivity tensor (ρ). Due to the symmetry in the crystal silicon, the resistivity tensor (ρ) is reduced from nine to six coefficients. The obtained resistivity tensors (ρ) and the stress tensor (σ) can be summarized in a 6-by-6 matrix using the piezoresistive coefficients π_{ij}. Because of the cubic symmetry in crystal silicon and germanium, the number of the piezoresistive coefficients is reduced down to three independent coefficients: π_{11}, π_{12}, π_{44}. These coefficients are material-specific properties and hence vary from one material to another describing the anisotropic behavior of the piezoresistive effect in the regarded material.

$$\pi_{ij} = \begin{pmatrix} \pi_{11} & \pi_{12} & \pi_{12} & 0 & 0 & 0 \\ \pi_{12} & \pi_{11} & \pi_{12} & 0 & 0 & 0 \\ \pi_{12} & \pi_{12} & \pi_{11} & 0 & 0 & 0 \\ 0 & 0 & 0 & \pi_{44} & 0 & 0 \\ 0 & 0 & 0 & 0 & \pi_{44} & 0 \\ 0 & 0 & 0 & 0 & 0 & \pi_{44} \end{pmatrix}$$

For most piezoresistors, two arrangements between strain and resistance change are of interest resulting in a longitudinal and transversal piezoresistive effect. The longitudinal effect describes the change of the resistance parallel to the applied strain, while the second transverse effect describes the change to a perpendicular applied strain. The effective values for the longitudinal piezoresistive coefficient π_l and the transverse piezoresistive coefficient π_t can be calculated from the coefficients π_{ij}. For anisotropic materials such as doped silicon π_l and π_t strongly depend on the crystal orientation of the resistor as the mobility of the charge carrier is anisotropic upon the strain. For lightly doped silicon (p- or n-type < 1018 cm^{-3}) relatively high piezoresistive coefficients are obtained compared to higher doping concentrations. Regardless higher dopant concentrations are used more often as the temperature effect on resistance and sensitivity is much lower. As can been seen in Table 2 the piezoresistive coefficient π_{44} dominates in p-doped silicon whereas in n-doped silicon π_{44} can be neglected. Therefore, the resistance path of the sensor should be aligned in the direction of the dominant piezoresistive coefficient.

In general, piezoresistors with larger sizes give better sensitivity and lower noise values. Commercially available microsystem devices are usually based on silicon and germanium and their alloys. In 1989, the piezoresistive effect on polycrystalline silicon showed that the conductivity change of the material due to stress is a result of the shifting of relative sub-bands and the carrier transfers [15]. The study also confirmed the theory of the difference in longitudinal and transverse strain measurements caused by the anisotropy of piezoresistance in silicon. Richter et al. investigated the piezoresistive effect on p-type silicon and strained $Si_{0.9}Ge_{0.1}$ as potential microelectromechanical systems (MEMS) device [16]. They found out that when stress was applied along the [100] direction, the piezoresistive coefficient of silicon is 30% lower than the lightly-doped silicon. In 2008, a polycrystalline silicon-germanium sample was studied by Lenci et al. which revealed longitudinal and transverse piezoresistive coefficients of 4.25×10^{-11} Pa^{-1} and 0.125×10^{-11} Pa^{-1}, respectively [17].

1.2.3. Piezoresistivity in percolating systems

Broadbent and Hammersley first introduced the percolation theory in 1957 to demonstrate the phase transition of a permeable 3D box [18]. In

Table 1
Comparison of typical metallic and semiconducting piezoresistive strain gauge materials.

Material	Thickness	Strain	Gauge factor *(GF)*
Cu–Ni-Alloy	80–100 μm	±0.1%	2
$Bi_2Ru_2O_7$	≤50 μm	±0.1%	12–18
TiON	≤1 μm	±0.1%	4–5
Poly-Si	≤1 μm	±0.1%	20–30
Doped silicon	10–15 μm	±0.2%	100–255
Silicon	2–4 μm	±0.05%	80–255

Table 2
Resistivity and piezoresistive coefficients for p- and n-doped silicon and germanium [Reprinted with permission from AIP Publishing] [8].

Materials	ρ [Ωcm]	π_{11} [10^{-31} Pa^{-1}]	π_{12} [10^{-31} Pa^{-1}]	π_{44} [10^{-31} Pa^{-1}]
Silicon				
n-type	11.7	−102.2	53.4	−13.6
p-type	7.8	6.6	−1.1	138.1
Germanium				
n-type	9.9	−4.7	−5.0	−137.9
p-type	15.0	10.6	5.0	46.5

1973, Kirkpatrick used the percolation theory to simulate the phase transition of conductive particle-based composites from being insulating to conducting [19]. In contrast to semiconductors, the piezoresistive effect in percolative nanocomposites is provided upon dispersing a conductive filler within an insulating matrix. The focus of the following section is on the relationship between piezoresistivity and the amount of the used carbon-based conductive fillers (e.g. carbon black, carbon nanofibers, carbon nanotubes, graphene, etc.). The typical evolution of the electrical conductivity as carbon fillers are gradually introduced into an insulating matrix is depicted in Fig. 1. At low filler contents, the electrical conductivity of the composites mainly refers to the insulating matrix (stage I in Fig. 1). As conductive pathways are formed upon increasing the carbon content through the formation of clusters, the conductivity of the composite drastically increases. The minimum volume fraction of the conductive admixture that causes significant electrical conductivity is called the percolation threshold (see stage II in Fig. 1). In the third stage, the increasing filler content causes the formation of several additional electrical pathways until the conductivity levels off at a constant value.

Recent studies have shown that if the polymers with low Young's modulus, just as silicone, epoxy, or PDMS, are chosen as the matrix, pressure can also lead to a rapid decrease of resistance in polymer-based conductive composites around the percolation threshold, named as piezoresistivity [20,21]. The conductive fillers are separated by the matrix layer and only a little conductive network appears when the filler content is just higher than the critical threshold. If a uniaxial pressure is applied to the composites, the polymer matrix deforms leading to a thinner insulating layer between conductive clusters. Some of the conducting fillers are forced close enough as the pressure increases, resulting in more tunneling paths of charge carriers. Thus, the conductivity increases under pressure.

1.3. Sensing devices based on the piezoresistive effect

The piezoresistive effect facilitates the design of various piezoresistors and sensors. A brief overview of available variants and design challenges follows in the section below.

1.3.1. Principles and fabrication of piezoresistors

Depending on the materials and fabrication technologies, different piezoresistive strain gauges are available on the market. Common and commercially available strain gauges can be divided into the following four categories: metal, thin film, thick film, and silicon-based.

Metal strain gauges have a large market share, as they show a simple structure and are inexpensive to manufacture. The typical arrangement is a layered composite of metal and polymer films. In metal, as described before, the main effect results from the change in geometry when stretched and piezoresistive effects play a minor role. In order to increase the useable geometry, etching, or laser processes in meandering form pattern thin metal foils. Protective layers of polymer material ensure better handling and application to the measuring surface. Due to the high conductivity of metals, the resistors are normally in the range of 120 Ω, 350, Ω or 1 kΩ and designed to have a low cross-sensitivity of less than 0.1%.

Further, the deposition of thin films in cleanroom processes such as vapor phase deposition is common. With appropriate substrates, platinum-based strain gauges reach maximum operating temperatures of up to 1000 °C [22]. As the report by Wilde et al. a thin-film platinum sensor on silicon substrate exhibited a gauge factor of two [23]. It is able to measure the pressure in a combustion chamber of an engine at temperatures up to 600 °C. Nevertheless, due to its low sensitivity, equivalent to a sensor signal prone to noise issues, the accuracy is limited, discouraging further development.

Another approach is the production of thick film piezoresistors. A widely used production method is screen printing and sintering of ceramic materials loaded with functional oxides as Ruthenium (IV). Low-cost and more versatile alternatives are the printing of resistors using inkjet or aerosol processes. Although the average gauge factor is slightly higher with an average of 8–12, sensors based on this principle are not suitable for ultra-high temperatures at present [24,25].

Due to their high piezoresistivity, semiconductors form the basis for the most sensitive elements. In comparison, the change in resistance caused by the change in geometry is negligible. Silicon sensor elements exhibit gauge factors two orders of magnitudes higher, up to a maximum of 200, and can reach negative values as well [26]. In terms of

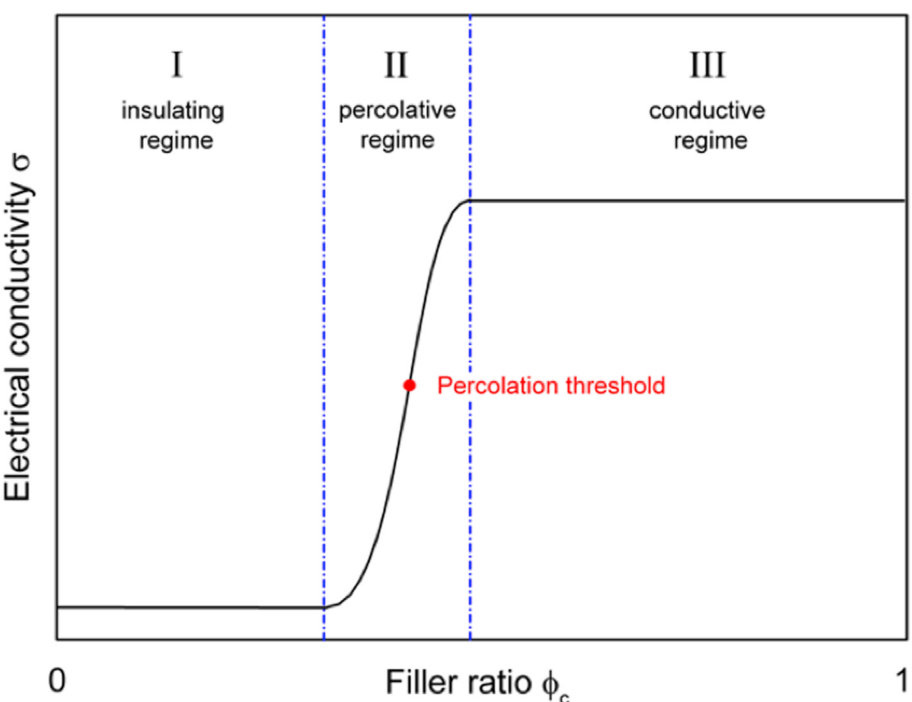

Fig. 1. Schematic depiction of the three conduction regimes of percolative systems.

fabrication, they belong to two groups, homogeneous and inhomogeneous silicon elements. The production of homogeneous elements involves photolithography and etching methods of uniformly doped silicon. The application is similar to classical metal strain gauges by gluing on. Inhomogeneous elements are made of boron diffusion or ion implantation on silicon substrates that form p-n junctions. This allows integrated and miniaturized sensors with high base resistances of several kΩ for low power applications. However, all silicon-based sensors have a high-temperature dependence, which must be compensated during operation. Further, the low bandgap of 1.12 eV limits the application range of silicon to 200 °C [27,28]. With special designs and single crystalline silicon, a maximum of 400 °C is possible, where the mechanical limit occurs through plastic deformation upon loading. This encourages the use of other materials or semiconductors with higher band gaps and electromechanical stability [29].

1.3.2. Device design and challenges

Except for simple strain measurements, strain gauges are integrated as parts in sensors for physical quantities such as force, torque, and pressure. The fundamental design of all sensors consists of a deformation body, the measuring element, leads, and readout electronics. Force and torque transducers usually have large dimensions with metal strain gauges glued to deformation bodies. Pressure transducers are easier to miniaturize and appear as MEMS in many devices. The production takes place in cleanroom processes on the wafer level. The most common deformation body for piezoresistive pressure sensors is a diaphragm as shown in Fig. 2.

The sensor elements are positioned on the thin and elastic diaphragm so that they are exposed to strain when external pressure occurs. Therefore, the placement of the elements follows the locations of the highest stress. Simple sensors consist of a p- or n-doped silicon substrate with n- or p-doped regions that form the piezoresistive elements. Heavily doped n+ or p+ areas enable low impedance contacts. Metallization or bonding wires serve as electrical supply and signal lines for the sensor elements. Bridge circuits, usually in the form of Wheatstone bridges, evaluate the electrical resistance of these elements. This allows a highly precise acquisition of the accumulating resistances with simultaneous rejection of temperature-induced influences by the silicon. Due to their high sensitivity, high linearity, and simplicity in the evaluation by bridge circuits they are dominating in many industrial sectors. However, the only possibility for use in harsh environments is to shield these elements due to the temperature issues described above, which reduces accuracy while increasing complexity.

The most essential criteria for the design of the sensor are a high sensitivity significantly above a gauge factor of two, low interference from external influences such as temperature or humidity, and established manufacturing technologies to reduce costs. Therefore, the sensor material defines the main properties. In harsh environmental conditions, not only the requirements for the functional material become higher, but other materials and the total number of components and processes also become decisive. In addition to temperature and chemical stability, the temperature dependence of the gauge factor should be as low as possible to enable accuracy at varying conditions. Moreover, not only thermal expansion coefficients of the materials must match, but also stable electrical lines and bonding techniques must be available. According to the current knowledge, this combination and the limitation of suitable functional materials prevents the development of ultra-high temperature resistant sensors above 400–600 °C with high sensitivity comparable to silicon at the same time [29].

2. The piezoresistive effect in carbon-containing semiconductors

Since the discovery of Smith of the piezoresistive effect on silicon and germanium in 1954, advances in materials science and processing technology have been conducted. New materials were also explored which possessed advantages over silicon in terms of better thermal stability, higher or lower modulus of elasticity, and stability on the oxidative environment.

2.1. Piezoresistivity in silicon carbide

One of the well-known carbon-containing semiconductors is silicon carbide (SiC) due to its superior mechanical properties. It has Young's modulus of 424 GPa, high thermal conductivity, and is inert to a corrosive environment [30]. Another advantage of SiC is its wide bandgap of 2.39–3.33 eV which results in increased reverse leakage of the current across the p-n junction at high temperature due to the reduction of the effect of the thermal generation of the carriers [30]. In 1993, longitudinal and transverse gauge factors were measured by Shor et al. for a β-SiC as a function of temperature [31]. Two years after, the first reported piezoresistive sensor made out of β-SiC on silicon on the insulator was made by Ziermann et al. [32] with a gauge factor of −32 in the [100]-direction.

Strass et al. explained that the shift from negative to positive gauge factor was influenced by the grain boundaries on polycrystalline SiC [33]. They also showed the dependence of gauge factor on the crystal quality of β-SiC layers wherein single-crystalline β-SiC provided a negative gauge factor value of 5, and 15 at [011], and [010] directions, respectively. The recorded values of the gauge factor for textured and randomly-oriented polycrystalline samples resulted in positive values greater than 5 for both [011] and [010] directions [33]. Toriyama and Sugiyama showed that increasing the temperature decreases the gauge factor of the SiC material [34,35]. They also mentioned that the piezoresistive effect of n-type SiC is based on three mechanisms namely electron transfer, mobility shift, and inter-valley scattering. This study was conducted on cubic 3C–SiC and hexagonal n-type 6H–SiC and showed that the anisotropy of the piezoresistance tensor vanishes at (0001) plane while the isotropic part remains. This revealed that longitudinal, transverse, and shear gauge factors are isotropic at the (0001) plane [34,35].

Feasibility studies of SiC-based sensors operating at 500 °C as a potential sensor for engines were presented by Phan et al. in a more detailed review on piezoresistivity in SiC material for MEMS application [36]. Furthermore, the review mentioned other applications of the SiC piezoresistive effect which includes mechanical sensors for high power density applications, bio applications, and high-frequency applications.

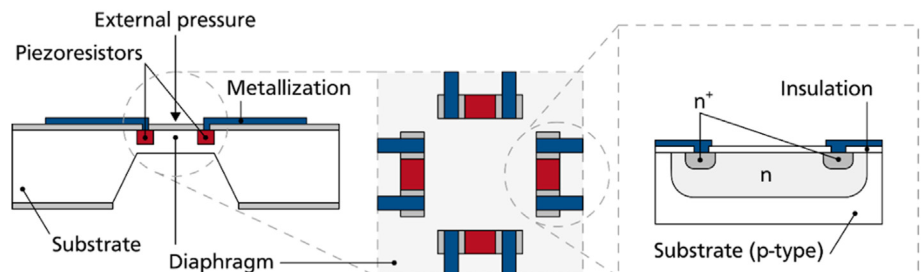

Fig. 2. Typical diaphragm-based design of a piezoresistive pressure sensor illustrated for sensor elements made of p-n-junctions in silicon.

2.2. Piezoresistivity in diamond

Similar to SiC, diamond has been an attractive material for micromechanical devices for high-temperature and harsh environments applications [37–39]. The Young's modulus of an experimental diamond film deposited via the CVD process was reported from 500 to 1000 GPa [40]. In 1992, the piezoresistive effect was demonstrated and studied in both polycrystalline and homoepitaxial CVD diamond films [39]. It was reported that the gauge factor for polycrystalline diamond film applied with 500 microstrains is as high as 6 at room temperature. This gauge factor increases rapidly upon an increase of temperature which brings values to >30 and > 120 at 35 °C and 50 °C, respectively [39]. These values are higher than the gauge factors reported for polycrystalline and single-crystal silicon exposed to similar conditions. Homoepitaxial p-type diamond films were found to have gauge factors of 200–550 when operated at room temperature [37]. In a study conducted by Sahli et al., it was highlighted that the intra- and inter-grain conduction in a CVD diamond with a large grain has lower resistivities on the intra-grain as compared to the grain boundaries [41]. It was also observed that the piezoresistive gauge factor weakens when the conduction path crosses the grain boundaries. Werner et al. used a boron-doped polycrystalline diamond film and reported that the usage of lower doping concentrations can improve the sensitivity of diamond film sensor [38].

3. The piezoresistive effect in carbon-containing ceramic nanocomposites

An inorganic composite is a solid material consisting of at least two inorganic material phases. If one dimension of the embedded material phase is on a nano-dimensional scale, the composite can be considered as nanocomposite [42]. Besides the different features of each component, their distribution and geometry play a certain role in defining the resulting properties of the new composite.

There are two methods of functionalization which are considered in this work. In the first method, the carbon phase is mechanically mixed into the ceramic composite by using dispersing agents to prevent agglomeration. The second method refers to the polymer-derived ceramic route [43–47]. Here, the carbon phase is generated in-situ during the polymer to ceramic transformation. In the following section, we look at differently prepared piezoresistive nanocomposites, with a nano-dimensional carbon phase embedded into an insulating ceramic bulk matrix.

3.1. Piezoresistivity in carbon-containing Al_2O_3 and MgO nanocomposites

Recently, Waku et al. investigated the electrical properties of carbon functionalized alumina and magnesia composites under applied load [48]. The piezoresistive measurements of magnesia with graphite particles in the amount of 5.0 wt% lead to a gauge factor value of 45 (see Table 3). The alumina system was equally functionalized with graphite particles in the amount of 3.5 wt% and reveals a gauge factor value of 42 (Table 3). In both cases, the amount of carbon was set near the percolation threshold as the electrical conductivity increases exponentially in this region assuming a high-pressure dependency of the resistivity. In a model developed by Kusy *et* al, they identified that the percolation threshold does not only depend on the amount of the conductive phase present on the system but it also depends on the initial coverage of the dispersed phase on the primary phase to create a continuity [49]. Therefore, Kishimoto et al. further investigated the most favorable particle size ratio to evaluate the compositional dependency of the sensitivity for an alumina carbon black composite system [50]. They concluded that the highest piezoresistive behavior could be found near the percolation threshold with a high initial particle ratio between the insulating/conductive components. The piezoresistive effect was explained using the void volume inside the composite which is assumed to decreases under applied pressure. As a result, the conductive volume fraction inside the composite formally increases upon loading, leading to an effective decrease of the overall resistivity.

Table 3
Piezoresistive behavior of Al_2O_3 and MgO reinforced with carbon.

Matrix	Carbon filler	An aspect ratio of the carbon phase	Threshold [vol %]	*GF*-value
Al_2O_3	graphite particles	~100	4.99	42[a]
	carbon black particles	~100	10.9	18[a]
MgO	graphite particles	~100	6.12	45[a]

[a] Values have been calculated by the author using literature known as Young's modulus of the ceramics [51].

3.2. Piezoresistivity in carbon-containing concrete nanocomposites

Demands for structural health monitoring (SHM) has been an area of interest since the 1990s to evaluate and predict the structure life of service. One of the methodologies explored for the SHM application is the use of a piezoresistive cement-based sensor which is an alternative for the existing strain gauges, fiber optic sensors, and shape memory alloys [52,53]. It was in 1993 when Chen and Chung described the linearity between the change of the volume resistivity and compressive stress of a mortar containing carbon fibers [54]. They further elaborated that an increase in electrical resistivity was observed during the crack generation or propagation and the decrease during crack closure. Studies focused on using concrete-based sensors mixed with various nanomaterials to explore traffic detection on the pavement [55], real-time damage detection and assessment of concrete structures [56], transducers for detection of dynamic strain behavior [57], and crack monitoring [58] had been widely explored.

In a review published by Han et al., three microscopic phases present in concrete-based sensors were highlighted, namely (1) cement matrix, (2) interfaces between fillers, and (3) the fillers [59]. Among these three, the interfaces between fillers which can form a conductive network have the greatest contribution to the electrical conductivity of the cement-based sensor [60]. Different types of fillers have been considered, including nickel powder, titanium dioxide, iron (III) oxide, graphite powder, carbon black (CB), carbon fiber (CF), and carbon nanotubes (CNT) [54,56–58,61,62].

In 2014, Loamrat et al. studied the effect of adding graphite powder and CFs on the resistivity of cement-based sensors [61]. It was stated that the fractional change in resistivity (FCR) of the sensors with graphite powder fillers dropped when subjected to a set of a compressive load done at three cycles with the strain of 0.0025, 0.005, and 0.01 respectively. In the end, CFs and graphite powder both decreased the resistivity of the concrete but graphite powder also decreased the compressive strength of the material. A similar result was obtained in a study conducted by Shasna et al. in 2019 [63]. It was also validated that the resistivity of the concrete increased during aging. CNF-concrete composites show better mechanical properties compared with those of plain concrete and a clear correlation between the electrical resistance and the applied strain was demonstrated [64,65]. Galao et al. performed a systematic study on the self-sensing properties of CNF-reinforced cement nanocomposites [66]. Several variables like concentration, curing, current density, loading rate, or maximum applied stress and their influence on the self-sensing properties were considered. The CNF-cement nanocomposites with the highest sensitivity under longitudinal compression exhibited a CNF concentration of 2 wt% and a gauge factor (GF) value of ca. 50. Furthermore, it was shown that the curing of the cement-based nanocomposites has a significant influence on their piezoresistive behavior. Thus, a longer curing time provided a tight fiber-matrix interface and thus was found to be beneficial for an enhanced k value [67]. Wen et al. were able to create a theoretical model that considers the

origin of the piezoresistive behavior of carbon fiber cement that relies on the slight pull-out of crack bridging fibers during the crack opening and consequently increasing the electrical resistivity of the fiber-matrix interface [68].

Carbon black reinforced cement-based nanocomposites were also reported. Due to their low aspect ratio, the carbon black particles are less effective in providing an electrically conductive cement composite [69]. However, CB particles are less expensive and have therefore been used as partial replacement of carbon fibers to lower the cost, while the sensing properties of the prepared nanocomposites were maintained [70,71]. CB-reinforced cement nanocomposites (15 wt% CB) were shown to provide k values of 55 under compressive loading. Even at markedly lower CB contents, significant k values were obtained. Thus, a cement-based nanocomposite containing 0.5 wt% CB exhibited a gauge factor value of 14.

Some studies were conducted to improve the piezoresistive behavior of multi-walled CNTs (MWCNT) by enhancing the surface of the nanotubes. According to Fu, the bond strength between the cement and the carbon fiber can be enhanced by using oxidizing chemical treatments, with ozone treatment giving the most effect [72]. Li et al. used H_2SO_4 and HNO_3 treatment to modify the surface of MWCNTs which led to improved compressive strength, flexural strength, and failure strain of the cement composite [73]. The resulting carboxylic acid groups on the CNT surface react with the calcium-silicate-hydrate (C–S–H) and/or $Ca(OH)_2$ from the cement matrix to form a strong covalent bond between the MWCNT and the matrix. Also, the different piezoresistive behavior between chemically treated and untreated CNT cement composites under cyclic compressive loading was investigated [74]. Both untreated and treated CNT used in the amount of 0.5 wt% by mass of cement greatly decrease the electrical resistivity and improve the pressure sensing properties of the cement nanocomposite. The authors assume that the contact points and the tunnel distance between the nanotubes are altered with increasing the compressive load and this induces a change of the resistivity. The untreated and treated CNT-reinforced cement composite (both containing 0.5 wt% CNTs) exhibit k values of 272 and 371, respectively. As revealed by the SEM micrograph in Fig. 3, the untreated CNTs form a network within the cement matrix; whereas the treated CNTs are finely dispersed and covered by C–S–H and do not form any network. Therefore, the untreated CNT composite has a stronger effect on reducing the overall electrical resistivity of the nanocomposite; whereas the treated CNTs have a remarkable effect on the pressure-sensing properties of the composite. Chemical modification of the nanotubes allows for tuning the interface between the CNTs and the cement matrix and thus to improve the piezoresistive response of the nanocomposites [74].

In a recent study by Wang et al., the piezoresistive behavior of cementitious composites incorporated with MWCNTs under different moisture conditions was investigated [75]. The results showed that the piezoresistive behavior of cementitious composites at high moisture is mainly controlled by ionic conduction. In Fig. 4, during cyclic compression, the strain variation was observed to have a linear behavior reaching a peak value of 0.3% which returns to 0 upon unloading which indicates the location of the strain to be within the elastic regime. On the other hand, a positive piezoresistivity was observed as shown by the increasing $\Delta R/R_0$ upon unloading.

Recently, mixed carbon fillers were explored as they may allow to finely tune the electrical and mechanical properties of the composites for sensing reliability and sensibility. Azhari and Banthia found that combining 15% CFs and 1% MWCNT results in composites with a higher ability to sense applied compressive load as well as with better reproducibility [76]. A similar study previously reported by Luo et al. was made using lower content of fillers at 0.5% CFs and 0.1% MWCNTs only [77]. In 2015, Ou and Han created a CB- and CF-reinforced self-sensing concrete with 0.0138%/με sensitivity, 0.007 με resolution, 4.25% linearity, 4.36% repeatability, and 3.63% hysteresis [71]. In 2017, Lee et al. showed that the percolation threshold of CFs and MWCNTs was 0.5–1.0

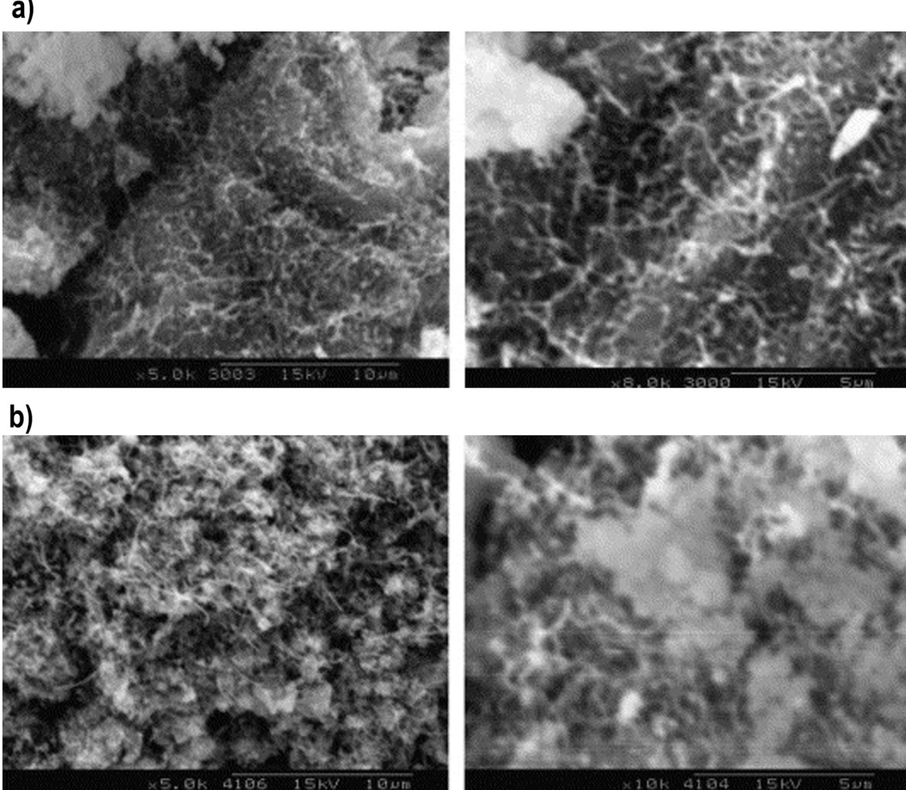

Fig. 3. SEM images of (A) untreated and (B) treated CNT-reinforced cement matrix composites revealed the dispersion of C–S–H on untreated samples which helps the pressing-sensing of the device [Reprinted with permission from Elsevier] [74].

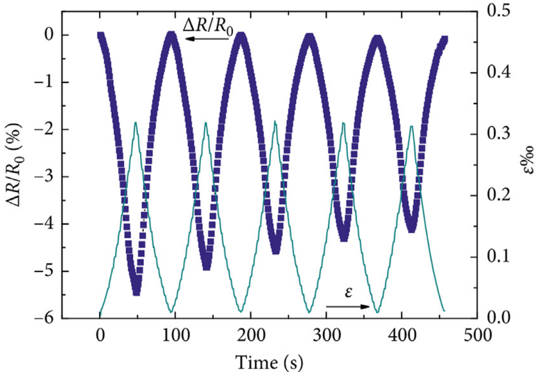

Fig. 4. Reversible piezoresistive behavior of a carbon-nanotube-containing cement composite during cyclic compression [Open access from Hindavi with Creative Common Attribute License] [75].

vol % and 1:0 vol%, respectively [78]. The gauge factor (GF) for that composite was 160.3 with an R-square value of 0.9274 and GF of 166.6 for the concrete sensor with 1.0 vol% MWCNTs. In Fig. 5, the Fractional Change in Resistivity (FCR) of the cementitious composite with 0.1% CF and 0.5% MWCNT was seen to be in linear relation with the applied compressive strain. This held even up to the second compressive loading [78].

The cementitious nanocomposites pose a drawback concerning their processing, as they suffer from agglomeration issues, which have a negative effect on providing high and reproducible GF values. Obtaining a properly dispersed conductive phase (such as carbon) within a matrix requires a combination of ultrasonic treatment and chemical modification steps to avoid (re)agglomeration in the matrix. An alternative way to avoid the drawback of agglomeration is to generate the carbon phase in situ during the preparation process, this has been discussed in the following section.

Chung's review on electrical-resistance-based sensing devices highlighted common pitfalls related to the GF measurement method and analysis method [79]. The first identified drawback of the current works was the assumption of the negligible effect of the contact resistance when performing a two-probe measurement [80–84]. The resistance between the sample and the contact material must be decoupled which can be achieved by using a four-probe method as described by the Van der Pauw methodology. The author also mentioned that not being able to distinguish the reversible and irreversible resistance change upon application of excessive strain can result in a considerable high GF. Related to it is the failure to readout the GF only on the slope of the linear part of the resistivity vs strain curve in the elastic regime. The last point from the mentioned review focused on not recognizing positive and negative piezoresistivity caused by the application of tension and compression, respectively [79].

3.3. Piezoresistivity of carbon-containing polymer-derived ceramics

Another type of carbon-containing ceramic nanocomposites that have shown interest in the microelectronic industry is represented by the so-called polymer-derived ceramics (PDC). Polymer derived ceramics have gained a lot of interest in recent years due to their excellent homogeneity as well as stability at high temperatures and in harsh environments. Since the discovery of Fritz and Raabe in 1956 [85], when they were able to transform monomeric organosilicon compounds to SiC through a thermal process at low-temperature conditions, numerous processes, and applications for PDC have been explored. This includes photoluminescence [86,87], Li-storage capacity [88–90], thermal shock resistance [91], high resistance to crystallization, and low creep rates up to very high temperatures [92–94], gas sensing behavior, and piezoresistivity.

3.3.1. Preparation of polymer-derived ceramics

The different properties of PDCs have been correlated with the microstructure and phase composition of the material which is

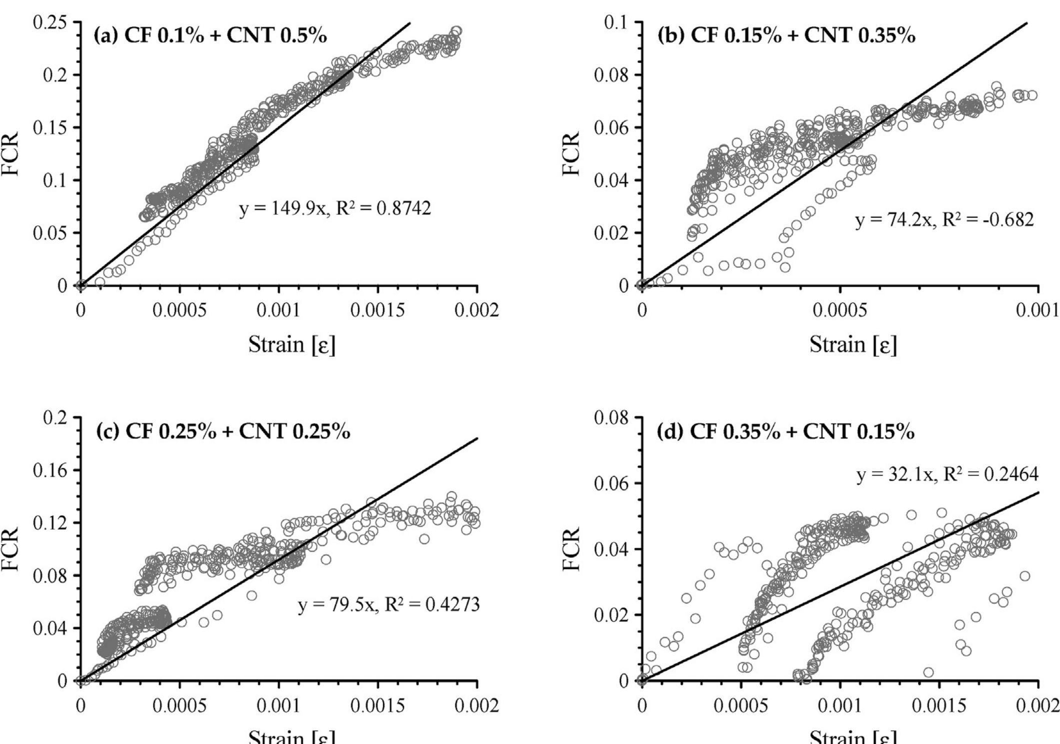

Fig. 5. Correlation between FCR and compressive strain of cement-based composites with both CFs and MWCNTs; (a) composites with 0.1 vol% CFs and 0.5 vol% MWCNTs; (b) composites with 0.15 vol% CFs and 0.35 vol% MWCNTs; (c) composites with 0.25 vol% CFs and 0.25 vol% MWCNTs; and (d) composites with 0.35 vol% CFs and 0.15 vol% MWCNTs [Open access from MDPI] [78].

dependent on the polymer-to-ceramic (PTC) transformation conditions as well as chemistry, and molecular structure of the polymeric precursor [46]. Silicon-containing PDCs including silicon carbonitrides and silicon oxycarbides (SiCN and SiOC) can be synthesized successfully at relatively low temperatures, i.e. at or below 1100 °C, from suitable Si-containing polymeric precursors, so-called preceramic polymers [46,95,96].

For the present paper, only the synthesis of ternary ceramic systems, SiOC and SiCN, will be in focus. A summary of the different synthesis routes for preceramic polymers for both ternary and quaternary ceramic systems can be found in References [41–45].

Preceramic polymers are transformed into ceramic material in several steps namely shaping, cross-linking, pyrolysis, and ceramization. Different methods can be employed to facilitate the shaping of preceramic polymers. In general, the shaping process is assisted with the use of binders which are dissolved in an aqueous solution and will be burned out during the sintering process. Some of the common processes include casting, injection molding, pressing, electrospinning, fiber drawing, coating, impregnation, and recently 3D printing. Rheology of the precursors plays a major part in deciding the proper method to be used and has a fundamental effect on the establishment of the number of additives to be used and the corresponding heating rate required for the process [97]. The cross-linking step of the precursor is necessary to control the weight loss during pyrolysis. This step is mostly supported with catalyst radiation at low temperatures to 500 °C, to improve the degrees of polymerization. Cross-linking also helps to keep the shapes of the material during pyrolysis and ceramization.

The cross-linked polymer is then pyrolyzed at elevated temperature (500–1400 °C). The pyrolysis process is controlled with several factors which include the heating rate, reaction temperature, holding time, and the reaction atmosphere. These factors govern the phase composition and microstructure of the resulting ceramic material. One of the main concerns of most ceramics fabricated using organosilicon materials relates to the formation of pores and cracks as well as the occurrence of a large shrinkage during the pyrolytic step. In previous studies, the addition of active fillers helps to solve these issues by having some reaction on the polymer precursors [98,99].

Shown in Fig. 6 are the possible routes of the polymer-to-ceramic transformation of organosilicon polymers (-$[SR_1R_2\text{-}X]_n$-with R^1 and R^2 as organic substituents) after thermal treatment at about 1000 °C. In the figure, X represents the different classes of organosilicon polymers including poly(organocarbosilanes) with X = –C(R [1]R [2])-, poly(-organosiloxanes) with X = -O-, poly(organosilazanes with X = –NR [3]-, and poly(organocarbosilylcarbodiimides) with X = –N=C=N-.

3.3.2. The microstructure of polymer-derived ceramics

Polymer-derived ceramics are amorphous materials consisting of nanodomains that persist up to very high temperatures. They remain amorphous up to temperatures ranging from 1000 to 1800 °C, depending on their chemical composition and structure. At high temperatures, partitioning processes occur and lead to amorphous multi-phase systems via redistribution reactions of the chemical bonds including phase separations which subsequently may nucleate and crystallize [43,100–104]. Single-phase silicon oxycarbide ceramics are amorphous materials showing silicon atoms tetrahedrally coordinated by carbon and oxygen atoms, i.e. SiC_4, SiC_3O, SiC_2O_2, and SiO_4 tetrahedral units [105–108]. Carbon with sp [3] hybridization is bonded to silicon (carbidic carbon) while sp [2] hybridized carbon (graphitic carbon) is present as a segregated phase. A microstructural model for SiOC was proposed which includes small silica-rich nanodomains (with a nanodomain size of 1–3 nm) incorporated in a graphene-like cellular network: the domain walls consist of graphene and mixed bond tetrahedra having silicon bonded to both carbon and oxygen as shown in Fig. 7 (a) [109]. The width of the interdomain boundaries connecting the silica-rich nanodomains and the graphene network were measured to be within the range of 0.8–1.5 nm [109].

Another model proposed by Widgeon et al. mentioned that the SiOC system has consisted of fractal O-rich SiOC domains which form a continuous network that is inefficiently packed forming voids. These voids are filled with segregated sp^2 carbon material with varying degrees of order [47]. In a recent review of Wen et al., the difference between the two models is discussed in more detail and a summary of suitable characterization methods that are useful to differentiate the formation of graphitic and carbidic carbons within the PDC microstructure is presented [110].

Structural studies of silicon carbonitride ceramics obtained via pyrolysis of polysilazanes showed that they consist of a single SiCN amorphous phase and segregated carbon [111,112]. In polysilazane derived SiCN materials, the amorphous SiCN phase consists of silicon atoms tetrahedrally coordinated by carbon and nitrogen [113–115]. Similar to the SiOC materials described above, carbon is bonded to silicon and has sp^3 hybridization; whereas segregated carbon exhibit an sp^2 hybridization, as shown by numerous MAS NMR studies [113,114]. The nanodomains in SiCN materials range in size from 1 to 3 nm which gradually increases with the annealing temperature [111,115–118].

The evolution of in situ formed free carbon showed a high dependency on increasing thermolysis temperature conditions [110,119,120]. Wen summarized this trend into four steps as illustrated in Fig. 8.

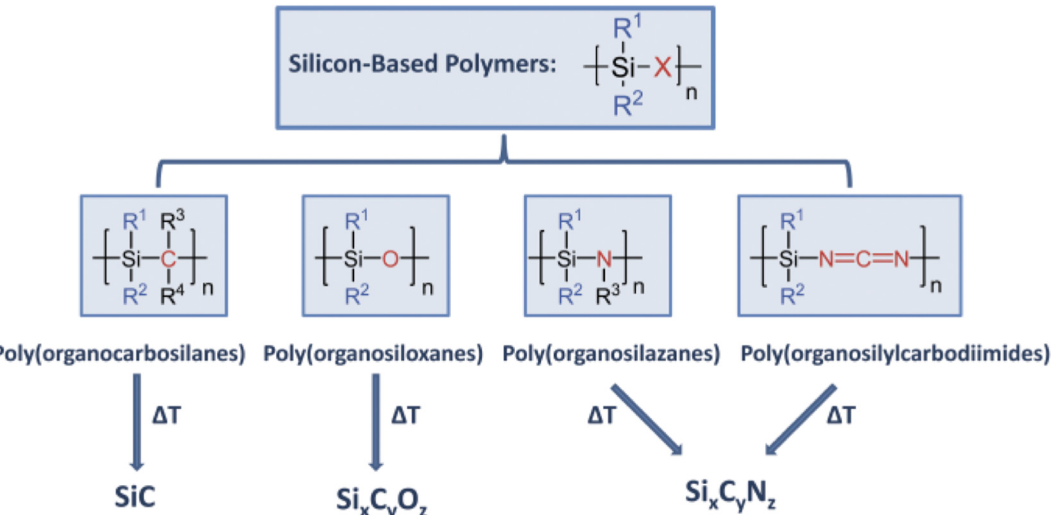

Fig. 6. Thermal decomposition of silicon-based polymers (oversimplified representation of the molecular structure of the precursors) [Reprinted with permission from John Wiley and Sons] [44].

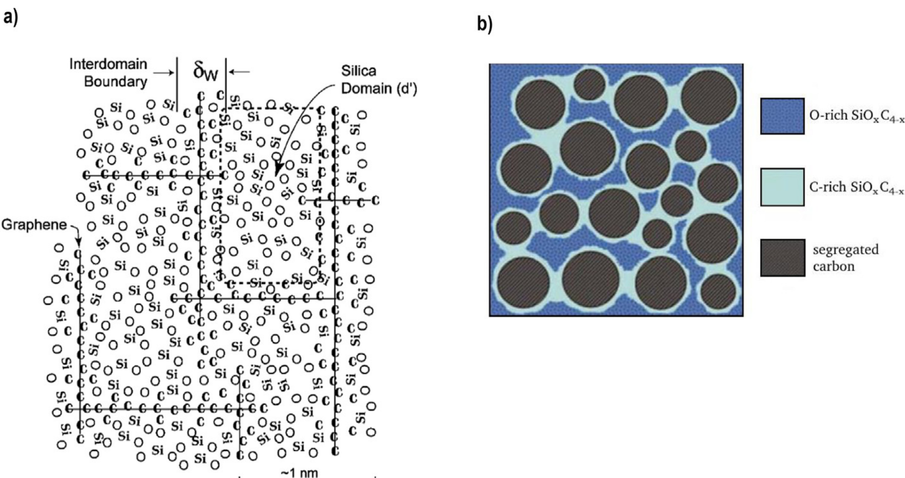

Fig. 7. Proposed models for the nano-domain structures in polymer derived SiOC. (a) The inter-domain boundary consists of graphene layers with mixed Si–O–C bonds forming the interfaces [Copyright from John Wiley and Sons] [109] (b) Precipitated carbon is encapsulated by O_2-rich SiOC domains forming a continuous network (Reprinted with permission from Royal Society of Chemistry) [47].

The process starts with *(1)* precipitation of hydrogenated amorphous excess carbon by the decomposition of aromatic hydrocarbons at a temperature above 600 °C. Organic to inorganic transition occurs at 400–900 °C wherein cleavage of the functional group is happening which results in to release of organic fragments [121]. As the temperature goes above 800 °C, the second step, *(2)* the nucleation of basic structural units (BSU) which are small stacks of 2–3 polyaromatic layers (graphenes) with 1 nm lateral extension occurs [122,123]. Investigation with NMR has shown that BSUs can be considered as independent entities and that the peripheral carbon atoms of graphenes are saturated with hydrogen atoms rather than linked with the neighboring medium [123]. At higher temperatures, 1000–1250 °C, the aromatic CH groups are unstable and the C–H bonds are broken which releases the hydrogen atoms as gaseous H_2. This phenomenon leads to the *(3)* turbostratic free carbon starting to grow to form linkages at the edges of the BSUs into larger distorted graphenes, and at a temperature above 1400 °C, *(4)* graphitization of free carbon nanodomain occurs followed by nucleation of SiC nanometric crystal phases [124]. The SiC phases are associated with the BSUs serving as nuclei which promote stacking of alternate Si and C atom layers.

Generally, excess carbon is present in many PDCs, i.e. for compositions with carbon contents beyond the stoichiometric amount necessary to saturate all Si valences. Although the exact nature of the segregated carbon has not been well understood, the exceptional properties of amorphous PDCs, such as high chemical durability in aggressive media and their resistance to crystallization, are often attributed to the distribution of the excess carbon within the PDC microstructure. Moreover, the recently shown piezoresistive behavior of those materials is considered also to rely on the presence of the segregated carbon phase within their microstructure. These carbon materials possess a variety of electrical properties depending on the structure and hybridization state which makes a material highly insulative in the case of a diamond, or highly conductive in the case of graphite. The correlation between the microstructure and the electrical conductivity in carbon materials can be assessed by Raman spectroscopy. Other than the crystalline structures of carbon materials, there are also types of disorders that affect the electrical conductivity namely turbostratic carbon, glassy carbon, or diamond-like carbon (DLC), and they are hydrogenated analogous. Turbostratic carbon is defined as a nano-scale imperfect graphite crystallite arranged parallel to each other but with random orientation. It is a structure identified as an intermediate between the ideal graphite with hexagonal ABA stacking structure and the amorphous material [125].

Fig. 9, shows the D-band at 1350 cm^{-1} which is attributed to the in-plane breathing vibrations of the aromatic ring or the A_{1g} symmetry caused by the double resonance Raman process [127,128] while the D′-band at 1620 cm^{-1} is also due to the double resonance process but is often found for nano-crystalline graphite [126]. The G-band at 1590 cm^{-1} is identified for the vibration of the in-plane stretching of the sp^2 carbon following the E_{2g} symmetry. Additionally, second-order Raman spectra, 2D, and D + G bands can also be observed at 2700 cm^{-1} and 2945 cm^{-1} respectively.

In the Raman spectra, the intensity ratio of the D- and G-bands (i.e., I_D/I_G) is used to measure the structural disorder of free carbon. The trend shows a higher free carbon phase disorder for a higher I_D/I_G ratio [129–131]. The disordered free carbon phases in PDCs can be attributed to *(1)* the presence of edges in the graphene layers, *(2)* the deviation from planarity of graphene layers, and *(3)* the presence of carbon atoms in sp^3 hybridization state [110].

Charge carrier transport in polymer-derived ceramics.

The electrical properties of polymer-derived-ceramics strongly depend on the starting composition and molecular architecture of the polymeric precursor, the processing, and the resulting composition and microstructure in the PDCs. Due to their multi-phase microstructure, PDCs can exhibit electrical conductivities located in a broad range between semiconductors (e. g. SiC) and insulators (e.g. SiO_2, Si_3N_4). A schematic depiction of the carbon allotropes was illustrated in Fig. 10. The properties of the carbon allotropes can be divided into three categories; (i) sp^2 to sp^3 site ratio, (ii) the local arrangement, and (iii) the hydrogen atoms concentration [132]. Each of the illustrated carbon allotropes plays a role in the electrical conduction of PDCs.

In 2007, Li et al. did a simulation of the X-ray diffraction pattern of graphitic carbon and turbostratic carbon to understand the influence of changes on microstructure by using the Debye equation [133]. Results supported the sensitivity of the numeric density of interatomic distance to the size and microstructure of carbon materials. It also revealed that diffraction angles and full width at half maximum (FWHM) were not sufficient to differentiate the crystal lattice parameters and sizes of the turbostratic carbon. A summarized table of the different carbon allotropes has been presented in Table 4.

The emerging carbon phase strongly influences the electrical behavior of the PDCs. Consequently, carbon-rich polymeric precursors lead to large amounts of segregated carbon even at relatively low temperatures in the resulting ceramic material and thus high electrical conductivity values might be achieved. A recently reported SiOC-based ceramic with a high carbon content (ca 30 vol%) showed a resistivity value of 0.35 Ω/m which further decreases to 0.14 Ω/m upon annealing [134]. Compared to resistivity values usually reported for SiOC systems

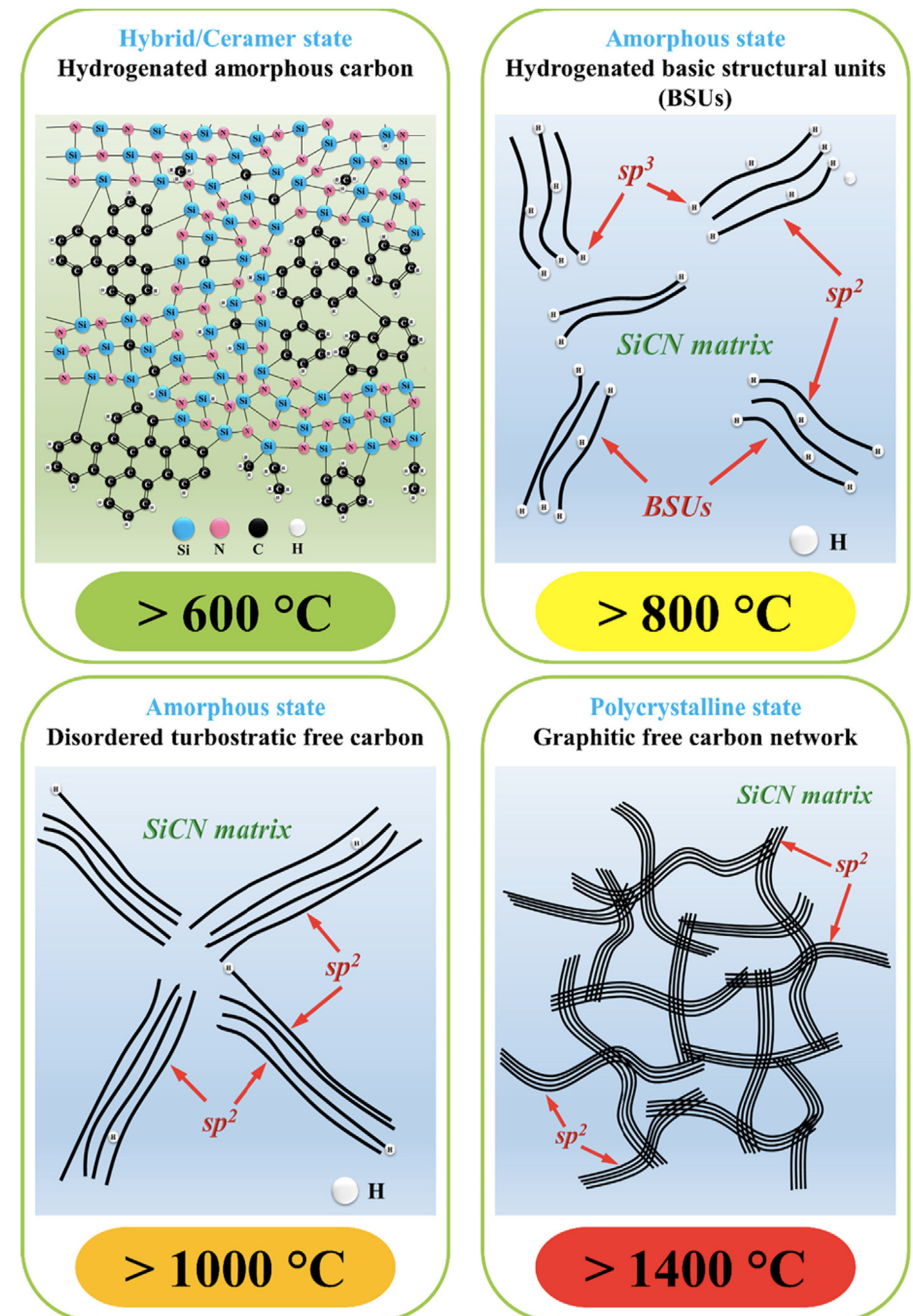

Fig. 8. Model for the structural evolution of free carbon during pyrolysis [Reprinted with permission from Elsevier] [110].

(107–1010 Ω/m) [121], these values are significantly lower. The difference in resistivity was attributed to the high amount of carbon which forms a percolative network throughout the SiOC ceramic. Besides the amount of segregated carbon, its graphitization degree is considered to significantly affect the electrical conductivity in PDC. Among the phases of PDCs mentioned in Section 3.3.2, most of them are generally insulators (SiO_2 and Si_3N_4) or semiconductors (SiC, SiO_xC_y, SiC_xN_y, and the amorphous carbons) with room-temperature electrical conductivities ranging from 10^{-14} to 10^{-12} S/cm and 10^{-4} to 10^2 S/cm respectively. On the other hand, the free carbon phase in the form of turbostratic carbon has a higher electrical conductivity value from 1 – 10^5 S/cm. The concentration of the free carbon phase in PDC greatly influences the electrical conduction mechanism of the system, as recently shown in a study revealing three regimes for the electrical charge carrier conduction in SiOC ceramics: first regime corresponds to low contents of free carbon (i.e., <1 vol%) and corresponds to transport within the amorphous SiO(C) matrix and has been characterized by an activation energy of ca. 1 eV; second regime, with an activation energy of ca. 0.3 eV, corresponds to carbon contents of 2–6 vol%, being close to the percolation threshold and indicating for instance hopping transport between the sp^2 hybridized carbon precipitations; whereas the third regime, with an activation energy of 0.03 eV, is assigned to carbon content beyond the percolation threshold and corresponds to charge carrier transport through the carbon phase [135].

In 2000, Cordelair et al. used the General Effective Media (GEM) Theory [136] to explain the electrical conduction mechanism of SiOC ceramic derived from polysiloxane [121]. In this case, the free carbon phase concentration is above the percolation threshold which results to

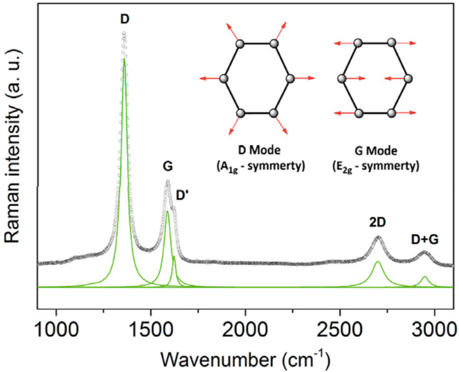

Fig. 9. Raman characterization of nanodomains in polymer-derived SiCN ceramics [Open access from MDPI] [126].

direct transportation of charge carriers, illustrated in Fig. 11 a. In this model, the percolation threshold was found to have a high dependency on the morphology of the particles namely the size and shape (aspect ratio). The formation of a ribbon-like shape of free carbon which has a high aspect ratio was found to be beneficial to lower the percolation threshold of a PDC system.

In the second model, Fig. 11b, the concentration of the free carbon phase is lower than the percolation threshold but is high enough to have tunneling conduction between the neighboring free carbon clusters [138, 139]. In this state, the clusters or the ribbons are not interconnected but keeps a small distance between their neighboring cluster. This conduction mechanism is called the tunneling-percolation regime. In Fig. 11c, the concentration of the free carbon phase is even lower than the tunneling-percolation regime. In this conduction mechanism called the semiconducting regime, the semiconducting behavior of the PDC plays a

Table 4
Comparison of RT conductivity, the bandgap, the lateral crystal size, and the interplane distance of the different carbon allotropes [132].

	σRT $(\Omega.cm)^{-1}$	E_g (eV)	L_a (Å)	I_C (Å)
Crystalline				
HOPG	3.5×10^5	0	$> 10^3$	3.35
Graphite	2.5×10^4	0	$> 10^3$	3.35
Diamond	10^{-16} - 10^{18}	5.5	–	–
Semi-crystalline				
Turbostratic Carbon	2.5×10^4	0	<100	3.44
Glassy Carbon	10^2–10^3	$\approx 10^{-2}$	15–50	3.75
Non-Crystalline				
Amorphous Carbon	10^{-1} - 10^{-3}	0.4–0.7	10–20	>3.75
Hydro. Amorphous Carbon	10^{-3}	1.5–2.8	≈5	–
Tetragonal Carbon	10^{-7} - 10^{-15}	3.0–3.5	–	–

major role. The semiconducting regime can be explained by the Variable-range Hopping (VRH) mechanism proposed by Mott in 1968 [140]. PDCs pyrolyzed at a temperature below 1200 °C, the electrical conductivity (σ_{dc}) obeys the Mott's law: $\sigma_{dc} = \sigma_0 \exp\left[-\left(\frac{T_0}{T}\right)^{\frac{1}{4}}\right]$, and $kT \ll E_{gap}$ (k is the Boltzmann constant, T is the Temperature, E_{gap} is the energy gap between the Fermi level and conduction band) [121,141, 142]. PDCs annealed at a temperature above 1200 °C are more crystalline and behaves under the condition of $kT \gg E_{gap}$, and shows an Arrhenius behavior$\sigma_{dc} = \sigma_0 \exp\left[-\frac{\Delta E}{kT}\right]$, ΔE is the activation energy [142,143]. Trassl et al. revealed the inverse proportionality of the pyrolysis temperature and the energy gap.

Haluschka et al. distinguished three temperature regimes for the conduction mechanism of poly(hydroxymethyl)-silazane-derived SiCN ceramic ranging from amorphous SiCN to completely phase-separated crystalline SiC and Si_3N_4, spanning a range of over 15 orders of

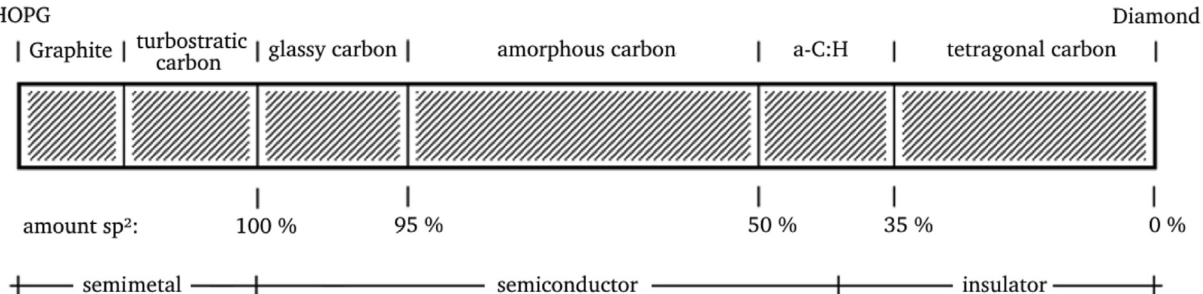

Fig. 10. Schematic depiction of the carbon allotropes hierarchy and the corresponding conductive class [Open access from TUprints of TU Darmstadt] [132].

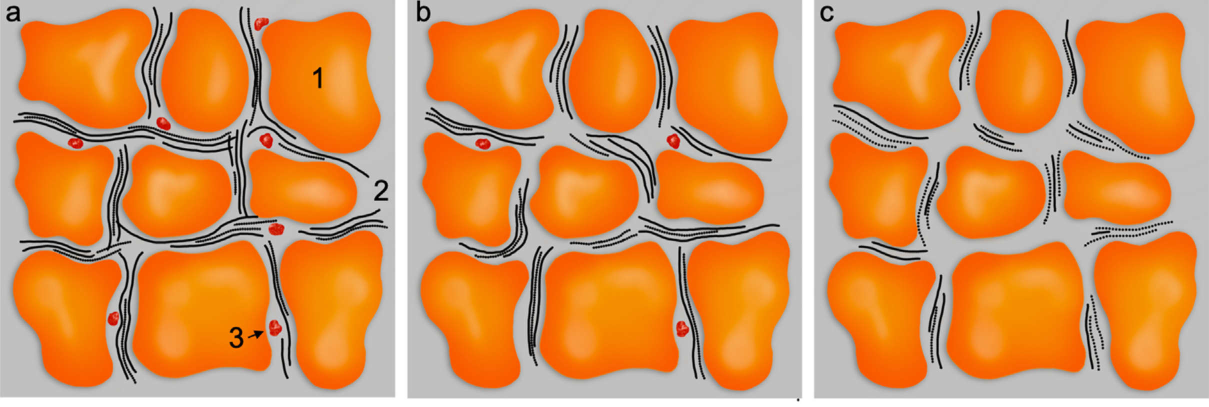

Fig. 11. Models for the microstructure of PDCs in different conducting regimes. (1), (2) and (3) are Si-based nanodomains, free carbon ribbons, and SiC nanoparticles, respectively [Reprinted with permission from Royal Society of Chemistry] [110,137].

magnitude for its electrical conductivity [143].

At the first regime (temperature range 1000–1400 °C), the conductivity of the material increases by three orders of magnitude with increasing the pyrolysis temperature. The increase of sp^2/sp^3 – the ratio of carbons accompanied by the loss of hydrogen atoms was found to be the main contributor to this phenomenon. On the second regime (1400–1600 °C), a larger increase in the conductivity was seen attributed to the formation of nano-crystalline SiC and a decrease of N-content on the amorphous matrix. Further annealing on the third regime (T > 1600 °C) leads to full crystallization of the sample with 40 wt% Si_3N_4 and 60 wt% SiC as the conducting phase [143,144]. Despite differences in the identification of the main conductive phases in SiOC- and SiCN(O)-based systems, all experimental studies showed an increase of the electrical conductivity with increasing the pyrolysis temperature [84,143,145,146].

Modifications on polymer precursors had been done to enhance the electrical conductivity of the ceramic with a higher ceramization yield [145,147,148]. In 2014, Nguyen et al. synthesized a SiOCN ceramic using preceramic polymers crosslinked with two N–containing compounds; silazane or ternary amines [145]. The electrical conductivity of the material was evaluated using the powder-solution-composite (PSC) technique which was first introduced by Ingram et al. in 2003 [149]. The conductivity of the ceramic powder was obtained by plotting the conductivity of the composite against the electrolyte which resulted in three orders of magnitude higher, 10^{-5} to 10^{-2} S/cm with increasing pyrolysis temperature from 1000 to 1400 °C. The N-doped C phase (N-Csp^2) near the percolation threshold is seen responsible for the increase in conductivity of the ceramic powder which was confirmed through XPS analysis [150]. Another attempt of doping the precursor was done by Sorarù et al. in 2017 using SiOC doped with boron [147]. A shown in Fig. 12, the conductivity of the ceramic material increased by twice as much in magnitude by incorporating boron into the system, and that the conductivity of the ceramic is directly proportional to the amount of the boron dopant.

A post-treatment using the microwave for a SiCN PDC was conducted by Shao et al. and had shown a significant increase in conductivity of the sample by 40 times [151]. Raman analysis revealed that the G-peak and D-peak of the microwave-treated samples have a narrower full width half maximum (FWHM) from 146.7 cm^{-1} to 90.0 cm^{-1} and 203.2 cm^{-1} to 123.1 cm^{-1} respectively. The FWHM reduction implied a more ordered free carbon phase after microwave treatment. Similar to the initial observations, XPS analysis showed sp^3 to the sp^2 transition of the carbon phase.

The work of Seo et al. in 2010 also supported that the magnitude of the conductivity of PDC depends on the annealing temperature. As shown in Fig. 13, the measured resistance for a film annealed at 1200 °C is two magnitudes lower than that of the sample annealed at 1400 °C. Moreover, they mentioned that PDCs have a stable electrical resistance response at high-temperature conditions [152]. It was indicated that PDCs without the oxide layer on the surface have less variability over the range of selected temperature as shown in Fig. 14.

Similarly, in a SiCNO PDC material synthesized by Ryu et al., the PDC demonstrated a stable conductivity at 1300 °C. The result showed the semiconductor behavior of PDC which is in accordance with the VRH model [153]. The results obtained also revealed not only the effect of the free carbon phase on the electrical conductivity of the material but also the effect of the N/O ratio which is most preferred when it is closer to unity.

3.3.3. State of the art for piezoresistivity of polymer-derived ceramic

In recent years, PDC is being explored for its piezoresistive behavior. In 2008, Zhang et al. achieved a GF of 1000–4000 for silicon carbonitride ceramic derived from a polymer precursor synthesized at 1400 °C [84]. A year later, they also stated that the applied stress is inversely proportional to the GF of the ceramic material which was supported by a theoretical model developed based on the tunneling-percolation mechanism [138].

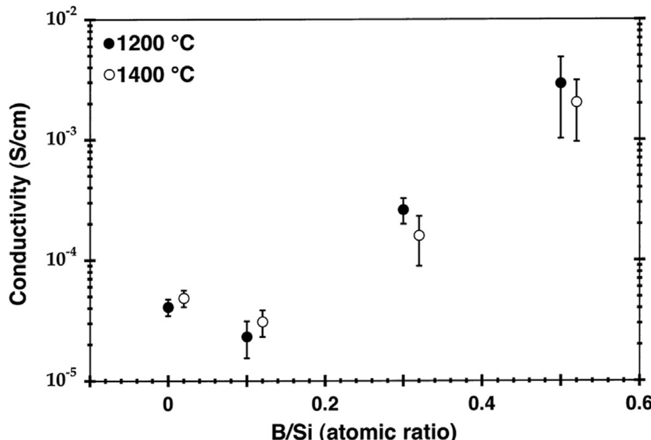

Fig. 12. Electrical conductivity measured on the SiOC and Si(B)OC ceramics pyrolyzed at 1200 and 1400 °C as a function of the nominal B/si atomic ratio [Reprinted with permission from John Wiley and Sons] [147].

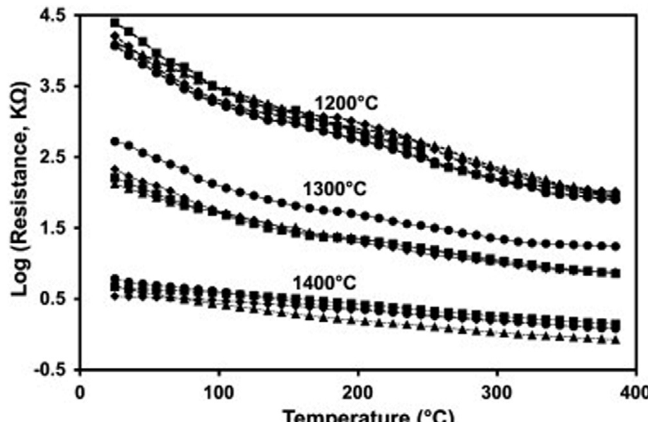

Fig. 13. Temperature dependence of the electrical resistance of PDC films as a function of annealing temperature [Reprinted with permission from Elsevier] [152].

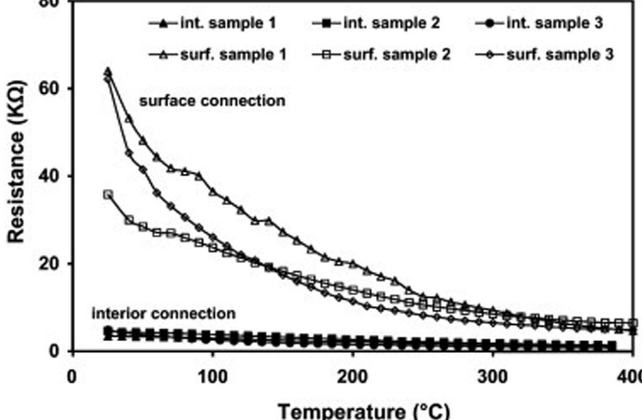

Fig. 14. Temperature dependence of the electric resistance of RTDs annealed at 1400 °C. The sensors are either directly connected to the surface or connected to the interior by grinding off the surface layer [Reprinted with permission from Elsevier] [15].2.

The model developed was fitted for both PDC and carbon-reinforced polymer composites which both showed reverse and logarithmic

dependence of GF to applied stress. The percolation theory was supported by Riedel et al. when they found GF of ~145 for a SiOC ceramic synthesized from a commercial polysiloxane at 1400 °C [154]. In the same study, it was observed that samples pyrolyzed at lower temperatures (1100 °C–1300 °C) do not show piezoresistive behavior.

In 2010, Terauds et al. reported giant piezoresistivity on SiOC PDC investigated at high temperatures. Gauge factor values of 322 at 1400 °C and 287 at 1500 °C were recorded for samples [155]. Their study has shown strong dependence of GF on stress and temperature applied to the samples as shown in Fig. 15. The result of their study is more based on the VRH model, indicating that the elastic strain applied to the samples alters the hopping distance or energy required. The study further opened the feasibility of the piezoresistive effect of PDC at high-temperature applications.

Wang et al. confirmed that the piezoresistive behavior of polysilazane-derived ceramic fits the tunneling-percolation mechanism [156]. This was conducted by pyrolyzing polysilazane at different temperatures between 900 and 1400 °C. Using elemental analysis, they were able to show that the volume fraction of the free carbon is essentially similar for all the samples regardless of the pyrolysis temperature. Using Raman analysis, they calculated the free carbon clusters by comparing the intensities of the D- and G-bands which are shown in Fig. 16. The results revealed the dependence of piezoresistive behavior on the pyrolysis temperature by decreasing the percolation threshold as the free carbon clusters also decrease.

Toma et al. studied the correlation of the intrinsic microstructure of PDC to explain the piezoresistive behavior of the material [157]. With the use of a transmission electron microscope (TEM), the analyzed a SiOC ceramic pyrolyzed at 1100 °C with GF of ~104 and revealed the presence of a network of nanopores as shown in Fig. 17A. These nanopores are partially filled with the amorphous residue of the bulk material. Upon annealing the samples at 1400 °C, the amorphous residue turned into turbostratic carbon and SiC only within the pores while keeping the bulk material in an amorphous state as shown in Fig. 17C and D.

In 2015, Roth et al. developed a high-temperature piezoresistive C/SiOC sensor with 13.5 vol% segregated carbon [158]. The material was synthesized using commercial poly(methyl silsesquioxane) crosslinked at 250 °C for 2 h, pyrolyzed at 900 °C for 2 h under flowing argon, ball-milled, and sieved to a particle size of less than 100 μm, the hot-pressed at 1500 °C to obtain a dense C/SiOC monolith. The GF for the studied monoliths were measured at temperatures up to 1300 °C and exhibited relatively large and, more important, highly reproducible values. For instance, the GF value at 1200 °C was ca. 80. In Fig. 17,

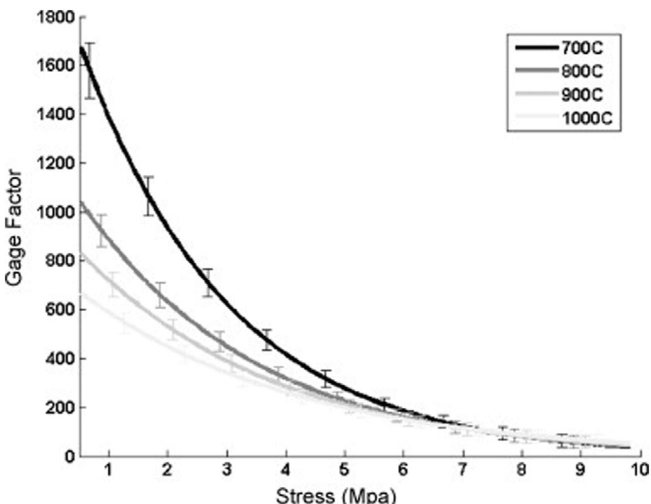

Fig. 15. (A) The Stress-dependence of the gauge factor measured up to 1000 °C [Copyright from Elsevier]. (B) Resistance load cycles *up to 1000 °C* [Copyright from Elsevier] [155].

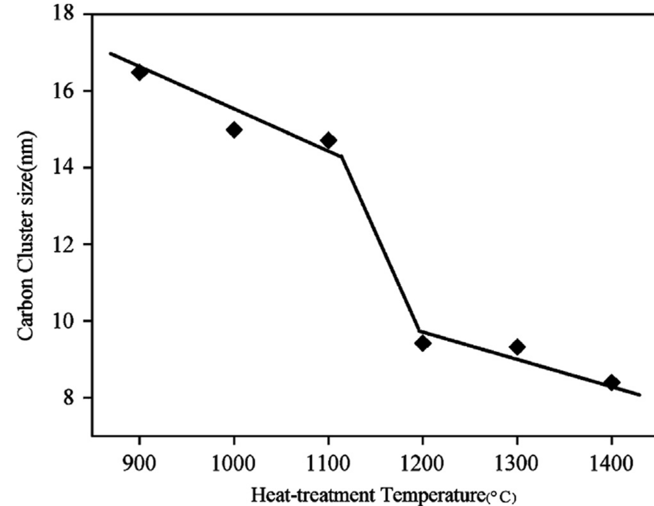

Fig. 16. The size of the carbon cluster as a function of pyrolysis temperature [Reprinted with permission from John Wiley and Sons] [156].

samples containing 13.5 wt% carbon were prepared at 1000–1500 °C showed a similar trend on SiOC material was observed for GF and line-widths of D- and G-bands which increases with increasing I_D/I_G ratio. In comparison, HOPG and graphene having highly-ordered sp [2] material with fewer defects displayed narrow linewidth and lower GF. It is believed that the non-crystalline carbon content in SiOC which is less ordered is responsible for the enhancement of the piezoresistive GF. Additionally, using the UV Raman analysis, graphitization of the free carbon phase was observed with increasing pyrolysis temperature at the range of 1100 °C–1600 °C [159] (see Fig. 18).

Ma and Wang fabricated a dense SiOC bulk PDC through the precursor infiltration and pyrolysis (PIP) process and was able to increase the conductivity of the bulk material by four orders of magnitude from 6.26×10^{-10} S/cm to 6.89×10^{-6} S/cm after four cycles of PIP [148]. On the other hand, the piezoresistivity of the materials was retained. The open porosity of the samples was varied from 32.75% to 4.14% after three PIP cycles. The sample that underwent four cycles of PIP resulted in fully densified material with some infiltrated pores.

Quaternary ceramics are lately showing giant piezoresistive effects. An amorphous SiAlCO ceramic was studied at 25–300 °C displayed a gauge factor of 7000–16,000 and also showed a positive temperature-dependent piezoresistive stress coefficient within the temperature range [160]. It is further discussed that the giant piezoresistivity is caused by the highly disordered graphene-like nanoclusters which are dispersed in an amorphous SiC_xO_{4-x} tetrahedral. A recent development on a remarkable piezoresistive gauge factor of 5500 was reported by Shao et al. for a SiBCN ceramic pressure sensor [161]. The pressure sensor was designed using SiBCN as the sensing material in a stainless-steel frame. The sensor exhibited high accuracy, repeatability, and stability in the pressure range of 0–10 MPa.

4. Conclusion

In the present review, the state of the art related to the development of carbon-containing ceramic nanocomposites as high-potential materials for piezoresistive sensing applications has been described. As the design criteria of piezoresistive sensors are often riveted by the material performance at high temperatures and in harsh environments, while at the same time providing the high piezoresistive response, the materials combination of choice consists of carbon-based percolative networks and robust ceramic matrix materials. The first component is responsible for the piezoresistive response, the latter assures the performance of the composite materials while operating in hostile conditions.

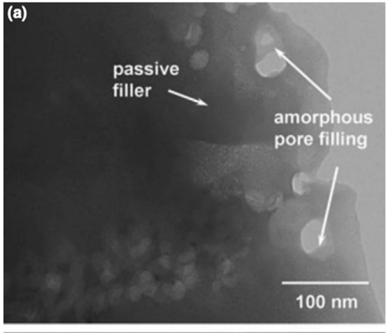

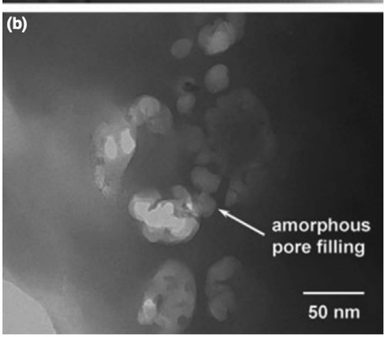

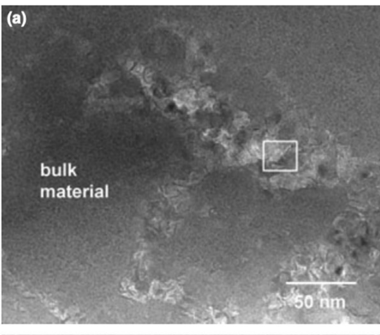

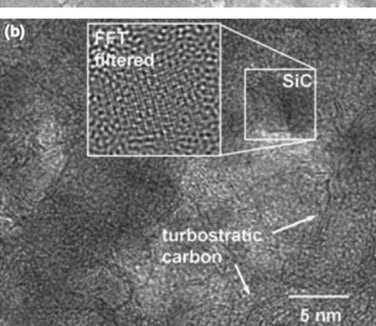

Fig. 17. TEM bright-field micrographs of sample MK1100 at lower magnification. Due to the special processing route followed, the material shows a residual porosity in a homogeneous dense and amorphous matrix (C) TEM bright-field micrograph of sample MK 1400 heat-treated at 1400 °C. The residual binder appears crystalline with turbostratic carbon and silicon carbide, as shown in the inset FFT filtered image in (D), an enlarged detail of (C) indicated by the boxed area [Reprinted with permission from John Wiley and Sons] [157].

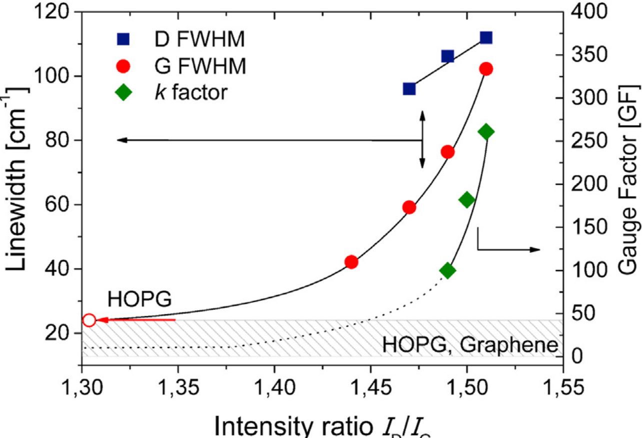

Fig. 18. Correlation of Raman and piezoresistivity data for C/SiOC (13.5 vol% C). The dashed area represents literature values for k and Raman linewidth of highly ordered carbon (HOPG, graphene)[Copyright from Copernicus Publications with Creative Common Attribute License] [158].

Two preparative methods for accessing carbon-containing ceramic nanocomposite are introduced. The first fabrication method involves the mechanical mixing of carbon materials with dispersing agents within a ceramic matrix; while the second method follows an in-situ generation of the carbon phase within the ceramic matrix, which is typically achieved by using preceramic precursors (the polymer-derived ceramics route).

Whereas the first class of the carbon-containing ceramic nanocomposites suffers from some disadvantages related to limitations of the fabrication process, the second group of nanocomposites possessing in-situ segregated carbon has been discussed as highly promising for achieving high sensor sensitivity (i.e., high gauge factor values) as well as for withstanding harsh operating conditions. Additionally, their preparative access from preceramic polymers allows for controlling and tuning the content, dispersion, and crystallinity of the segregated carbon phase, thus consequently offering the possibility to optimize the piezoresistive behavior in a knowledge-based, controlled manner. Moreover, the polymer-derived ceramic route has been highly flexible, thus providing piezoresistive nanocomposites as monolithic parts or as thin films. It is considered that the novel carbon-containing ceramic nanocomposites prepared from preceramic polymers may be used to explore novel designs of strain gauges that can withstand harsh environmental conditions.

Declaration of competing interest

The authors declare that they have no known competing financial interests or personal relationships that could have appeared to influence the work reported in this paper.

Acknowledgments

The authors gratefully acknowledge funding from the German Science Foundation (DFG, Germany) – grants no. 232234385 (High-temperature piezoresistivity in carbon-containing silicon oxycarbide nanocomposites) and 411658150 (Microstructured C/SiCX (X = O, N)-based high-temperature strain gauge). Additionally, EI acknowledges funding from DFG within the Heisenberg program (IO 64/14–1).

References

[1] XIX, On the electro-dynamic qualities of metals:—effects of magnetization on the electric conductivity of nickel and of iron, Proc. Roy. Soc. Lond. 8 (1857) 546–550, https://doi.org/10.1098/rspl.1856.0144.
[2] H. Tomlinson, The Influence of Stress and Strain on the Action of Physical Forces, vol. 174, 1883, https://doi.org/10.1098/rstl.1883.0001.
[3] H. Rolnick, Tension coefficient of resistance of metals, Phys. Rev. 36 (3) (1930) 506–512, https://doi.org/10.1103/PhysRev.36.506.
[4] J.W. Cookson, Theory of the piezo-resistive effect, Phys. Rev. 47 (2) (1935) 194–195, https://doi.org/10.1103/PhysRev.47.194.2.
[5] J. Bardeen, W. Shockley, Deformation potentials and mobilities in non-polar crystals, Phys. Rev. 80 (1) (1950) 72–80, https://doi.org/10.1103/PhysRev.80.72.
[6] C.S. Smith, Piezoresistance effect in germanium and silicon, Phys. Rev. 94 (1) (1954) 42–49, https://doi.org/10.1103/PhysRev.94.42.
[7] F.J. Morin, T.H. Geballe, C. Herring, Temperature dependence of the piezoresistance of high-purity silicon and germanium, Phys. Rev. 105 (2) (1957) 525–539, https://doi.org/10.1103/PhysRev.105.525.
[8] W.P. Mason, R.N. Thurston, Use of piezoresistive materials in the measurement of displacement, force, and torque, J. Acoust. Soc. Am. 29 (10) (1957) 1096–1101, https://doi.org/10.1121/1.1908710.
[9] A.A. Barlian, W.-T. Park, J.R. Mallon, A.J. Rastegar, B.L. Pruitt, Review: semiconductor piezoresistance for microsystems, Proc. IEEE Inst. Electr. Electron. Eng. 97 (3) (2009) 513–552, https://doi.org/10.1109/JPROC.2009.2013612.

[10] O.N. Tufte, E.L. Stelzer, Piezoresistive properties of silicon diffused layers, J. Appl. Phys. 34 (2) (1963) 313–318, https://doi.org/10.1063/1.1702605.
[11] W.G. Pfann, R.N. Thurston, Semiconducting stress transducers utilizing the transverse and shear piezoresistance effects, J. Appl. Phys. 32 (10) (1961) 2008–2019, https://doi.org/10.1063/1.1728280.
[12] Y. Kanda, A graphical representation of the piezoresistance coefficients in silicon, IEEE Trans. Electron. Dev. 29 (1) (1982) 64–70, https://doi.org/10.1109/T-ED.1982.20659.
[13] C. Herring, E. Vogt, Transport and deformation-potential theory for Many-Valley semiconductors with anisotropic scattering, Phys. Rev. 101 (3) (1956) 944–961, https://doi.org/10.1103/PhysRev.101.944.
[14] J.F. Nye, P.P.L.J.F. Nye, Physical Properties of Crystals: Their Representation by Tensors and Matrices, Clarendon Press, 1985.
[15] P.J. French, A.G.R. Evans, Piezoresistance in polysilicon and its applications to strain gauges, Solid State Electron. 32 (1) (1989) 1–10, https://doi.org/10.1016/0038-1101(89)90041-5.
[16] J. Richter, O. Hansen, A. Nylandsted Larsen, J. Lundsgaard Hansen, G.F. Eriksen, E.V. Thomsen, Piezoresistance of silicon and strained Si0.9Ge0.1, Sens. Actuators Phys. 123–124 (2005) 388–396, https://doi.org/10.1016/j.sna.2005.02.038.
[17] S. Lenci, P. Gonzalez, K. De Meyer, R. Van Hoof, D. Frederickx, A. Witvrouw, Determination of the piezoresistivity of microcrystalline silicon-germanium and application to a pressure sensor, in: 2008 IEEE 21st International Conference on Micro Electro Mechanical Systems, IEEE, Tucson, AZ, USA, 2008, pp. 427–430, https://doi.org/10.1109/MEMSYS.2008.4443684.
[18] S.R. Broadbent, J.M. Hammersley, Percolation processes: I. Crystals and mazes, Math. Proc. Camb. Phil. Soc. 53 (3) (1957) 629–641, https://doi.org/10.1017/S0305004100032680.
[19] S. Kirkpatrick, Percolation and conduction, Rev. Mod. Phys. 45 (4) (1973) 574–588, https://doi.org/10.1103/RevModPhys.45.574.
[20] G. Yin, N. Hu, Y. Karube, Y. Liu, Y. Li, H. Fukunaga, A carbon nanotube/polymer strain sensor with linear and anti-symmetric piezoresistivity, J. Compos. Mater. (2011), https://doi.org/10.1177/0021998310393296.
[21] S. Shang, Y. Yue, X. Wang, Piezoresistive strain sensing of carbon black/silicone composites above percolation threshold, Rev. Sci. Instrum. 87 (12) (2016), 123910, https://doi.org/10.1063/1.4973274.
[22] N. Miyakawa, W. Legner, T. Ziemann, D. Telitschkin, H.-J. Fecht, A. Friedberger, MEMS-based microthruster with integrated platinum thin film resistance temperature detector (RTD), heater meander and thermal insulation for operation up to 1,000°C, Microsyst. Technol. 18 (7–8) (2012) 1077–1087, https://doi.org/10.1007/s00542-012-1441-0.
[23] J. Wilde, P. Wagner, R. Zeiser, Assembly and interconnection technologies for sensors for very high temperature applications, in: Proceedings SENSOR 2013, AMA, 2013, pp. 229–235, https://doi.org/10.5162/sensor2013/B3.1.
[24] C. Canali, D. Malvasi, B. Morten, M. Prudenziati, A. Taroni, Strain sensitivity in thick-film resistors, IEEE Trans. Compon. Hybrids Manuf. Technol. 3 (3) (1980) 421–423, https://doi.org/10.1109/TCHMT.1980.1135638.
[25] T. Maeder, C. Jacq, P. Ryser, Assessment of Thick-Film Resistors for Manufacturing Piezoresistive Sensors, Addit. Conf. Device Packag. HiTEC HiTEN CICMT vol. 2015, CICMT, 2015, pp. 213–223, https://doi.org/10.4071/CICMT-WP12.
[26] S. Beeby, MEMS mechanical sensors, in: Artech House Microelectromechanical System Series, Artech House, Boston, 2004.
[27] P.G. Neudeck, R.S. Okojie, Liang-Yu Chen, High-temperature electronics - a role for wide bandgap semiconductors? Proc. IEEE 90 (6) (2002) 1065–1076, https://doi.org/10.1109/JPROC.2002.1021571.
[28] W.R. Fahrner, M. Werner, R. Job, Sensors and smart electronics in harsh environment applications, Microsyst. Technol. 7 (4) (2001) 138–144, https://doi.org/10.1007/s005420100089.
[29] H.-D. Ngo, O. Ehrmann, M. Schneider-Ramelow, K.-D. Lang, Piezoresistive pressure sensors for applications in harsh environments—a roadmap, Mod. Sens. Technol. (2019) 231–251, https://doi.org/10.1007/978-3-319-99540-3_12.
[30] A. Agarwal, S. Saddow. Advances in Silicon Carbide Processing and Applications (Semiconductor Materials and Devices Series), Artech House, Inc, 2004.
[31] J.S. Shor, D. Goldstein, A.D. Kurtz, Characterization of N-type beta -SiC as a piezoresistor, IEEE Trans. Electron. Dev. 40 (6) (1993) 1093–1099, https://doi.org/10.1109/16.214734.
[32] R. Ziermann, J. von Berg, W. Reichert, E. Obermeier, M. Eickhoff, G. Krotz, A high temperature pressure sensor with β-SiC piezoresistors on SOI substrates, Proceedings of International Solid State Sensors and Actuators Conference (Transducers '97) Vol. 2, IEEE, Chicago, IL, USA, 1997, pp. 1411–1414, https://doi.org/10.1109/SENSOR.1997.635502.
[33] J. Strass, M. Eickhoff, G. Kroetz, The influence of crystal quality on the piezoresistive effect of/spl beta/-SiC between RT and 450/spl deg/C measured by using microstructures, in: Proceedings of International Solid State Sensors and Actuators Conference (Transducers '97) vol. 2, 1997, pp. 1439–1442, https://doi.org/10.1109/SENSOR.1997.635735.
[34] T. Toriyama, S. Sugiyama, Analysis of piezoresistance in N-type 6H SiC for high-temperature mechanical sensors, in: TRANSDUCERS '03. 12th International Conference on Solid-State Sensors, Actuators and Microsystems. Digest of Technical Papers (Cat. No.03TH8664), vol. 1, IEEE, Boston, MA, USA, 2003, pp. 758–761, https://doi.org/10.1109/SENSOR.2003.1215584.
[35] T. Toriyama, Piezoresistance consideration on N-type 6H SiC for MEMS-based piezoresistance sensors, J. Micromech. Microeng. 14 (11) (2004) 1445–1448, https://doi.org/10.1088/0960-1317/14/11/002.
[36] H.-P. Phan, D.V. Dao, K. Nakamura, S. Dimitrijev, N.-T. Nguyen, The piezoresistive effect of SiC for MEMS sensors at high temperatures: a review, J. Microelectromechanical Syst. 24 (6) (2015) 1663–1677, https://doi.org/10.1109/JMEMS.2015.2470132.
[37] I. Taher, M. Aslam, M.A. Tamor, T.J. Potter, R.C. Elder, Piezoresistive microsensors using P-type CVD diamond films, Sens. Actuators Phys. 45 (1) (1994) 35–43, https://doi.org/10.1016/0924-4247(94)00817-5.
[38] M. Werner, O. Dorsch, E. Obermeier, High-temperature pressure sensor using p-type diamond piezoresistors, Diam. Relat. Mater. 4 (5–6) (1995) 873–876, https://doi.org/10.1016/0925-9635(94)05231-X.
[39] M. Aslam, I. Taher, A. Masood, M.A. Tamor, T.J. Potter, Piezoresistivity in vapor-deposited diamond films, Appl. Phys. Lett. 60 (23) (1992) 2923–2925, https://doi.org/10.1063/1.106821.
[40] M.P. D'Evelyn, D.E. Slutz, B.E. Williams, Elastic properties of CVD diamond via dynamic resonance measurements, MRS Proc 383 (1995) 115, https://doi.org/10.1557/PROC-383-115.
[41] S. Sahli, D.M. Aslam, Ultra-high sensitivity intra-grain poly-diamond piezoresistors, Sens. Actuators Phys. 71 (3) (1998) 193–197, https://doi.org/10.1016/S0924-4247(98)00181-2.
[42] P.H.C. Camargo, K.G. Satyanarayana, F. Wypych, Nanocomposites: synthesis, structure, properties and new application opportunities, Mater. Res. 12 (1) (2009) 1–39, https://doi.org/10.1590/S1516-14392009000100002.
[43] R. Riedel, G. Mera, R. Hauser, A. Klonczynski, Silicon-based polymer-derived ceramics: synthesis properties and applications-A review: dedicated to prof. Dr. Fritz aldinger on the occasion of his 65th birthday, J. Ceram. Soc. Jpn. 114 (1330) (2006) 425–444, https://doi.org/10.2109/jcersj.114.425.
[44] P. Colombo, G. Mera, R. Riedel, G.D. Sorarù, Polymer-derived ceramics: 40 Years of research and innovation in advanced ceramics, J. Am. Ceram. Soc. 93 (7) (2010) 1805–1837, https://doi.org/10.1111/j.1551-2916.2010.03876.x.
[45] S. Fu, M. Zhu, Y. Zhu, Organosilicon polymer-derived ceramics: an overview, J. Adv. Ceram. 8 (4) (2019) 457–478, https://doi.org/10.1007/s40145-019-0335-3.
[46] E. Ionescu, G. Mera, R. Riedel, Polymer-derived ceramics (PDCs): materials design towards applications at ultrahigh-temperatures and in extreme environments, in: Y. Sakka, C. Hu, J. LowPublisher (Eds.), MAX Phases and Ultra-High Temperature Ceramics for Extreme Environments, IGI Global, Hershey, PA, USA, 2013, pp. 225–268.
[47] G. Mera, A. Navrotsky, S. Sen, H.-J. Kleebe, R. Riedel, Polymer-derived SiCN and SiOC ceramics – structure and energetics at the nanoscale, J. Mater. Chem. 1 (12) (2013) 3826–3836, https://doi.org/10.1039/C2TA00727D.
[48] K. Waku, H. Hayashi, A. Kishimoto, Resistivity of alumina–graphite composite ceramics, J. Am. Ceram. Soc. 91 (12) (2008) 4168–4170, https://doi.org/10.1111/j.1551-2916.2008.02820.x.
[49] R.P. Kusy, Influence of particle size ratio on the continuity of aggregates, J. Appl. Phys. 48 (12) (1977) 5301–5305, https://doi.org/10.1063/1.323560.
[50] A. Kishimoto, Y. Takagawa, T. Teranishi, H. Hayashi, Effect of varying the ratio of matrix/dispersoid particle size on the piezoresistivity of alumina/carbon-black composite ceramics, Mater. Lett. 65 (14) (2011) 2197–2200, https://doi.org/10.1016/j.matlet.2011.04.042.
[51] Auerkari, P. Mechanical and Physical Properties of Engineering Alumina Ceramics. vol. 26.
[52] G. Song, Y.L. Mo, K. Otero, H. Gu, Health monitoring and rehabilitation of a concrete structure using intelligent materials, Smart Mater. Struct. 15 (2) (2006) 309–314, https://doi.org/10.1088/0964-1726/15/2/010.
[53] C.S. Wang, F. Wu, F.-K. Chang, Structural health monitoring from fiber-reinforced composites to steel-reinforced concrete, Smart Mater. Struct. 10 (3) (2001) 548–552, https://doi.org/10.1088/0964-1726/10/3/318.
[54] P.-W. Chen, D.D.L. Chung, Carbon fiber reinforced concrete for smart structures capable of non-destructive flaw detection, Smart Mater. Struct. 2 (1) (1993) 22–30, https://doi.org/10.1088/0964-1726/2/1/004.
[55] B. Han, K. Zhang, T. Burnham, E. Kwon, X. Yu, Integration and road tests of a self-sensing CNT concrete pavement system for traffic detection, Smart Mater. Struct. 22 (1) (2012), 015020, https://doi.org/10.1088/0964-1726/22/1/015020.
[56] M.S. Konsta-Gdoutos, C.A. Aza, Self sensing carbon nanotube (CNT) and nanofiber (CNF) cementitious composites for real time damage assessment in smart structures, Cement Concr. Compos. C (53) (2014) 162–169, https://doi.org/10.1016/j.cemconcomp.2014.07.003.
[57] F. Ubertini, A.L. Materazzi, A. D'Alessandro, S. Laflamme, Natural frequencies identification of a reinforced concrete beam using carbon nanotube cement-based sensors, Eng. Struct. 60 (2014) 265–275, https://doi.org/10.1016/j.engstruct.2013.12.036.
[58] M.-J. Lim, H.K. Lee, I.-W. Nam, H.-K. Kim, Carbon nanotube/cement composites for crack monitoring of concrete structures, Compos. Struct. 180 (2017) 741–750, https://doi.org/10.1016/j.compstruct.2017.08.042.
[59] B. Han, S. Ding, X. Yu, Intrinsic self-sensing concrete and structures: a review, Measurement 59 (2015) 110–128, https://doi.org/10.1016/j.measurement.2014.09.048.
[60] Mehta, P. K.; Monteiro, P. J. M. Concrete, Microstructure, Properties and Materials. 239.
[61] Loamrat, K.; Sappakittipakorn, M.; Sukontasukkul, P.; Banthia, N. Effect of Carbon Fiber and Graphite Powder on Resistivity of Cement-Based Sensor under Compression.
[62] B.G. Han, B.Z. Han, J.P. Ou, Experimental study on use of nickel powder-filled portland cement-based composite for fabrication of piezoresistive sensors with high sensitivity, Sens. Actuators Phys. 1 (149) (2009) 51–55, https://doi.org/10.1016/j.sna.2008.10.001.

[63] V. Shasna, B. Geethu, Sensing concrete using hybrid conductive fillers for structural health monitoring, Int. Res. J. Eng. Technol. IRJET 6 (5) (2019) 1928–1933.
[64] D.D.L. Chung, Piezoresistive cement-based materials for strain sensing, J. Intell. Mater. Syst. Struct. 13 (9) (2002) 599–609, https://doi.org/10.1106/104538902031861.
[65] X. Fan, D. Fang, M. Sun, Z. Li, Piezoresistivity of carbon fiber graphite cement-based composites with CCCW, J. Wuhan Univ. Technol.-Materials Sci. Ed. 26 (2) (2011) 339, https://doi.org/10.1007/s11595-011-0226-0.
[66] O. Galao, F.J. Baeza, E. Zornoza, P. Garcés, Strain and damage sensing properties on multifunctional cement composites with CNF admixture, Cement Concr. Compos. 46 (2014) 90–98, https://doi.org/10.1016/j.cemconcomp.2013.11.009.
[67] B.M. Tyson, R.K. Abu Al-Rub, A. Yazdanbakhsh, Z. Grasley, Carbon nanotubes and carbon nanofibers for enhancing the mechanical properties of nanocomposite cementitious materials, J. Mater. Civ. Eng. 23 (7) (2011) 1028–1035, https://doi.org/10.1061/(ASCE)MT.1943-5533.0000266.
[68] S. Wen, D.D.L. Chung, Model of piezoresistivity in carbon fiber cement, Cement Concr. Res. 36 (10) (2006) 1879–1885, https://doi.org/10.1016/j.cemconres.2006.03.029.
[69] D.D.L. Chung, Electrically conductive cement-based materials, Adv. Cement Res. 16 (4) (2004) 167–176, https://doi.org/10.1680/adcr.2004.16.4.167.
[70] B. Han, J. Ou, Embedded piezoresistive cement-based stress/strain sensor, Sens. Actuators Phys. 138 (2) (2007) 294–298, https://doi.org/10.1016/j.sna.2007.05.011.
[71] Jinping Ou, Baoguo Han, Piezoresistive cement-based strain sensors and self-sensing concrete components, J. Intell. Mater. Syst. Struct. 20 (3) (2009) 329–336, https://doi.org/10.1177/1045389X08094190.
[72] X. Fu, W. Lu, D.D.L. Chung, Improving the bond strength between carbon fiber and cement by fiber surface treatment and polymer addition to cement mix, Cement Concr. Res. 26 (7) (1996) 1007–1012, https://doi.org/10.1016/0008-8846(96)00084-1.
[73] G.Y. Li, P.M. Wang, X. Zhao, Mechanical behavior and microstructure of cement composites incorporating surface-treated multi-walled carbon nanotubes, Carbon 43 (6) (2005) 1239–1245, https://doi.org/10.1016/j.carbon.2004.12.017.
[74] G.Y. Li, P.M. Wang, X. Zhao, Pressure-sensitive properties and microstructure of carbon nanotube reinforced cement composites, Cement Concr. Compos. 29 (5) (2007) 377–382, https://doi.org/10.1016/j.cemconcomp.2006.12.011.
[75] Y. Wang, X. Zhao, Y. Zhao, Piezoresistivity of cement matrix composites incorporating multiwalled carbon nanotubes due to moisture variation, Adv. Civ. Eng. (2020). https://www.hindawi.com/journals/ace/2020/5476092. (Accessed 16 March 2020).
[76] F. Azhari, N. Banthia, Cement-based sensors with carbon fibers and carbon nanotubes for piezoresistive sensing, Cement Concr. Compos. 34 (7) (2012) 866–873, https://doi.org/10.1016/j.cemconcomp.2012.04.007.
[77] J.L. Luo, Z.D. Duan, T.J. Zhao, Q.Y. Li, Hybrid effect of carbon fiber on piezoresistivity of carbon nanotube cement-based composite, Adv. Mater. Res. 143–144 (2010) 639–643. https://doi.org/10.4028/www.scientific.net/AMR.143-144.639.
[78] S.-J. Lee, I. You, G. Zi, D.-Y. Yoo, Experimental investigation of the piezoresistive properties of cement composites with hybrid carbon fibers and nanotubes, Sensors 17 (11) (2017), https://doi.org/10.3390/s17112516.
[79] D.D.L. Chung, A critical review of piezoresistivity and its application in electrical-resistance-based strain sensing, J. Mater. Sci. 55 (32) (2020) 15367–15396, https://doi.org/10.1007/s10853-020-05099-z.
[80] Y.-F. Fu, Y.-Q. Li, Y.-F. Liu, P. Huang, N. Hu, S.-Y. Fu, High-performance structural flexible strain sensors based on graphene-coated glass fabric/silicone composite, ACS Appl. Mater. Interfaces 10 (41) (2018) 35503–35509, https://doi.org/10.1021/acsami.8b09424.
[81] S. Yu, X. Wang, H. Xiang, L. Zhu, M. Tebyetekerwa, M. Zhu, Superior piezoresistive strain sensing behaviors of carbon nanotubes in one-dimensional polymer fiber structure, Carbon 140 (2018) 1–9, https://doi.org/10.1016/j.carbon.2018.08.028.
[82] S. Cruz, L.A. Rocha, J.C. Viana, Piezo-resistive behaviour at high strain levels of PEDOT:PSS printed on a flexible polymeric substrate by a novel surface treatment, J. Mater. Sci. Mater. Electron. 28 (3) (2017) 2563–2573, https://doi.org/10.1007/s10854-016-5832-3.
[83] S. Zhao, J. Li, D. Cao, Y. Gao, W. Huang, G. Zhang, R. Sun, C.-P. Wong, Percolation threshold-inspired design of hierarchical multiscale hybrid architectures based on carbon nanotubes and silver nanoparticles for stretchable and printable electronics, J. Mater. Chem. C 4 (27) (2016) 6666–6674, https://doi.org/10.1039/C6TC01728B.
[84] L. Zhang, Y. Wang, Y. Wei, W. Xu, D. Fang, L. Zhai, K.-C. Lin, L. An, A silicon carbonitride ceramic with anomalously high piezoresistivity, J. Am. Ceram. Soc. 91 (4) (2008) 1346–1349, https://doi.org/10.1111/j.1551-2916.2008.02275.x.
[85] G. Fritz, B. Raabe, Bildung siliciumorganischer Verbindungen. V. Die Thermische Zersetzung von Si(CH3)4 und Si(C2H5)4, Z. Für Anorg. Allg. Chem. 286 (3–4) (1956) 149–167, https://doi.org/10.1002/zaac.19562860307.
[86] G. Mera, I. Menapace, S. Widgeon, S. Sen, R. Riedel, Photoluminescence of as-synthesized and heat-treated phenyl-containing polysilylcarbodiimides: role of crosslinking and free carbon formation in polymer-derived ceramics: photoluminescence of phenyl-containing polysilylcarbodiimides, Appl. Organomet. Chem. 27 (11) (2013) 630–638, https://doi.org/10.1002/aoc.2993.
[87] E. Bernardo, G. Parcianello, S. Pilati, P. Colombo, A.C.A. Delsing, H.T. Hintzen, Novel synthesis of Eu-doped SiAlON luminescent materials from a preceramic polymer and nano-sized fillers, J. Asian Ceram. Soc. 2 (2) (2014) 158–164, https://doi.org/10.1016/j.jascer.2014.03.002.
[88] R. Bhandavat, Z. Pei, G. Singh, Polymer-derived ceramics as anode material for rechargeable Li-ion batteries: a review, Nanomater. Energy 1 (6) (2012) 324–337, https://doi.org/10.1680/nme.12.00030.
[89] A. Wilson, J. Reimers, E. Fuller, J. Dahn, Lithium insertion in pyrolyzed siloxane polymers, Solid State Ionics 74 (3–4) (1994) 249–254, https://doi.org/10.1016/0167-2738(94)90217-8.
[90] D. Ahn, R. Raj, Cyclic stability and C-rate performance of amorphous silicon and carbon based anodes for electrochemical storage of lithium, J. Power Sources 196 (4) (2011) 2179–2186, https://doi.org/10.1016/j.jpowsour.2010.09.086.
[91] L. Bergero, V.M. Sglavo, G.D. Soraru, Processing and thermal shock resistance of a polymer-derived MoSi2/SiCO ceramic composite, J. Am. Ceram. Soc. 88 (11) (2005) 3222–3225, https://doi.org/10.1111/j.1551-2916.2005.00550.x.
[92] Y. Iwamoto, W. Völger, E. Kroke, R. Riedel, T. Saitou, K. Matsunaga, Crystallization behavior of amorphous silicon carbonitride ceramics derived from organometallic precursors, J. Am. Ceram. Soc. 84 (10) (2004) 2170–2178, https://doi.org/10.1111/j.1151-2916.2001.tb00983.x.
[93] Z. Qing, W. Zhou, W. Xia, H. Li, Crystallization kinetics, sintering, microstructure, and properties of low temperature Co-fired magnesium aluminum silicate glass-ceramic, J. Non-Cryst. Solids 486 (2018) 14–18, https://doi.org/10.1016/j.jnoncrysol.2018.02.006.
[94] R. Harshe, C. Balan, R. Riedel, Amorphous Si(Al)OC ceramic from polysiloxanes: bulk ceramic processing, crystallization behavior and applications, J. Eur. Ceram. Soc. 24 (12) (2004) 3471–3482, https://doi.org/10.1016/j.jeurceramsoc.2003.10.016.
[95] K. Su, E.E. Remsen, G.A. Zank, L.G. Sneddon, Synthesis, characterization, and ceramic conversion reactions of borazine-modified hydridopolysilazanes: new polymeric precursors to silicon nitride carbide boride (SiNCB) ceramic composites, Chem. Mater. 5 (4) (1993) 547–556, https://doi.org/10.1021/cm00028a024.
[96] D. Seyferth, H. Plenio, Borasilazane polymeric precursors for borosilicon nitride, J. Am. Ceram. Soc. 73 (7) (1990) 2131–2133, https://doi.org/10.1111/j.1151-2916.1990.tb05286.x.
[97] C. Balan, R. Riedel, Rheological investigations of a polymeric precursor for ceramic materials: experiments and theoretical modeling, J. Optoelectron. Adv. Mater. 8 (2006) 561–567.
[98] E. Bernardo, P. Colombo, E. Dainese, G. Lucchetta, P.F. Bariani, Novel 3D wollastonite-based scaffolds from preceramic polymers containing micro- and nano-sized reactive particles, Adv. Eng. Mater. 14 (4) (2012) 269–274, https://doi.org/10.1002/adem.201100241.
[99] E. Bernardo, G. Parcianello, P. Colombo, S. Matthews, Wollastonite foams from an extruded preceramic polymer mixed with CaCO3 microparticles assisted by supercritical carbon dioxide, Adv. Eng. Mater. 15 (1–2) (2013) 60–65, https://doi.org/10.1002/adem.201200202.
[100] P. Colombo, G. Mera, R. Riedel, G.D. Sorarù, Polymer-derived ceramics: 40 Years of research and innovation in advanced ceramics, J. Am. Ceram. Soc. 93 (7) (2010) 1805–1837, https://doi.org/10.1111/j.1551-2916.2010.03876.x.
[101] G. Mera, A. Tamayo, H. Nguyen, S. Sen, R. Riedel, Nanodomain structure of carbon-rich silicon carbonitride polymer-derived ceramics, J. Am. Ceram. Soc. 93 (4) (2010) 1169–1175, https://doi.org/10.1111/j.1551-2916.2009.03558.x.
[102] H.-J. Kleebe, C. Turquat, G.D. Sorarù, Phase separation in an SiCO glass studied by transmission electron microscopy and electron energy-loss spectroscopy, J. Am. Ceram. Soc. 84 (5) (2001) 1073–1080, https://doi.org/10.1111/j.1151-2916.2001.tb00792.x.
[103] C. Turquat, H.-J. Kleebe, G. Gregori, S. Walter, G.D. Sorarù, Transmission electron microscopy and electron energy-loss spectroscopy study of nonstoichiometric silicon-carbon-oxygen glasses, J. Am. Ceram. Soc. 84 (10) (2004) 2189–2196, https://doi.org/10.1111/j.1151-2916.2001.tb00986.x.
[104] A. Saha, R. Raj, Crystallization maps for SiCO amorphous ceramics, J. Am. Ceram. Soc. 90 (2) (2007) 578–583, https://doi.org/10.1111/j.1551-2916.2006.01423.x.
[105] L. Bois, J. Maquet, F. Babonneau, H. Mutin, D. Bahloul, Structural characterization of sol-gel derived oxycarbide glasses. 1. Study of the pyrolysis process, Chem. Mater. 6 (6) (1994) 796–802, https://doi.org/10.1021/cm00042a016.
[106] L. Bois, J. Maquet, F. Babonneau, D. Bahloul, Structural characterization of sol-gel derived oxycarbide glasses. 2. Study of the thermal stability of the silicon oxycarbide phase, Chem. Mater. 7 (5) (1995) 975–981, https://doi.org/10.1021/cm00053a025.
[107] G. Trimmel, R. Badheka, F. Babonneau, J. Latournerie, P. Dempsey, Solid state NMR and TG/MS study on the transformation of methyl groups during pyrolysis of preceramic precursors to SiOC glasses - ProQuest, J. Sol. Gel Sci. Technol. 26 (1–3) (2003) 279–283, https://doi.org/10.1023/A:1020719720137.
[108] S.J. Widgeon, S. Sen, G. Mera, E. Ionescu, R. Riedel, A. Navrotsky, 29Si and 13C solid-state NMR spectroscopic study of nanometer-scale structure and mass fractal characteristics of amorphous polymer derived silicon oxycarbide ceramics, Chem. Mater. 22 (23) (2010) 6221–6228, https://doi.org/10.1021/cm1021432.
[109] A. Saha, R. Raj, D.L. Williamson, A model for the nanodomains in polymer-derived SiCO, J. Am. Ceram. Soc. (2006), 60428035142017, https://doi.org/10.1111/j.1551-2916.2006.00920.x.
[110] Q. Wen, Z. Yu, R. Riedel, The fate and role of in situ formed carbon in polymer-derived ceramics, Prog. Mater. Sci. 109 (2020), 100623, https://doi.org/10.1016/j.pmatsci.2019.100623.
[111] H.-J. Kleebe, H. Störmer, S. Trassl, G. Ziegler, Thermal stability of SiCN ceramics studied by spectroscopy and electron microscopy: thermal stability of SiCN ceramics, Appl. Organomet. Chem. 15 (10) (2001) 858–866, https://doi.org/10.1002/aoc.243.
[112] R.M. Laine, F. Babonneau, K.Y. Blowhowiak, R.A. Kennish, J.A. Rahn, G.J. Exarhos, K. Waldner, The evolutionary process during pyrolytic

transformation of poly(N-methylsilazane) from a preceramic polymer into an amorphous silicon nitride/carbon composite, J. Am. Ceram. Soc. 78 (1) (1995) 137–145, https://doi.org/10.1111/j.1151-2916.1995.tb08373.x.

[113] J. Seitz, J. Bill, N. Egger, F. Aldinger, Structural investigations of Si/C/N-ceramics from polysilazane precursors by nuclear magnetic resonance, J. Eur. Ceram. Soc. 16 (8) (1996) 885–891, https://doi.org/10.1016/0955-2219(96)00007-6.

[114] S. Traßl, D. Suttor, G. Motz, E. Rössler, G. Ziegler, Structural characterisation of silicon carbonitride ceramics derived from polymeric precursors, J. Eur. Ceram. Soc. 20 (2) (2000) 215–225, https://doi.org/10.1016/S0955-2219(99)00142-9.

[115] J. Bill, J. Seitz, G. Thurn, J. Dürr, J. Canel, B.Z. Janos, A. Jalowiecki, D. Sauter, S. Schempp, H.P. Lamparter, J. Mayer, F. Aldinger, F. Aldinger, Structure analysis and properties of Si–C–N ceramics derived from polysilazanes, Phys. Status Solidi 166 (1) (1998) 269–296, https://doi.org/10.1002/(SICI)1521-396X(199803)166:1<269::AID-PSSA269>3.0.CO;2-7.

[116] S. Schempp, J. Dürr, P. Lamparter, J. Bill, F. Aldinger, Study of the atomic structure and phase separation in amorphous Si-C-N ceramics by X-ray and neutron diffraction, Z. Naturforsch. 53 (3–4) (2014) 127–133, https://doi.org/10.1515/zna-1998-3-405.

[117] H.-J. Kleebe, Microstructure and stability of polymer-derived ceramics; the Si–C–N system, Phys. Status Solidi 166 (1) (1998) 297–313, https://doi.org/10.1002/(SICI)1521-396X(199803)166:1<297::AID-PSSA297>3.0.CO;2-3.

[118] A. Saha, R. Raj, D.L. Williamson, H.-J. Kleebe, Characterization of nanodomains in polymer-derived SiCN ceramics employing multiple techniques, J. Am. Ceram. Soc. 88 (1) (2005) 232–234, https://doi.org/10.1111/j.1551-2916.2004.00034.x.

[119] O. Funayama, H. Nakahara, M. Okoda, M. Okumura, T. Isoda, Conversion mechanism of polyborosilazane into silicon nitride-based ceramics, J. Mater. Sci. 30 (2) (1995) 410–416, https://doi.org/10.1007/BF00354405.

[120] K. Kakimoto, F. Wakai, J. Bill, F. Aldinger, Synthesis of Si–C–O bulk ceramics with various chemical compositions from polycarbosilane, J. Am. Ceram. Soc. 82 (9) (1999) 2337–2341, https://doi.org/10.1111/j.1151-2916.1999.tb02088.x.

[121] J. Cordelair, P. Greil, Electrical conductivity measurements as a microprobe for structure transitions in polysiloxane derived Si–O–C ceramics, J. Eur. Ceram. Soc. 20 (12) (2000) 1947–1957, https://doi.org/10.1016/S0955-2219(00)00068-6.

[122] M. Monthioux, O. Delverdier, Thermal behavior of (organosilicon) polymer-derived ceramics. V: main facts and trends, J. Eur. Ceram. Soc. 16 (7) (1996) 721–737, https://doi.org/10.1016/0955-2219(95)00186-7.

[123] R.T Bhatt, A. Garg, Thermal stability of Hi-Nicalon SiC fiber in nitrogen and silicon environments, in: 10. International Conference on Composite Materials, Vancouver (Canada), 14-18 Aug 1995, 2021. https://www.osti.gov/biblio/188450-thermal-stability-hi-nicalon-sic-fiber-nitrogen-silicon-environments. (Accessed 13 January 2021).

[124] Y. Xu, A. Zangvil, J. Lipowitz, J.A. Rabe, G.A. Zank, Microstructure and microchemistry of polymer-derived crystalline SiC fibers, J. Am. Ceram. Soc. 76 (12) (1993) 3034–3040, https://doi.org/10.1111/j.1151-2916.1993.tb06606.x.

[125] X. Li, Z. Zhu, M. Lu, R. Marco, Characterization of turbostratic carbons synthesized by catalytic decomposition of acetylene, in: 2006 International Conference on Nanoscience and Nanotechnology, IEEE, Brisbane, QLD, Australia, 2006, 4143474, https://doi.org/10.1109/ICONN.2006.340694.

[126] Felix Rosenburg, Emanuel Ionescu, Norbert Nicoloso, Ralf Riedel, High-temperature Raman spectroscopy of nano-crystalline carbon in silicon oxycarbide, Materials 11 (1) (2018) 93, https://doi.org/10.3390/ma11010093.

[127] A.V. Baranov, A.N. Bekhterev, Ya S. Bobovich, V.I. Petrov, Interpretation of certain characteristics in Raman spectra of graphite and glassy carbon, Optic Spectrosc. 62 (1987) 612–616.

[128] C. Thomsen, S. Reich, Double resonant Raman scattering in graphite, Phys. Rev. Lett. 85 (24) (2000) 5214–5217, https://doi.org/10.1103/PhysRevLett.85.5214.

[129] P. Lespade, R. Al-Jishi, M.S. Dresselhaus, Model for Raman scattering from incompletely graphitized carbons, Carbon 20 (5) (1982) 427–431, https://doi.org/10.1016/0008-6223(82)90043-4.

[130] Q. Wen, Y. Feng, Z. Yu, D.-L. Peng, N. Nicoloso, E. Ionescu, R. Riedel, Microwave absorption of SiC/HfCxN1−x/C ceramic nanocomposites with HfCxN1−x-carbon core–shell particles, J. Am. Ceram. Soc. 99 (8) (2016) 2655–2663, https://doi.org/10.1111/jace.14256.

[131] Q. Wen, Y. Xu, B. Xu, C. Fasel, O. Guillon, G. Buntkowsky, Z. Yu, R. Riedel, E. Ionescu, Single-source-precursor synthesis of dense SiC/HfCxN1−x-Based ultrahigh-temperature ceramic nanocomposites, Nanoscale 6 (22) (2014) 13678–13689, https://doi.org/10.1039/C4NR03376K.

[132] F. Rosenburg, The State of Carbon and the Piezoresistive Effect in Silicon Oxycarbide Ceramics, Ph.D. Thesis, Technische Universität, Darmstadt, 2018.

[133] Z.Q. Li, C.J. Lu, Z.P. Xia, Y. Zhou, Z. Luo, X-ray diffraction patterns of graphite and turbostratic carbon, Carbon 45 (8) (2007) 1686–1695, https://doi.org/10.1016/j.carbon.2007.03.038.

[134] S. Martínez-Crespiera, E. Ionescu, H.-J. Kleebe, R. Riedel, Pressureless synthesis of fully dense and crack-free SiOC bulk ceramics via photo-crosslinking and pyrolysis of a polysiloxane, J. Eur. Ceram. Soc. 31 (5) (2011) 913–919, https://doi.org/10.1016/j.jeurceramsoc.2010.11.019.

[135] F. Rosenburg, B. Balke, N. Nicoloso, R. Riedel, E. Ionescu, Effect of the content and ordering of the sp^2 free carbon phase on the charge carrier transport in polymer-derived silicon oxycarbides, Molecules 25 (24) (2020) 5919, https://doi.org/10.3390/molecules25245919.

[136] D.S. McLachlan, M. Blaszkiewicz, R.E. Newnham, Electrical resistivity of composites, J. Am. Ceram. Soc. 73 (8) (1990) 2187–2203, https://doi.org/10.1111/j.1151-2916.1990.tb07576.x.

[137] Q. Wen, Z. Yu, X. Liu, S. Bruns, X. Yin, M. Eriksson, Z.J. Shen, R. Riedel, Mechanical properties and electromagnetic shielding performance of single-source-precursor synthesized dense monolithic SiC/HfCxN1−x/C ceramic nanocomposites, J. Mater. Chem. C 7 (34) (2019) 10683–10693, https://doi.org/10.1039/C9TC02369K.

[138] Y. Wang, L. Zhang, Y. Fan, D. Jiang, L. An, Stress-dependent piezoresistivity of tunneling-percolation systems, J. Mater. Sci. 44 (11) (2009) 2814–2819, https://doi.org/10.1007/s10853-009-3371-5.

[139] Y. Wang, L. Zhang, W. Xu, T. Jiang, Y. Fan, D. Jiang, L. An, Effect of thermal initiator concentration on the electrical behavior of polymer-derived amorphous silicon carbonitrides, J. Am. Ceram. Soc. 91 (12) (2008) 3971–3975, https://doi.org/10.1111/j.1551-2916.2008.02782.x.

[140] N.F. Mott, Conduction in non-crystalline materials, Philos. Mag. J. Theor. Exp. Appl. Phys. 19 (160) (1969) 835–852, https://doi.org/10.1080/14786436908216338.

[141] K. Wang, X. Li, B. Ma, Y. Wang, L. Zhang, L. An, On electronic structure of polymer-derived amorphous silicon carbide ceramics, Appl. Phys. Lett. 104 (22) (2014), 221902, https://doi.org/10.1063/1.4881139.

[142] S. Trassl, M. Puchinger, E. Rössler, G. Ziegler, Electrical properties of amorphous SiCxNyHz-ceramics derived from polyvinylsilazane, J. Eur. Ceram. Soc. 23 (5) (2003) 781–789, https://doi.org/10.1016/S0955-2219(02)00155-3.

[143] C. Haluschka, C. Engel, R. Riedel, Silicon carbonitride ceramics derived from polysilazanes. Part 2: investigation of electrical properties, J. Eur. Ceram. Soc. 20 (9) (2000) 1365–1374.

[144] P. Colombo, Polymer Derived Ceramics: from Nano-Structure to Applications, DEStech Publications, Inc, 2010.

[145] V.L. Nguyen, C. Zanella, P. Bettotti, G.D. Sorarù, Electrical conductivity of SiOCN ceramics by the powder-solution-composite technique, J. Am. Ceram. Soc. 97 (8) (2014) 2525–2530, https://doi.org/10.1111/jace.12963.

[146] K.J. Kim, J.-H. Eom, Y.-W. Kim, W.-S. Seo, Electrical conductivity of dense, bulk silicon-oxycarbide ceramics, J. Eur. Ceram. Soc. 5 (35) (2015) 1355–1360, https://doi.org/10.1016/j.jeurceramsoc.2014.12.007.

[147] G.D. Sorarù, G. Kacha, R. Campostrini, A. Ponzoni, M. Donarelli, A. Kumar, G. Mariotto, The effect of B-doping on the electrical conductivity of polymer-derived Si(B)OC ceramics, J. Am. Ceram. Soc. 100 (10) (2017) 4611–4621, https://doi.org/10.1111/jace.14986.

[148] B. Ma, Y. Wang, Fabrication of dense polymer-derived silicon carbonitride ceramic bulks by precursor infiltration and pyrolysis processes without losing piezoresistivity, J. Am. Ceram. Soc. 101 (7) (2018) 2752–2759, https://doi.org/10.1111/jace.15442.

[149] B.J. Ingram, T.O. Mason, Powder-solution-composite technique for measuring electrical conductivity of ceramic powders, J. Electrochem. Soc. 150 (8) (2003) E396, https://doi.org/10.1149/1.1591754.

[150] V.L. Nguyen, N.B. Laidani, G.D. Sorarù, N-doped polymer-derived Si(N)OC: the role of the N-containing precursor, J. Mater. Res. 30 (6) (2015) 770–781, https://doi.org/10.1557/jmr.2015.44.

[151] G. Shao, W. Peng, C. Ma, W. Zhao, J. Guo, Y. Feng, H. Wang, R. Zhang, L. An, Enhanced electric conductivity of polymer-derived SiCN ceramics by microwave post-treatment, J. Am. Ceram. Soc. 100 (3) (2017) 842–847, https://doi.org/10.1111/jace.14590.

[152] D. Seo, S. Jung, S.J. Lombardo, Z.C. Feng, J.K. Chen, Y. Zhang, Fabrication and electrical properties of polymer-derived ceramic (PDC) thin films for high-temperature heat flux sensors, Sens. Actuators Phys. 165 (2) (2011) 250–255, https://doi.org/10.1016/j.sna.2010.11.013.

[153] H.-Y. Ryu, Q. Wang, R. Raj, Ultrahigh-temperature semiconductors made from polymer-derived ceramics, J. Am. Ceram. Soc. 93 (6) (2010) 1668–1676, https://doi.org/10.1111/j.1551-2916.2010.03623.x.

[154] R. Riedel, L. Toma, E. Janssen, J. Nuffer, T. Melz, H. Hanselka, Piezoresistive effect in SiOC ceramics for integrated pressure sensors, J. Am. Ceram. Soc. 93 (4) (2010) 920–924, https://doi.org/10.1111/j.1551-2916.2009.03496.x.

[155] K. Terauds, P.E. Sanchez-Jimenez, R. Raj, C. Vakifahmetoglu, P. Colombo, Giant piezoresistivity of polymer-derived ceramics at high temperatures, J. Eur. Ceram. Soc. 30 (11) (2010) 2203–2207, https://doi.org/10.1016/j.jeurceramsoc.2010.02.024.

[156] Y. Wang, J. Ding, W. Feng, L. An, Effect of pyrolysis temperature on the piezoresistivity of polymer-derived ceramics, J. Am. Ceram. Soc. 94 (2) (2011) 359–362, https://doi.org/10.1111/j.1551-2916.2010.04330.x.

[157] L. Toma, H.-J. Kleebe, M.M. Müller, E. Janssen, R. Riedel, T. Melz, H. Hanselka, Correlation between intrinsic microstructure and piezoresistivity in a SiOC polymer-derived ceramic, J. Am. Ceram. Soc. 95 (3) (2012) 1056–1061, https://doi.org/10.1111/j.1551-2916.2011.04944.x.

[158] F. Roth, C. Schmerbauch, E. Ionescu, N. Nicoloso, O. Guillon, R. Riedel, High-temperature piezoresistive C/SiOC sensors, J. Sens. Sens. Syst. 4 (1) (2015) 133–136, https://doi.org/10.5194/jsss-4-133-2015.

[159] F. Roth, P. Waleska, C. Hess, E. Ionescu, N. Nicoloso, UV Raman spectroscopy of segregated carbon in silicon oxycarbides, J. Ceram. Soc. Jpn. 124 (10) (2016) 1042–1045, https://doi.org/10.2109/jcersj2.16100.

[160] Y. Cao, X. Yang, R. Zhao, Y. Chen, N. Li, L. An, Giant piezoresistivity in polymer-derived amorphous SiAlCO ceramics, J. Mater. Sci. 51 (12) (2016) 5646–5650, https://doi.org/10.1007/s10853-016-9866-y.

[161] G. Shao, J. Jiang, M. Jiang, J. Su, W. Liu, H. Wang, H. Xu, H. Lit, R. Zhang, Polymer-derived SiBCN ceramic pressure sensor with excellent sensing performance, J. Adv. Ceram. 9 (3) (2020) 374–379, https://doi.org/10.1007/s40145-020-0377-6.

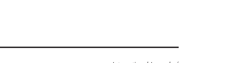

Received: 10 February 2021 | Revised: 12 April 2021 | Accepted: 10 May 2021

DOI: 10.1111/ijac.13800

International Journal of Applied Ceramic TECHNOLOGY

SPECIAL ISSUE ARTICLE

Electrically conductive silicon oxycarbide thin films prepared from preceramic polymers

Emmanuel III Ricohermoso[1] | **Florian Klug**[2] | **Helmut Schlaak**[2] | **Ralf Riedel**[1] | **Emanuel Ionescu**[1]

[1]Fachbereich Material- und Geowissenschaften, Technische Universität Darmstadt, Darmstadt, Germany

[2]Fachbereich Elektrotechnik und Informationstechnik, Technische Universität Darmstadt, Darmstadt, Germany

Correspondence
Emmanuel III Ricohermoso, Fachbereich Material- und Geowissenschaften, Technische Universität Darmstadt, Otto-Berndt-Str. 3, D-64287 Darmstadt, Germany.
Email: emmanuel_iii.ricohermoso@tu-darmstadt.de

Funding information
The authors gratefully acknowledge funding from the German Science Foundation (DFG, Germany)—grants no. 411658150 (Microstructured C/SiCX (X = O,N)-based high-temperature strain gauge). Additionally, EI acknowledges funding from DFG within the Heisenberg program (IO 64/14-1).

Abstract

This work focuses on silicon oxycarbide thin film preparation and characterization. The Taguchi method of experimental design was used to optimize the process of film deposition. The prepared ceramic thin films with a thickness of c. 500 nm were characterized concerning their morphology, composition, and electrical properties. The molecular structure of the preceramic polymers used for the preparation of the ceramic thin films as well as the thermomechanical properties of the resulting SiOC significantly influenced the quality of the ceramic films. Thus, an increase in the content of carbon was found beneficial for the preparation of crack-free thin films. The obtained ceramic films exhibited increased electrical conductivity as compared to monolithic SiOC of similar chemical composition. This was shown to correlate with the unique hierarchical microstructure of the SiOC films, which contain large oxygen-depleted particles, mainly consisting of highly graphitized carbon and SiC, homogeneously dispersed in an oxygen-containing amorphous matrix. The matrix was shown to also contain free carbon and to contribute to charge carrier transport between the highly conductive large particles. The ceramic thin films possess electrical conductivities in the range from 5.4 to 8.8 S/cm and may be suitable for implementation in miniaturized piezoresistive strain gauges.

KEYWORDS

electrical conductivity, polymer-derived ceramics, thin film

1 | INTRODUCTION

Over the past six decades, there have been numerous studies reporting on synthesis routes, characterization methods, and the development of new types of polymer-derived ceramics (PDCs).[1,2] Most of the existing studies are intensively done on powders, fibers, and monoliths based on PDCs, while relatively few are conducted on thick and thin film samples. Furthermore, the applicability of PDC for industrial and commercial consumers is getting recognition only in recent years.

Silicon oxycarbide, a type of PDC mostly derived from polysiloxanes, is of interest because of its thermal stability, relatively low process temperature, tunable microstructure, chemical and oxidation resistance, and functional properties which includes electrical conductivity and piezoresistivity.[1,3] Interestingly, the aforementioned properties of

This is an open access article under the terms of the Creative Commons Attribution License, which permits use, distribution and reproduction in any medium, provided the original work is properly cited.
© 2021 The Authors. *International Journal of Applied Ceramic Technology* published by Wiley Periodicals LLC on behalf of American Ceramics Society (ACERS)

SiOC are dependent on the content of the free carbon phase present in the system. Precursors lead to different microstructures and rearrangements depending on the process temperature. It has been identified that in the SiOC system, the free carbon phase is always the first one to segregate at 500–800°C in the form of polycyclic aromatic hydrocarbons (PAHs). As the heat treatment temperature increases, these aromatics tend to stack up forming carbon-based basic structural units (BSUs) consisting of at least two layers with c. 1 nm lateral extension.[4,5] At 1000–1200°C, hydrogen removal occurs leaving neighboring BSU to form edge-to-edge linkages. This leads to clusters of graphene-like carbon with an increased degree of ordering. Thermal treatment at 1300°C promotes the crystallization of the SiC phase parting the SiO_2 as the matrix of the material.[6] Additional heat treatment above 1700°C results in the ordering of crystallites forming misaligned graphene sheets stacked in a turbostratic manner.[7,8]

Several studies on SiOC ceramics showed conductive behavior having conductivity values ranging from 10^{-3} to 10 S/cm at room temperature conditions.[8–10] Rosenburg et al showed the logarithmic dependence of the SiOC conductivity on the content of segregated carbon of the sample.[10] The dependence showed attribution to the nature of the percolating system which is reliant on the aspect ratio of the free carbon phase.[11] The ordering of the free carbon phase leads to a higher aspect ratio of the conductive phase within the system thus decreasing the percolation threshold. While these data are available for bulk samples, reports for SiOC films are still scarce.

The present work is dedicated to promoting the knowledge transfer of monolithic SiOC to thin film materials to be integrated into microelectromechanical systems (MEMS), for example, as miniaturized SiOC-based strain sensor elements. Specific to this study is producing the base functional material as a homogenous SiOC film on a silicon wafer substrate. The SiOC films are extensively characterized concerning their morphology and microstructure, composition, and electrical properties. As part of the main challenge, this work emphasizes the production of thin films without using filler materials and is done in a single-layer deposition technique. Additionally, the technique must be simple and reproducible and will be analyzed statistically to evaluate the microstructural and electrical properties of the thin film.

2 | MATERIALS AND METHODS

2.1 | Materials

Commercially available Polyramic® SPR 212 (Starfire Systems Ltd.), and BELSIL® PMS-MK (Wacker Chemie AG) were used as polymer precursors for the synthesis of SiOC thin films. To improve the polymerization process, catalysts were used namely 1 wt% of dicumyl peroxide (added as a 50 wt% solution in toluene) and 1 wt% zirconium acetylacetonate for SPR 212 and MK PMS, respectively. Toluene was also added to obtain a 40% dilution of the polymers prior to the spin coating deposition on circular boron-doped p-type Si (100) substrates with 525 μm thickness (Prime Si + SiO_2, MicroChemicals GmbH). The used substrates have a SiO_2 passivation layer with a thickness of 500 nm.

2.2 | Coating preparation

The spin coating process was carried out using LabSpin 8 (Süss MicroTec SE) with a static dispense technique. The substrate was firstly cleaned with acetone and isopropanol before carrying out the process as designed in Table S2. The process was optimized using three parameters namely the initial spin speed, the acceleration profile, and the final spin speed. All three parameters were identified to influence the thickness and uniformity of the film. The design of the experiment (DOE) presented in Table S2 utilized the L9 (33) Taguchi static design which reduced the number of trials to 9 instead of 27 of the full factorial design.[12–14] The film thickness was chosen as the response factor which was measured using a profilometer (Dektak XT Advanced System, Brucker), in three different positions. The final set of parameters used in the experiments is listed in Table S1.

The samples were then thermally cross-linked at 250°C in air. After cross-linking, the sample was pyrolyzed in a graphite crucible placed in a high-temperature furnace (FCT-Uniaxial hot-press, FCT Systeme GmbH). The temperature was first ramped up to 1100°C then held for 2 h. It was then ramped up to 1400°C for an additional heat treatment step which was then held for 3 h. The whole heat treatment process used constant heating and cooling rates at 5°C/min and was all done under a high purity nitrogen atmosphere.

2.3 | Coating characterization

The coatings were analyzed using a profilometer, an in-house four-probe resistance measurement device, Raman Spectroscopy (LabRAM Horiba HR Raman Spectroscope HR800, Horiba Jobin Yvon GmbH), Scanning Electron Microscopy [SEM] coupled with Energy Dispersive Spectroscopy [EDS] (JEOL JSM 7600F, JEOL Ltd.), and Conductive-[C-AFM], and Tunneling Atomic Force Microscopy [TUNA] (Bruker Dimension Icon, Bruker) with AC240 TM conductive tip (Oxford Instruments).

3 | RESULTS AND DISCUSSION

3.1 | Thin film deposition optimization

According to the review article of Barroso et al, a critical coating thickness of several μm (up to 10 μm) must be considered when dealing with PDCs for thin film application, to prevent cracking and spallation.[15] For instance, the work of Günthner and Kraus showed that a filler-free PDC-based coating has a critical coating thickness of 1 μm which is in agreement with the preliminary experiments of this study.[16,17] For thicker PDC-based coatings, the use of suitable fillers is required to compensate for the formation of cracks during shrinkage of the film.[15]

Conducive to these findings, the envisaged film thickness for the SiOC films prepared in the present study was kept below 1 μm to partake a crack-free SiOC coating on a silicon substrate. The spin coating process has been used in a wide variety of industries and technology sectors for silicon wafer coatings due to its simplicity, readiness, and high reproducibility. The use of the spin coating process in nanotechnology has been prevalent especially for semiconductor applications that require thin films with high uniformity. The thickness of the film depends on several factors such as rotational forces, precursor viscosity, and the adhesion of the solution with the substrate.[18,19] In the present study, the process-related factors namely the initial and secondary spin speed, as well as the acceleration was identified as the control factors while the deviations in solution concentration, working environment conditions, and user effect were considered being the noise factors.

To analyze the effect of the three factors identified in Table S2, the Taguchi method is utilized. The Taguchi method was championed by Genichi Taguchi in 1987 and is a powerful approach to optimize the experimental design performance. This method determines the robustness of the design by taking the prime permutation of design parameters from a minimum number of experiments hence ensuring the reproducibility of the results. In this experiment, results are obtained by performing 9 trials instead of 27 rivaled to a full factorial design of the experiment.

As shown in Table S3, analysis of variance (ANOVA) done at 95% confidence level revealed the initial spin speed as the main control factor responsible for the film thickness uniformity with a p-value of 0.027, F-statistic (df = 2) of 36.64. Given that the p-values of the second spin speed and the acceleration were both more than the alpha = 0.05, the null hypothesis was accepted stating the insignificance of both factors to the thickness homogeneity. Although statistically insignificant, it is imperative to look at the practical aspect of the experiment. Considering Figure 1, the significance of using the high initial spin speed has been highlighted by the decreasing number of cracks seen on the surface of the film, however, some cracks are still present on the sample

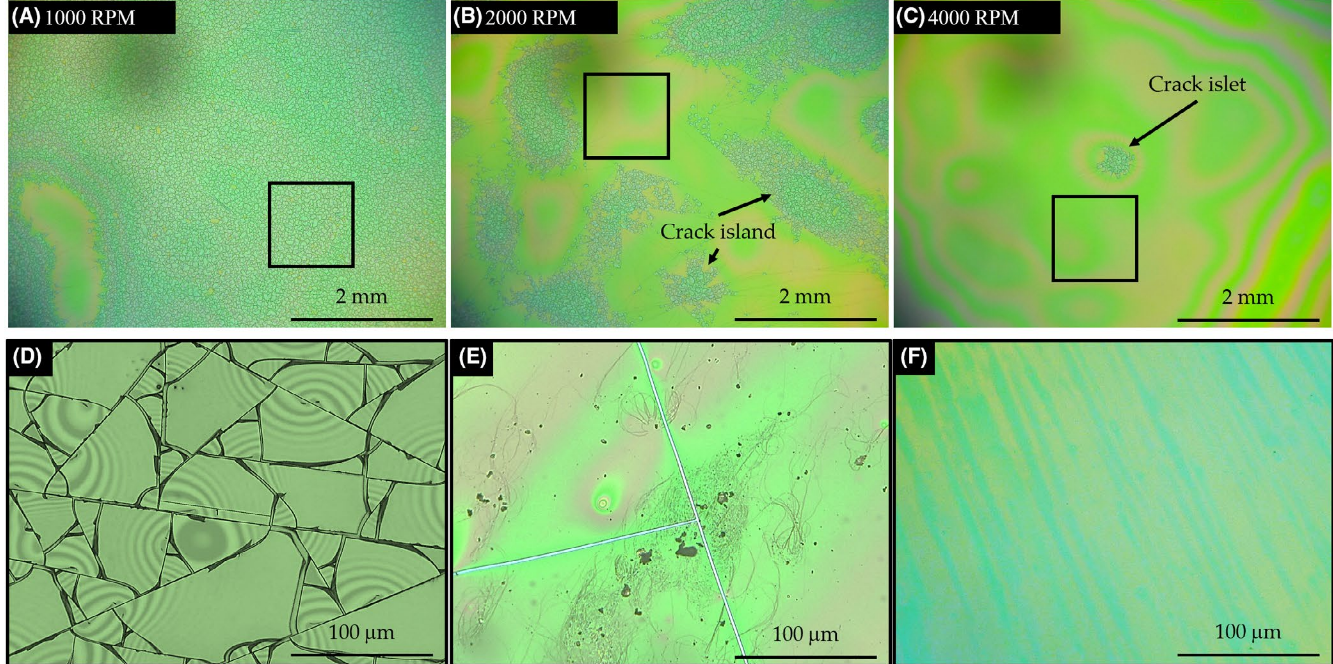

FIGURE 1 Optical microscopic images of the thin Si-polymer film derived from SPR 212 after crosslinking at 250°C. Samples were spin coated at different initial spin speeds with the acceleration of 300 rpm per second, and a second spin speed of 6000 rpm. (A) At the initial spin speed of 1000 rpm, almost the whole surface is crammed with micro-cracks. (B) Crack islands can be seen on the surface of samples spin coated at an initial speed of 2000 rpm which then decreased as the spin speed was changed to (C) 4000 rpm. (D–F) Magnified areas of images (A–C) highlighting the quality of the film surface

spun at 4000 rpm. These cracks are then eliminated when the effect of the second spin speed at 8000 rpm is taken into consideration. The film thickness measured with this set of the parameter is approximately 500 nm after the final heat treatment process.

The Taguchi method considers the means and the signal-to-noise (S/N) ratio of the results to reduce the variability of the design. The S/N ratio is the response tradeoff when setting the mean value to the desired level while keeping the variance low.[12,14,20] The S/N ratios are defined so that a maximum value of the ratio minimizes variability transmitted from the noise variables.[12] In Figure 2A, it can be seen that most of the runs resulted in mean values close to or above the target thickness of less than 1 μm. Considering these values, the S/N ratio of the results was calculated to minimize the response or using the "smaller-is-better" $(S/N)_S$ type. The desired factors resulted in an initial spin speed of 4000 rpm for 30 s then accelerated to a second spin speed of 8000 rpm for 30 s with an acceleration of 500 rpm/s as shown in Figure 2B.

Following the optimized spin coating parameters, eight supplementary samples were prepared to confirm the effectiveness of the design to which none of the samples manifested crack formation after thermal treatment and ceramization. The samples were cross-linked at 250°C and subsequently pyrolyzed at 1100 and 1400°C, respectively, as the last ceramization step. The samples prepared from Polyramic SPR 212 provided a SiOC material containing c. 17 vol% free carbon (C17-1100 and C17-1400) and produced a homogeneous and crack-free film after heat treatment, as shown in Figures 3C,D and 4. The SEM image of the C17-1100 sample exhibits a smooth surface while phase separation is evident for the C17-1400 sample as supported by the color contrast shown in the backscattered SEM image in Figure 4.

Additionally, samples are prepared from Belsil PMS-MK, a precursor that delivers a SiOC ceramic containing c. 11 vol% free carbon (i.e., C11-1100 and C11-1400). However, SEM images of C11-1100, which are shown in Figure 3A,B, indicated micro-crack formation and spallation. The samples annealed at 1400°C, C11-1400 (not shown), exhibited complete

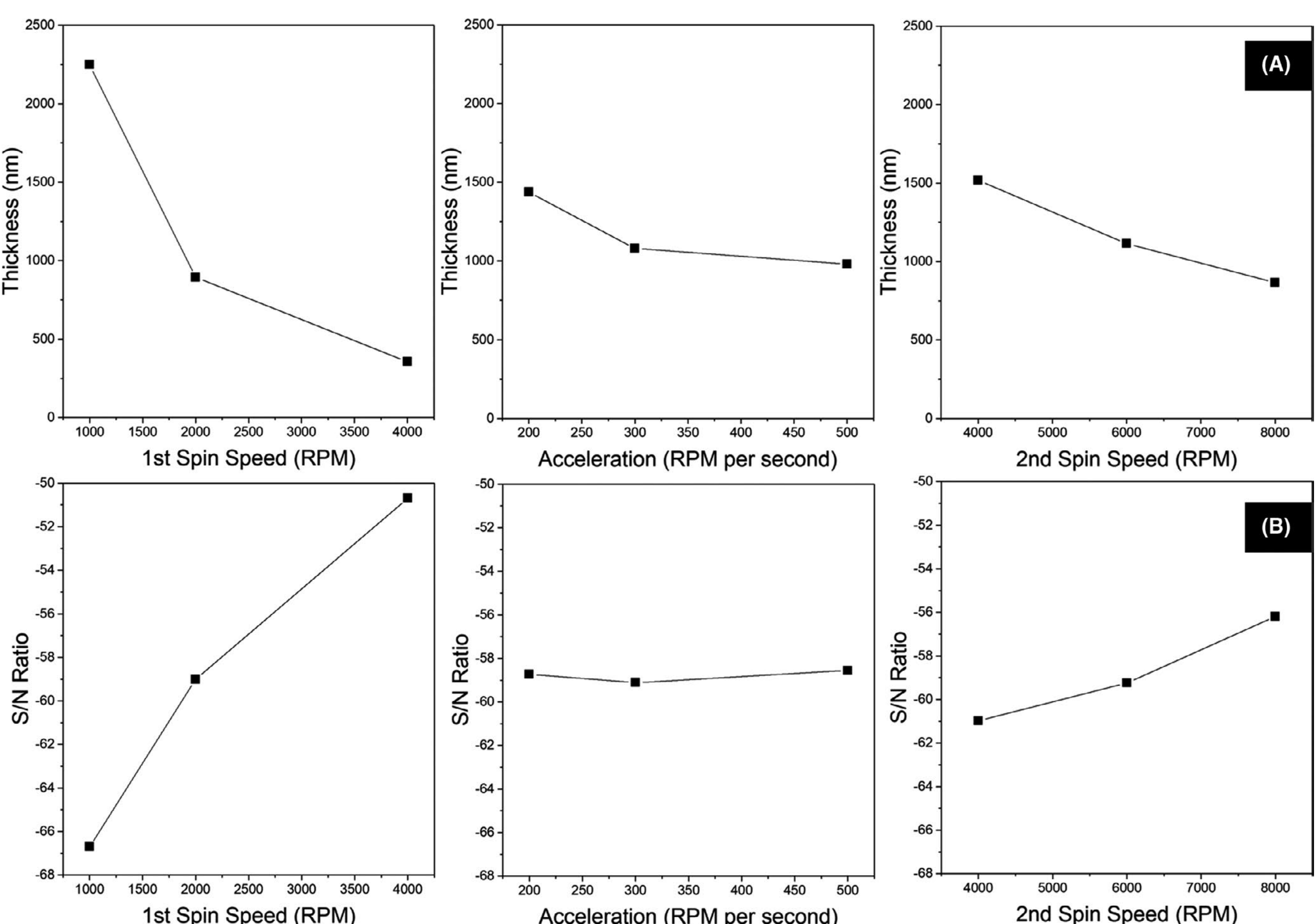

FIGURE 2 Statistical analysis of spin coating process optimization. (A) Main effect analysis of the average thickness obtained after crosslinking. (B) Main effect analysis of the S/N ratio of film thickness as a response to different factors with maximum S/N ratio as the desired outcome. Taguchi design analysis resulted in 4000 rpm, and 8000 rpm as the optimal spin speeds with 500 rpm per second as the acceleration. First spin speed showed to have the most significance in the spin coating process of the preceramic polymer

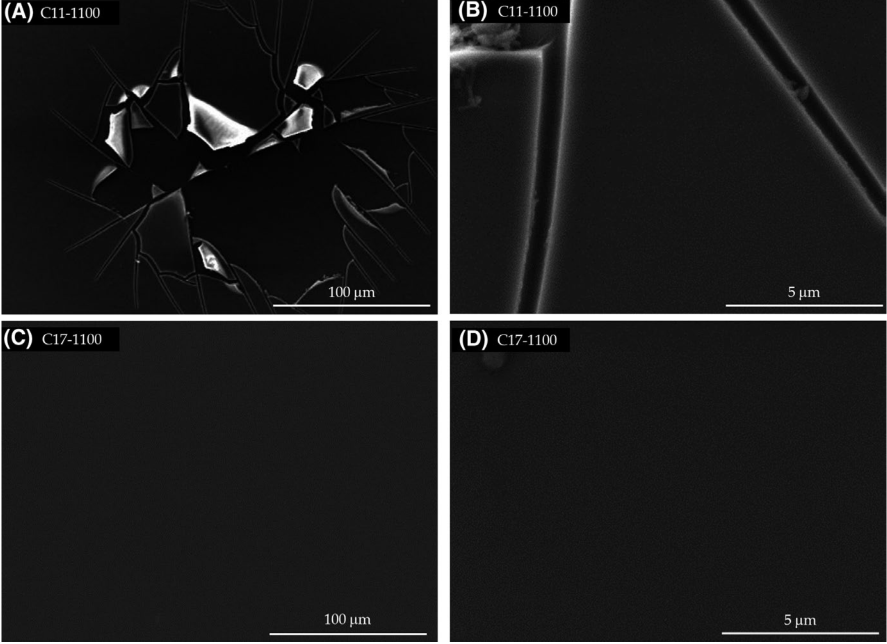

FIGURE 3 SEM images of spin-coated samples after heat treatment at 1100°C. (A and B) Formation of microcracks and spallation on C11-1100 sample. (A) Homogenous coating of sample C17-1100

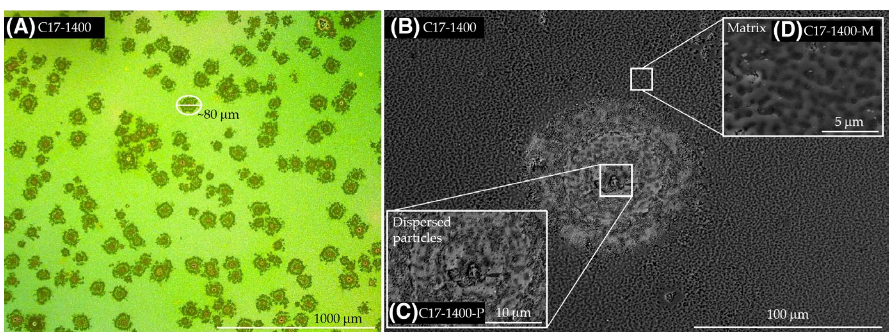

FIGURE 4 Phase separation was observed on the C17 sample heat treated at 1400°C. (A) Optical microscopic image of the C17-1400 film showing the presence of dispersed particles with ~90 μm in size. (B) Backscattered SEM image displaying the color contrast (topographical difference) of the dispersed particle from the matrix of the C17-1400 sample. (C) Magnified image of the precipitate, and (D) magnified image of the matrix

delamination of the film after the heat treatment process. As the preparation parameters for both samples C11 and C17 compositions were kept the same, it is obvious that the use of different preceramic polymers (i.e., SPR-212 vs. PMS-MK) leads to large differences in film quality/integrity besides different composition of the resulting SiOC ceramic films.

In previous studies related to the gel-to-ceramic conversion (e.g., 21–23), it was mentioned that sol–gel films undergo significant structural changes and subsequently suffer from mechanical stresses developed during their thermal treatment, namely heating up, isothermal heat treatment (annealing), and cooling down. These three steps lead to intrinsic and thermal stresses on the thermally treated sol–gel films. Intrinsic stress is experienced by the film during the heating up and annealing steps, during which densification occurs accompanied by chemical and structural changes. In addition, the difference between the coefficients of thermal expansion (α) of the film and the substrate during cooling down gives rise to thermal stress. The TGA results of the preceramic polymers used in this study showed three weight loss steps during their pyrolysis at 1100°C, with onset temperatures at 210, 520, and 700°C, respectively.[24,25] No further weight loss was analyzed in both studied ceramic systems, indicating that the ceramization process is completed at temperatures as high as 700–800°C. Consequently, it is considered that up to temperatures ranging between 700 and 800°C, densification occurs and generating in-plane tensile stress in the films. For thin films, stresses are mainly concentrated on the biaxial direction since shrinkage is not restricted in the direction perpendicular to the substrate.[26] As the film is constrained in two dimensions (i.e., in the plane of the substrate), the tensile stress experienced by the film may cause bending of the substrate or/and indeed cracking of the ceramic film.[15,22,27]

The values of the thermal expansion coefficients and the Poisson's ratio of the SiOC samples and the silicon substrate are presented in Table 1. After cooling, the residual stress

on the film, σ_f, as well as the radius of curvature (R) of the coated substrate was calculated using Equations (1 and 2), respectively, and are presented in Table 1.

In Equation (1), ΔT is the difference between the heat treatment temperature and the room temperature, and $\Delta\alpha$ is the difference between the thermal expansion coefficients of the silicon substrate and the SiOC thin film. The term $\left[\frac{E_f}{1-\nu_f}\right]$ or E^* is the effective stiffness or the biaxial modulus of the film raised by the Poisson effect.[30] Equation (2) was derived from Stoney's equation where E, t, and ν are Young's modulus, thickness, and Poisson's ratio of the silicon substrate, respectively.[27,31]

$$\sigma_f = \left[\frac{E_f}{1-\nu_f}\right] \Delta T * \Delta\alpha \tag{1}$$

$$R = \left[\frac{1}{6 * \sigma_f * t_f}\right] * \left[\frac{E_{Si} * t_{Si}^2}{1-\nu_{Si}}\right] \tag{2}$$

It can be seen from the values of the residual stresses in Table 1 that upon cooling, sample C11 was under tension while sample C17 was under compression. Based on Equation (1) and Table 1, for both samples, the first two terms (E^* and ΔT) of the equation are similar, thus the difference of the residual stresses is mainly caused by the mismatch of the thermal coefficients ($\Delta\alpha$) of the film and the substrate. Given that the thickness of the silicon substrate is much larger than that of the film (t_{Si} (500 μm) >> t_f (500 nm)), the film is forced to follow the dimension of the substrate as reinforced by the calculated radius of curvatures. The positive values of R indicate the concave warpage of the substrate resulting in tensile stress on the film.[32]

As a result, the C11 samples showed the formation of cracks and complete delamination of the film, therefore not meeting the criteria for a uniform and homogenous thin film compatible for MEMS applications. Consequently, the following sections will deal with the study of the samples with 17 vol% C, that is, C17-1100 and C17-1400.

3.2 | Thin film composition

Former studies showed that pyrolysis of the SiOC matrix at 1200°C generally promotes phase separation into SiO_2 and SiC. It has been shown also that with supplementary heat treatment of the sample, SiC can further crystallize as a product of the carbothermal reduction of the SiO_2 phase at a temperature above 1400°C.[9,33,34] These phenomena found in the SiOC system are explained by the Reactions (3) and (4).

$$\mathrm{SiOC} \rightarrow \mathrm{SiO_2} + \mathrm{SiC} + \mathrm{C}, \tag{3}$$

$$\mathrm{SiO_2} + 3\mathrm{C} \rightarrow \mathrm{SiC} + 2\mathrm{CO} \tag{4}$$

The backscattered electron image presented in Figure 5 displays two distinct phases on the surface of C17-1400, with different morphologies. The first phase consists of round-shaped structures evenly distributed (Figure 4A) within the second phase acting as the matrix. SEM images taken at higher magnification revealed that the disperse phase has a porous structure with a sponge-like morphology. The phases were differentiated by their amounts of carbon and oxygen. Thus, the dispersed phase is C-rich and O-depleted; whereas the matrix is O-rich (Figure 5). Therefore, it is assumed that the matrix consists of amorphous, sp^2-hybridized carbon-containing SiOC (C/SiOC); whereas the dispersed phase most probably contains sp^2-hybridized carbon and SiC (C/SiC). The formed SiC usually segregates in form of nanometer-sized crystallites in bulk SiOC while the resulting SiC phase in the SiOC film appears as micrometer-sized particles. In relation to Figure 4A, by particle count distribution, these dispersed particles took up ~16 vol% of the surface of a representative $1 \times 1\ cm^2$ sample size. This value is comparable to the known volume fraction of carbon in the preceramic polymer amounting to 17 vol% with the deviation accounted to the amount of carbon identified in the matrix as per the EDS map shown in Figure 5.

To confirm the presence of sp^2-hybridized C in the thin film samples, Raman spectra of the samples were taken and the results are presented in Figure 6. It can be seen that both samples pyrolyzed at 1100°C have broader peaks and high-intensity values as compared to that of the C17-1400 sample. The matrix and the dispersed particles were analyzed separately and the

TABLE 1 Poisson's ratios (ν (1100°C), ν (1400°C)), and coefficient of thermal expansion (α) values of the SiOC samples, and the silicon substrate.[28,29] Calculated residual thermal stresses on the film (σf-1100, σf-1400) and the calculated curvatures of the coated substrate (R1100, R1400)

Sample	α (10^{-6} K^{-1})	ν (1100°C)	ν (1400°C)	E (GPa)	σf−1100 (MPa)	σf−1400 (MPa)	R_{1100} (mm)	R_{1400} (mm)
C11	2.02	0.11	0.17	90	52.1	71.6	0.26	0.19
C17	3.23	0.11	0.17	90	−79.3	−108.8	−0.17	−0.12
Si	2.5	0.22	-	125	-	-	-	-

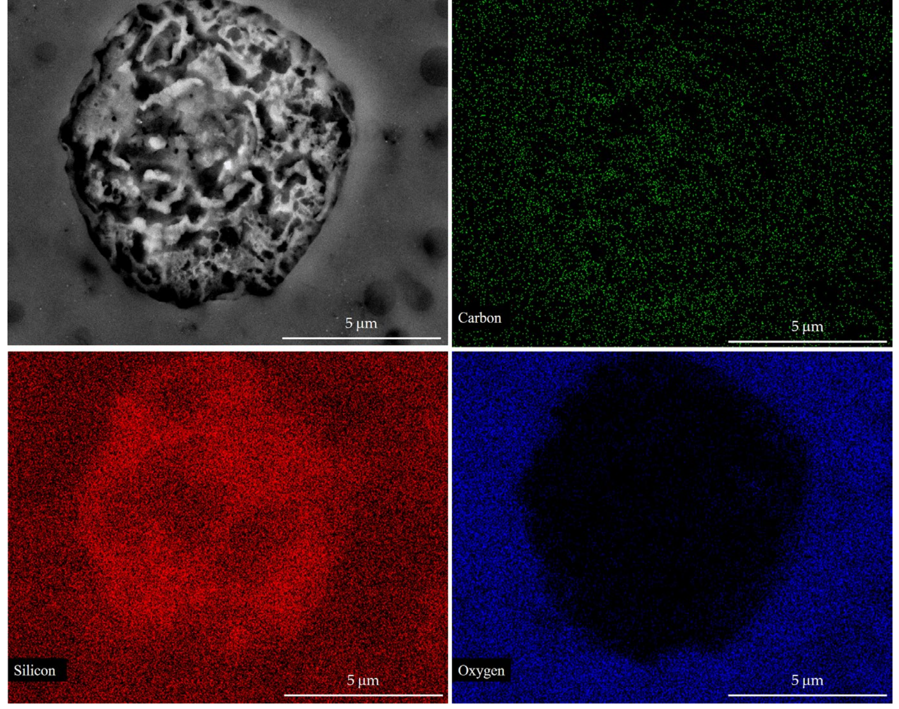

FIGURE 5 Backscattered SEM image and EDS map of C17-1400 thin film: two phases were observed on the film surface. The SEM image reveals a porous structure of the disperse phase

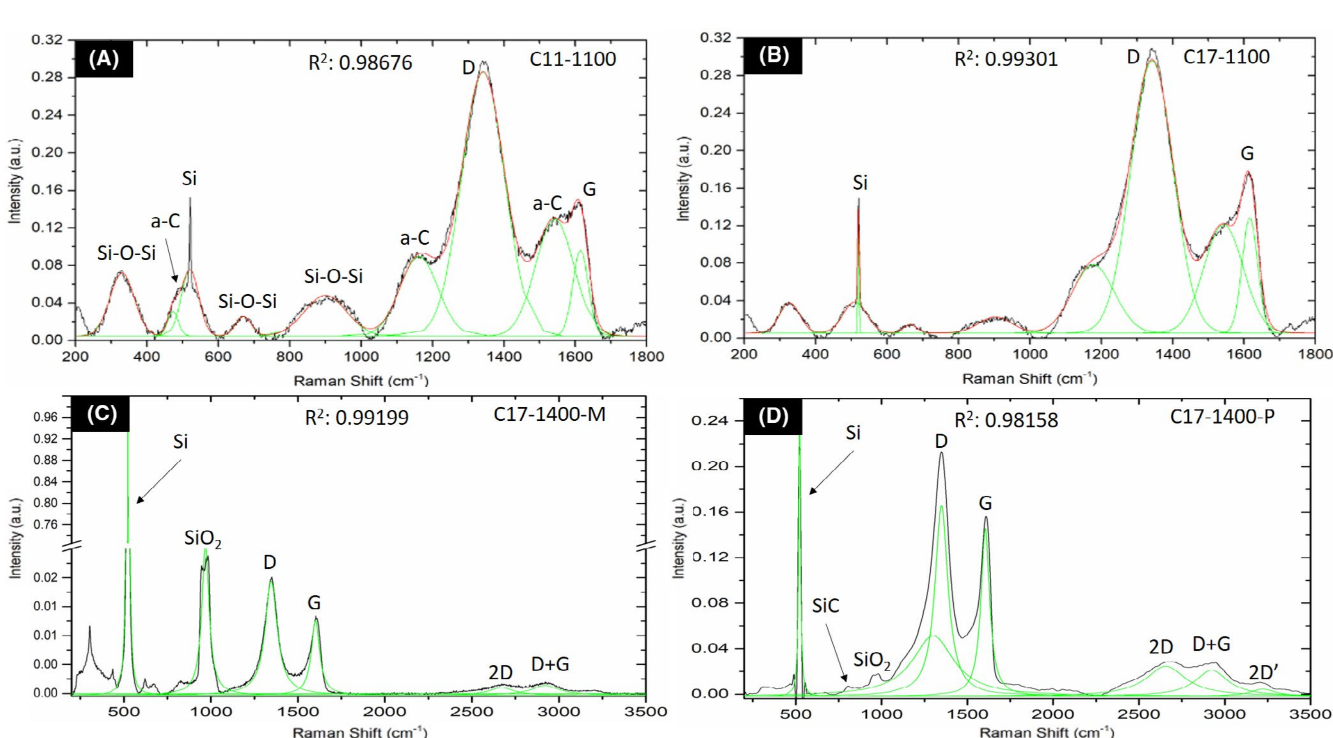

FIGURE 6 Raman spectra of SiOC-based thin film samples. Samples synthesized at 1100°C (i.e., C11-1100 and C17-1100) are shown in (A) and (B), respectively. Spectra in (C) and (D) represent the matrix and C-rich precipitates, respectively, in C17-1400

spectra are presented in Figure 6C,D. Three dominant peaks are found one associated with Si, and the D and G bands of the free carbon phase present in the system.

Having a closer look at the fingerprint area of the Raman spectra depicted in Figure 6, six other peaks are analyzed in the sample obtained at 1100°C which partially or fully disappeared in the sample annealed at 1400°C. In addition to a sharp band at c. 521 cm^{-1}, which was assigned to crystalline Si, silicon substrate-related bands (more precisely, bands related to the silica scale present on the silicon substrate) are

located at 330 and 670 cm^{-1} which are both attributed to the asymmetric and symmetric Si-O-Si vibrations while the peak at 950 cm^{-1} is due to the second-order transverse optic phonon of the silica scale.[35–40] A broad peak at 500 cm^{-1} can also be seen on the samples pyrolyzed at 1100°C which is attributed to the presence of amorphous sp^3 bonded carbon.[41] A peak at 1150 cm^{-1} has been matched with the amorphous carbon phases (a-C) which are related to the used precursor and were found to resemble the theoretical phonon density of states of sp^3 domains.[42–46] A conclusion has been drawn by Chu et al that peak shifts and widening are related to the number of sp^3 and sp^2 neighbors which varies locally. It is further discussed that the peak at 1150 cm^{-1} disappears with decreasing amount of sp^3 carbon atoms.[47]

The shoulder of the Raman peak at 1500 cm^{-1} is also credited to the presence of amorphous carbon (a-C). It is known that the graphitization rate increases with an increasing amount of carbon. Roth et al reported that the disappearance of the a-C peak at higher temperatures indicates the completion of the graphitization process forming nanocrystalline graphitic domains.[48] In this work, amorphous carbon (a-C) fully disappeared after heat treatment at 1600°C which we could not achieve in our present work due to the limitation of the heat treatment temperature related to the melting temperature of the silicon substrate at 1414°C. Looking at the predominant peaks presented in Figure 6, the intensities of the silica-scale related bands for the 1100°C-treated samples are less than those of the 1400°C sample, with the highest relative intensity found in its matrix; this is correlated with the fact that the thickness of the ceramic film decreases as the thermal treatment temperature increases from 1100 to 1400°C. As explained in Section 3A, the film is generally under biaxial stress and is free to move in the z-direction, thus a temperature dependence of the thickness of the film has to be considered. It can be seen that a larger thickness of the film in C11-1100 and C17-1100 results in less intensity of the substrate-related signals (i.e., Si signal at 520 cm^{-1}) as compared to the analogous samples thermally treated at 1400°C. On the other hand, the matrix of the C17-1400 sample has a more intense Si peak as compared to that of the dispersed particles. Additionally, the SiO_2 peak is also more visible in the matrix than that of the dispersed particle area. This finding suggests a thinner structure of the matrix relative to the dispersed particles of the C17-1400 sample and agrees well with the contrast observed in the SEM micrographs (see Figure 5B). The SiC band at 801 cm^{-1} is found in the dispersed particle in the Raman spectrum of the sample C17-1400, which supports the C-rich nature of the segregated particles as already analyzed via EDS mapping shown in Figure 5.

After performing Lorentzian fitting of the Raman spectra presented in Figure 6, first- and second-order features for the sp^2-hybridized free carbon phase were identified in the SiOC thin film. The corresponding values of the Raman line characteristics are listed in Table 2. The presence of the D (disorder) and the G (graphitic) bands of the Raman spectra confirms the formation of segregated carbon phases in samples.[48–50] Both of these bands were acknowledged to have originated from sp^2 hybridized carbon.[42] The D band is the defect-induced double resonance process that activates at the transverse optical (TO) phonon and is often referred to as the disorder band originating with the out-of-plane vibrational mode of graphene at the A_{1g} zone edges. The disorder in the sp^2-hybridized carbon systems results in a resonance of the Raman spectra. The optical phonon dispersion in graphitic material is classified based on the direction of the nearest C-C atoms. The in-plane modes known as transverse (TO) and longitudinal (LO) refer to vibrations perpendicular and

TABLE 2 Mean values of the Lorentzian fitting of the Raman spectra of the SiOC thin film samples as compared to monolithic samples

		Thin film				Monolith			
		C11-1100	C17-1100	C17-1400 M	C17-1400 P	C11-1200	C11-1400	C17-1200	C17-1400
D	Raman Shift	1341.5	1342.3	1346.8	1348.3	1347.9	1362.9	1340.8	1350.8
	FWHM	142.5	139.6	83.6	88.9	97.0	65.5	143.8	97.7
G	Raman Shift	1614.5	1616.1	1601.4	1606.5	1595.0	1597.7	1588.8	1606.2
	FWHM	51.3	51.6	54.5	62.7	66.0	75.9	74.8	60.1
2D	Raman Shift	-	-	2675.7	2656.3	-	-	2611.9	2626.2
	FWHM	-	-	133.9	306.2	-	-	74.8	60.1
Calculations	A_D/A_G	8.6	6.4	2.3	1.4	2.3	1.9	2.8	2.0
	L_a [nm]	2.0	2.6	7.2	11.9	7.3	8.9	6.0	8.3
	L_D [nm]	3.9	4.6	7.5	9.7	7.6	8.4	6.9	8.1
	n_D ($\times 10^{11}$) [cm^{-3}]	29	22	8.0	5.0	7.9	6.4	9.5	6.9
	L_{eq} [nm]	-	-	7.1	56.3	-	-	21.6	23.5

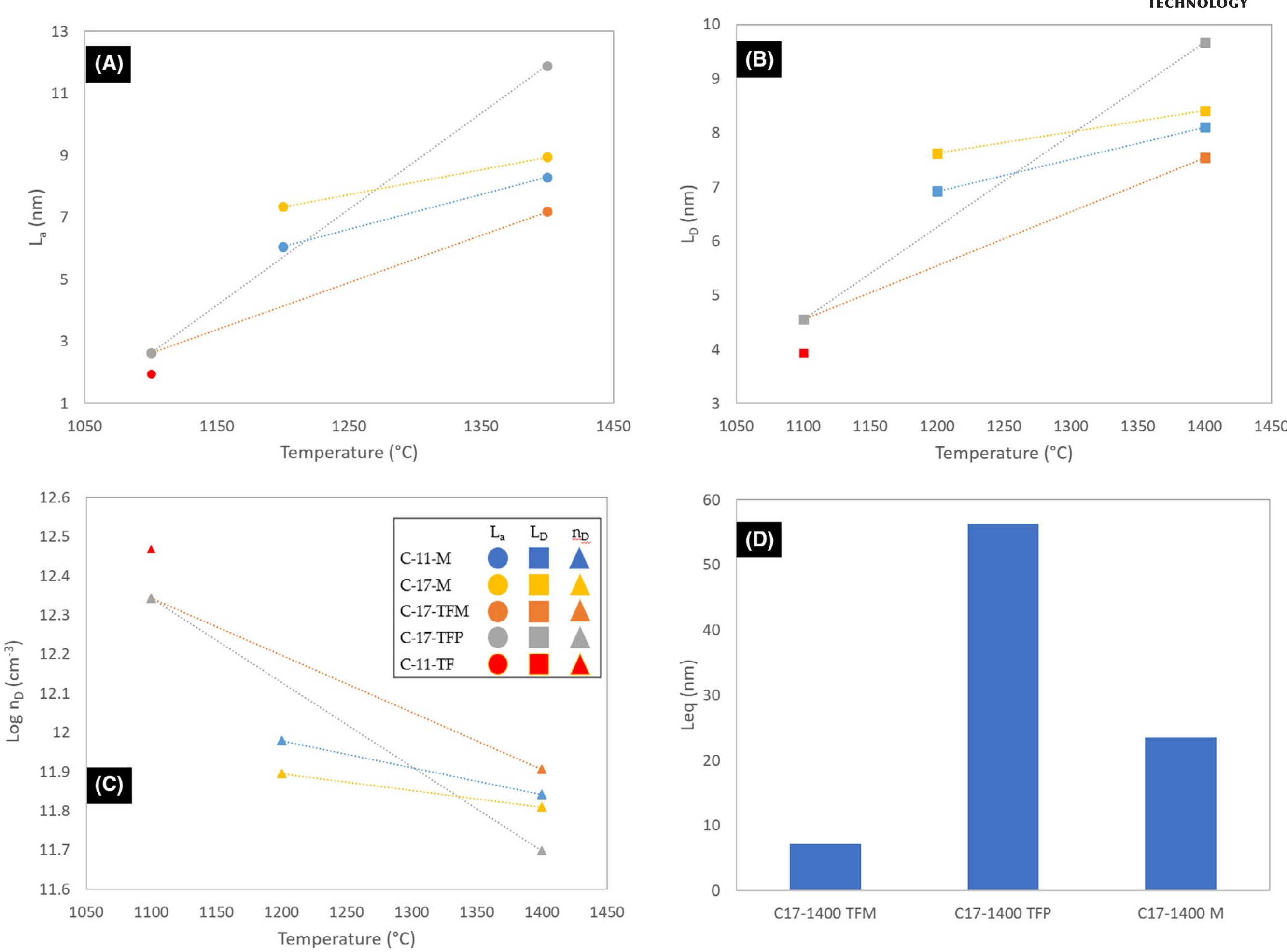

FIGURE 7 Calculated (A) lateral crystal size (L_a), (B) average defect distance (L_D), (C) defect density (n_D), and (D) tortuosity of sp^2 domains of the thin film samples as compared to the work of Rosenburg on SiOC monoliths. Samples are named after the system (C-[vol%C Content]-[M (monolith), TFM (thin film Matrix, TFP (thin film particle)]

parallel to the C-C directions, respectively. On the other hand, the G band is a result of the first-order scattering of the zone-center E_{2g} optical mode of the sp^2 domains primarily caused by in-plane vibrations of carbon atoms.[42,47,51,52] The 2D band, also known as G' band, at 2675 cm^{-1}, is due to the second-order Raman scattering of the in-plane TO phonons near the Brillouin zone.[52–55]

It can be seen that in total, the main bands of the films are blue shifted as compared to pristine graphite with a known G-band located at 1580 cm^{-1}. Three reasons were classified to explain the observed shift of the D and G band peaks of the samples; (1) thermal shift due to the effect of annealing temperature which, however, causes a redshift, (2) due to the increase in sp^3 C amount which results in a blue shift, and (3) due to the effect of the substrate.[8,39,47,51,56–62] For all the thin film samples, it can be seen that the G peak is overlapping with the literature-known position of the D' peak, a double resonance process similar to the D band but occurs at the LO phonon.[55,63,64] The superposition of the G and D' peaks is commonly observed for defective graphenes with a D' shifting to 1580 cm^{-1} for higher defect density.[64] Given the overlap between the two peaks, differentiation between the D' from the G peak can better be done by looking at the presence of the second-order 2D' peak at 3200 cm^{-1} which is also detected here. In the succeeding calculations, the peak at 1610 cm^{-1} is assigned to the G band influenced by the D' band with a high defect contribution. The work of Rosenburg et al demonstrates the temperature dependence of the G-peak position for SiOC samples.[8] Accordingly, the thermal shift is accounted for by the anharmonicity of the in-plane angular modes that are activated as the movement of the atoms directly relates to the increase in temperature. This effect is more pronounced on the optical branches of graphene on its transverse and longitudinal atomic motions.[56,57] As the measurement is conducted at room temperature only, the effect of thermal shifts for SiOC films is hard to notice as compared to the effect of the sp^3 C fraction. This effect has been demonstrated in the work of Merkulov *et al* for samples with 6–75 at.% sp^3 C.[65] Due to the resonant character of the D and G peaks, excitation at the visible range causes the blue shift

which saturates at 1600 cm^{-1}. Lastly, it has been reported that Si/SiO_2 substrate generally causes the shift of the G band up to 12 cm^{-1} which can be attributed to the effect of unintentional doping of the film caused by the charge impurities present on the substrate.[60–62]

The ratio of the intensities of the D and G bands (I_D/I_G) of our thin SiOC films shows a decreasing trend as the C-content and process temperature increase. This observation is analogous to the trend measured for monolithic samples. The lateral crystal sizes are calculated using the Cançado correlation[66] in Equation (5) while Equations (6), (7), and (8) were used to calculate the inter-defect distances, the defect density, and the tortuosity, respectively, for the free carbon phase.[28,49,51,67,68] All values are presented in Table 2. The area under each peak is considered for all calculations taking into account all the uncertainties of the process.[67] As can be seen in Table 2, for the thin film samples, it is evident that the degree of graphitization is improved as the carbon content and temperature increase. In addition, the dispersed particles display a higher degree of graphitization than that of the matrix of the thin film with A_D/A_G equal to 1.4.

$$L_a = \left(2.4\times10^{-10}\right)\lambda^4\left(\frac{A_D}{A_G}\right)^{-1}, \tag{5}$$

$$L_D^2 = 1.8\times10^{-9}\lambda_L^4\frac{A_G}{A_D}, \tag{6}$$

$$n_D = \frac{2.4\times10^{22}}{\lambda_L^4}\frac{A_D}{A_G}, \tag{7}$$

$$L_{eq} = 77.0648\frac{A_{2D}}{A_D}. \tag{8}$$

As shown in Figure 7, the general trend corresponds to an increase in the lateral crystal size L_a and the inter-defect distance L_D as the heat treatment temperature increases. This trend holds for both thin film and monolithic samples. Conversely, the defect density behaved inversely proportional to the heat treatment temperature with the C17-1400 thin film sample showing a high degree of steepness on its slope. Until now, there is no direct correlation found on how the defect density responds to the decreasing thickness of a material.[69–71] In comparison with the previous work of Rosenburg on the SiOC monolithic sample,[8] the calculated L_a and L_D of the SiOC film were of similar magnitude; the dispersed particles giving the largest L_a and L_D values. The L_D calculation followed the assumption that point defects are present on the phases and that the radius around the defect (r_A) where D band scattering takes place is equal to 3.1 nm.[67] Comparing the calculated L_D in this work with that of Cançado in 2011, our thin film samples obtained at 1100°C show that $L_D < r_A$, which is categorized as a highly defective region. Also in agreement with the work of Rosenburg, as the heat treatment temperature is increased, the defect density decreases (Figure 7C), and L_a and L_D increase.[10] Looking at the calculated L_{eq} of the C17-1400 samples (Figure 7D), the value calculated for the C-rich dispersed particles of the thin film is double in size as compared to that of the monolithic SiOC; while the L_{eq} of the matrix of the thin film is less than half of the value calculated for the SiOC monolith. This finding clearly indicates that the C-rich and O-depleted precipitates in the prepared SiOC-based thin films possess a significantly higher degree of graphitization than that of the matrix.

Additionally, the I_{2D}/I_G ratio of the C17-1400 sample was calculated to gain an idea of the number of graphene layers present in sample.[54,72,73] In the work of Bleu et al, a summary of I_{2D}/I_G ratio values was presented, in order to correlate the number of graphene layers in carbon-based samples.[72] The value obtained in this study which is equal to 0.144 fell under the multilayered graphene with at least 5–10 layers. In this range of graphene layers, the FWHM of the 2D peak is less reliable as it starts to appear like that of graphite. A method to confirm whether multilayered graphene or graphite exists was proposed by Roscher et al who used the coefficient of determination, namely the R^2-value, to assess the closeness of the value to the fitted regression line.[53] Multilayered graphene generates an R^2-value above the defined threshold value of 0.985 after using the Voigt profile fitting against the spectra. An R^2-value of 0.99194 is obtained for the Voigt-fitted C17-1400. This result combined with an I_{2D}/I_G ratio value of 0.144 indicates that the sp^2-hybridized carbon phase in sample C17-1400 can be described as multilayered graphene.

3.3 | Electrical conductivity of the thin film

With regard to integrating the SiOC thin film into MEMS application for further studies, it is important to investigate the electrical property of the thin SiOC films. A common way of characterizing the electrical property of a conducting or semiconducting thin film is by measuring the sheet resistance or the surface resistivity which is the lateral resistance measured across the opposite sides of a square sample.[74] In relation to other resistance measurements, the sheet resistance is independent of the size of the square allowing an easier judgment between different samples. Commonly, the four-point probe technique is preferred to measure the surface resistance as it eliminates the effect of the contact resistance and wire resistance.[75,76] In this method, the applied current comes in and out of the sample through the outer probes. The high electrical impedance of the voltmeter prevents the current from entering the inner probes, between which the voltage drop is measured. The sheet resistance measured for C11-1100 and

C17-1100 samples ranges from 765–940 kΩ/sq and 640–860 kΩ/sq, respectively. On the other hand, the sheet resistance of the C17-1400 ranges from 3.4 to 4.19 kΩ/sq.

In general, there are no explicit limits for the resistance values needed for the implementation of the material in piezoresistive thin film-based strain sensors. Different sheet resistances can be addressed by geometry changes in the design of MEMS devices. Anyway, high values (>100 kΩ/sq) result in small piezoresistors that are difficult to match to the deformation element and are strongly affected by manufacturing tolerances, reducing the overall sensitivity.[77] Furthermore, high base resistances are energy efficient but lead to noise and limit the range of measurement. In contrast, metal-like resistance values (<<1 kΩ/sq) typically require meander-like geometries to achieve sufficient base resistances. This is because low base resistances introduce large amounts of thermal energy and are therefore susceptible to thermal noise.[78] However, spatial expansion can also lead to stress average effects if it is not matched to the deforming body.[79] In addition, evaluation electronics for resistive elements in the mid-range of 0.1−5 kΩ are easier to design and available. For this reason, a resistance target range of 2−10 kΩ/sq was used in this study to perform electrical property screening of the samples. Thus, the samples prepared at 1100°C (i.e., C11-1100 and C17-1100) are considered to be not suitable for device implementation; however, C17-1400 exhibits appropriate resistance and thus high potential to be used/implemented in MEMS strain sensors.

To further characterize the electrical property and the surface quality of the sample, the topography of the film was analyzed using tunneling AFM (TUNA) and is presented in Figure 8. The roughness of the dispersed particle area (see Figure 8B), was measured to be c. 300 nm with the highest elevation at 510 nm. The average roughness of the matrix (Figure 8A) was significantly lower, that is, c. 80 nm. The roughness difference of the two phases is well-supported by the color contrast shown in Figure 4B. As mentioned above, the average thickness of the film obtained from profilometer measurement was approximately 500 nm. Using these profiles and the sheet resistance measured with the four-point probe, the conductivity of the film was calculated to be in the range of 5.27 to 8.79 S/cm. These values are two to three magnitudes larger than that of the electrical conductivities measured for monolithic samples with a similar chemical composition.[10,80–82]

Another advantage of the tunneling AFM is the simultaneous mapping of the mechanical and electrical property of sample.[83] TUNA is known to have higher current sensitivity than that of the conductive AFM mode which can measure currents down to sub-picoampere range through a highly resistive sample. In principle, the measurement depends on the tip geometry to define the lateral resolution. A bias voltage is applied between the conductive tip and the sample while scanning in contact mode generates topographic and current images.[83] With Figure 4, a representative area of $95 \times 60\ \mu m^2$ was used to map out the AFM-based conductivity of the sample C17-1400 and is presented in Figure 9. A range of 0.001–2 nA was detected forming regions within the map. The current map shown in Figure 9A, which corresponds to the matrix of C17-1400, indicates that these regions are of varying sizes, and are spaced from each other by approximately 2 μm. In Figure 9B, which represents the current map of a particle in C17-1400, these regions are denser and more interconnected with each other. Some sites, depicted in dark blue color, show current values above 200 nA with the highest value recorded at 454 nA.

By comparing the electrical conductivity of C17-1100 and C17-1400, it can be concluded that the in-situ generation

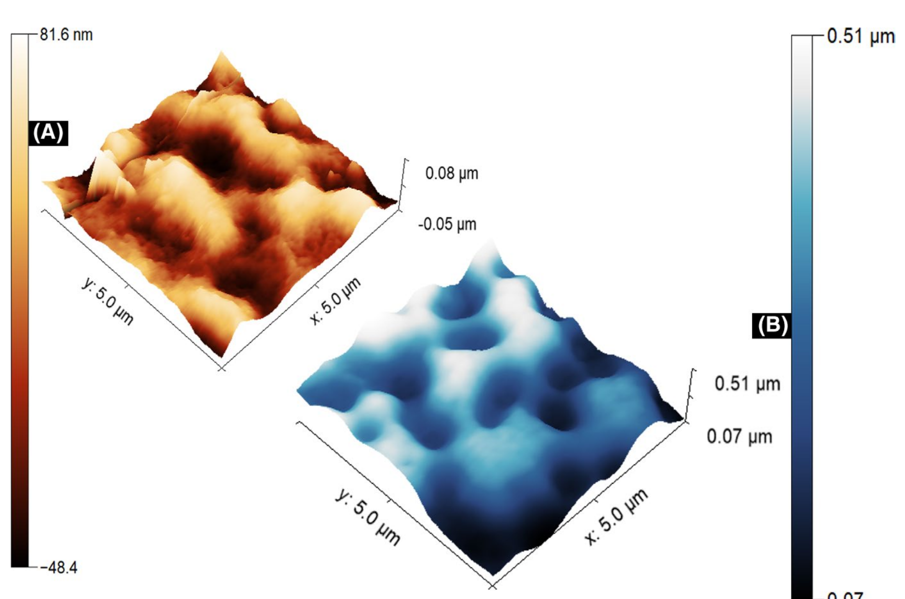

FIGURE 8 AFM Z Sensor map of C17-1400 sample. (A) The topography of the O-rich SiOC matrix with 80 nm roughness. (B) The topography of the C-rich SiOC phase with approximately 500 nm roughness. Images were taken with a 5 μm scan at a DC sample bias of 1 V

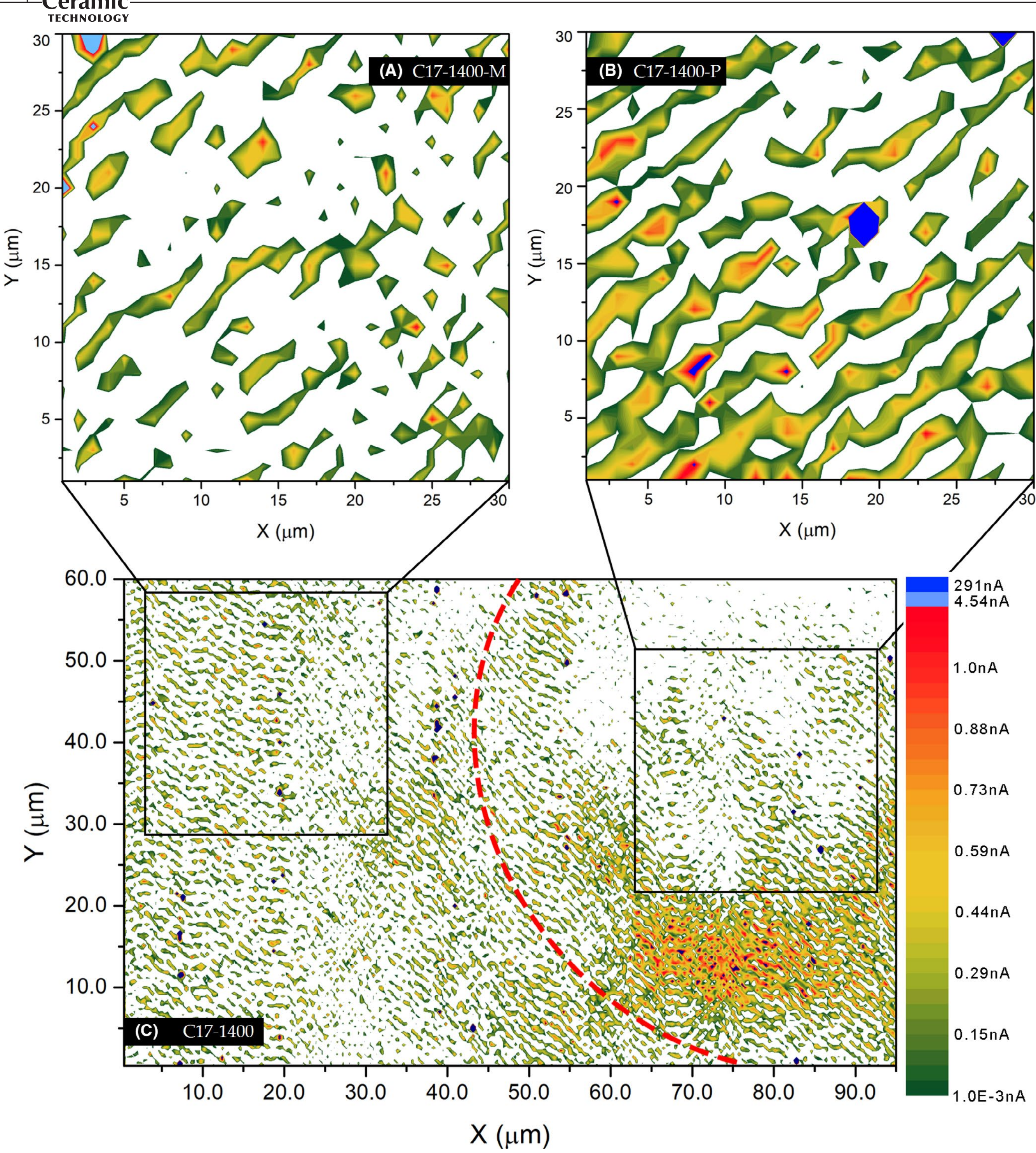

FIGURE 9 TUNA current map of the C17-1400 sample including both the matrix and a dispersed particle is shown in Image C. The red dotted line signifies the boundary of the particle from the matrix. (A) Elongated regions with current values of 0.01–2 nA were observed on the C17-1400 matrix with ~2 μm spacing between each other. (B) Elongated regions observed within the dispersed particles are denser and more interconnected as compared to those observed within the matrix. In dark blue are specific areas on the particle with current values above 100 nA with the highest recorded at 454 nA. The current map was recorded with a 5 μm scan at a DC sample bias of 1 V

of C-rich particles helps to boost the electrical conductivity of the prepared SiOC-based thin film samples (i.e., compare C17-1100 with C17-1400). This may be explained as follows: First, the C-rich particles in C17-1400 were shown to possess a higher graphitization degree of the sp^2 carbon as compared to the carbon present in the matrix of C17-1400. Consequently, the particles possess higher electrical conductivity as compared to the matrix, as supported by the TUNA

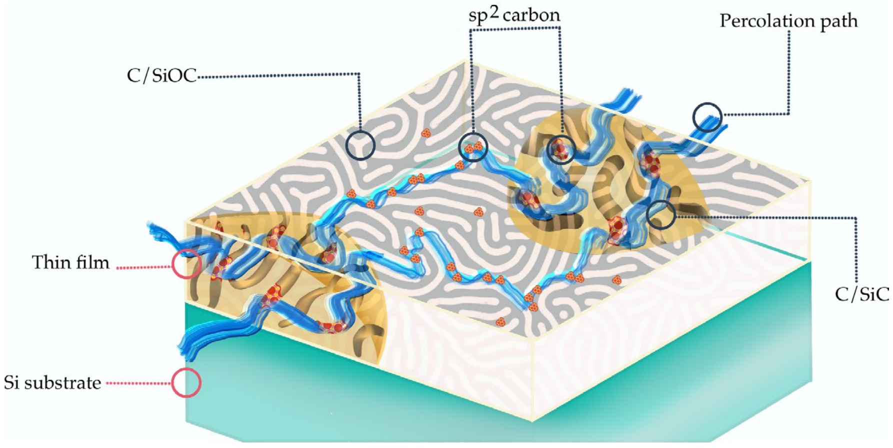

FIGURE 10 The proposed hierarchical microstructure of the prepared SiOC thin film. The yellow regions represent the large particles containing highly graphitized carbon (represented by the red hexagonal structures). The matrix also contains sp^2-hybridized carbon (small hexagonal structures) and contributes to the charge carrier transport between the large particles. The blue lines represent percolation paths throughout the sample

measurements. Even though the electrical conductivity of the particles in C17-1400 is enhanced, this is not sufficient to explain the overall increase in the electrical conductivity of C17-1400 as related to C17-1100. The volume fraction of the particles in C17-1400 was estimated to be c. 16 vol%, which is significantly lower than the percolation threshold in systems consisting of spherical conductive particles dispersed in an insulating matrix (i.e., >25 vol%[84]). This agrees with the distance between the carbon-rich particles in C17-1400, which has been estimated to be c. 2 μm. Consequently, the matrix is considered to also contribute to the electrical conductivity of C17-1400, as revealed by the TUNA measurements (Figure 9A). Thus, the electrical conduction occurs in C17-1400 through both the matrix and the dispersed particles. C17-1400 possesses a hierarchical microstructure which provides appropriate charge carrier transport: first, the carbon-enriched micro-sized particles are generated throughout the thin film upon exposure to 1400°C and exhibit enhanced electrical conductivity due to the relatively high graphitization degree of their sp^2-hybridized carbon; second, sp^2-hybridized carbon is present in the oxygen-rich matrix of C17-1400 and is responsible for the charge carrier transport between the large C-rich particles. Thus, the phase separation of sp^2-carbon, which typically occurs in polymer-derived ceramics at the nanometer scale, corroborates with the precipitation of large C-rich particles at the micro-scale and thus sustains charge carrier transport paths throughout the sample. Interestingly, the formation of the large carbon-enriched particles occurred to an extent that was sufficient to provide a large fraction of highly conductive particles in the SiOC based thin films while keeping an adequate amount of sp^2-hybridized carbon back in the matrix to sustain charge carrier transport between the large particles.

The observed microstructure in the SiOC-based thin film samples is unique and has not been observed in monolithic silicon oxycarbides. Monolithic SiOC samples were shown to provide charge carrier transport through the formation of a percolative network of sp^2-hybridized carbon via segregation at nanoscale.[85] Whereas in SiOC-based thin films, the electrical conductivity is boosted by the additional in-situ formation of large particles possessing highly graphitized carbon (see Figure 10). However, the reason for the formation of the large carbon-rich particles has not been elucidated.

4 | CONCLUSIONS

In summary, a spin coating process was designed and optimized using the Taguchi method. The initial spin speed was identified as the main factor contributing to the uniformity and homogeneity of the preceramic thin films. It was shown that the quality of the resulting ceramic thin films strongly correlates with the molecular architecture of the preceramic polymers as well as to the thermomechanical properties of the resulting SiOC composition. Thus, while a SiOC composition with a fair amount of carbon was shown to be exposed to tensile thermal stress which contributed to extensive cracking and spallation, improving the carbon content induced compressive thermal stress in the film and thus cracking and spallation were suppressed.

The prepared crack-free SiOC thin films were shown to possess a unique hierarchical microstructure consisting of large oxygen-depleted particles, mainly consisting of highly graphitized carbon and SiC, homogeneously dispersed in an oxygen-containing amorphous matrix. The matrix was shown to also contain sp^2-hybridized carbon and to contribute to charge carrier transport between the highly conductive large particles. The hierarchical microstructure of the prepared thin films has been shown to provide improved electrical conductivity as compared to

monolithic SiOC possessing the same chemical composition. Thus, the SiOC thin film prepared at 1400°C exhibits a sheet resistance of c. 2 −10 kΩ/sq and is thus considered suitable for implementation and use in miniaturized strain gauges.

CONFLICT OF INTEREST

The authors declare no conflict of interest.

AUTHOR CONTRIBUTIONS

E.R. III. and E.I. were involved in conceptualization. E.R. III and F.K. were involved in methodology, software, formal analysis, investigation, resources, data curation, and writing—original draft preparation. E.I., R.R., and H.F.S. were involved in writing—review and editing funding acquisition. E.R. III. was involved in visualization. E.I. was involved in supervision. E.R.III, F.K., and E.I. were involved in project administration. All authors have read and agreed to the published version of the manuscript.

ORCID

Emmanuel III Ricohermoso https://orcid.org/0000-0002-4093-4751
Ralf Riedel https://orcid.org/0000-0001-6888-7208
Emanuel Ionescu https://orcid.org/0000-0002-3266-3031

REFERENCES

1. Colombo P, Mera G, Riedel R, Sorarù GD. Polymer-derived ceramics: 40 years of research and innovation in advanced ceramics. J Am Ceram Soc. 2010;93(7):1805–37.
2. Riedel R, Mera G, Hauser R, Klonczynski A. Silicon-based polymer-derived ceramics: synthesis properties and applications-a review: dedicated to Prof. Dr. Fritz Aldinger on the occasion of his 65th birthday. J Ceram Soc Jpn. 2006;114(1330):425–44.
3. Ionescu E, Kleebe H-J, Riedel R. Silicon-containing polymer-derived ceramic nanocomposites (PDC-NCs): preparative approaches and properties. Chem Soc Rev. 2012;41(15):5032–52.
4. Monthioux M, Delverdier O. Thermal behavior of (organosilicon) polymer-derived ceramics. V: Main facts and trends. J Eur Ceram Soc. 1996;16(7):721–37.
5. Mera G, Navrotsky A, Sen S, Kleebe H-J, Riedel R. Polymer-derived SiCN and SiOC ceramics – structure and energetics at the nanoscale. J Mater Chem A. 2013;1(12):3826–36.
6. Bois L, Maquet J, Babonneau F, Mutin H, Bahloul D. Structural characterization of sol-gel derived oxycarbide glasses. 1. Study of the pyrolysis process. Chem Mater. 1994;6(6):796–802.
7. Schuepfer DB, Badaczewski F, Guerra-Castro JM, Hofmann DM, Heiliger C, Smarsly B, et al. Assessing the structural properties of graphitic and non-graphitic carbons by Raman spectroscopy. Carbon. 2020;1(161):359–72.
8. Rosenburg F, Ionescu E, Nicoloso N, Riedel R. High-temperature raman spectroscopy of nano-crystalline carbon in silicon oxycarbide. Materials. 2018;11(1):93.
9. Lu K, Erb D, Liu M. Thermal stability and electrical conductivity of carbon-enriched silicon oxycarbide. J Mater Chem C. 2016;4(9):1829–37.
10. Rosenburg F, Balke B, Nicoloso N, Riedel R, Ionescu E. Effect of the content and ordering of the sp2 free carbon phase on the charge carrier transport in polymer-derived silicon oxycarbides. Molecules. 2020;25(24):5919.
11. Li J, Ma PC, Chow WS, To CK, Tang BZ, Kim J-K. Correlations between percolation threshold, dispersion state, and aspect ratio of carbon nanotubes. Adv Funct Mater. 2007;17(16):3207–15.
12. Montgomery D. Design and analysis of experiments. 8th ed. Hoboken, NJ: John Wiley & Sons, Inc; 2013. 757 p.
13. Dean A, Voss D, Draguljić D. Springer Texts in Statistics: Design and Analysis of Experiments. 2nd ed., Vol. XXV. Cham: Springer International Publishing AG; 2017. p. 840.
14. Roy RK. A Primer on the Taguchi Method [Internet]. Dearborn, MI: Society of Manufacturing Engineers; 2010. [cited 2021 Jan 20]. Available from: http://search.ebscohost.com/login.aspx?direct=true&scope=site&db=nlebk&db=nlabk&AN=860349
15. Barroso G, Li Q, Bordia RK, Motz G. Polymeric and ceramic silicon-based coatings – a review. J Mater Chem A. 2019;7(5):1936–63.
16. Günthner M, Kraus T, Krenkel W, Motz G, Dierdorf A, Decker D. Particle-filled PHPS silazane-based coatings on steel. Int J Appl Ceram Technol. 2009;6(3):373–80.
17. Kraus T, Günthner M, Krenkel W, Motz G. cBN particle filled SiCN precursor coatings. Adv Appl Ceram. 2009;108(8):476–82.
18. Mandoj F, Nardis S, Di Natale C, Paolesse R. Porphyrinoid thin films for chemical sensing. In: Wandelt K, editor. Encyclopedia of Interfacial Chemistry [Internet]. Oxford: Elsevier; 2018 [cited 2020 Dec 28]. p. 422–43. Available from: http://www.sciencedirect.com/science/article/pii/B9780124095472116774
19. Makhlouf ASH. 1 - Current and advanced coating technologies for industrial applications. In: Makhlouf ASH, Tiginyanu I, editors. Nanocoatings and Ultra-Thin Films [Internet]. Woodhead Publishing; 2011 [cited 2020 Dec 28]. p. 3–23. (Woodhead Publishing Series in Metals and Surface Engineering). Available from: http://www.sciencedirect.com/science/article/pii/B9781845698126500014
20. Mukerjee R, Wu CFJ, editors. Robust parameter design. In: A Modern Theory of Factorial Designs [Internet]. New York, NY: Springer; 2006 [cited 2020 Dec 28]. p. 197–210. (Springer Series in Statistics). Available from: https://doi.org/10.1007/0-387-37344-6_9
21. Kozuka H. On ceramic thin film formation from gels: evolution of stress, cracks and radiative striations. J Ceram Soc Jpn. 2003;111(1297):624–32.
22. Kozuka H. Stress evolution on gel-to-ceramic thin film conversion. J Sol-Gel Sci Technol. 2006;40(2):287–97.
23. Kozuka H, Takenaka S, Tokita H, Hirano T, Higashi Y, Hamatani T. Stress and cracks in gel-derived ceramic coatings and thick film formation. J Sol-Gel Sci Technol. 2003;26(1):681–6.
24. Ionescu E, Linck C, Fasel C, Müller M, Kleebe H-J, Riedel R. Polymer-derived SiOC/ZrO_2 ceramic nanocomposites with excellent high-temperature stability. J Am Ceram Soc. 2010;93(1):241–50.
25. Kaspar J, Terzioglu C, Ionescu E, Graczyk-Zajac M, Hapis S, Kleebe H-J, et al. Stable SiOC/Sn nanocomposite anodes for lithium-ion batteries with outstanding cycling stability. Adv Funct Mater. 2014;24(26):4097–104.
26. Martínez-Crespiera S, Ionescu E, Schlosser M, Flittner K, Mistura G, Riedel R, et al. Fabrication of silicon oxycarbide-based microcomponents via photolithographic and soft lithography approaches. Sens Actuators Phys. 169(1):242–9.

27. Hu YY, Huang WM. Thermal stress analysis and characterization of thermomechanical properties of thin films on an elastic substrate. In: Nee A, editor. Handbook of Manufacturing Engineering and Technology [Internet]. London: Springer; 2013 [cited 2020 Dec 29]. p. 1–71. Available from: https://doi.org/10.1007/978-1-4471-4976-7_51-1
28. Stabler C, Reitz A, Stein P, Albert B, Riedel R, Ionescu E. Thermal properties of SiOC glasses and glass ceramics at elevated temperatures. Mater Basel Switz. 2018;11(2):279.
29. Rouxel T, Massouras G, Sorarù G-D. High temperature behavior of a gel-derived SiOC glass: elasticity and viscosity. J Sol-Gel Sci Technol. 1999;14(1):87–94.
30. Barber JR, editor. Plane strain and plane stress. In: Elasticity [Internet]. Dordrecht, Netherlands: Springer; 2004 [cited 2021 Jan 20]. p. 33–40. (Solid Mechanics and Its Applications). Available from: https://doi.org/10.1007/0-306-48395-5_3
31. Stoney GG, Parsons CA. The tension of metallic films deposited by electrolysis. Proc R Soc Lond Ser Contain Pap Math Phys Character. 1909;82(553):172–5.
32. Piombini H, Compoint F, Ambard C, Picart D, Belleville P, Damamme G, et al. Stress measurement of elastic sol-gel layer by photoelasticimetry - comparison with stoney. Opt Mater Express. 2016;6(2):469–85.
33. Lu K. Porous and high surface area silicon oxycarbide-based materials—a review. Mater Sci Eng R Rep. 2015;1(97):23–49.
34. Wang L, Lu K. Phase development of silicon oxycarbide nanocomposites during flash pyrolysis. J Mater Sci. 2019;54(8):6073–87.
35. Griffith WP. Raman, studies on rock-forming minerals. Part I. Orthosilicates and cyclosilicates. J Chem Soc Inorg Phys Theor. 1969;1372–7.
36. Juroszek R, Czaja M, Lisiecki R, Krüger B, Hachuła B, Galuskina I. Spectroscopic and structural investigations of blue afwillite from Ma'ale Adummim locality, Palestinian Autonomy. Spectrochim Acta A Mol Biomol Spectrosc. 2020;15(227):117688.
37. Frost RL, Čejka J, Weier ML, Martens W. Molecular structure of the uranyl silicates—a Raman spectroscopic study. J Raman Spectrosc. 2006;37(4):538–51.
38. Handke M, Urban M. IR and raman spectra of alkaline earth metals orthosilicates. J Mol Struct. 1982;1(79):353–6.
39. Chen ZY, Zhao JP, Yano T, Ooie T, Yoneda M, Sakakibara J. Observation of sp3 bonding in tetrahedral amorphous carbon using visible Raman spectroscopy. J Appl Phys. 2000;88(5):2305–8.
40. Mafra DL, Samsonidze G, Malard LM, Elias DC, Brant JC, Plentz F, et al. Determination of LA and TO phonon dispersion relations of graphene near the Dirac point by double resonance Raman scattering. Phys Rev B. 2007;76(23):233407.
41. Hodkiewicz J, Scientific TF. Characterizing carbon materials with Raman spectroscopy. 5.
42. Robertson J. Properties of diamond-like carbon. Surf Coat Technol. 1992;50(3):185–203.
43. Schwan J, Ulrich S, Batori V, Ehrhardt H, Silva SRP. Raman spectroscopy on amorphous carbon films. J Appl Phys. 1996;80(1):440–7.
44. Nemanich RJ, Glass JT, Lucovsky G, Shroder RE. Raman scattering characterization of carbon bonding in diamond and diamondlike thin films. J Vac Sci Technol A. 1988;6(3):1783–7.
45. Shroder RE, Nemanich RJ, Glass JT. Analysis of the composite structures in diamond thin films by Raman spectroscopy. Phys Rev B. 1990;41(6):3738–45.
46. Wang CZ, Ho KM. Structure, dynamics, and electronic properties of diamondlike amorphous carbon. Phys Rev Lett. 1993;71(8):1184–7.
47. Chu PK, Li L. Characterization of amorphous and nanocrystalline carbon films. Mater Chem Phys. 2006;96(2–3):253–77.
48. Roth F, Waleska P, Hess C, Ionescu E, Nicoloso N. UV Raman spectroscopy of segregated carbon in silicon oxycarbides. J Ceram Soc Jpn. 2016;124(10):1042–5.
49. Wen Q, Yu Z, Riedel R. The fate and role of in situ formed carbon in polymer-derived ceramics. Prog Mater Sci. 2020;109:100623.
50. Hodkiewicz J, Scientific TF. Characterizing carbon materials with Raman spectroscopy. 5.
51. Saini P, Sharma R, Chadha N. Determination of defect density, crystallite size and number of graphene layers in graphene analogues using X-ray diffraction and Raman spectroscopy. Indian J Pure Appl Phys IJPAP. 2017;55(9):625–9.
52. Ferrari AC, Meyer JC, Scardaci V, Casiraghi C, Lazzeri M, Mauri F, et al. Raman spectrum of graphene and graphene layers. Phys Rev Lett. 2006;97(18):187401.
53. Roscher S, Hoffmann R, Ambacher O. Determination of the graphene–graphite ratio of graphene powder by Raman 2D band symmetry analysis. Anal Methods. 2019;11(9):1224–8.
54. Ferrari AC. Raman spectroscopy of graphene and graphite: Disorder, electron–phonon coupling, doping and nonadiabatic effects. Solid State Commun. 2007;143(1):47–57.
55. Zólyomi V, Koltai J, Kürti J. Resonance Raman spectroscopy of graphite and graphene. Phys Status Solidi B. 2011;248(11):2435–44.
56. Lindsay L, Broido DA. Optimized Tersoff and Brenner empirical potential parameters for lattice dynamics and phonon thermal transport in carbon nanotubes and graphene. Phys Rev B. 2010;81(20):205441.
57. Koukaras EN, Kalosakas G, Galiotis C, Papagelis K. Phonon properties of graphene derived from molecular dynamics simulations. Sci Rep. 2015;5(1):12923.
58. Roth F, Schmerbauch C, Ionescu E, Nicoloso N, Guillon O, Riedel R. High-temperature piezoresistive C/SiOC sensors. J Sens Sens Syst. 2015;4(1):133–6.
59. Bokobza L, Bruneel J-L, Couzi M. Raman spectra of carbon-based materials (from graphite to carbon black) and of some silicone composites. C. 2015;1(1):77–94.
60. Das A, Chakraborty B, Sood AK. Raman spectroscopy of graphene on different substrates and influence of defects. Bull Mater Sci. 2008;31(3):579–84.
61. Calizo I, Ghosh S, Bao W, Miao F, Ning Lau C, Balandin AA. Raman nanometrology of graphene: temperature and substrate effects. Solid State Commun. 2009;149(27):1132–5.
62. Calizo I, Bao W, Miao F, Lau CN, Balandin AA. The effect of substrates on the Raman spectrum of graphene: Graphene- on-sapphire and graphene-on-glass. Appl Phys Lett. 2007;91(20):201904.
63. Kaniyoor A, Ramaprabhu S. A Raman spectroscopic investigation of graphite oxide derived graphene. AIP Adv. 2012; 2(3):032183.
64. King AAK, Davies BR, Noorbehesht N, Newman P, Church TL, Harris AT, et al. A new Raman metric for the characterisation of graphene oxide and its derivatives. Sci Rep. 2016;6(1):19491.
65. Merkulov VI, Lannin JS, Munro CH, Asher SA, Veerasamy VS, Milne WI. UV studies of tetrahedral bonding in diamondlike amorphous carbon. Phys Rev Lett. 1997;78(25):4869–72.
66. Cançado LG, Takai K, Enoki T, Endo M, Kim YA, Mizusaki H, et al. General equation for the determination of the crystallite

size La of nanographite by Raman spectroscopy. Appl Phys Lett. 2006;88(16):163106.
67. Cançado LG, Jorio A, Ferreira EHM, Stavale F, Achete CA, Capaz RB, et al. Quantifying defects in graphene via Raman spectroscopy at different excitation energies. Nano Lett. 2011;11(8):3190–6.
68. Larouche N, Stansfield BL. Classifying nanostructured carbons using graphitic indices derived from Raman spectra. Carbon. 2010;48(3):620–9.
69. Wang Y, Liu H, Shen W. A convenient and effective method to deposit low-defect-density nc-Si:H thin film by PECVD. Nanoscale Res Lett. 2018;13(1):234.
70. La Via F, Severino A, Anzalone R, Bongiorno C, Litrico G, Mauceri M, et al. From thin film to bulk 3C-SiC growth: understanding the mechanism of defects reduction. Mater Sci Semicond Process. 2018;1(78):57–68.
71. Takami A, Arimoto S, Naomoto H, Hamamoto S, Ishihara T, Kumabe H, et al. Thickness dependence of defect density in thin film silicon formed on insulator polycrystalline by zone-melting recrystallization [solar cells]. In: Proceedings of 1994 IEEE 1st World Conference on Photovoltaic Energy Conversion - WCPEC (A Joint Conference of PVSC, PVSEC and PSEC). Vol. 2. 1994. p. 1394–7. Available from: https://doi.org/10.1109/WCPEC.1994.520208
72. Bleu Y, Bourquard F, Loir A-S, Barnier V, Garrelie F, Donnet C. Raman study of the substrate influence on graphene synthesis using a solid carbon source via rapid thermal annealing. J Raman Spectrosc. 2019;50:1630–41.
73. Gayathri S, Jayabal P, Kottaisamy M, Ramakrishnan V. Synthesis of few layer graphene by direct exfoliation of graphite and a Raman spectroscopic study. AIP Adv. 2014;4(2):027116.
74. Ghorbani MM, Taherian R. 12 - Methods of Measuring Electrical Properties of Material**Hereby from Keithley Co. and Dr. Michael B. Heaney is appreciated due to valuable content used in this chapter. In: Taherian R, Kausar A, editors. Electrical Conductivity in Polymer-Based Composites [Internet]. William Andrew Publishing; 2019 [cited 2021 Jan 26]. p. 365–94. (Plastics Design Library). Available from: http://www.sciencedirect.com/science/article/pii/B9780128125410000124
75. Chung DDL. A critical review of piezoresistivity and its application in electrical-resistance-based strain sensing. J Mater Sci. 2020;55(32):15367–96.
76. Smits FM. Measurement of sheet resistivities with the four-point probe. Bell Syst Tech J. 1958;37(3):711–8.
77. Kumar SS, Pant BD. Design principles and considerations for the 'ideal' silicon piezoresistive pressure sensor: a focused review. Microsyst Technol. 2014;20(7):1213–47.
78. Lotichius J. Modellbildung der Messunsicherheit resistiver Sensorsysteme [Internet] [Ph.D. Thesis]. [Darmstadt]: Technische Universität Darmstadt. 2017. Available from: http://tuprints.ulb.tu-darmstadt.de/6845
79. Clark SK, Wise KD. Pressure sensitivity in anisotropically etched thin-diaphragm pressure sensors. IEEE Trans Electron Devices. 1979;26(12):1887–96.
80. Cordelair J, Greil P. Electrical conductivity measurements as a microprobe for structure transitions in polysiloxane derived Si–O–C ceramics. J Eur Ceram Soc. 2000;20(12):1947–57.
81. Nguyen VL, Zanella C, Bettotti P, Soraru GD. Electrical conductivity of SiOCN ceramics by the powder-solution-composite technique. J Am Ceram Soc. 2014;97(8):2525–30.
82. Terauds K, Sanchez-Jimenez PE, Raj R, Vakifahmetoglu C, Colombo P. Giant piezoresistivity of polymer-derived ceramics at high temperatures. J Eur Ceram Soc. 2010;30(11):2203–7.
83. Li C, Minne S, Pittenger B, Mednick A. Simultaneous Electrical and Mechanical Property Mapping at the Nanoscale with PeakForce TUNA. Santa Barbara, CA: Bruker Corporation; 2011. p. 12 (Application Note 132).
84. Rahaman M, Aldalbahi A, Govindasami P, Khanam N, Bhandari S, Feng P, et al. A new insight in determining the percolation threshold of electrical conductivity for extrinsically conducting polymer composites through different sigmoidal models. Polymers. 2017;9(10):527.
85. Toma L, Kleebe H-J, Müller MM, Janssen E, Riedel R, Melz T, et al. Correlation between intrinsic microstructure and piezoresistivity in a SiOC polymer-derived ceramic. J Am Ceram Soc. 2012;95(3):1056–61.

SUPPORTING INFORMATION

Additional supporting information may be found online in the Supporting Information section.

How to cite this article: Ricohermoso EI, Klug F, Schlaak H, Riedel R, Ionescu E. Electrically conductive silicon oxycarbide thin films prepared from preceramic polymers. *Int J Appl Ceram Technol*. 2021;00:1–16. https://doi.org/10.1111/ijac.13800

Journal of the European Ceramic Society xxx (xxxx) xxx

Contents lists available at ScienceDirect

Journal of the European Ceramic Society

journal homepage: www.elsevier.com/locate/jeurceramsoc

Compressive thermal stress and microstructure-driven charge carrier transport in silicon oxycarbide thin films

Emmanuel Ricohermoso III [a,*], Florian Klug [b], Helmut Schlaak [b], Ralf Riedel [a], Emanuel Ionescu [a]

[a] Fachbereich Material- Und Geowissenschaften, Technische Universität Darmstadt, Otto-Berndt-Str. 3, D-64287, Darmstadt, Germany
[b] Fachbereich Elektrotechnik Und Informationstechnik, Technische Universität Darmstadt, Merckstr. 23, D-64283, Darmstadt, Germany

ARTICLE INFO

Keywords:
Polymer derived ceramics
Conductivity
Hall effect measurement

ABSTRACT

This work correlates the charge carrier transport mechanism of silicon oxycarbide-based thin films with their morphology and thermal stress. Segregation of highly-graphitized carbon-rich, oxygen-depleted C/SiC areas homogeneously dispersed within an oxygen-rich C/SiOC matrix was seen on the 500 nm-SiOC thin films. Compressive biaxial stress induced by the mismatch with the Si-substrate thermal expansion coefficient was calculated at 109 MPa. Through Hall measurements, p-type carriers were shown dominating the SiOC film similar to monolithic samples. Thin films and monoliths have comparable carrier concentrations while the carrier mobility in SiOC thin films was 2 magnitudes higher than that of monolithic samples and is considered a consequence of the compressive thermal stress acting on the film. Improved conductivity of 16 S cm -1 is measured for the SiOC thin film sample which is assumed considering the enhanced carrier mobility alongside the reduced percolation threshold ascribed to the phase-separated morphology of the thin film.

1. Introduction

Motivated by the continuous demand for miniaturization of micro/nanosystems, thin-film technology has been the center of interest of over 20,000 papers published in recent years [1]. Two reports published in 2019 highlighted the increasing market share of thin-film technology over piezoelectric and piezoresistive devices that are expected to have a 12.6 % compound annual growth rate and are projected to reach US$ 48.5 billion in 2024 [2,3]. The deposition process of thin-film is dominated by two technologies namely sol-gel and physical vapor deposition, in which sol-gel bids better intrinsic film properties with good homogeneity. Silicon oxycarbide, a type of polymer-derived ceramic that uses polysiloxane as a polymer precursor synthesized through the sol-gel method has shown good thermal resistance, abrasive resistance, electrical conductivity, piezoresistive behavior, and have been a promising coating material to be used in hostile environments such as high temperatures, moisture, and corrosive atmosphere [4–7].

Silicon oxycarbides typically consist of a glassy network in which Si shares bonds with oxygen and carbon; additionally, an sp^2-hybridized and disordered carbon secondary phase is found in SiOC, with its amount and ordering strongly depending on the molecular structure of the precursor as well as on the pyrolysis conditions. Consequently, the charge transport mechanism of the SiOC sample is strongly influenced by the carbon phase as discussed in a recent review article [8]. Several works reported the dependence of the electrical property of SiOC on high carbon content resulting in an improved electrical conductivity of the material which is attributed to the ease of formation of a percolative network [9–11]. The degree of graphitization of the segregated carbon phase was also identified to enhance the electrical conductivity of SiOC [12–15]. The electronic transport of (nano)graphitic materials is mainly governed by intrinsic and excess carriers as proposed by Mrozowski in 1952 [16]. The intrinsic charge carrier π-electrons are located at the upper π-band and holes at the lower π-band. In these corners of the hexagonal Brillouin zone, the π and π* bands are in contact with each other. As the number of C atoms increases, the valence and conduction bands approach each other and at ca. 50 C atoms, the conduction and valence bands are in contact [17]. When the crystal size reaches ca. 1000 Å, the bandgap vanishes leading to an overlap. Consequently, a great number of electrons can freely move to the conduction band [16].

Hall effect measurement can provide information on material properties such as the Hall voltage (V_H), charge carrier mobility (μ_H), charge density or charge concentration (N), Hall coefficient (R_H), resistivity, magnetoresistance (R), and conductivity type of the material either n- or p-type carriers [18,19]. A thorough search of related literature

* Corresponding author.
E-mail address: iii.ricohermoso@tu-darmstadt.de (E. Ricohermoso).

https://doi.org/10.1016/j.jeurceramsoc.2021.07.001
Received 4 June 2021; Received in revised form 30 June 2021; Accepted 2 July 2021
Available online 6 July 2021
0955-2219/© 2021 Elsevier Ltd. All rights reserved.

specifically targeted the use of Hall measurement to investigate the charge transport mechanism of SiOC samples only yielded two relevant articles to date. In 2016, Kim et al. revealed the presence of p-type carriers on SiOC bulk samples pyrolyzed at 1100 °C and hot-pressed at 1550 °C for 1 h [14]. In conjunction, the carrier densities of the SiOC samples exhibited a direct association with the increasing carbon content of the samples while the carrier mobility behaved contrarily. These findings were supported by the work of Rosenburg et al. in 2020 with the addition that the Hall coefficient of SiOC samples is independent of the carbon content equal to 5×10^{-2} cm^3 C^{-1} similar to the literature value of a glassy carbon [9].

The present work focuses on outlining structural differences between SiOC-based monoliths and thin films, and how these affect their charge carrier transport properties. A comparative discussion is performed based on structural data obtained from Raman spectroscopy, X-ray diffraction (XRD), and scanning electron microscopy (SEM). Furthermore, correlations between structural features and charge carrier transport in SiOC monolith *vs* thin film are highlighted and critically discussed.

2. Materials and methods

In this work, 500-nm SiOC thin film deposited by spin coating on a silicon substrate with a SiO_2 barrier layer is cut into 1×1 cm^2 samples for characterization purposes. The film is previously prepared using commercially available SPR 212 (Starfire Systems, USA) catalyzed with 1 wt% of dicumyl peroxide. The film was crosslinked at 250 °C for 2 h, pyrolyzed at 1100 °C for 2 h, then annealed at 1400 °C for 3 h. The samples were characterized with Raman Spectroscopy (LabRAM Horiba HR Raman Spectroscope HR800, Horiba Jobin Yvon GmbH, Bensheim, Germany), Seifert XRD 3003 PTS-3 (XRD Eigenmann GmbH, Schnaittach-Hormersdorf, Germany), and Scanning Electron Microscopy [SEM] coupled with Energy Dispersive Spectroscopy [EDS] (JEOL JSM 7600 F, JEOL Ltd., Chiyoda, Tokyo, Japan).

The electrical properties of the thin film are assessed using an in-house in-situ Hall effect measurement set-up following the Van der Pauw method as illustrated in Fig. 1 with the B-arrow representing the applied magnetic field on the sample. Van der Pauw's method gives a more reliable resistivity using the four-point probe technique which eliminates the effect of contact resistance [20]. Additionally, it is an advantageous technique for two-dimensional materials of arbitrary shape as long as the sample is much thinner than its width.

3. Results and discussion

Earlier studies have shown that the densification of SiOC bulk materials is regulated by the amount of the segregated carbon and the carbothermal reaction that occurs at temperatures beyond 1400 °C leading to the decomposition of the material [21]. Monolithic samples prepared from the work of Rosenburg used samples with 17 vol% carbon content densified with less than 1% of porosity [22]. The process was further improved with the use of graphite sealing foil to suppress the carbothermal reaction by increasing the partial pressure of CO at the surface of the sample [23]. As a result, dense SiOC monoliths can be produced. The surface morphology of the samples, i.e. monolith and thin films, are presented in Fig. 2.

While the monolithic sample possesses a dense, homogeneous appearance, significant phase separation can be easily recognized in the SiOC-based thin film. In our recently reported work, this microstructure of oxygen-depleted area is mainly composed of sp^2-hybridized carbon and silicon carbide homogenously distributed in an oxygen-containing amorphous matrix [24]. The dispersed particles cover ca. 16 % of the total surface of the film.

In Fig. 3A, the X-ray diffraction pattern of C17−1400 thin-film measured with a 1° grazing incident angle is shown and indicates the presence of β-SiC, based on the (002), (111), and (103) reflections at 2θ values of 36, 38, and 64°. Furthermore, two additional reflections are detected at 2θ values of ca. 44, and 55° and assigned to the presence of turbostratic carbon on the sample. The broad bump at the 2θ value of ca. 22° assigned to SiO_2 has been qualitatively deconvoluted to reveal the shoulder peak at ca. 25.5° which is identified as the amorphous carbon peak. The symmetric deconvolution of the amorphous carbon peak supported by the broadened of the peak demonstrates the graphite-like structure or the turbostratic nature of the carbon phase in the material [25,26]. As per Fig. 3B, only broad peaks of SiO_2 and β-SiC are observed at 2θ values of ca. 22, and 36° respectively.

Attributed to the evident phase separation in the SiOC-based thin film, the dispersed particles are characterized separately from the matrix of the film samples by Raman spectroscopy. Thus, the D and G bands with higher intensity are observed in the particles (Fig. 4C) as compared with those recorded from the matrix (Fig. 4B). Furthermore, substrate-related peaks, i.e. corresponding to Si (Raman shift at 520 cm^{-1}) and SiO_2 (940 cm^{-1} [27–29]) have higher intensity on the matrix as compared to those recorded from the particular segregations. This phenomenon suggests the lower thickness (and roughness) of the matrix in comparison to that of the dispersed particles, as also reported recently [24]. The Raman spectrum of the segregated particles indicates the presence of a band at 801 cm^{-1} which was assigned to SiC. As the D and G bands are present in both components of the film, i.e. matrix and particles, sp^2-hybridized carbon is consequently considered to be present in both disperse particles and matrix. Thus, the matrix containing segregated sp^2-hybridized carbon can be considered as an oxygen-rich C/SiOC component; while the carbon-rich and oxygen-depleted particles consist of C/SiC components.

The Raman spectra of the monolithic SiOC, as well as those recorded from the matrix and disperse particles in the thin-film SiOC sample, were deconvoluted and fitted to attain structural information about the sp^2-hybridized carbon phase. A comparative table containing values for

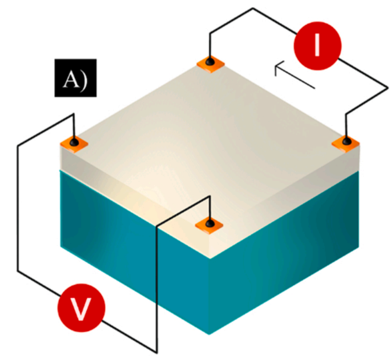

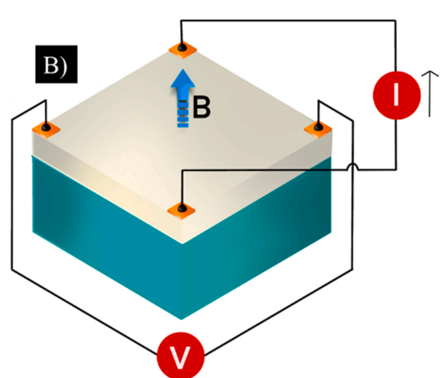

Fig. 1. Van der Pauw measurement set-up for (A) conductivity measurement and (B) Hall Effect study.

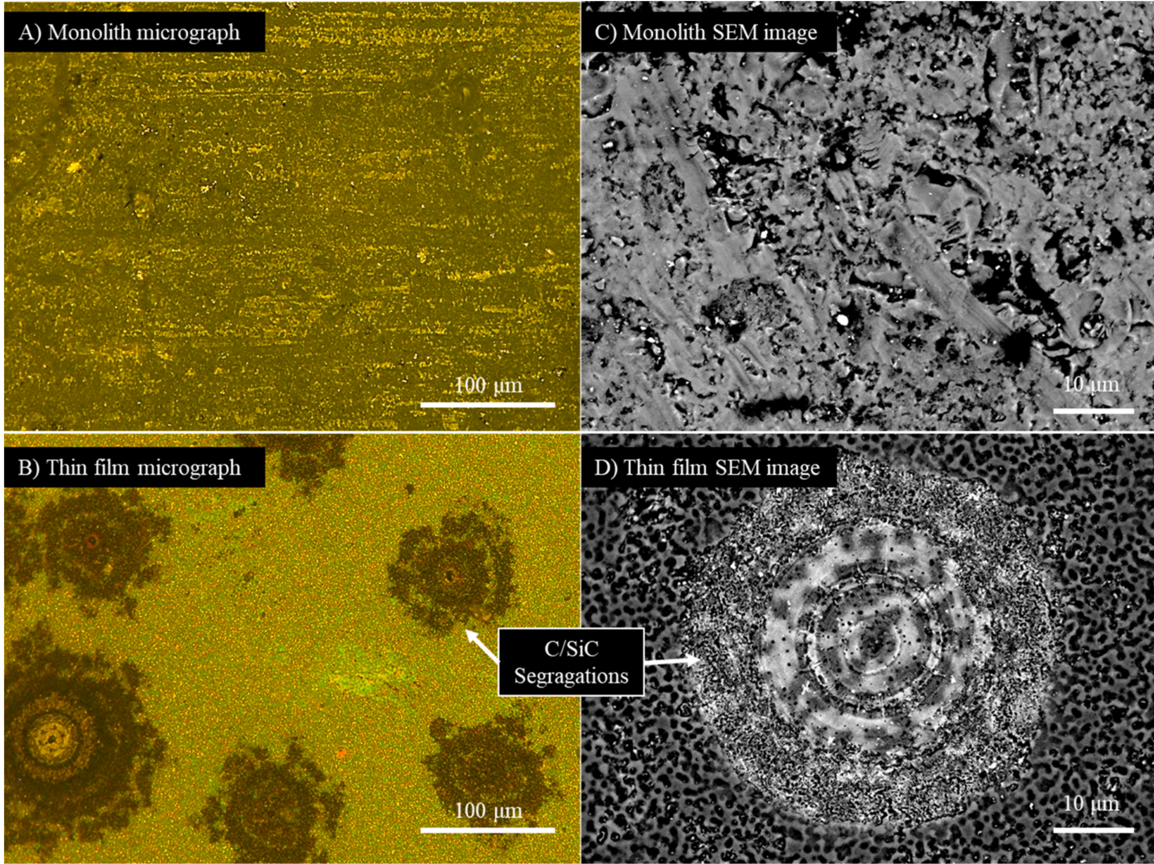

Fig. 2. Optical and electron micrographs of SiOC monolith and thin-film samples. B and D) Thin-film sample exhibited microstructural formation of segregated oxygen-depleted particles containing highly graphitized carbon and SiC homogeneously dispersed on an oxygen-containing amorphous matrix.

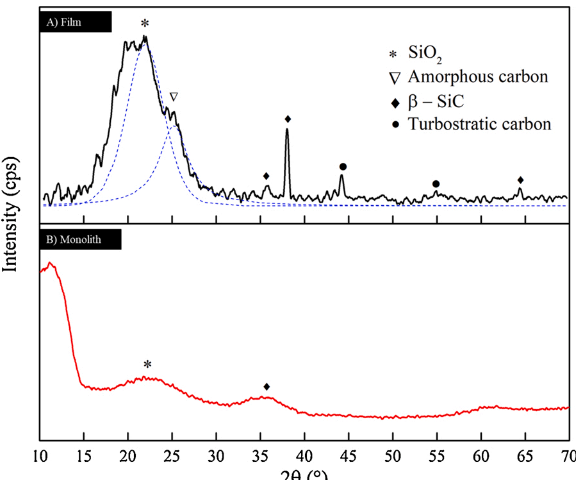

Fig. 3. A) X-ray diffraction patterns of C17-1400 thin film measured with a grazing incident angle of 1° with Cu-Kα as the radiation source. A qualitative deconvolution is made on the broad peak at 22° to discriminate the shoulder seen at ca. 26°, which has been assigned to amorphous carbon. B) X-ray diffraction pattern of SiOC monolithic sample taken with Kα radiation.

various graphitization indices of monolithic SiOC *vs* thin film SiOC samples is presented in Table 1. Lorentzian fitting was used to analyze the Raman spectra where the area under the curve is used to account for all the uncertainties of the process [30]. The lateral crystal size (L_a), inter-defect distance (L_D), defect density (n_D), and the average continuous graphene length including tortuosity (L_{eq}) were calculated using Eqs. (1),(2),(3), and (4), respectively [30–33]. A_D, A_G, and A_{2D} represent the areas under the D, G, and 2D peaks, respectively; while λ_L^4 represents the wavelength of the laser beam used in the analysis.

$$L_a = (2.4 \text{ x } 10^{-10})\lambda_L^4\left(\frac{A_D}{A_G}\right)^{-1} \quad (1)$$

$$L_D^2 = 1.8 \text{ x } 10^{-9}\lambda_L^4\frac{A_G}{A_D} \quad (2)$$

$$n_D = \frac{2.4 \text{ x } 10^{22}}{\lambda_L^4}\frac{A_D}{A_G} \quad (3)$$

$$L_{eq} = 77.0648\frac{A_{2D}}{A_D} \quad (4)$$

For the data listed in Table 1, it can be concluded that the phase separation occurring in the thin-film SiOC sample leads to sp^2-hybridized carbon phase in both matrix and disperse particle and that furthermore, the segregated carbon in the two components of the thin-film SiOC hold significantly different graphitization parameters. Hence, the segregated carbon phase present in the C/SiOC matrix of the thin film exhibits similar L_a and L_D values as compared to those calculated for monolithic SiOC; whereas the L_{eq} value is significantly smaller than that of monolithic SiOC. Accordingly, the carbon phase present in the matrix of the thin film SiOC sample consist of similar graphitization and smaller segregation size as related to monolithic SiOC. The segregated carbon phase present in the particles present in the thin film SiOC sample shows a significantly higher graphitization as well as segregation size as compared to both monolithic SiOC and matrix of SiOC films. Therefore, the phase separation occurring in the thin film samples leads to a microstructure not only related to the film morphology but also

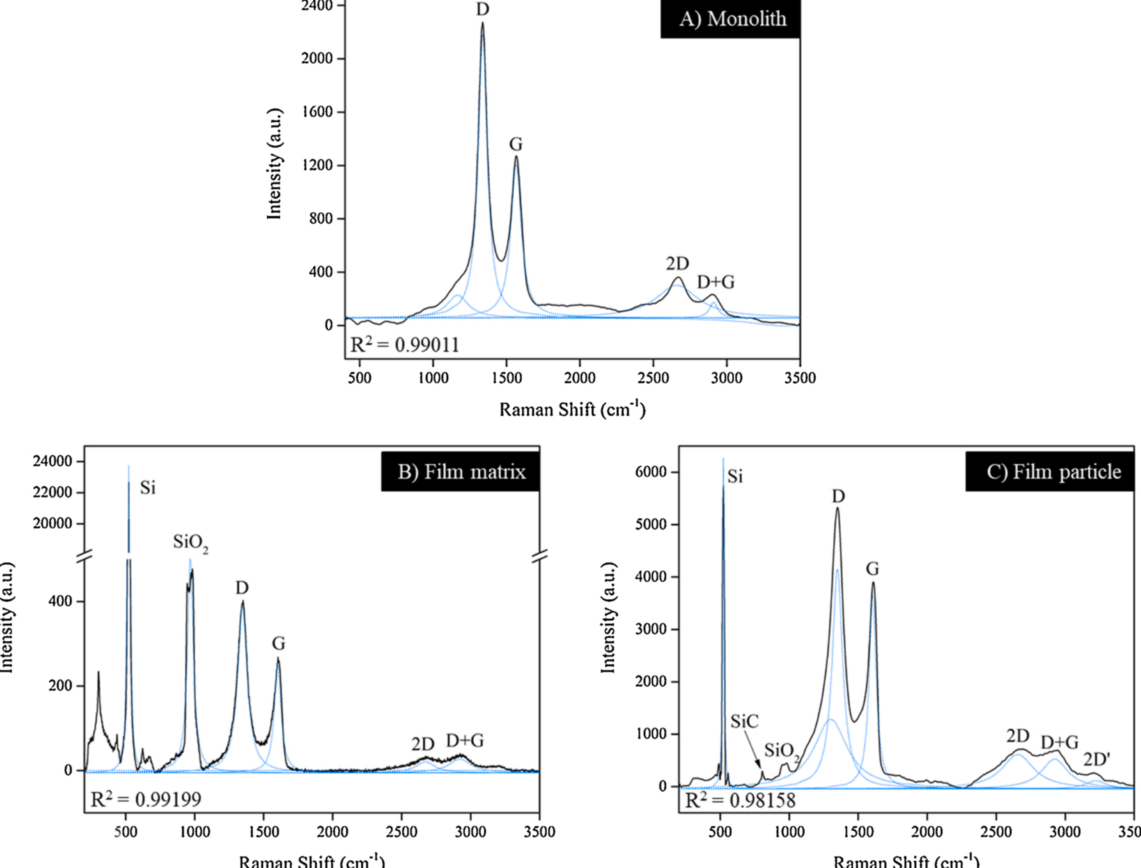

Fig. 4. A) Raman spectrum of a monolithic SiOC sample annealed at 1600 °C. B) Raman spectrum of a SiOC thin-film sample focused on the matrix showing high-intensity values of substrate-related peaks, Si and SiO_2. C) Raman spectrum of the dispersed particle, C/SiC, of the thin film showing more intense D and G bands and the manifestation of SiC peak.

Table 1
Graphitization indices of SiOC monolith [9] and thin-film samples calculated using the Raman spectra using Eqs. (1),(2),(3), and (4).

Parameters	SiOC Monolith		SiOC Thin Film	
			Matrix (C/SiOC)	Particle (C/SiC)
Carbon content [vol%]	17 %	17 %	17 %	
Annealing temperature [°C]	1400	1600	1400	
Crystallite size, L_a [nm]	8.3	10.3	7.2	11.9
Inter-defect distance, L_D [nm]	8.1	9	7.5	9.7
Defect density, n_D [10^{11} cm^{-3}]	6.9	5.6	8.0	5.0
L_{eq} [nm]	23.5	38.3	7.1	56.3

considering the size and graphitization degree of the sp^2-hybridized carbon phase.

The electrical conductivity of SiOC materials was shown in various studies to be mainly governed by the presence of the sp^2-hybridized carbon in the system. Also, the conductivity of the SiOC samples scales with the content and graphitization degree of the carbon phase [9,13,34,35]. In Table 1, the L_a, L_D, L_{eq}, and n_D of the dispersed particle on the film are of similar magnitude as the monolithic sample annealed at a higher temperature, 1600 °C. The effect of temperature on the crystal size is evident as it is directly proportional to increasing temperature and has a higher tendency to align along the basal plane [36]. The transport phenomena are then conditioned by the basal plane and the degree of orientation of the graphene sheets on the material. In the Brillouin zone, at the K point in the second order, the number of phonons generated (2D band) can be divided by the number of phonons generated at the Γ point in the first order (G band) to calculate the tortuosity ratio (R_{Tor}) [33]. On a similar trend with L_a, it is seeming that the average size of the continuous carbon precipitate including the tortuosity in the monolithic sample increases as the annealing temperature increases. Remarkably, a larger L_{eq} is calculated for the dispersed particle on the film which is much larger than the monolithic sample annealed at the same temperature. The increase in the crystal size and the L_{eq} demonstrates a higher degree of graphitization of the sample and shows the progressive transformation of the film from semiconductive to a semi-metallic behavior. This result demonstrates the effect of stress graphitization on the SiOC film. Stress-induced on the film enables partial graphitization of the secondary carbon phase at temperatures as low as 800 °C [37,38].

The G band of the C17−1400 film, matrix, and particle, displayed a Raman redshift of ca. 20 cm^{-1} as compared to unconstrained graphene which can be explained by the compressive biaxial strain induced on the film due to the coefficient of thermal expansion (CTE) mismatch with the SiO_2/Si substrate [39–44].

Based on the CTE mismatch, the compressive stress acting on the thin film sample was calculated to be ca. 109 MPa using Eq. (5), where ΔT is the difference between the heat-treatment temperature and the room temperature, and Δα is the difference between the CTE values of the silicon substrate and the SiOC thin film. The term $\left[\frac{E_f}{1-\nu_f}\right]$ or E* is the effective stiffness or the biaxial modulus of the film raised by the Poisson effect. In our previous work, we have shown that the residual compressive stress is directly proportional to the thin film thickness which leads to cracking when the thickness is above 1 μm [24].

$$\sigma_f = \left[\frac{E_f}{1-\nu_f}\right]\Delta T * \Delta\alpha \quad (5)$$

As shown in Fig. 5, a 60 µm by 60 µm area is scanned to map out the L_a and L_{eq} of the SiOC thin film sample. The micrograph of the area where the spectra are taken is shown in Fig. 5A as a reference. The blue line in Fig. 5 A, B, and C represents the edge of the dispersed particle on the film. In Fig. 5B, three regions are illustrated with average different crystal sizes of 7 nm, 10 nm, and 12 nm. In Fig. 5C, the gradient of colors from dark green to red represents the increasing size of the sp^2-hybridized carbon with the effect of tortuosity. L_{eq} along the edges of the particle (red map) is measured ca. 90 nm on average, while L_a decreases as the acquisition transitioned from the particle region to the matrix region. On the matrix, the L_{eq} is of the same magnitude as L_a and thus indicates the existence of short and planar graphene layers wherein the interconnection quality is relatively low and the phonon propagation is limited by L_a [33].

Apart from the phonon dispersion, the electrical properties of the SiOC film can also be assessed with the use of Raman data by e.g. calculating the activation energy (E_a) in relation to its lateral crystal size using equations $E_a = \frac{2.1}{L_a}$ for a semiconducting carbon-based material [17], and $E_a = \frac{7.7}{L_a}$ for graphitic-like materials [45]. In this case, the activation energy is defined as the energy required for the charge carriers to be thermally excited to move from the trap state into the extended state or the mobility gap [46]. The activation energy is related to the energy gap between the π and π* states of the material which can be associated with the amount of disorder on the sample acting as an effective barrier that promotes localization of charge carriers [47]. Moreover, the activation energy is related to the amount of disorder in the sample assuming that the carbon secondary phase is highly disordered in the matrix and of nanographitic nature within the segregated particles, 0.08 eV and 0.11 eV were calculated for the particle and matrix, respectively.

In an ideal model of planar graphene without any disorder, the Fermi energy level lies at the Dirac point making it a zero bandgap material, where the valence band and conduction band intersect, and the dispersion relation around the Dirac point is linear and isotropic [48]. However, for disordered carbons similar to that present in the SiOC thin film, the electronic homogeneity of graphene would be significantly altered by the introduction of disorder into the structure, which can alter the bond length of the interatomic bonds and lead to re-hybridization of σ and π orbitals. Moreover, all defects present in the carbon phase may cause the scattering of electron waves and eventually change the electron trajectories [49,50].

As mentioned by Cordelair et al., the conduction mechanism in SiOC is based on the presence of turbostratic carbon, also regarded as disordered graphite [11]. This is supported by the thermally activated conductivity of the SiOC film as shown in Fig. 6A. Conduction for graphitic films under optimal growth conditions is dominated by elastic scattering with no trace of bandgap while activated transport governs the conduction of disordered carbon films thus activation energies can be calculated [47]. Using the Arrhenius relation plotted in Fig. 6B, the activation energy of the film is determined from the slope of the fitted line resulting in a value of 0.07 eV ($R^2 = 0.99$).

In Fig. 7, the activation energies measured for the SiOC film are calculated using the Raman data, and the Arrhenius plot, and are compared to the works of Rosenburg et al. [9] and Lu et al. [51]. Three different electrical conduction regimes are known for SiOC material in which the first regime at E_a ca. 1 eV is conduction through the amorphous silica network and is mainly attributed to the variable range hopping (VRH) mechanism for low carbon-containing material [52]. The second regime features lower activation energy at ca. 0.3 eV

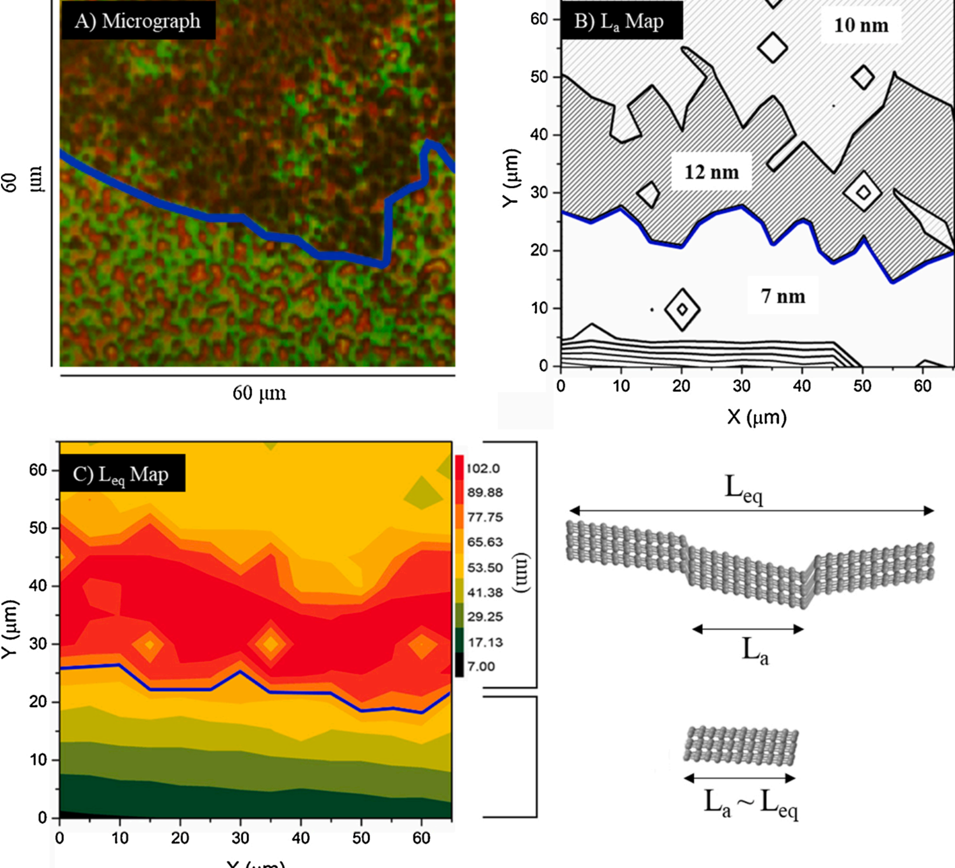

Fig. 5. Raman map of the average L_a and L_{eq} size for the sp^2-hybridized carbon phase in C17-1400 thin-film. The blue lines on Figures A, B, and C indicate the boundary between a C/SiC-based disperse particle and the C/SiOC matrix. (B) Each marked region indicates the different lateral crystal sizes within the C/SiC particle and the C/SiOC matrix. The gradient of colors from dark green to red illustrated in (C) denotes the increasing crystal size, in nm, with the effect of tortuosity. A gradient in L_a and L_{eq} is observed across the particle diameter, with the highest values located at the particle edge (For interpretation of the references to colour in this figure legend, the reader is referred to the web version of this article).

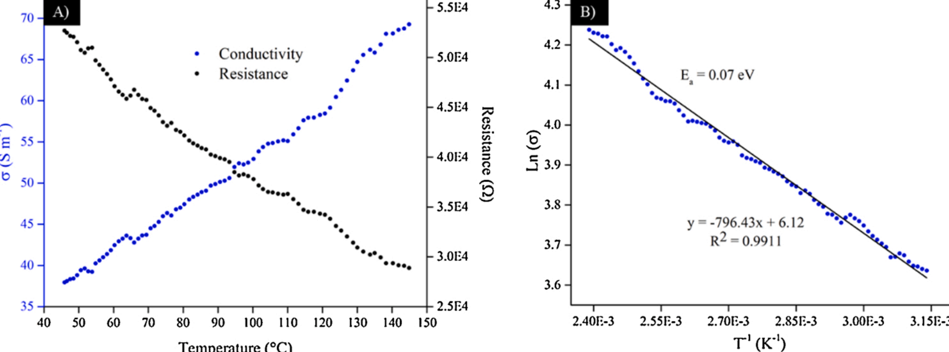

Fig. 6. Thermally activated electrical conductivity of C17-1400 thin film. A) In-situ measurement of resistance and conductivity of the thin film sample as a function of temperature. B) Arrhenius plot of electrical conductivity against reciprocal temperature.

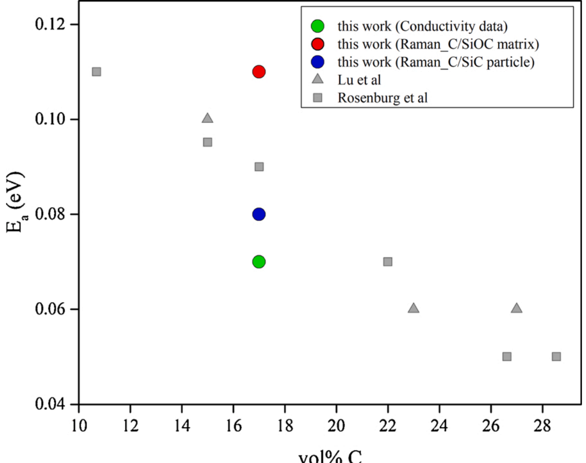

Fig. 7. Activation energies of thin-film samples as compared to the literature values of monolithic samples pyrolyzed at 1400 °C with different volume percent of sp^2 carbon. Comparison is demarcated by the percolation threshold region known at 6 – 20 vol% C. Grayish squares and triangles represent data from [9] and [51], respectively.

wherein the potential barrier is lowered by the additional carbon defects causing an overlap of the energy bandgap and the silicon dangling bond states. On the third regime, as plotted in Fig. 7, $E_a < 0.1$ eV, the amount of carbon is within the percolation threshold and is driven by continuous sp^2 carbon networks [11].

In C/SiOC material, the critical percolation threshold is known at 6–20 vol% sp^2 carbon depending on the synthesis temperature and the aspect ratio of the sp^2 carbon cluster [11,22]. Comparing all the data of the samples with 17 vol% C, using the one-sample Z-test statistic (*p-value* < 0.05), the activation energies calculated from the Raman data of the particle (E_a =0.08 eV, *p-value* = *0.019*), and the Arrhenius plot (E_a = 0.07 eV, *p-value* = *0.038*) have a positive significant effect in reference to the monolithic sample (E_a =0.09 eV). Conversely, E_a from the the Raman data of the matrix (E_a =0.11 eV, *p-value* = *0.002*) has a negative significant effect. These values substantiate the effect of segregations on microstructural features manifested on the thin film samples concerning its charge carrier transport behavior. However, the origin of the C/SiC particle formation requires further research.

In Table 2, the Hall coefficients (R_H) of the C/SiOC monolith and thin-film are presented together with the measured charge densities (*N*) and carrier mobilities (μ_H) obtained using the Van der Pauw method shown in Section 2 Fig. 1B. In both samples, the R_H values are positive, indicating p-type behavior with holes as the main charge carrier of the system. With the SiOC film at 500 nm thickness, the carrier densities of both samples, monolith, and thin film, are of the same magnitude.

Table 2
Hall coefficients, charge carrier densities, carrier mobilities, and conductivities of C/SiOC samples with 17 vol% C and heat-treated at 1400 °C.

Parameters	Unit of Measure	SiOC Monolith	SiOC Thin Film
Hall Coefficient (R_H)	$cm^3\ C^{-1}$	0.074	11.25
Carrier density (*N*)	cm^{-3}	6.22×10^{17}	5.55×10^{17}
Carrier mobility (μ_H)	$cm^2\ V^{-1}s^{-1}$	3.0	184.48
Conductivity (σ)	$S\ cm^{-1}$	0.32	16.40

Furthermore, the carrier mobility of the thin film is measured to be 2 magnitudes larger than that of the monolith.

Using Eq. (6), the charge carrier mobility can be estimated, with μ_0 assumed to be the band mobility of graphene equal to 15,000 $cm^2\ V^{-1}\ s^{-1}$ [53], k_B is the Boltzmann in eV K^{-1}, T as the temperature in Kelvin, and E_a as the calculated activation energy. The calculated carrier mobilities of the SiOC-based thin film are >100 $cm^2\ V^{-1}\ s^{-1}$ and hence comparable to values obtained experimentally for turbostratic graphitic microstructures [54].

$$\mu = \mu_0 e^{-\left(\frac{E_a}{k_B T}\right)} \tag{6}$$

Studies on compressive biaxial strain have shown a boosting effect on the carrier mobility of graphitic materials both on suspended membranes and on a substrate [55–58]. In retrospect to the redshift on the G-band of the Raman data of the SiOC film, the CTE mismatch of the film and the Si/SiO_2 substrate puts the film under compressive biaxial strain. This compressive biaxial strain produces carriers with lower effective mass and an increase in Fermi velocity thus improving the mobility of the charge carriers [43,55–57].

The conductivity of the C/SiOC samples is also measured using the Van der Pauw configuration illustrated in Fig. 1A. Additionally, the conductivity can be directly calculated from the Hall measurement data using Eq. (7) where *q* is the electronic charge magnitude equal to 1.6×10^{-19} C.

$$\sigma = q * N * \mu_H \tag{7}$$

A plotted summary presented in Fig. 8 compares the conductivity values of different C/SiOC samples with 17 vol% sp^2 carbon annealed at 1400 °C. It is distinct from the plot that the conductivity of the samples is enhanced by increasing the amount of the sp^2 hybridized carbon within the material. The conductivity of the thin film sample is comparable to that of turbostratic and glassy carbon and is 2 magnitudes larger as compared to its monolithic counterpart. This can be related to the improved carrier mobility of the thin film which is also 2 magnitudes larger than the monolithic sample. Likewise, the microstructure of the film is assumed to affect (i.e., decrease) the percolation threshold.

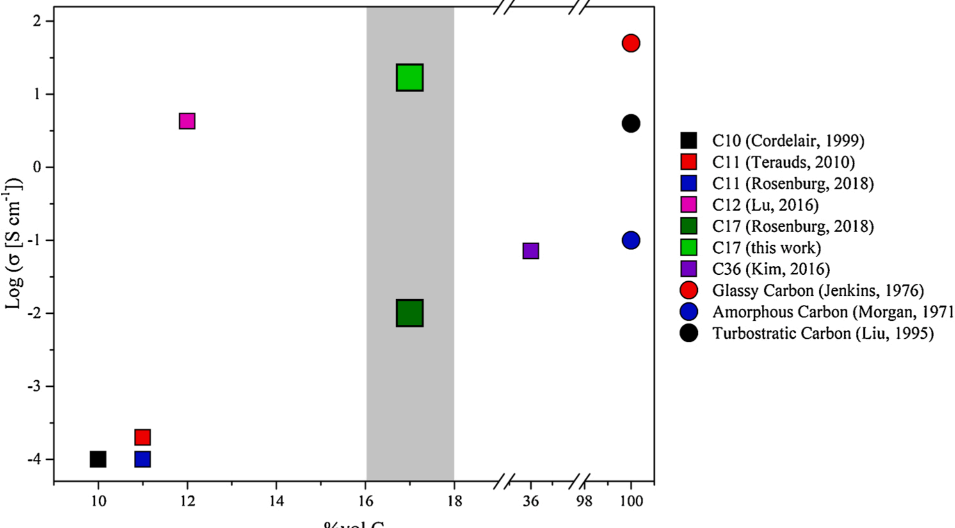

Fig. 8. Conductivity values of carbon allotropes and polymer-derived ceramic C/SiOC samples with different % volume carbon content. Highlighted data points are monolithic and thin-film samples synthesized using a similar preceramic polymer with 17 %vol C. (Nomenclature: C(%vol) [11–13,51,59–62].

4. Conclusions

The effect of varying the structure going from bulk to thin-film sample to improve the electrical transport mechanism in C/SiOC is established in this work. It is found that the substrate induces compressive strain on the film in the biaxial direction which boosts the charge carrier mobility of the material. The decrease in activation energy, Ea ca. 0.07 eV, is correlated to the increased size of the sp^2 carbon domains with an average of ca. 40 nm which supports the positive effect of the microstructure of the film. Hall measurement revealed p-type carriers as the main charge carrier of the system. The charge carrier concentration of both monolith and thin-film samples is found to be comparable while a significant increase in mobility, by 2 orders of magnitude, is realized for the SiOC thin film. The conductivity of the C/SiOC thin film, ca. 16 S cm^{-1}, is also 2 magnitudes higher as compared to monolithic samples and is supposed to rely on the improved charge carrier mobility as well as on the decreased percolation threshold due to the phase-separated morphology of the thin film. The present study indicates that the charge carrier transport in SiOC-based systems can be modulated not only by adjusting the chemical composition (i.e., carbon content) of SiOC but also by tailoring its morphology and residual stress.

Author contributions

Conceptualization, E.R. III., and E.I.; methodology, software, formal analysis, investigation, resources, data curation, E.R. III, F.K.; writing—original draft preparation, E.R. III.; writing—review and editing, E.I., R.R., H.F.S.; visualization, E.R. III.; supervision, E.I.; project administration, E.R.III, F.K., E.I.; funding acquisition, E.I., R.R., H.F.S. All authors have read and agreed to the published version of the manuscript.

Funding

The authors gratefully acknowledge funding from the German Science Foundation (DFG Germany) – grants no. 411658150 (Microstructured C/SiCX (X = O,N)-based high temperature strain gauge). Additionally, EI acknowledges funding from DFG within the Heisenberg program (IO 64/14−1).

Declaration of Competing Interest

The authors declare no conflict of interest.

Acknowledgments

The authors would like to express their gratitude towards the Electronic Structure of Materials (ESM) group headed by Prof. Dr. Andreas Klein at TU Darmstadt, Germany for letting us use the in-situ Hall-effect and conductivity measurement device. In particular, the assistance provided by Ms. Nicole Bein in performing the experimental task is greatly appreciated.

References

[1] H.W. van Zeijl, (Invited) thin film technologies for Micro/Nano systems; a review, ECS Trans. 61 (2014) 191, https://doi.org/10.1149/06103.0191ecst.
[2] Piezoelectric Material From Bulk to Thin Film – Comparison, 2019. I-Micronews. (n.d.). https://www.i-micronews.com/products/piezoelectric-material-from-bulk-to-thin-film-comparison-2019/ (accessed March 9, 2021).
[3] Piezoelectric Devices: From Bulk to Thin-Film, 2019. I-Micronews. (n.d.). https://www.i-micronews.com/products/piezoelectric-devices-from-bulk-to-thin-film-2019/ (accessed March 9, 2021).
[4] P. Colombo, G. Mera, R. Riedel, G.D. Sorarù, Polymer-Derived Ceramics: 40 Years of Research and Innovation in Advanced Ceramics, J. Am. Ceram. Soc. 93 (2010) 1805–1837, https://doi.org/10.1111/j.1551-2916.2010.03876.x.
[5] K. Lu, D. Erb, Polymer derived silicon oxycarbide-based coatings, Int. Mater. Rev. 63 (2018) 139–161, https://doi.org/10.1080/09506608.2017.1322247.
[6] E. Ionescu, G. Mera, R. Riedel, Polymer-Derived Ceramics (PDCs): Materials Design Towards Applications at Ultrahigh-temperatures and in Extreme Environments, MAX Phases and Ultra-high Temperature Ceramics for Extreme Environments, 2013, pp. 203–245, https://doi.org/10.4018/978-1-4666-4066-5.ch007.
[7] R. Riedel, G. Mera, R. Hauser, A. Klonczynski, Silicon-based polymer-derived ceramics: synthesis properties and Applications-A review: dedicated to Prof. Dr. Fritz Aldinger on the occasion of his 65th birthday, Nippon Seramikkusu Kyokai Gakujutsu Ronbunshi 114 (2006) 425–444, https://doi.org/10.2109/jcersj.114.425.
[8] E. Ricohermoso, F. Rosenburg, F. Klug, N. Nicoloso, H.F. Schlaak, R. Riedel, E. Ionescu, Piezoresistive carbon-containing ceramic nanocomposites – a review, Open Ceramics. 5 (2021) 100057, https://doi.org/10.1016/j.oceram.2021.100057.
[9] F. Rosenburg, B. Balke, N. Nicoloso, R. Riedel, E. Ionescu, Effect of the content and ordering of the sp2 free carbon phase on the charge carrier transport in Polymer-Derived Silicon Oxycarbides, Molecules 25 (2020) 5919, https://doi.org/10.3390/molecules25245919.
[10] S. Martínez-Crespiera, E. Ionescu, H.-J. Kleebe, R. Riedel, Pressureless synthesis of fully dense and crack-free SiOC bulk ceramics via photo-crosslinking and pyrolysis of a polysiloxane, J. Eur. Ceram. Soc. 31 (2011) 913–919, https://doi.org/10.1016/j.jeurceramsoc.2010.11.019.

[11] J. Cordelair, P. Greil, Electrical conductivity measurements as a microprobe for structure transitions in polysiloxane derived Si–O–C ceramics, J. Eur. Ceram. Soc. 20 (2000) 1947–1957, https://doi.org/10.1016/S0955-2219(00)00068-6.

[12] F. Rosenburg, E. Ionescu, N. Nicoloso, R. Riedel, High-temperature raman spectroscopy of Nano-Crystalline Carbon in Silicon Oxycarbide, Materials 11 (2018) 93, https://doi.org/10.3390/ma11010093.

[13] K.J. Kim, J.-H. Eom, Y.-W. Kim, W.-S. Seo, Electrical conductivity of dense, bulk silicon-oxycarbide ceramics, J. Eur. Ceram. Soc. 5 (2015) 1355–1360, https://doi.org/10.1016/j.jeurceramsoc.2014.12.007.

[14] K.J. Kim, J.-H. Eom, T.Y. Koh, Y.-W. Kim, W.-S. Seo, Effects of carbon addition on the electrical properties of bulk silicon-oxycarbide ceramics, J. Eur. Ceram. Soc. 11 (2016) 2705–2711, https://doi.org/10.1016/j.jeurceramsoc.2016.04.034.

[15] M. Wilamowska-Zawlocka, P. Puczkarski, Z. Grabowska, J. Kaspar, M. Graczyk-Zajac, R. Riedel, G.D. Sorarù, Silicon oxycarbide ceramics as anodes for lithium ion batteries: influence of carbon content on lithium storage capacity, RSC Adv. 6 (2016) 104597–104607, https://doi.org/10.1039/C6RA24539K.

[16] S. Mrozowski, Semiconductivity and diamagnetism of polycrystalline graphite and condensed ring systems, Phys. Rev. 85 (1952) 609–620, https://doi.org/10.1103/PhysRev.85.609.

[17] M.S. Dresselhaus, G. Dresselhaus, K. Sugihara, I.L. Spain, H.A. Goldberg, Synthesis of graphite fibers and filaments, in: M.S. Dresselhaus, G. Dresselhaus, K. Sugihara, I.L. Spain, H.A. Goldberg (Eds.), Graphite Fibers and Filaments, Springer, Berlin, Heidelberg, 1988, pp. 12–34, https://doi.org/10.1007/978-3-642-83379-3_2.

[18] P. Esquinazi, J. Krüger, J. Barzola-Quiquia, R. Schönemann, T. Herrmannsdörfer, N. García, On the low-field Hall coefficient of graphite, AIP Adv. 4 (2014) 117121, https://doi.org/10.1063/1.4902099.

[19] K. Ellmer, Hall effect and conductivity measurements in semiconductor crystals and thin films, in: characterization of materials, Cancer Epidemiol. Biomarkers Prev. (2012) 1–16, https://doi.org/10.1002/0471266965.com035.pub2.

[20] D.W. Koon, C.J. Knickerbocker, What do you measure when you measure resistivity? Rev. Sci. Instrum. 63 (1992) 207–210, https://doi.org/10.1063/1.1142958.

[21] C. Stabler, E. Ionescu, M. Graczyk-Zajac, I. Gonzalo-Juan, R. Riedel, Silicon oxycarbide glasses and glass-ceramics: "All-Rounder" materials for advanced structural and functional applications, J. Am. Ceram. Soc. 101 (2018) 4817–4856, https://doi.org/10.1111/jace.15932.

[22] F. Rosenburg, The State of Carbon and the Piezoresistive Effect in Silicon Oxycarbide Ceramics, Ph.D. Thesis, Technische Universität, 2018 (accessed June 28, 2020), https://tuprints.ulb.tu-darmstadt.de/7517/.

[23] M. Esfehanian, R. Oberacker, T. Fett, M.J. Hoffmann, Development of dense filler-free polymer-derived SiOC ceramics by field-assisted sintering, J. Am. Ceram. Soc. 91 (2008) 3803–3805, https://doi.org/10.1111/j.1551-2916.2008.02730.x.

[24] E.I. Ricohermoso, F. Klug, H. Schlaak, R. Riedel, E. Ionescu, Electrically conductive silicon oxycarbide thin films prepared from preceramic polymers, International Journal of Applied Ceramic Technology. n/a (n.d.). https://doi.org/10.1111/ijac.13800.

[25] Z.Q. Li, C.J. Lu, Z.P. Xia, Y. Zhou, Z. Luo, X-ray diffraction patterns of graphite and turbostratic carbon, Carbon 45 (2007) 1686–1695, https://doi.org/10.1016/j.carbon.2007.03.038.

[26] A.M. Molodets, A.A. Golyshev, Structural transformations of amorphous carbon (Glassy carbon) at high shock pressures, J. Exp. Theor. Phys. Lett. 126 (2018) 772–778, https://doi.org/10.1134/S1063776118060079.

[27] W.P. Griffith, Raman studies on rock-forming minerals. Part I. Orthosilicates and cyclosilicates, Journal of the Chemical Society A: Inorganic, Stud. Phys. Theor. Chem. 0 (1969) 1372–1377, https://doi.org/10.1039/J19690001372.

[28] R. Juroszek, M. Czaja, R. Lisiecki, B. Krüger, B. Hachuła, I. Galuskina, Spectroscopic and structural investigations of blue afwillite from Ma`ale Adummim locality, Palestinian Autonomy, Spectrochim. Acta A. Mol. Biomol. Spectrosc. 227 (2020) 117688, https://doi.org/10.1016/j.saa.2019.117688.

[29] R.L. Frost, J. Čejka, M.L. Weier, W. Martens, Molecular structure of the uranyl silicates—a Raman spectroscopic study, J. Raman Spectrosc. 37 (2006) 538–551, https://doi.org/10.1002/jrs.1430.

[30] L.G. Cançado, A. Jorio, E.H.M. Ferreira, F. Stavale, C.A. Achete, R.B. Capaz, M.V. O. Moutinho, A. Lombardo, T.S. Kulmala, A.C. Ferrari, Quantifying defects in graphene via raman spectroscopy at different excitation energies, Nano Lett. 11 (2011) 3190–3196, https://doi.org/10.1021/nl201432g.

[31] T. Rouxel, G. Massouras, G.-D. Sorarù, High temperature behavior of a gel-derived SiOC glass: elasticity and viscosity, J. Solgel Sci. Technol. 14 (1999) 87–94, https://doi.org/10.1023/A:1008779915809.

[32] P. Saini, R. Sharma, N. Chadha, Determination of defect density, crystallite size and number of graphene layers in graphene analogues using X-ray diffraction and Raman spectroscopy, Indian J. Pure & Appl. Phys. (IJPAP). 55 (2017) 625–629, 629.

[33] N. Larouche, B.L. Stansfield, Classifying nanostructured carbons using graphitic indices derived from Raman spectra, Carbon 48 (2010) 620–629, https://doi.org/10.1016/j.carbon.2009.10.002.

[34] A. Xia, J. Yin, X. Chen, X. Liu, Z. Huang, Polymer-derived Si-Based ceramics: recent developments and perspectives, Crystals 10 (2020) 824, https://doi.org/10.3390/cryst10090824.

[35] C. Stabler, A. Reitz, P. Stein, B. Albert, R. Riedel, E. Ionescu, Thermal properties of SiOC glasses and glass ceramics at elevated temperatures, Materials (Basel). 11 (2018), https://doi.org/10.3390/ma11020279.

[36] C.A. Klein, Electrical properties of pyrolytic graphites, Rev. Mod. Phys. 34 (1962) 56–79, https://doi.org/10.1103/RevModPhys.34.56.

[37] M. Inagaki, F. Kang, M. Toyoda, H. Konno, Chapter 5 - stress graphitization, in: M. Inagaki, F. Kang, M. Toyoda, H. Konno (Eds.), Advanced Materials Science and Engineering of Carbon, Butterworth-Heinemann, Boston, 2014, pp. 87–110, https://doi.org/10.1016/B978-0-12-407789-8.00005-3.

[38] M. Ghazinejad, S. Holmberg, O. Pilloni, L. Oropeza-Ramos, M. Madou, Graphitizing non-graphitizable carbons by stress-induced routes, Sci. Rep. 7 (2017) 16551, https://doi.org/10.1038/s41598-017-16424-z.

[39] Y. Shibazaki, Y. Kono, G. Shen, Compressed glassy carbon maintaining graphite-like structure with linkage formation between graphene layers, Sci. Rep. 9 (2019) 7531, https://doi.org/10.1038/s41598-019-43954-5.

[40] D. Liu, P. Flewitt, Chapter 5:Raman Measurements of Stress in Films and Coatings, 2014, https://doi.org/10.1039/9781782621485-00141.

[41] Z.H. Ni, H.M. Wang, Y. Ma, J. Kasim, Y.H. Wu, Z.X. Shen, Tunable stress and controlled thickness modification in graphene by annealing, ACS Nano 2 (2008) 1033–1039, https://doi.org/10.1021/nn800031m.

[42] H. Windischmann, K.J. Gray, Stress measurement of CVD diamond films, Diam. Relat. Mater. 4 (1995) 837–842, https://doi.org/10.1016/0925-9635(94)05327-8.

[43] W. Jie, Y. Yu Hui, Y. Zhang, S. Ping Lau, J. Hao, Effects of controllable biaxial strain on the Raman spectra of monolayer graphene prepared by chemical vapor deposition, Appl. Phys. Lett. 102 (2013) 223112, https://doi.org/10.1063/1.4809922.

[44] C. Bousige, F. Balima, D. Machon, G.S. Pinheiro, A. Torres-Dias, J. Nicolle, D. Kalita, N. Bendiab, L. Marty, V. Bouchiat, G. Montagnac, A.G. Souza Filho, P. Poncharal, A. San-Miguel, Biaxial strain transfer in supported graphene, Nano Lett. 17 (2017) 21–27, https://doi.org/10.1021/acs.nanolett.6b02981.

[45] J. Robertson, Properties of diamond-like carbon, Surf. Coat. Technol. 50 (1992) 185–203, https://doi.org/10.1016/0257-8972(92)90001-Q.

[46] X. Wang, L.F. Register, A. Dodabalapur, Redefining the mobility edge in thin-film transistors, Phys. Rev. Appl. 11 (2019), 064039, https://doi.org/10.1103/PhysRevApplied.11.064039.

[47] C. Coleman, R. McIntosh, S. Bhattacharyya, Controlling the activation energy of graphene-like thin films through disorder induced localization, J. Appl. Phys. 114 (2013), 043716, https://doi.org/10.1063/1.4817067.

[48] S. Das Sarma, S. Adam, E.H. Hwang, E. Rossi, Electronic transport in two-dimensional graphene, Rev. Mod. Phys. 83 (2011) 407–470, https://doi.org/10.1103/RevModPhys.83.407.

[49] A. Cortijo, M.A.H. Vozmediano, Effects of topological defects and local curvature on the electronic properties of planar graphene, Nucl. Phys. B 763 (2007) 293–308, https://doi.org/10.1016/j.nuclphysb.2006.10.031.

[50] G.M. Rutter, J.N. Crain, N.P. Guisinger, T. Li, P.N. First, J.A. Stroscio, Scattering and interference in epitaxial graphene, Science 317 (2007) 219–222, https://doi.org/10.1126/science.1142882.

[51] K. Lu, D. Erb, M. Liu, Thermal stability and electrical conductivity of carbon-enriched silicon oxycarbide, J. Mater. Chem. C 4 (2016) 1829–1837, https://doi.org/10.1039/C6TC00069J.

[52] N.F. Mott, Conduction in non-crystalline materials, Philos. Mag. 19 (1969) 835–852, https://doi.org/10.1080/14786436908216338.

[53] M.S. Dresselhaus, G. Dresselhaus, Intercalation compounds of graphite, Adv. Phys. 51 (2002) 1–186, https://doi.org/10.1080/00018730110113644.

[54] Y.R. Hernandez, S. Schweitzer, J.-S. Kim, A.K. Patra, J. Englert, I. Lieberwirth, A. Liscio, V. Palermo, X. Feng, A. Hirsch, M. Kläui, K. Müllen, Turbostratic graphitic microstructures: electronically decoupled multilayer graphene devices with robust high charge carrier mobility, Phys. Rev. Appl. 7 (2017), 024022, https://doi.org/10.1103/PhysRevApplied.7.024022.

[55] M. Zhou, X. Chen, M. Li, A. Du, Widely tunable and anisotropic charge carrier mobility in monolayer tin(II) selenide using biaxial strain: a first-principles study, J. Mater. Chem. C 5 (2017) 1247–1254, https://doi.org/10.1039/C6TC04692D.

[56] H.V. Phuc, N.N. Hieu, B.D. Hoi, N.V. Hieu, T.V. Thu, N.M. Hung, V.V. Ilyasov, N. A. Poklonski, C.V. Nguyen, Tuning the electronic properties, effective mass and carrier mobility of MoS2 monolayer by strain engineering: first-principle calculations, J. Elec Mater. 47 (2018) 730–736, https://doi.org/10.1007/s11664-017-5843-8.

[57] A.D. Smith, F. Niklaus, A. Paussa, S. Schröder, A.C. Fischer, M. Sterner, S. Wagner, S. Vaziri, F. Forsberg, D. Esseni, M. Östling, M.C. Lemme, Piezoresistive properties of suspended graphene membranes under uniaxial and biaxial strain in nanoelectromechanical pressure sensors, ACS Nano 10 (2016) 9879–9886, https://doi.org/10.1021/acsnano.6b02533.

[58] Md.H. Alam, K.I. Masood, Q.D.M. Khosru, Effect of biaxial strain on structural and electronic properties of graphene / boron nitride hetero bi-layer structure, 8th International Conference on Electrical and Computer Engineering (2014) 381–384, https://doi.org/10.1109/ICECE.2014.7027025.

[59] M.A. Short, P.L. Walker, Measurement of interlayer spacings and crystal sizes in turbostratic carbons, Carbon 1 (1963) 3–9, https://doi.org/10.1016/0008-6223(63)90003-4.

[60] M. Morgan, Electrical conduction in amorphous carbon films, Thin Solid Films 7 (1971) 313–323, https://doi.org/10.1016/0040-6090(71)90049-6.

[61] K. Terauds, P.E. Sanchez-Jimenez, R. Raj, C. Vakifahmetoglu, P. Colombo, Giant piezoresistivity of polymer-derived ceramics at high temperatures, J. Eur. Ceram. Soc. 30 (2010) 2203–2207, https://doi.org/10.1016/j.jeurceramsoc.2010.02.024.

[62] C.-C. Liu, A.B. Walters, M.A. Vannice, Measurement of electrical properties of a carbon black, Carbon 33 (1995) 1699–1708, https://doi.org/10.1016/0008-6223(95)00125-4.

Materials & Design 213 (2022) 110323

Contents lists available at ScienceDirect

Materials & Design

journal homepage: www.elsevier.com/locate/matdes

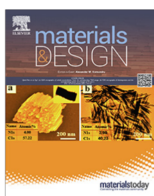

Microstrain-range giant piezoresistivity of silicon oxycarbide thin films under mechanical cyclic loads

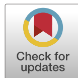

Emmanuel Ricohermoso III [a,*], Florian Klug [b], Helmut Schlaak [b], Ralf Riedel [a], Emanuel Ionescu [a]

[a] Fachbereich Material- und Geowissenschaften, Technische Universität Darmstadt, Otto-Berndt-Str. 3, D-64287 Darmstadt, Germany
[b] Fachbereich Elektrotechnik und Informationstechnik, Technische Universität Darmstadt, Merckstr. 23, D-64283 Darmstadt, Germany

HIGHLIGHTS

- The work used simple fabrication process with polymer-derived ceramics as a highly-responsive piezoresistive active material.
- The highly sensitive SiOC-based strain sensor is tested at microstrain range to both compressive and tensile cyclic loads.
- Giant piezoresistivity was observed with values of ca. 5050 and 3010 for both compressive and tensile cyclic loads.
- Gauge factor is assessed in view of the hysteresis and nonlinear response of the material and reported with standard errors.
- Replicability and reproducibility of the processes and the responses are statistically analyzed at a 95% confidence level.

GRAPHICAL ABSTRACT

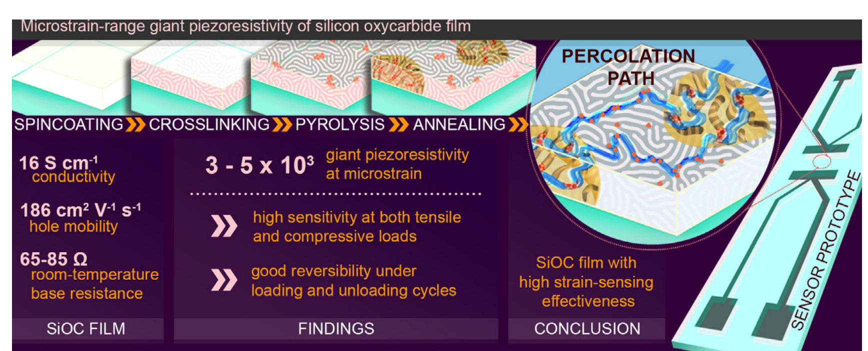

ARTICLE INFO

Article history:
Received 7 October 2021
Revised 9 December 2021
Accepted 11 December 2021
Available online 13 December 2021

Keywords:
Polymer derived ceramics
Piezoresistivity
Strain gauge
sensor

ABSTRACT

In the present study, thin-film strain gauge element arrays were prepared based on large-area silicon oxycarbide thin films and lithographic deposition of structured electrodes. The individual strain gauge elements were systematically investigated concerning their piezoresistive behavior at ambient temperature and shown to possess giant piezoresistivity with gauge factors in the range of 3–5 $\times$ 10^3. This has been correlated with the large charge carrier mobility in the silicon oxycarbide thin films (i.e., 186 $cm^2 V^{-1} s^{-1}$) as well as with a unique phase composition and morphology thereof, consisting of high-conductivity carbon-rich segregations homogeneously dispersed within a silicon oxycarbide-based matrix. The studied strain gauge elements were evaluated in both cyclic tensile and compression load modes and showed excellent reversibility and short response times. The process capability of the strain gauge elements has been statistically assessed and revealed good robustness and replicability which may be further improved. The present work provides a robust and highly reproducible manufacturing process for an ultrasensitive strain gauge prototype and thus points towards a great potential concerning the use of silicon oxycarbides in MEMS-related applications.

© 2021 The Author(s). Published by Elsevier Ltd. This is an open access article under the CC BY license (http://creativecommons.org/licenses/by/4.0/).

Abbreviations: PDC, Polymer-derived ceramics; SiOC, silicon oxycarbide; GF, Gauge factor.

* Corresponding author.
E-mail address: emmanuel_iii.ricohermoso@tu-darmstadt.de (E. Ricohermoso III).

https://doi.org/10.1016/j.matdes.2021.110323
0264-1275/© 2021 The Author(s). Published by Elsevier Ltd.
This is an open access article under the CC BY license (http://creativecommons.org/licenses/by/4.0/).

1. Introduction

Being one of the first devices developed for microelectromechanical systems (MEMS) applications, piezoresistivity-based sensing devices cover force, pressure, accelerometers, and inertial sensors [1–3] which are acknowledged but not limited to the fields of automotive, roads, and infrastructures [4–6], ventilation, and air conditioning, and recently on wearable devices for health monitoring [7,8]. The brevity and precision of instrumentation of piezoresistive sensors offer those a substantial share on the MEMS sensors market today. In various review articles, the general concepts of assessing the piezoresistive effect in different classes of materials have been extensively discussed [1,2,5,9,10]. Since the patent of Ruge in 1944 on bonded metallic strain gauges [11], the sensitivity of those devices, defined by their gauge factor (GF, $GF = \frac{\Delta R/R_0}{\varepsilon}$, with R_0 being the zero load resistance, ΔR being the change of the resistance upon applying a mechanical load and ε being the strain), has been the center of interest in enhancing their capability. Given the low sensitivity of metallic gauges, GF $\sim$ 2, primarily based on geometrical change due to applied strain, the material choice has been fundamental in the development of strain gauges. In 1950, Bardeen and Shockley reported the correlation of electron and hole mobilities to the shifts in conduction and filled valence bands associated with dilations induced by crystal lattice deformations in semiconducting materials [12]. This was further substantiated by Smith in 1954, who noticed an exceptionally large change in resistivity of silicon and germanium as a tensile load was applied [13]. In 1957, reports of Mason and Thurston on the first silicon-based strain gauge to measure force, torque, and displacement with a sensitivity being 50 times larger than that of conventional metal strain gauges started the discussion of using semiconductor strain gauges which eventually been exploited to create the first commercial device produced in the late 1950s [14]. At the forefront of these developments is the fact that carrier mobilities of semiconductors govern the high sensitivity of the device. This then makes the effect of geometrical change (which dominates the behavior of metallic strain gauges) almost negligible, driving the movement to further miniaturization of devices.

Several carbon-based materials such as silicon carbide (SiC) [9,15–17], graphene oxides [18–20], carbon black [5,6], diamond [9,21,22], carbon nanotubes [8,19,23–27], and nanowires[28–30] are currently leading the pack posting GF values considered as giant piezoresistivity [1]. Giant piezoresistivity is used to characterize a material with a gauge factor of above 500 [5]. Despite of giant piezoresistivity still being controversial, another type of material, polymer-derived ceramics (PDC), positioned itself as a competent material with high sensitivity. In 2008, Zhang firstly reported a GF value of 1000–4000 for silicon carbonitride (SiCN) synthesized at 1400 °C, which was explained to be stress-dependent [31,32]. The piezoresistive effect was explained as a consequence of silicon carbonitrides being percolative systems consisting of a non-conductive SiCN matrix and an sp^2 carbon-based conductive disperse phase. The percolation theory was also backed up by the result of Riedel *et al* in 2010 for a carbon-containing silicon oxycarbide (SiOC) possessing a GF of 145 [33]. Furthermore, the temperature dependence of the piezoresistive effect in PDCs was explored by Terauds in 2010 [34], revealing the potential of this class of materials for applications at high temperatures. Other works focusing on the effect of carbon content, process temperature, synthesis routes, and use of additives and quaternary ceramics have also been well studied in the past 10 years. Some of the studies reported extremely large GF values for specific PDC composition, e.g., a huge GF value of 16,000 was mentioned for a SiAlOC-based ceramic [35–38].

In the present work, the potential use of SiOC-based PDC materials for a piezoresistive thin-film strain gauge has been assessed and demonstrated. Silicon oxycarbide is advantageous in this field of application due to its relatively low synthesis and processing temperature, thermal stability, and oxidation resistance [39,40]. The process of converting the polymer precursor to ceramic is also simple and can easily be executed in an ambient atmosphere. Previous work on the fabrication, morphology [41] and charge carrier characteristics [42] of SiOC-based thin films serve as the starting material of this study.

The process of photolithography is used to design a sensor element. A systematic approach of designing the piezoresistive (PZR) test setup, measurement of resistance, force, and deflections, as well as a methodical calculation of the GF are presented comprehensively, intending to understand and to amend common mishaps on giant piezoresistivity of PDCs. The simplicity of the processes used in this work offers an easy and reproducible approach in designing a low-cost sensor prototype with high sensitivity at the microstrain range exposed to both cyclic tensile and compressive loads.

2. Materials and methods

2.1. SiOC thin film preparation

A preceramic polymer Polyramic ® SPR 212 (Starfire Systems, USA), with 17 wt% C, modified with 1 wt% of dicumyl peroxide (used as a cross-linking catalyst) was spin-coated on a 525 µm silicon substrate with a 500 nm SiO_2 barrier layer. SPR 212 is a commercial polymer containing both Si-C and Si-O bond structures which cure to a thermoset at room temperature to 180 °C. The process of spin coating is optimized considering the initial spin speed, acceleration, and final spin speed of the device used. Three milliliters of the precursor are deposited prior to spinning following a static spin coating process. The polymeric film underwent a three-step thermal treatment process as shown in Fig. 1 including crosslinking at 250 °C for 2 h in the air, followed by pyrolysis at 1100 °C for 2 h, and annealing at 1400 °C for 3 h; both high-temperature steps were performed in a nitrogen atmosphere. The resulting SiOC-based thin film was continuous and defect-free and had a thickness of 500 nm. All samples were inspected through a microscope before and after each step of the heat-treatment process to look for the presence of any crack on the surface. Full optimization of the spin coating process was conducted considering three parameters of the device; initial spin speed, acceleration,

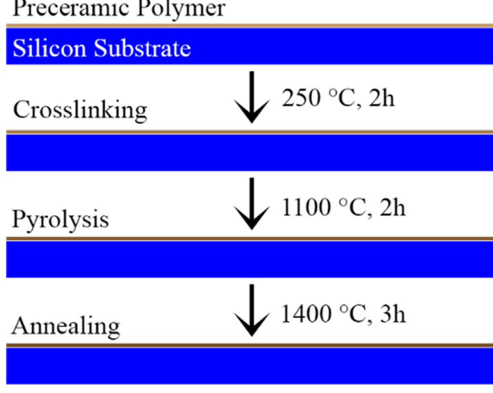

Fig. 1. Preparation of SiOC thin film through the spin coating of preceramic polymer on a silicon substrate followed by three-step thermal treatment; crosslinking, pyrolysis and annealing.

and final spin speed. In the end, the optimum condition resulted in an initial spin speed of 4000 rpm for 30 s, then accelerated to 8000 rpm for 30 s with an acceleration of 5000 rpm/s. The full optimization process of the SiOC film is reported in one of our previous works [41]. The fabricated thin-film samples were characterized with Raman Spectroscopy (LabRAM Horiba HR Raman Spectroscope HR800, Horiba Jobin Yvon GmbH, Bensheim, Germany), and Scanning Electron Microscopy [SEM] coupled with Energy Dispersive Spectroscopy [EDS] (JEOL JSM 7600F, JEOL Ltd., Chiyoda, Tokyo, Japan). The full optimization of the fabrication process, as well as the structural characterization of the SiOC-based films, have been reported in two previous works in references [41,42].

2.2. Strain gauge fabrication

In a cleanroom environment, structured platinum electrodes were deposited on the surface of the SiOC thin film via a photolithographic process shown in Fig. 2. Firstly, the surface was cleaned with a cascading method of acetone and isopropanol to remove the organic compounds on the surface of the film. Subsequently, a 14-μm layer of AZ-10XT photoresist (Merck Performance Materials GmbH, Wiesbaden, Germany) was spin-coated with 1000 RPM at 60 s spinning time onto the SiOC surface. To increase the stability of the resist structure, a soft baking procedure was implemented for 180 s at 110 °C on a direct contact hotplate, followed by a 30-minute rehydration process at room temperature. The rehydration process is a necessary step for the photochemistry of the resist which requires water as a precursor for a faster development rate. Since water is scarce after softbaking, giving sufficient time to reabsorb the moisture from the cleanroom atmosphere.

The exposure process was made with a mask aligner with parallel light passing through the quartz carrier wherein a thin layer of the chromium-coated photomask is attached. The exposure time was set at 240 s with a 1:1 congruent transfer of structure dimensions from the photomask to the resist film. The structure was then developed by dipping the sample on a 1:4 AZ400K solution (Microchemicals GmbH, Ulm, Germany) for at least 5 min with vigorous shaking. The sample was then rinsed with deionized (DI) water, dried with pressurized air, and then post-baked at 110 °C for 180 s on a direct contact hotplate.

The Pt-based electrodes were sputtered using the sputtercoater Quorum Q300TD (Quorum Technologies, East Sussex, United Kingdom). To improve the adhesion of Pt on the SiOC film, a thin layer of 100-nm Cr film was initially sputtered on the sample, followed by sputtering of 1 μm Pt film with a 300 mA current for 1500 s. After the metal deposition, the resist was stripped off by dipping in acetone in an ultrasonic bath, subsequently rinsed with DI water, and dried with compressed air. The resulting sample possessing eight individual sensing elements is shown in Fig. 3. The white region represents the Pt electrode while the dark region represents the SiOC thin film on Si substrate. For the assessment of their piezoresistive performance, individual elements were cut subsequently using a diamond cutter.

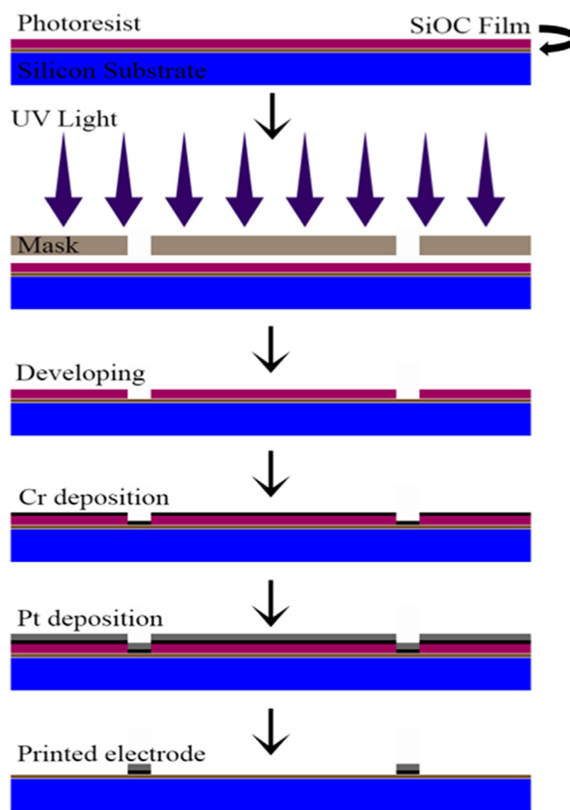

Fig. 2. Photolithography process of the Pt electrode over the SiOC thin film.

2.3. Piezoresistivity measurement

The piezoresistive (PZR) test setup shown in Fig. 4 is an in-house design assembled with multiple parts including a wave function generator (Gwinstek AFG-2225 Arbitrary Function Generator, Good Will Instrument Euro BV, Veldhoven, Netherlands) with 1 μHz resolution, amplified with an analog amplifier (LE 150/100 EBW Amplifier (Piezosystem Jena GmbH, Jena, Germany) with enhanced bandwidth and an output current of 1A. The generated wave function is monitored using a digital oscilloscope (Rohde & Schwarz RTB2004 Digital Oscilloscope, Rohde & Schwarz Finland Oy, Vantaa, Finland) with a bandwidth of 70–300 MHz, and with a high resolution and fast sampling rate. The response factors, i.e. force, resistance, and deflection are measured using an S-form force sensor (ME KD80se s-form force sensor, ME-Meßsysteme GmbH, Hennigsdorf, Germany), a sourcemeter (Keithley 2636 System Sourcemeter, Tektronix Inc., Oregon, United States), and an infrared sensor (Micro-epsilon confocalDT IFS2405-6 sensor, Micro-epsilon Messtechnik, Orenburg, Germany), respectively. The internal software is developed using PyCharm written in Python to record all responses simultaneously. In order to prevent that the contact resistance of the wires used in the test setup interferes with the measurement, a four-wire configuration was taken into consideration when designing the PZR test setup.

Once the individual elements were cut, the sample to be measured was clamped on both ends of the test sample holder as shown in Fig. 5. Then, the resistance change while applying a cyclic load, either tensile or compressive, was measured.

2.4. Data treatment and statistical approach

For the calculation of the GF values, based on the structured element in Fig. 3 and the test setup in Fig. 4, each element was treated as a fixed beam with a concentrated load applied at the center. The recorded applied force, the change in resistance, as well as the deflection of the beam as the cyclic load is applied, were used to calculate the radius of curvature of the beam using the classical beam theory [43]. The strain is calculated on the surface of the beam in relation to the radius of curvature as displayed in Fig. 6B using Eqs. (1) and (2). In Eq. (1), E, I, and M correspond to the elastic modulus of the SiOC film, the second moment of inertia, and the bending moment, respectively. The free-body, shear, and force diagrams used in the derivation of the bent structure are shown in Fig. 6A.

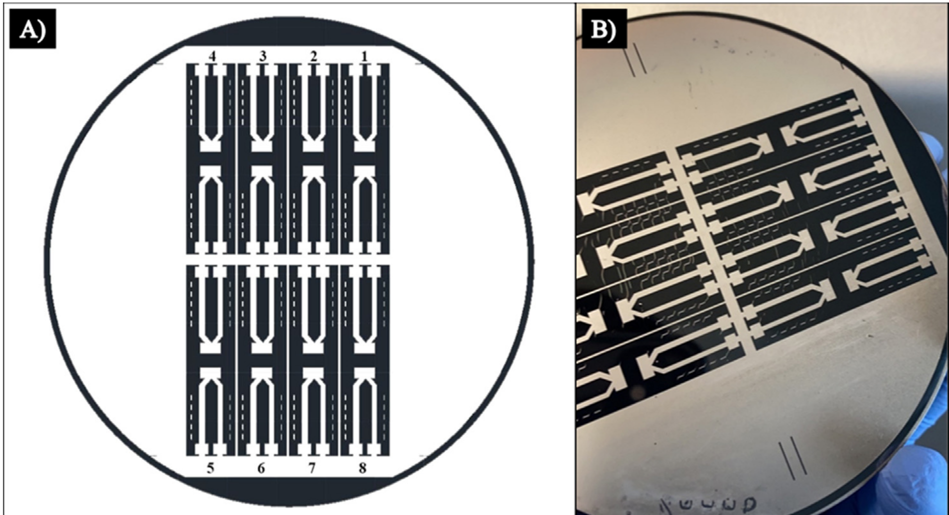

Fig. 3. Element design after the printing of Pt electrode. The white region represents the Pt electrode while the dark region represents the SiOC thin film on Si substrate. Each element is labeled from 1 to 8 according to the numbering shown on the image.

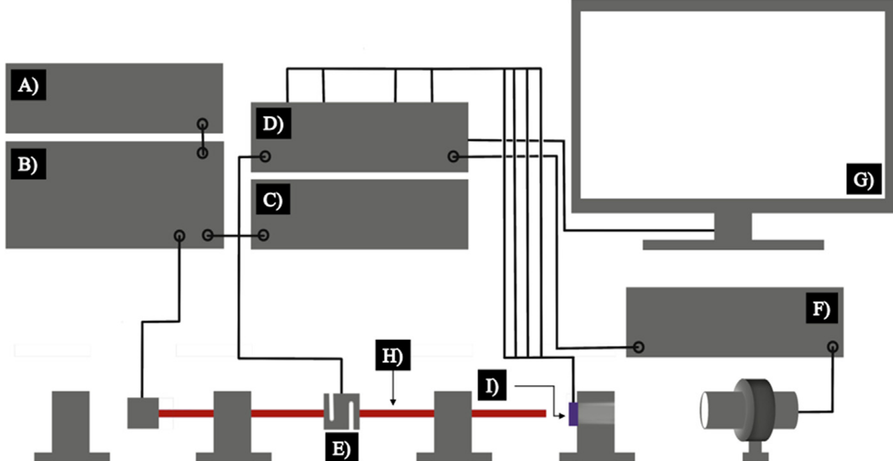

Fig. 4. PZR test setup. A) Wave function generator. B) Amplifier. C) Digital Oscillator. D) Sourcemeter. E) S-form Force sensor. F) Deflection infrared sensor. G) Monitor. H) Force applicator. I) Sample holder.

$$R = \frac{EI}{M} = \frac{L^2}{24\delta} \tag{1}$$

$$\varepsilon = \frac{t}{2R} \tag{2}$$

A series of experiments are conducted in order to optimize the design and performance of the elements used in this work. Firstly, the parameters of the test setup, amplitude, and frequency, are tested to identify the linear strain range with full resistance response reversibility. The data are treated by performing nonlinear regression on each curve. By fitting with the sine waveform, the applied and fitted amplitudes are determined and compared. Subsequently, the deflection responses are used to limit the response quality as the frequency or the number of cycles per minute increases. The waveform is also changed from a sine to a square waveform to determine the relaxation time of the responses (resistance and force) during loading and unloading.

In order to narrow down the difference in the process, analysis of variance (ANOVA) is used to establish the effect of the position or the location of each element on the substrate. Then, the capability sixpack which assesses the process indices (C_{pk} *and* P_{pk}) by comparing the GF values relative to individual elements taken from different substrates.

3. Results and discussion

The relation of the high mobility and the resistance change of semiconducting materials was been explained by the Many-Valley theory of Herring in 1955, which e.g. showed refined models on energy band structures and charge carrier transport mechanisms in n-type silicon and germanium materials [12,44,45]. For p-type materials, empirical results based on Hamiltonian strain and cyclotron resonance experiments revealed that hole mobilities are affected by band splitting, band warping, mass change, etc [46–49]. There is various information concerning the charge carrier transport in SiOC-based ceramic materials is available in the literature [35,50]. As reported in our previous work [42], SiOC-based thin films possess significantly larger charge carrier mobility relative to that of the monolithic SiOC valued at 186 $cm^2\ V^{-1}\ s^{-1}$ with room-temperature base resistance ca. 65–85 Ω, i.e., a resistivity of 6.52×10^{-2} Ω.cm. The enriched mobility of the SiOC thin film has been accounted for the improved percolation threshold due to the

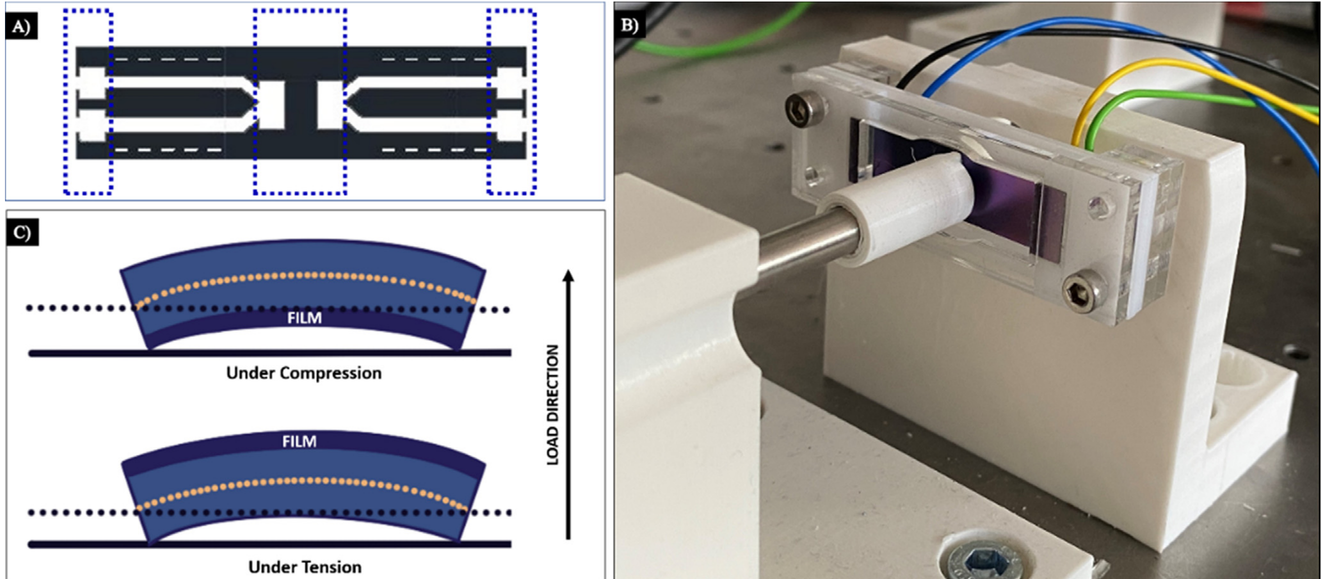

Fig. 5. Clamping setup of the element to the test sample holder. A) Both ends are clamped making a Fixed-beam configuration. The resistance is measured in the middle between the two Pt pads as indicated on the marked area. B) Actual photo of the clamped element. C) The sample is under compression if it is oriented front-facing the force applicator otherwise it is under tension.

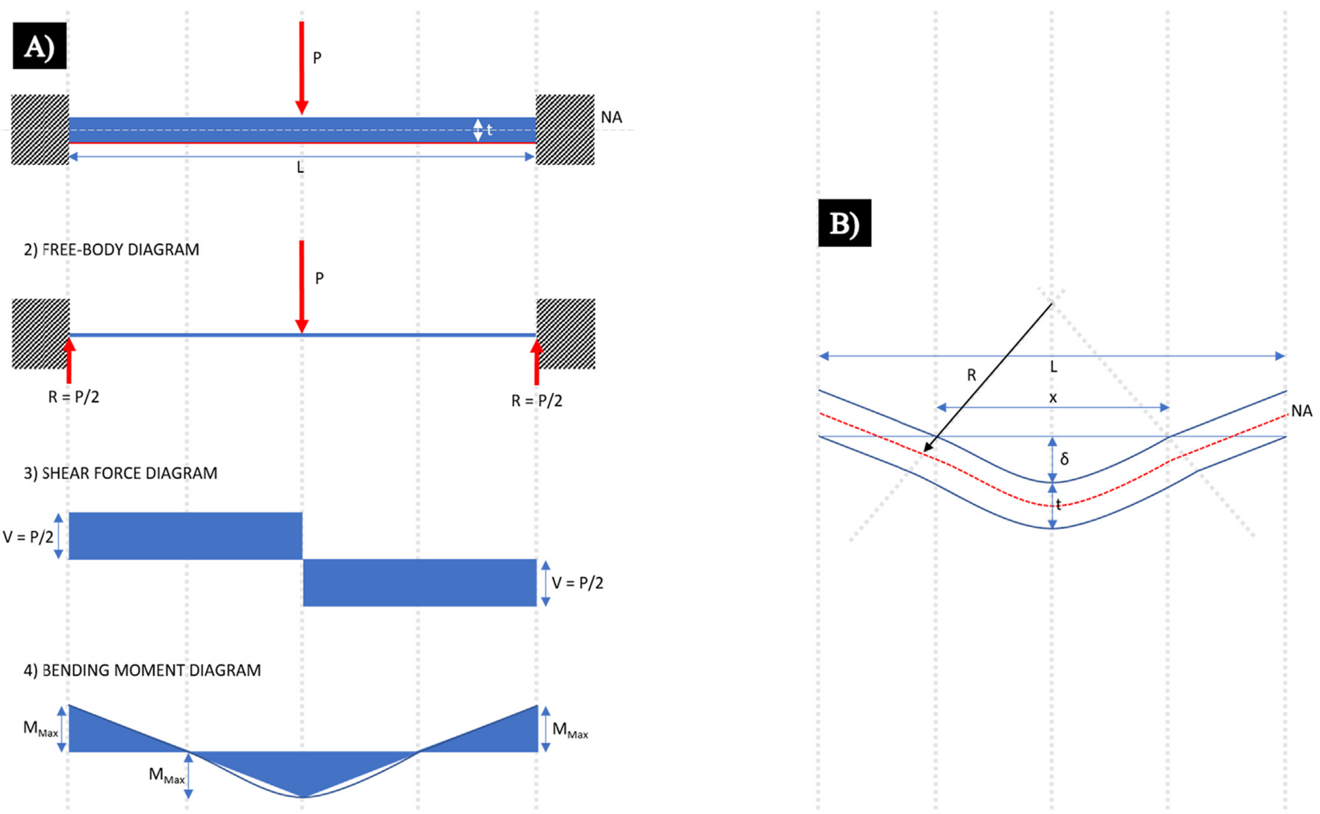

Fig. 6. A) Diagrams that are used for the derivation of the radius of curvature of the bent element. 2) Free-body diagram, 3) Shear force diagram, and 4) Bending moment diagram. B) Diagram of the radius of curvature of the bent element. [R: Radius of curvature, L Length of an element, x: Length of the bent region, t: the thickness of the element, NA: Neutral axis, δ: deflection]

phase-separated morphology of the material indicated in Fig. 7C. In Fig. 7A and B, defined edges of the Pt electrodes are visible on the surface of the SiOC film. By profilometry, the thickness of the printed electrode is measured at ca. 1 μm with a roughness of 100 nm. Tape test and exposure to 700 °C in air for 24 h exhibited good adhesion of the Pt electrode to the film with no sign of peel-off. No bleeding of platinum is detected on the surface of the film as can be seen in Fig. 7B also supported by EDS analysis. The elemental mapping of Fig. 7C revealed a composition with 36.32 wt % oxygen, 12.23 wt% carbon, and 51.45 wt% silicon. In Fig. 7D, E,

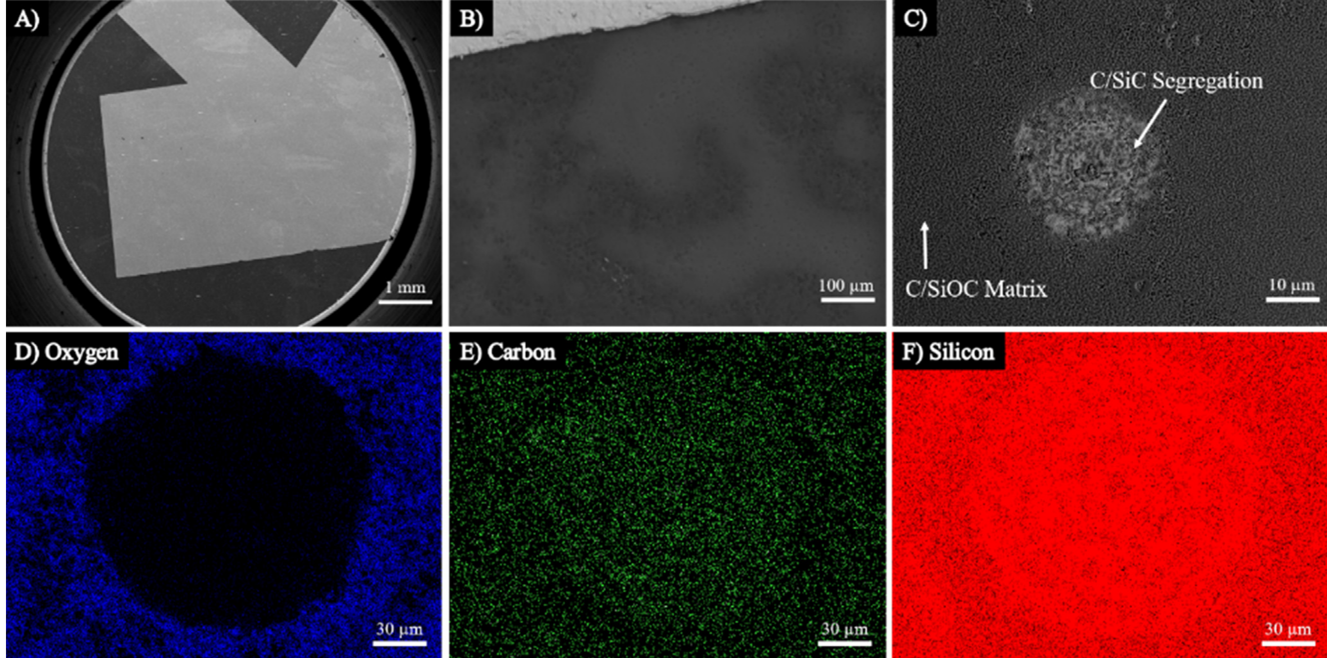

Fig. 7. SEM images of Pt electrode on SiOC film taken at a magnification of A) 25x and B) 1000x. Defined edges of the PT electrode are distinguishable; no peel-off or bleeding is detected, indicating very good adhesion of the electrode. C) Magnified view of the SiOC thin film exhibiting the segregation of C/SiC from the C/SiOC matrix [41,42] supported by EDS elemental mapping of D) Oxygen, E) Carbon, and F) Silicon.

and F, the segregated area can easily be visualized as a carbon-rich and oxygen-deficient region relative to the matrix.

The first set of values taken from the experimental setup concentrates on finding out the appropriate strain range for the applicability of the GF of the material. By non-linear regression, the amplitude of the sine waveform on the data points is acquired and rivaled in Table 1 wherein $A_{Applied}$ is the set amplitude using the function generator, and A_{Fitted} is the amplitude taken from the regression. As displayed in Fig. 8, the distribution of data points at 12 mVPP (millivolt peak-to-peak) is more scattered relative to that of 200 mVPP, with R^2 values of 0.7431 and 0.9919, respectively. At amplitudes below 40 mVPP, the response factor (Amplitude) showed negative ca. 30% deviation from the applied amplitudes, while negative ca 5% deviation at amplitudes above 200 mVPP. Given these data, the range of amplitude application is identified and restricted to 50–200 mVPP for the succeeding measurements.

The frequency values (i.e., corresponding to the number of load cycles applied per minute, see Table 2) were varied from 50 mHz to 1000 mHz to assess the stability of the resistance response. No significant changes are detected on both deflection and resistance changes as the number of cycles per minute increases from 3 to 30. At frequencies beyond 500 mHz, the response started to surge, giving an inconsistent waveform with varying amplitudes. In the succeeding trials, the frequency was consequently held constant at 200 mHz for simpler analysis of the hysteresis of the GF plots.

In Fig. 9, the resistance response of a representative element tested in both tensile and compressive cyclic load is shown. Both plots exhibit a sine wave response of the resistance when the force is applied with a frequency of 200 mHz. It is shown that the curves of resistance and applied force were synchronous when the sensing element was tested in tension; while a 180° phase shift of the resistance curve concerning the applied force curve was observed when the element was measured in compression. This is in agreement with the expected response of percolative systems, such as polymer-matrix nanocomposites [51–53]. Additionally, the response of the sensing elements tested in both tensile and compression mode is shown to be fully reversible (Fig. 9). Furthermore, it can be seen that the relative change in resistance of the element under compression (0.35 Ω) is larger than that of the element tested under tension, i.e., 0.25 Ω.

As emphasized in a review paper of Chung in 2020, the GF of a piezoresistive material must be reported based on a strain range instead of a particular strain value [5]. Application of excessive strain on the material results in the inclusion of irreversible resistance change which then translates to large $\Delta R/R_0$. Failure to acknowledge this linear relationship between the resistance change and the applied strain only gives an overestimated sensitivity of the gauge. Thus, in Fig. 10, the fractional change in resistance with respect to the zero resistance is plotted against the strain values to obtain the slope of the linear part of the curve which denotes the true GF of the elements. Several findings can be deduced from Fig. 10 including:

a. *$\Delta R/R_0$ is higher when a compressive load is applied to the sample.* Upon application of compressive load, the conduction of the material improved leading to a decrease in resistance. In retrospect from previous works [35,42], an average size including tortuosity (L_{eq}) of ca. 50 nm is measured for the

Table 1
Optimization of applied amplitude on the piezoresistive test setup by non-linear regression.

Sample	$A_{Applied}$ [mVPP]	A_{Fitted} [mVPP]	$\frac{A_{Fitted}-A_{Applied}}{A_{Applied}}$ [%]
1	0.013	0.0085	−34.62%
2	0.025	0.0170	−32.00%
3	0.038	0.0253	−33.42%
4	0.050	0.0507	1.40%
5	0.100	0.1064	6.40%
6	0.150	0.1553	3.53%
7	0.200	0.2031	1.55%
8	0.225	0.2129	−5.38%
9	0.250	0.2329	−6.84%

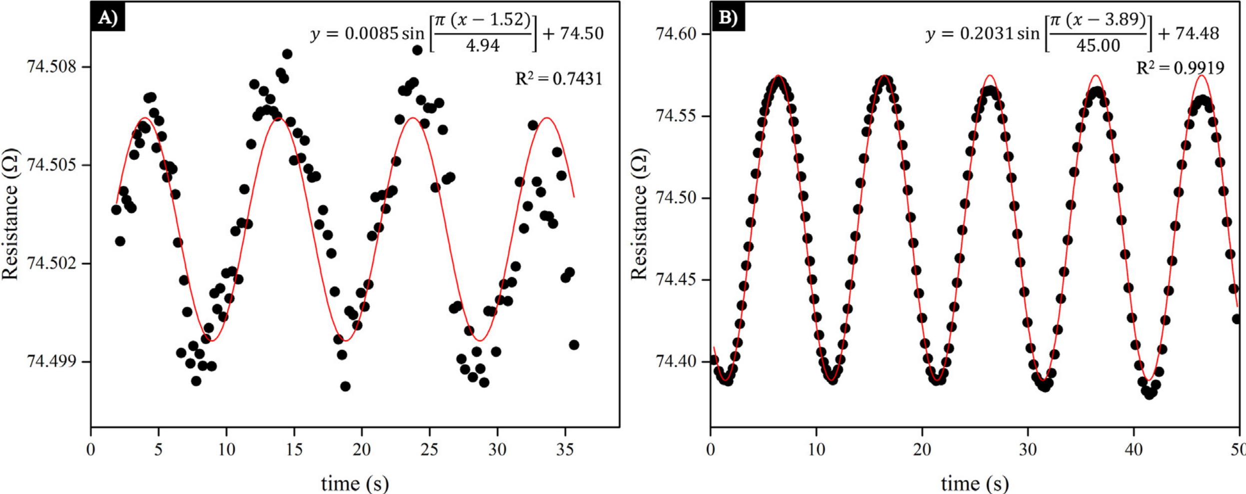

Fig. 8. Non-linear regression of the electrical resistance response at different applied amplitudes. A) 12 mVPP, and B) 200 mVPP. The red line represents the fitted sinusoidal curve with the equations shown on respective graphs. (For interpretation of the references to colour in this figure legend, the reader is referred to the web version of this article.)

Table 2
Effect of the applied load frequency on the deflection and resistance change of the studied samples. The response is stable in a frequency range up to 500 mHz. Based on this finding, a load frequency of 200 mHz was chosen for the testing experiments.

Frequency (mHz)	Cycle per minute (cpm)	Deflection (m)	$\Delta R/R_0$
50	3	1.45E−04	0.002356
100	6	1.41E−04	0.002177
200	12	1.47E−04	0.002483
300	18	1.45E−04	0.002194
400	24	1.44E−04	0.002323
500	30	1.42E−04	0.002208
800	48	1.34E−04	0.002931
1000	60	1.27E−04	0.003167

segregated sp^2-hybridized carbon phase in SiOC thin films with distinguishable segregation in a partially conductive C/SiOC matrix shown in Fig. 7C. This is one magnitude larger than the measured L_{eq} for SiOC monolithic sample [35]. As reported, the electrical conductivity of the film is improved ca. 16 S cm^{-1} which is comprehensively linked to the enriched carrier mobility of the film. In a theoretical framework postulated by Cattin and Hubert in 2014 [54], the effect of the aspect ratio of the segregated conductive phase on the dependence of the electrical response of an electroconductive polymer nanocomposite was addressed. The resistance change of the materials depends on the concentration of the conductive phase and the spacing between them which in turn is primarily governed by quantum mechanical tunneling through the insulating matrix. Thus, the resistance change of the film depends on the interparticle separation which increases as the particle network is stretched and the electrical continuity is broken increasing the resistance. Conversely, the interparticle separation decreases as the network is compressed resulting in more interconnected conductive particles which lower the resistance of the material. Although $\Delta R/R_0$ is larger for compression against tension, the difference of values is statistically insignificant analyzed using a two-sample T-test at a 95% confidence interval *(T = 3.07, degrees of freedom = 19, and p = 0.006)*. Also related to the change in resistance observed in Fig. 9A, this denotes that the applied tensile load on the material is insufficient to break the percolation path of the material. It can be remembered that the SiOC matrix is also

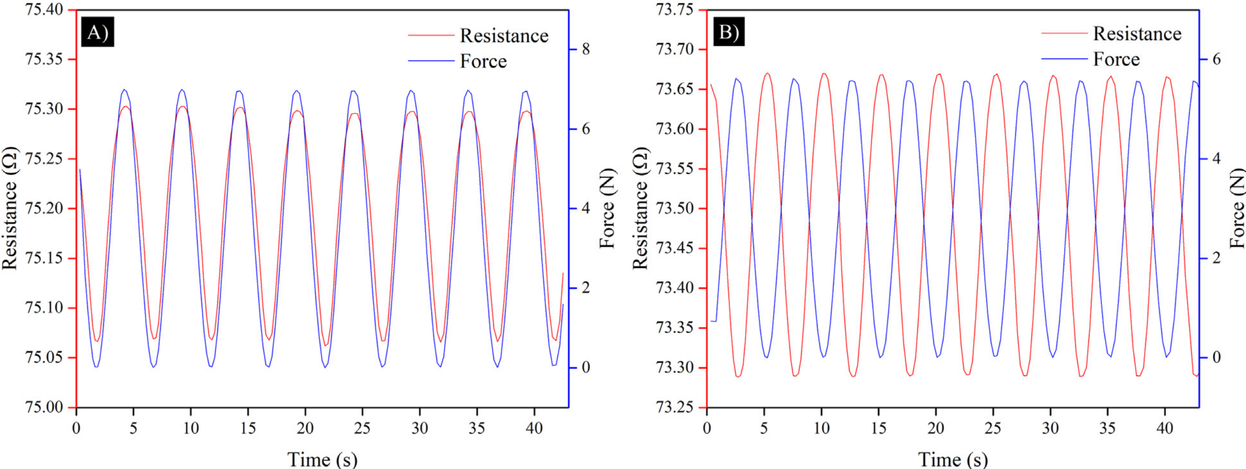

Fig. 9. Resistance response of a sensing element as a function of the time during testing under A) tensile cyclic load, and B) compressive cyclic load. The applied force during the tests was 6.2 and 5.8 N for tensile and compressive load, respectively. For both tests, a lead frequency of 200 mHz was used.

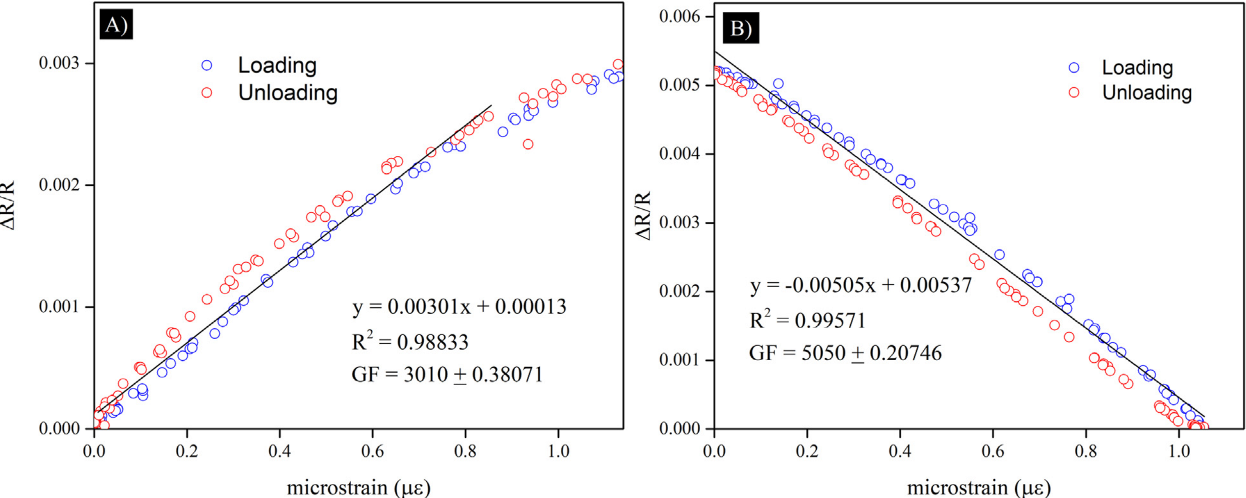

Fig. 10. Gauge factor of SiOC film after cyclic loading. Gauge factor derived from the slope of strain *vs* $\Delta R/R_0$ when the sample is under A) tension and B) compression.

partially conductive in itself containing carbons with L_{eq} of 7 nm which can bridge the gap of the percolative path between the bigger carbon precipitates [42]. This SiOC matrix follows a similar mechanism of previously proposed performance of monolithic samples with less charge mobility than the SiOC film which is dependent on the temperature of thermal treatment, and carbon content [35,50,55].

b. *The linear strain range is larger when a compressive load is applied.* In theory, GF is independent of the strain range and only proportional to changes in resistance and strain [10], yet the reversible effect of strain on the material microstructure varies in the elastic regime. Hence, the assessment of the piezoresistive response must be conducted within the elastic region which can be obtained by using cyclic loading. Consequently, the strain range wherein linearity is evident can be identified and should be the extent of applicability of the device. In Fig. 10A showing the response of the SiOC thin film under tensile load, nonlinearity is observed at strains above 0.8×10^{-6}; whereas the whole measurement region under compression showed linear behavior as reflected in Fig. 10B.

c. *The studied strain gauge elements possess giant piezoresistivity, which is higher in compression than that in tensile loading.* Despite positive piezoresistivity being more common especially on commercialized piezoresistivity-based sensors, Fig. 10 confirms a higher sensitivity of the samples under compression (GF $\sim 5 \times 10^3 \pm 0.20746$) than that measured upon tensile load (GF $\sim 3 \times 10^3 \pm 0.38071$). This is of particular consideration when designing the sensor for the SiOC thin film placement. However, the SiOC thin film element can be considered as possessing ultrahigh sensitivity in both loading modes.

d. *Very narrow mechanical hysteresis (loading vs. unloading cycles) and no significant value fluctuation are observed on both loading types,* i.e. *compressive and tensile.* Hysteresis on piezoresistive sensors limits the accuracy of the device in microscale applications. In our case, the hysteresis characteristic of elements corresponds to the change in resistance in the strain loading and unloading intervals that do not overlap, and that there is ΔR difference between these two curves. It has been pointed out that hysteresis poses problems in piezoresistive sensors, which originates from weak interactions between the conductive material and the amorphous matrix [56,57]. These effects cause slow recovery of signal with relaxation time that can be more detrimental leading to a permanent change in the initial resistance or the resistance in the absence of pressure. In our recent work [42], the x-ray diffraction pattern of the synthesized SiOC film showed a broad bump at the 2θ value of 22° which is assigned to amorphous silica. Qualitative deconvolution of the peak revealed the shoulder peak at 25.5° which was assigned to amorphous carbon. These results are further supported by Raman analysis data which discriminated the graphitization indices between the film matrix and the phase separation. In Table 3, it is indicated that the free carbon phases are larger on the phase-segregated area as compared to the matrix of the film wherein the L_{eq}, the average continuous graphene length including tortuosity [58], is 8 times larger.

Using Eq. (3), the degree of hysteresis (DH) in Fig. 10 is calculated, with $A_{Unloading}$ and $A_{Loading}$ representing the areas under the unloading and loading curves, respectively [59,60]. Samples under tension revealed a DH value of ca. 15%, which is almost three times larger than that of samples under compression (DH ca. 5.6%). In a table of values collected by Oh *et al* [60], strain sensors typically operate with DH values being above 30%. The strain gauge elements produced in this work possess significantly lower DH values (especially when compression load is applied), indicating impressively high reversibility of their piezoresistive response which may make periodic calibrations less mandatory.

$$DH = \frac{|A_{Unloading} - A_{Loading}|}{A_{Loading}} \quad (3)$$

The piezoresistive response and the relaxation time of the sensor elements obtained by generating a square wave function are shown in Fig. 11. The value of the relative resistance is constant when there is no pressure applied to the sensor, but when an external tensile load is applied, the bending causes a relative change of the resistance $\Delta R/R_0$ of ca. 0.03 Ω; subsequently, the

Table 3
Graphitization indices of SiOC film as calculated from the Raman analysis data.

Graphitization Index	Matrix	Phase segregation
Crystallite size, L_a [nm]	7.2	11.9
Inter-defect distance, L_D [nm]	7.5	9.7
Defect density, n_D [10^{11} nm^{-3}]	8.0	5.0
L_{eq} [nm]	7.1	56.3

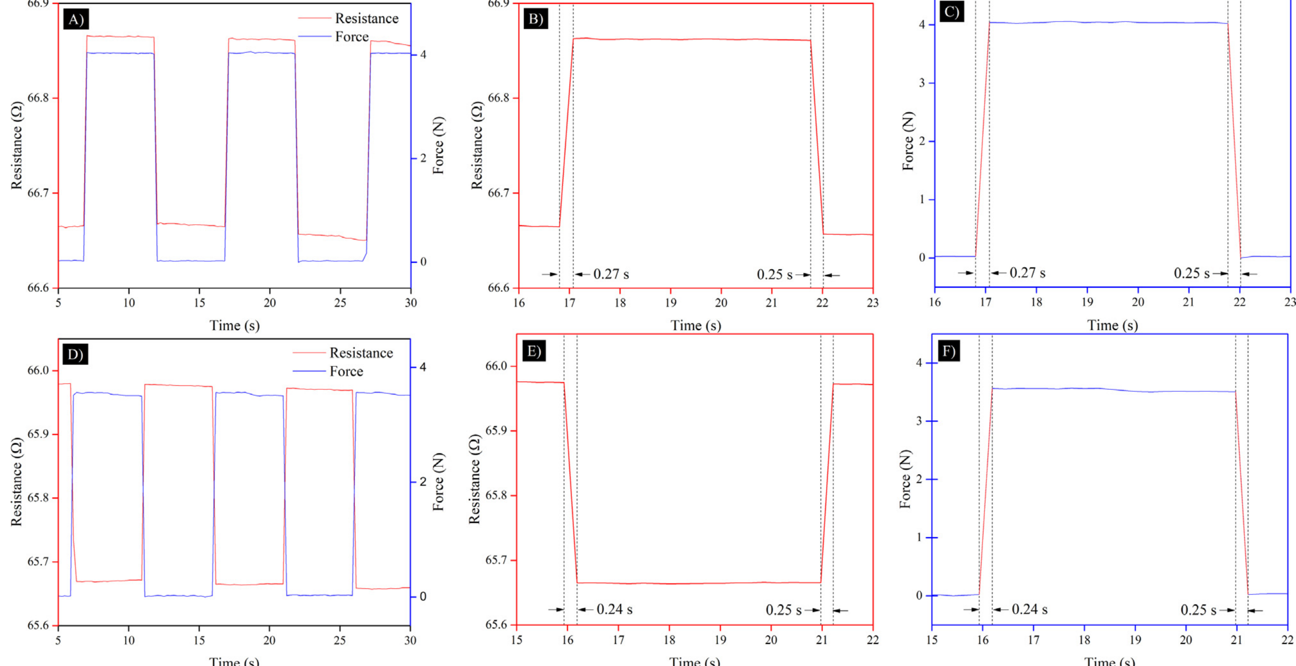

Fig. 11. Resistance response and relaxation time of the strain sensor. A) Square waveform applied on the sensor element under tension with a magnified view of (B) change in resistance, and (C) change in applied force. D) Square waveform applied on the sensor element under compression with a magnified view of (E) change in resistance, and (F) change in applied force.

resistance remains constant until the load is released. By linear regression on both force and resistance responses, the slopes of the lines are parallel. It is also evident that resistance and force responses are synchronous indicating excellent responsiveness of the material to the applied load.

Considering the plot in Fig. 11B and C showing the resistance and force responses during one tensile load cycle, the recovery time of the resistance and force during unloading (250 ms) is slightly shorter than that of the response during loading (270 ms). This finding further explains the hysteresis seen in Fig. 10A. When a compressive load is applied, this difference is smaller, the recovery time (250 ms) being slightly larger than the response time (240 ms). These results are in approval that compressive load applied on the element gives a slightly better resistance response within a shorter period.

The variability of the process used in the present study can be significant, given that 8 sensing elements were fabricated on one substrate. To distinguish the stability and capability of the process as well as the performance of the elements, a general ANOVA (Analysis of Variance) and a normal capability sixpack analysis are employed [61–63].

In Fig. 12, the means and variances of the eight individual elements prepared on a single substrate (see Fig. 3 in the Experimental Part) are presented through a boxplot. The absolute values of the gauge factors are used in this approach wherein the GF under compressive load takes the upper bounds while the GF under tensile load is on the lower bounds. The stepwise mean connector displayed a rather significant difference of the GF average values of Elements 1 and 2, and a more spread out means on the first four elements (upper layer in Fig. 3). On the other hand, the bottom half elements are more controlled with Elements 7 and 8 having comparable means.

To understand the effect of these variances on individual performances of the elements, the ANOVA result is presented in Table 4. It is hypothesized that the element position on the substrate has a significant effect on the measured GF. Since the p-value (0.73) is greater than 0.05, it can be deduced that at a 95% confidence level, the differences measured on the GF of each element at different positions within the substrate are not significant. It can be assumed from this result that the Si substrate is evenly coated with the SiOC film with uniform thickness.

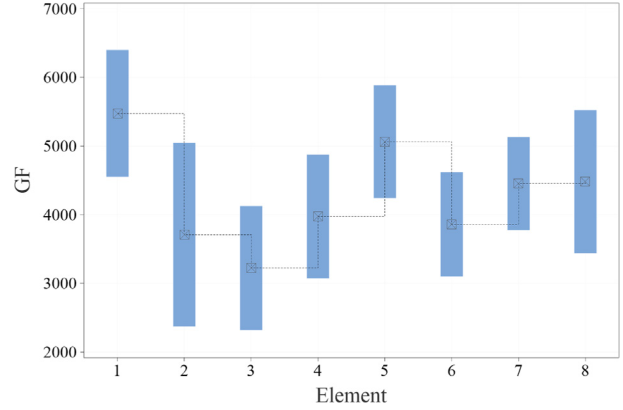

Fig. 12. Boxplot of elements taken from one sample substrate in response to compressive and tensile loads. The upper bounds represent the absolute values of the GF in compression while the lower bounds represent the GF values in tension. The stepwise mean connector line showed the largest variance on the first two elements while the Elements 5–8 displays (bottom layer in Fig. 3) more controlled mean values with Elements 7 and 8 having comparable means.

For capability assessment, the analysis is performed considering 10 groups comprising of 4 elements each, taken from 6 different SiOC thin film batches. Each element is tested at least in triplicate. In Fig. 13 on both types of applied load, on the I Chart, zero out-of-control points are identified with all data within the upper and lower control limits *(UCL and LCL)* of the calculated gauge factors with a normal distribution *(p-values above 0.05)* and good spread reflected on the histogram and probability plots. Process indices are used to know the capability of the process to be within the

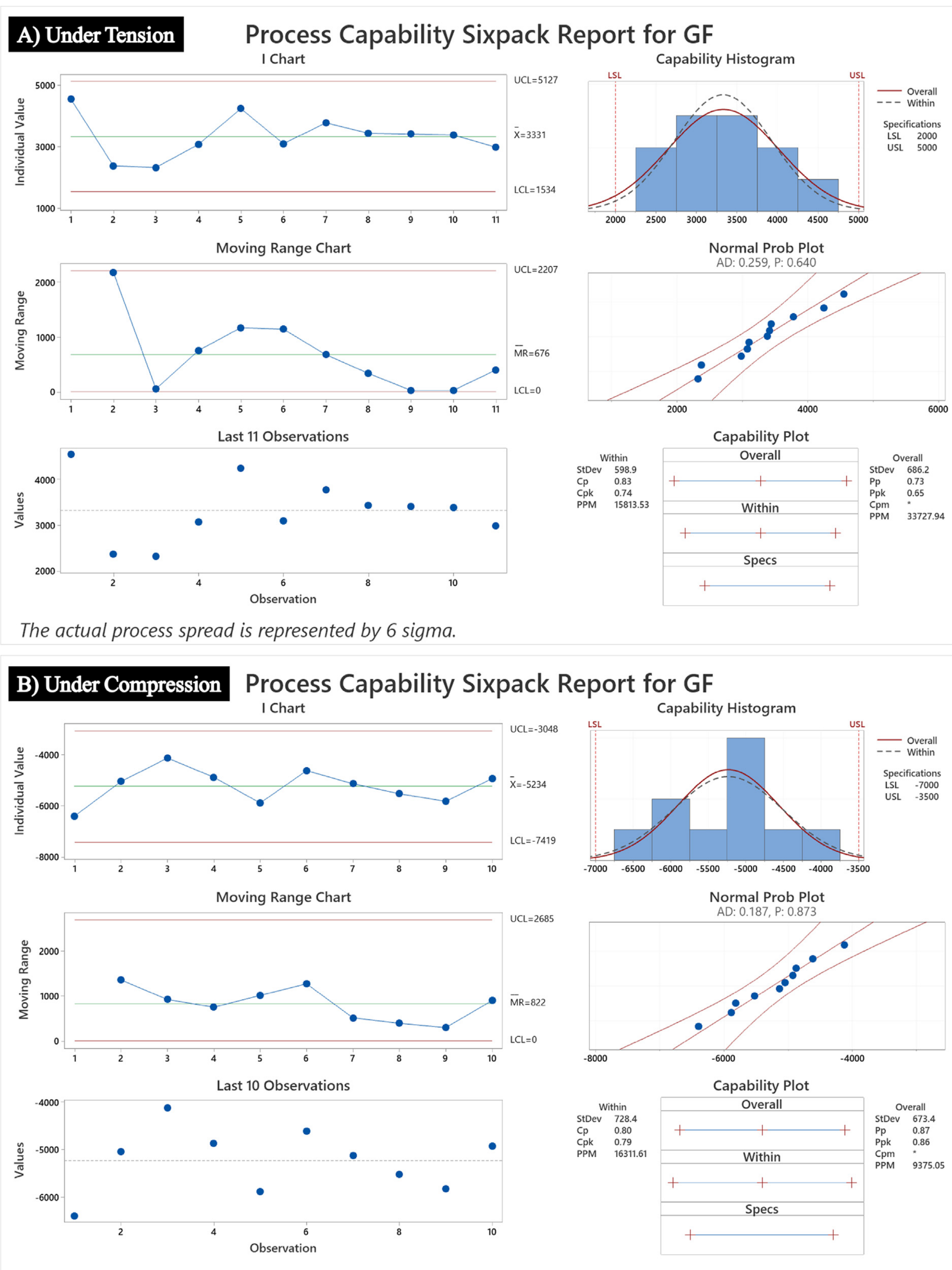

Fig. 13. Process capability sixpack analysis of sensor elements under A) Tension and B) Compression. The analysis is performed at a 95% confidence level over 10 groups comprised of 4 elements per group taken from 6 different substrate batches with 3 replicates.

specification limits or the tolerance range [64,65]. The indices also help to assess the consistency of the process over time with generally higher C_{pk} *(process capability index)* values indicating a more capable process. Comparing the indices, C_{pk} and P_{pk} *(process potential index)*, both values are less than 1 and are close to each other. Although values are statistically controlled, C_{pk} values being less

than 1 revealed that the process is only at 87% yield and requires further improvement by controlling several process-related factors such as the environment, test setup, and human interventions.

4. Conclusions

A highly sensitive SiOC-based piezoresistive sensor prototype operating at a microstrain range is devised and verified in this work. It started with a methodical approach addressing known misperceptions around giant piezoresistivity on PDCs. Using a previously prepared and characterized SiOC thin film, a simple process is used to create a sensor prototype that is tested in two different mechanical cyclic loads, tensile and compressive. The first part of this work focuses on designing the piezoresistivity test setup that is internally developed and assembled. Here, the effect of the inclusion of contact resistance on the measurement is alleviated. Secondly, cyclic load application confirmed the good reversibility of the resistance changes.

The prototype is found to have a good performance at the microstrain range below 1 for compressive loading, and 0.8 for tensile loading. Instead of concentrating the GF over a certain strain value, the GF is calculated by linear regression of the $\Delta R/R_0$ *vs* microstrain which revealed the giant piezoresistivity of the SiOC thin film sensor element valued at 3010 and 5050 under tension and compression, respectively. Relaxation time for both cases is found to be 250 ms while faster response time is detected under compression coupled with higher resistance change of the material which was justified by the higher aspect ratio of the carbon L_{eq} on the SiOC thin-film decreasing the interparticle spacing of the conductive particles. Consequently, tensile loading posed a smaller change in resistance perhaps caused by the smaller carbon crystals distributed within the SiOC matrix serving as a secondary conductive phase. The process capability of the prototype is also analyzed revealing a statistically stable process and good replicability. Though capability indices indicated the statistical stability of the process, the current approach can further be optimized for improvements that can be done in a more controlled environment.

The fabricated sensor prototype from this work can be used to challenge the current status quo of self-sensing devices due to its simplistic and cost-efficient fabrication process with high reproducibility. Functionally, the prototype can operate at the microstrain with high sensitivity. Moreover, the thermal stability of the material used, SiOC, provides an opportunity for further applications which can be explored at elevated temperature, above 400 °C, higher than the current maximum temperature of commercial Si-based piezoresistive sensors.

Funding

The authors gratefully acknowledge funding from the German Science Foundation (DFG Germany) – grants no. 411658150 (Microstructured C/SiCX (X = O,N)-based high temperature strain gauge). Additionally, EI acknowledges funding from DFG within the Heisenberg program (IO 64/14-1).

CRediT authorship contribution statement

Emmanuel Ricohermoso: Conceptualization, Methodology, Software, Formal analysis, Investigation, Resources, Data curation, Writing – original draft, Visualization, Project administration. **Florian Klug:** Methodology, Software, Formal analysis, Investigation, Resources, Data curation, Project administration. **Helmut Schlaak:** Writing – review & editing, Funding acquisition. **Ralf Riedel:** Writing – review & editing, Funding acquisition. **Emanuel Ionescu:** Conceptualization, Writing – review & editing, Supervision, Project administration, Funding acquisition.

Declaration of Competing Interest

The authors declare that they have no known competing financial interests or personal relationships that could have appeared to influence the work reported in this paper.

Acknowledgments

In this section, you can acknowledge any support given which is not covered by the author's contribution or funding sections. This may include administrative and technical support, or donations in kind (e.g., materials used for experiments).

References

[1] A.A. Barlian, W.-T. Park, J.R. Mallon, A.J. Rastegar, B.L. Pruitt, Review: Semiconductor Piezoresistance for Microsystems, Proc. IEEE Inst. Electr. Electron. Eng. 97 (3) (2009) 513–552, https://doi.org/10.1109/JPROC.2009.2013612.

[2] A.S. Fiorillo, C.D. Critello, S.A. Pullano, Theory, technology and applications of piezoresistive sensors: A review, Sens. Actuators, A 281 (2018) 156–175, https://doi.org/10.1016/j.sna.2018.07.006.

[3] J. Teixeira, L. Horta-Romarís, M.-J. Abad, P. Costa, S. Lanceros-Méndez, Piezoresistive response of extruded polyaniline/(styrene-butadiene-styrene) polymer blends for force and deformation sensors, Mater. Des. 141 (2018) 1–8, https://doi.org/10.1016/j.matdes.2017.12.011.

[4] M. Mohammed, M. Farman, M. Salah, State of the art of the use of strain gauges in roads, AIP Conf. Proc. 2404 (2021), https://doi.org/10.1063/5.0069098 080018.

[5] D.D.L. Chung, A critical review of piezoresistivity and its application in electrical-resistance-based strain sensing, J. Mater. Sci. 55 (32) (2020) 15367–15396, https://doi.org/10.1007/s10853-020-05099-z.

[6] W. Dong, W. Li, L. Shen, D. Sheng, Piezoresistive behaviours of carbon black cement-based sensors with layer-distributed conductive rubber fibres, Mater. Des. 182 (2019) 108012, https://doi.org/10.1016/j.matdes.2019.108012.

[7] S. Nauman, Piezoresistive Sensing Approaches for Structural Health Monitoring of Polymer Composites—A Review, Eng. 2 (2021) 197–226, https://doi.org/10.3390/eng2020013.

[8] M. Tendo Innocent, W. Ma, H. Xiang, J. Zhou, S. Yu, M. Zhu, Nonmonotonic piezoresistive fibers tuned towards biomechanical sensing, Mater. Des. 205 (2021) 109715, https://doi.org/10.1016/j.matdes.2021.109715.

[9] E. Ricohermoso, F. Rosenburg, F. Klug, N. Nicoloso, H.F. Schlaak, R. Riedel, E. Ionescu, Piezoresistive carbon-containing ceramic nanocomposites – A review, Open Ceramics. 5 (2021) 100057, https://doi.org/10.1016/j.oceram.2021.100057.

[10] J.W. Cookson, Theory of the Piezo-Resistive Effect, Phys. Rev. 47 (2) (1935) 194–195, https://doi.org/10.1103/PhysRev.47.194.2.

[11] A.C. Ruge, Strain gauge, US2350972A, 1944. https://patents.google.com/patent/US2350972A/en (accessed August 24, 2021).

[12] J. Bardeen, W. Shockley, Deformation Potentials and Mobilities in Non-Polar Crystals, Phys. Rev. 80 (1) (1950) 72–80, https://doi.org/10.1103/PhysRev.80.72.

[13] C.S. Smith, Piezoresistance Effect in Germanium and Silicon, Phys. Rev. 94 (1) (1954) 42–49, https://doi.org/10.1103/PhysRev.94.42.

[14] W.P. Mason, R.N. Thurston, Use of Piezoresistive Materials in the Measurement of Displacement, Force, and Torque, J. Acoust. Soc. America 29 (10) (1957) 1096–1101, https://doi.org/10.1121/1.1908710.

[15] H.-P. Phan, D.V. Dao, L.i. Wang, T. Dinh, N.-T. Nguyen, A. Qamar, P. Tanner, S. Dimitrijev, Y. Zhu, The effect of strain on the electrical conductance of p-type nanocrystalline silicon carbide thin films, J. Mater. Chem. C 3 (6) (2015) 1172–1176, https://doi.org/10.1039/C4TC02679A.

[16] H.-P. Phan, D.V. Dao, K. Nakamura, S. Dimitrijev, N.-T. Nguyen, The Piezoresistive Effect of SiC for MEMS Sensors at High Temperatures: A Review, J. Microelectromech. Syst. 24 (6) (2015) 1663–1677, https://doi.org/10.1109/JMEMS.2015.2470132.

[17] T.-K. Nguyen, H.-P. Phan, T. Dinh, J. Han, S. Dimitrijev, P. Tanner, A.R. Md Foisal, Y. Zhu, N.-T. Nguyen, D.V. Dao, Experimental Investigation of Piezoresistive Effect in p-Type 4H–SiC, IEEE Electron Device Lett. 38 (7) (2017) 955–958, https://doi.org/10.1109/LED.2017.2700402.

[18] R. Guo, Y. Suo, H. Xia, Y. Yang, Q. Ma, F. Yan, Study of Piezoresistive Behavior of Smart Cement Filled with Graphene Oxide, Nanomaterials 11 (2021) 206, https://doi.org/10.3390/nano11010206.

[19] C. Hu, Z. Li, Y. Wang, J. Gao, K. Dai, G. Zheng, C. Liu, C. Shen, H. Song, Z. Guo, Comparative assessment of the strain-sensing behaviors of polylactic acid nanocomposites: reduced graphene oxide or carbon nanotubes, J. Mater. Chem. C 5 (9) (2017) 2318–2328, https://doi.org/10.1039/C6TC05261D.

[20] Y.-F. Fu, Y.-Q. Li, Y.-F. Liu, P. Huang, N. Hu, S.-Y. Fu, High-Performance Structural Flexible Strain Sensors Based on Graphene-Coated Glass Fabric/Silicone Composite, ACS Appl. Mater. Interfaces 10 (41) (2018) 35503–35509, https://doi.org/10.1021/acsami.8b0942410.1021/acsami.8b09424.s001.

[21] S. Sahli, D.M. Aslam, Ultra-high sensitivity intra-grain poly-diamond piezoresistors, Sens. Actuators, A 71 (3) (1998) 193–197, https://doi.org/10.1016/S0924-4247(98)00181-2.

[22] A. Yamamoto, T. Tsutsumoto, Piezoresistive effect of CVD polycrystalline diamond films, Diam. Relat. Mater. 13 (4-8) (2004) 863–866, https://doi.org/10.1016/j.diamond.2003.12.017.

[23] H.C. Chiamori, J.W. Brown, E.V. Adhiprakasha, E.T. Hantsoo, J.B. Straalsund, N.A. Melosh, B.L. Pruitt, Suspension of nanoparticles in SU-8: Processing and characterization of nanocomposite polymers, Microelectron. J. 39 (2) (2008) 228–236, https://doi.org/10.1016/j.mejo.2007.05.012.

[24] R.J. Grow, Q. Wang, J. Cao, D. Wang, H. Dai, Piezoresistance of carbon nanotubes on deformable thin-film membranes, Appl. Phys. Lett. 86 (9) (2005) 093104, https://doi.org/10.1063/1.1872221.

[25] Alamusi, N. Hu, H. Fukunaga, S. Atobe, Y. Liu, J. Li, Li, Piezoresistive Strain Sensors Made from Carbon Nanotubes Based Polymer Nanocomposites, Sensors (Basel) 11 (11) (2011) 10691–10723, https://doi.org/10.3390/s111110691.

[26] G. Yin, N. Hu, Y. Karube, Y. Liu, Y. Li, H. Fukunaga, A carbon nanotube/polymer strain sensor with linear and anti-symmetric piezoresistivity, J. Compos. Mater. (2011), https://doi.org/10.1177/0021998310393296.

[27] G. Yamamoto, M. Omori, T. Hashida, H. Kimura, A novel structure for carbon nanotube reinforced alumina composites with improved mechanical properties, Nanotechnology. 19 (31) (2008) 315708, https://doi.org/10.1088/0957-4484/19/31/315708.

[28] J. Zhou, Y. Gu, P. Fei, W. Mai, Y. Gao, R. Yang, G. Bao, Z.L. Wang, Flexible Piezotronic Strain Sensor, Nano Lett. 8 (9) (2008) 3035–3040, https://doi.org/10.1021/nl802367t.

[29] J.S. Milne, A.C.H. Rowe, S. Arscott, C.h. Renner, Giant Piezoresistance Effects in Silicon Nanowires and Microwires, Phys. Rev. Lett. 105 (2010), https://doi.org/10.1103/PhysRevLett.105.226802 226802.

[30] H.-P. Phan, T. Dinh, T. Kozeki, T.-K. Nguyen, A. Qamar, T. Namazu, N.-T. Nguyen, D.V. Dao, Nano strain-amplifier: Making ultra-sensitive piezoresistance in nanowires possible without the need of quantum and surface charge effects, Appl. Phys. Lett. 109 (12) (2016) 123502, https://doi.org/10.1063/1.4963258.

[31] L. Zhang, Y. Wang, Y. Wei, W. Xu, D. Fang, L. Zhai, K.-C. Lin, L. An, A Silicon Carbonitride Ceramic with Anomalously High Piezoresistivity, J. Am. Ceram. Soc. 91 (4) (2008) 1346–1349, https://doi.org/10.1111/j.1551-2916.2008.02275.x.

[32] Y. Wang, L. Zhang, Y.i. Fan, D. Jiang, L. An, Stress-dependent piezoresistivity of tunneling-percolation systems, J. Mater. Sci. 44 (11) (2009) 2814–2819, https://doi.org/10.1007/s10853-009-3371-5.

[33] R. Riedel, L. Toma, E. Janssen, J. Nuffer, T. Melz, H. Hanselka, Piezoresistive Effect in SiOC Ceramics for Integrated Pressure Sensors, J. Am. Ceram. Soc. 93 (2010) 920–924, https://doi.org/10.1111/j.1551-2916.2009.03496.x.

[34] K. Terauds, P.E. Sanchez-Jimenez, R. Raj, C. Vakifahmetoglu, P. Colombo, Giant piezoresistivity of polymer-derived ceramics at high temperatures, J. Eur. Ceram. Soc. 30 (11) (2010) 2203–2207, https://doi.org/10.1016/j.jeurceramsoc.2010.02.024.

[35] F. Rosenburg, B. Balke, N. Nicoloso, R. Riedel, E. Ionescu, Effect of the Content and Ordering of the sp2 Free Carbon Phase on the Charge Carrier Transport in Polymer-Derived Silicon Oxycarbides, Molecules 25 (2020) 5919, https://doi.org/10.3390/molecules25245919.

[36] L. Toma, H.-J. Kleebe, M.M. Müller, E. Janssen, R. Riedel, T. Melz, H. Hanselka, P. Colombo, Correlation Between Intrinsic Microstructure and Piezoresistivity in a SiOC Polymer-Derived Ceramic, J. Am. Ceram. Soc. (2011) n/a–n/a, https://doi.org/10.1111/j.1551-2916.2011.04944.x.

[37] Y. Cao, X. Yang, R. Zhao, Y. Chen, N.i. Li, L. An, Giant piezoresistivity in polymer-derived amorphous SiAlCO ceramics, J. Mater. Sci. 51 (12) (2016) 5646–5650, https://doi.org/10.1007/s10853-016-9866-y.

[38] B. Ma, Y. Wang, Fabrication of dense polymer-derived silicon carbonitride ceramic bulks by precursor infiltration and pyrolysis processes without losing piezoresistivity, J. Am. Ceram. Soc. 101 (7) (2018) 2752–2759.

[39] P. Colombo, G. Mera, R. Riedel, G.D. Sorarù, Polymer-Derived Ceramics: 40 Years of Research and Innovation in Advanced Ceramics, J. Am. Ceram. Soc. 93 (2010) 1805–1837, https://doi.org/10.1111/j.1551-2916.2010.03876.x.

[40] E. Ionescu, H.-J. Kleebe, R. Riedel, Silicon-containing polymer-derived ceramic nanocomposites (PDC-NCs): preparative approaches and properties, Chem. Soc. Rev. 41 (2012) 5032–5052, https://doi.org/10.1039/C2CS15319J.

[41] E.I. Ricohermoso, F. Klug, H. Schlaak, R. Riedel, E. Ionescu, Electrically conductive silicon oxycarbide thin films prepared from preceramic polymers, Int. J. Appl. Ceram. Technol. 19 (1) (2022) 149–164, https://doi.org/10.1111/ijac.13800.

[42] E. Ricohermoso, F. Klug, H. Schlaak, R. Riedel, E. Ionescu, Compressive thermal stress and microstructure-driven charge carrier transport in silicon oxycarbide thin films, J. Eur. Ceram. Soc. 41 (13) (2021) 6377–6384, https://doi.org/10.1016/j.jeurceramsoc.2021.07.001.

[43] E.C. Tupper, Chapter 13 - Structures, in: E.C. Tupper (Ed.), Introduction to Naval Architecture (Fifth Edition), Butterworth-Heinemann, Oxford, 2013, pp. 299–341, https://doi.org/10.1016/B978-0-08-098237-3.00013-8.

[44] C. Herring, Transport Properties of a Many-Valley Semiconductor, Bell Syst. Tech. J. 34 (1955) 237–290, https://doi.org/10.1002/j.1538-7305.1955.tb01472.x.

[45] C. Herring, E. Vogt, Transport and Deformation-Potential Theory for Many-Valley Semiconductors with Anisotropic Scattering, Phys. Rev. 101 (3) (1956) 944–961, https://doi.org/10.1103/PhysRev.101.944.

[46] G.L. Bir, Symmetry and strain-induced effects in semiconductors, Wiley, New York, 1974.

[47] J.C. Hensel, G. Feher, Cyclotron Resonance Experiments in Uniaxially Stressed Silicon: Valence Band Inverse Mass Parameters and Deformation Potentials, Phys. Rev. 129 (3) (1963) 1041–1062, https://doi.org/10.1103/PhysRev.129.1041.

[48] J.C. Hensel, H. Hasegawa, M. Nakayama, Cyclotron Resonance in Uniaxially Stressed Silicon. II. Nature of the Covalent Bond, Phys. Rev. 138 (1A) (1965) A225–A238, https://doi.org/10.1103/PhysRev.138.A225.

[49] K. Suzuki, J.C. Hensel, Quantum resonances in the valence bands of germanium. I. Theoretical considerations, Phys. Rev. B. 9 (10) (1974) 4184–4218, https://doi.org/10.1103/PhysRevB.9.4184.

[50] K.J. Kim, J.-H. Eom, T.Y. Koh, Y.-W. Kim, W.-S. Seo, Effects of carbon addition on the electrical properties of bulk silicon-oxycarbide ceramics, J. Eur. Ceram. Soc. 36 (11) (2016) 2705–2711, https://doi.org/10.1016/j.jeurceramsoc.2016.04.034.

[51] T. Zhai, D. Li, G. Fei, H. Xia, Piezoresistive and compression resistance relaxation behavior of water blown carbon nanotube/polyurethane composite foam, Compos. A Appl. Sci. Manuf. 72 (2015) 108–114, https://doi.org/10.1016/j.compositesa.2015.02.003.

[52] T. Nguyen, T. Dinh, A.R.M. Foisal, H.-P. Phan, T.-K. Nguyen, N.-T. Nguyen, D.V. Dao, Giant piezoresistive effect by optoelectronic coupling in a heterojunction, Nat. Commun. 10 (2019) 4139, https://doi.org/10.1038/s41467-019-11965-5.

[53] L. Wang, T. Ding, P. Wang, Effects of compression cycles and precompression pressure on the repeatability of piezoresistivity for carbon black-filled silicone rubber composite, J. Polym. Sci., Part B: Polym. Phys. 46 (11) (2008) 1050–1061, https://doi.org/10.1002/polb.21438.

[54] C. Cattin, P. Hubert, Piezoresistance in Polymer Nanocomposites with High Aspect Ratio Particles, ACS Appl. Mater. Interfaces 6 (3) (2014) 1804–1811, https://doi.org/10.1021/am404808u.

[55] K. Lu, D. Erb, M. Liu, Thermal stability and electrical conductivity of carbon-enriched silicon oxycarbide, J. Mater. Chem. C 4 (9) (2016) 1829–1837, https://doi.org/10.1039/C6TC00069J.

[56] M. Amjadi, A. Pichitpajongkit, S. Lee, S. Ryu, I. Park, Highly Stretchable and Sensitive Strain Sensor Based on Silver Nanowire-Elastomer Nanocomposite, ACS Nano 8 (5) (2014) 5154–5163, https://doi.org/10.1021/nn501204t.

[57] J.-S. Kim, G.-W. Kim, Hysteresis Compensation of Piezoresistive Carbon Nanotube/Polydimethylsiloxane Composite-Based Force Sensors, Sensors. 17 (2017) 229, https://doi.org/10.3390/s17020229.

[58] N. Larouche, B.L. Stansfield, Classifying nanostructured carbons using graphitic indices derived from Raman spectra, Carbon 48 (3) (2010) 620–629, https://doi.org/10.1016/j.carbon.2009.10.002.

[59] K. Park, S. Kim, H. Lee, I. Park, J. Kim, Low-hysteresis and low-interference soft tactile sensor using a conductive coated porous elastomer and a structure for interference reduction, Sens. Actuators, A 295 (2019) 541–550, https://doi.org/10.1016/j.sna.2019.06.026.

[60] J. Oh, J.-O. Kim, Y. Kim, H.B. Choi, J.C. Yang, S. Lee, M. Pyatykh, J. Kim, J.Y. Sim, S. Park, Highly Uniform and Low Hysteresis Piezoresistive Pressure Sensors Based on Chemical Grafting of Polypyrrole on Elastomer Template with Uniform Pore Size, Small 15 (2019) 1901744, https://doi.org/10.1002/smll.201901744.

[61] D.C. Montgomery, Design and analysis of experiments, eighth ed., John Wiley & Sons Inc, Hoboken, NJ, 2013.

[62] O. Senvar, H. Tozan, in: Process Capability and Six Sigma Methodology Including Fuzzy and Lean Approaches, IntechOpen, 2010, https://doi.org/10.5772/10389.

[63] G.R. Henderson, Process Capability Analysis, in: Six Sigma Quality Improvement with Minitab, second ed., John Wiley & Sons, Ltd, 2011, pp. 203–223. https://doi.org/10.1002/9781119975328.ch6.

[64] D.V.N. Sambrani, in: Process Capability–A Managers Tool for 6 Sigma Quality Advantage, Global Journals Inc. (USA), 2016, p. 9.

[65] J. Rajashekharaiah, Six sigma benchmarking of process capability analysis and mapping of process parameters, JOSCM 9 (2017) 60. https://doi.org/10.12660/joscmv9n2p60-71.

Check for updates

Received: 1 July 2022 | Revised: 16 July 2022 | Accepted: 22 July 2022

DOI: 10.1111/ijac.14185

SPECIAL ISSUE ARTICLE

Hierarchical microstructure growth in a precursor-derived SiOC thin film prepared on silicon substrate

Emmanuel III Ricohermoso[1] | **Eva Heripre**[2] | **Susana Solano-Arana**[3] | **Ralf Riedel**[1] | **Emanuel Ionescu**[1,4]

[1]Fachbereich Material–und Geowissenschaften, Technische Universität Darmstadt, Darmstadt, Germany

[2]LMPS–Laboratoire de Mécanique Paris-Saclay, Université Paris-Saclay, ENS Paris-Saclay, Gif-sur-Yvette, France

[3]Fachbereich Elektrotechnik und Informationstechnik, Technische Universität Darmstadt, Darmstadt, Germany

[4]Fraunhofer IWKS, Digitalization of Resources Department, Alzenau, Germany

Correspondence
Emmanuel III Ricohermoso and Emanuel Ionescu, Fachbereich Material- und Geowissenschaften, Technische Universität Darmstadt, Otto-Berndt-Str. 3, D-64287 Darmstadt, Germany.
Email: emmanuel_iii.ricohermoso@tu-darmstadt.de; emanuel.ionescu@iwks.fraunhofer.de

Funding information
German Science Foundation (DFG Germany), Grant/Award Number: 411658150; German Science Foundation (DFG Germany),, Grant/Award Number: 411658150

Abstract

Silicon oxycarbide film deposited on a silicon substrate has shown superior electrical conductivity relative to its monolithic counterpart. In this work, the evolution of different microstructures detected on the SiOC film reveals its hierarchical microstructure. The existence of sp^2-hybridized carbon domains has been unambiguously confirmed by means of Raman spectroscopy and transmission electron microscopy corroborated with electron energy loss spectroscopy. The diffusion coefficient of carbon in silica and its dependence on temperature were studied by assessing energy-dispersive X-ray spectroscopy profiles taken from the cross-sections of samples annealed at temperatures in the range from 1100°C to 1400°C. The activation energy for diffusion of carbon in silica was determined to be approximately 3.05 eV, which is significantly lower than the values related to the self-diffusion of silicon and oxygen. The microstructural evolution of precursor to SiC_nO_{4-n} and SiC serves as migration path of sp^2-hybridized carbon to the SiO_x layer. With increasing temperature, the formation of microscale carbon-rich segregation is promoted while the SiOC film becomes thinner.

KEYWORDS
carbon segregation, growth kinetics, polymer-derived ceramics, thin films

1 | INTRODUCTION

Silicon oxycarbide (SiOC) is a type of amorphous ceramics that is preparatively accessible from polysiloxane precursors and can be described as a glassy network consisting of the corner-sharing tetrahedra of $SiO_{4-x}C_x$ ($x = 0$–4)[1]; consequently, silicon oxycarbide may be considered as silicate-based glasses in which oxygen has been partly replaced by carbon. Multiple studies using different characterization methods, including IR spectroscopy, Raman

This is an open access article under the terms of the Creative Commons Attribution License, which permits use, distribution and reproduction in any medium, provided the original work is properly cited.
© 2021 The Authors. *International Journal of Applied Ceramic Technology* published by Wiley Periodicals LLC on behalf of American Ceramics Society.

spectroscopy, XRD, NMR spectroscopy, TGA/MS, and TEM, have been conducted to understand the (thermal) polysiloxane-to-SiOC transformation and to elucidate the structure of SiOC as well as its evolution at different thermal treatment stages.[1–15] Initially, the polysiloxane can be cross-linked via hydrosilylation, free-radical initiation, or condensation, which can be assisted with catalysts such as peroxides and metal acetylacetonates. Polymer-to-ceramic conversion of the cross-linked polysiloxane initiates at 400–600°C upon the evolution of hydrogen and hydrocarbons, mainly CH_4.[5,16–18] Pyrolysis at 600–1100°C results in continuous cleavage of the Si-O, Si-C, and C-H bonds producing free carbons with an onset at 800°C in an amorphous silicon oxycarbide ceramic phase.[19,20] Bois et al. explained with the use of solid-state[29] Si MAS NMR that the glassy network of the SiOC continuously evolves in the temperature range of 1200–1600°C.[21] At 1500°C, the evolution of β-SiC and an sp2 -hybridized segregated carbon phase has been confirmed by XRD analysis.[22,23]

A significant amount of literature is available on the synthesis approach and characterization of SiOC, although the majority is dedicated to powder and monolithic samples. In our latest work on SiOC thin film deposited on a silicon substrate, the evolution of the SiC and free carbon phases were documented at a temperature of 1400°C.[24,25] A micro-scale segregation of phases was observed on the surface of the film; the segregations were found to consist of sp[2-h]ybridized carbon and nanocrystalline β-SiC dispersed within an amorphous silicon oxycarbide matrix. The Si-O-C system is known to follow two processes when exposed to temperatures well beyond 1000°C: The first process involves the partitioning of the glassy $SiO_{4-x}C_x$ network and the formation of amorphous silica and SiC nanodomains, latter may crystallize; the second process represents the carbothermal reaction between the phase-separated silica and the excess carbon, complemented by the growth of crystalline SiC and release of gaseous CO.[9] These processes were extensively studied and are relatively well understood for monolithic SiOC. While they are still scarcely understood for polymer-derived SiOC thin films, as in this case, the substrate may have a significant impact on the phase separation and carbothermal decomposition of SiOC.

The specifics of the present work comprise a thorough investigation of the phases present on the SiOC thin film and first insights related to their segregation and growth. Multiple techniques, including Raman spectroscopy, TEM coupled with EDS, and EELS, were used to further understand the growth kinetics of the C-rich phase segregation in the SiOC-based film. The diffusivity of carbon to the SiO_x layer was carefully assessed and correlated to the formation and the growth of the C-rich segregation within the film.

2 | MATERIALS AND METHOD

2.1 | Materials

Polyramic® SPR 212, a commercially available polysiloxane (Starfire Systems Ltd., Glenville, NY, USA), was used as a polymer precursor for the synthesis of the SiOC thin films. In order to provide an effective crosslinking process of the polymeric films, free radical initiation was catalyzed with 1 wt% of dicumyl peroxide (added as a 50 wt% solution in toluene). A supplementary amount of toluene was added to achieve a 40% dilution of the polymers before the spin-coating deposition.

A 100-mm diameter boron-doped p-type Si (100) wafer with 525 μm thickness (Prime Si + SiO_2, MicroChemicals GmbH, Ulm, Germany) was chosen as the substrate. The Si substrates have a SiO_2 passivation layer with a thickness of ≈500 nm grown in successive dry-wet-dry oxidation processes.

2.2 | Thin film preparation

In a cleanroom, spin coating was performed using LabSpin 8 (Süss MicroTec SE, Garching, Germany) with a static dispense technique. A cascading technique of sequential acetone and isopropanol was used to clean the surface of the Si substrate prior to precursor deposition. The spin coating process was optimized concerning three main parameters: (1) initial spin speed, (2) acceleration profile, and (3) final spin speed. Using the Taguchi method, the design of experiment was carried out with the film thickness as the response factor. The film thickness was determined using a profilometer (Dektak XT Advanced System, Brucker, Karlsruhe, Germany) and measured in three different positions for each sample. The full details of the optimization process including the statistical approach are reported in detail in Reference 24. A favorable response was obtained using the setting of an initial spin speed of 4000 rpm for 30 s, then accelerated to a second spin speed of 8000 rpm for 30 s with an acceleration of 500 rpm/s.

The samples were thermally cross-linked at 250°C in air on a direct-contact hot plate. Subsequently, the samples were pyrolyzed in a graphite crucible placed in a high-temperature furnace (FCT-Uniaxial hot-press, FCT Systeme GmbH, Frankenblick, Germany) under a high purity nitrogen atmosphere. The thermal profile involved heating to 1100°C with a rate of 100 K min^{-1} followed by a dwell time of 2 h. Finally, the samples were annealed at different temperatures, 1200°C, 1300°C, or 1400°C with dwell times of 1, 2, or 3 h before cooling down to room temperature.

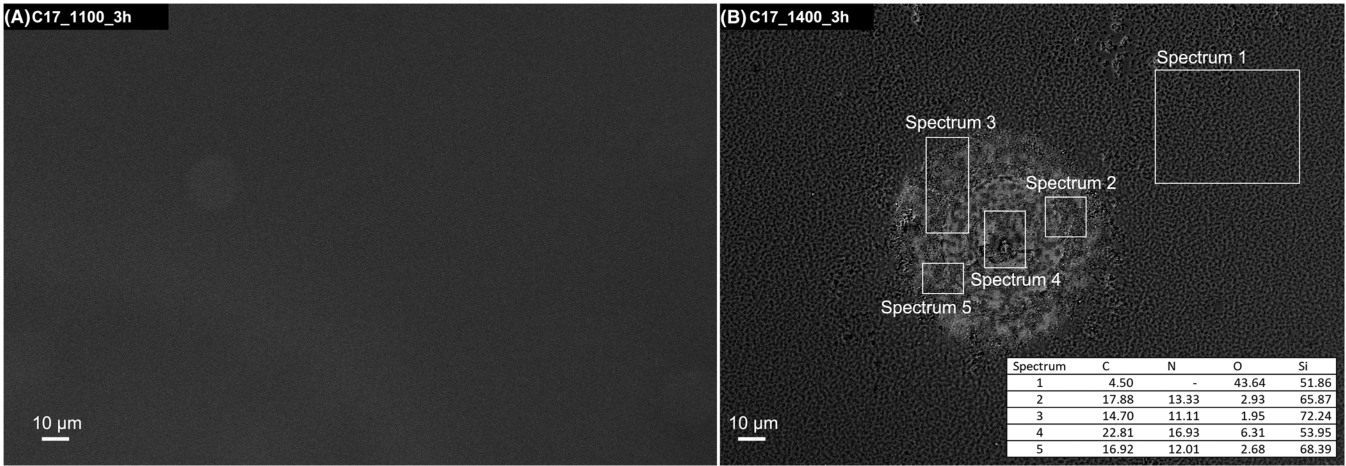

Spectrum	C	N	O	Si
1	4.50	-	43.64	51.86
2	17.88	13.33	2.93	65.87
3	14.70	11.11	1.95	72.24
4	22.81	16.93	6.31	53.95
5	16.92	12.01	2.68	68.39

FIGURE 1 Backscattered SEM micrograph of C17_1400_3h sample with five EDS spectra. Spectrum 1 is taken on the matrix of the film while Spectra 2–5 were taken on the particle.

For nomenclature, the prepared samples are labeled following the format of *C17_Annealing temperature_Dwell time*. In this case, C17 stands for the 17 wt% free carbon content of the sample.

2.3 | Characterization

The SiOC thin film deposited on a silicon substrate was cut into 1×1 cm^2 coupons for characterization purposes. The samples were primarily characterized by Raman Spectroscopy (LabRAM Horiba HR Raman Spectroscope HR800, Horiba Jobin Yvon GmbH, Bensheim, Germany), scanning electron microscopy [SEM] coupled with energy dispersive spectroscopy [EDS] (JEOL JSM 7600F, JEOL Ltd., Chiyoda, Tokyo, Japan).

For the cross-section preparation of the thin-film specimens, a Helios Nanolab 660 scanning electron microscope (FEI Thermofischer) was used in combination with a high-precision ion milling using FIB. A Titan3 G2 80–300 microscope (FEI Thermofisher) with probe (STEM) and conventional TEM modes was used to analyze the prepared sample. The device was coupled with EDS analysis and an Enfinium EELS detector (Gatan) with a resolution of 0.8 eV.

3 | RESULTS AND DISCUSSION

The morphology of the prepared SiOC-based thin films was studied by means of SEM as shown in Figure 1. A homogeneous SiOC film is clearly seen in Figure 1A with no manifestation of carbon segregation. Based on the backscattered SEM micrograph shown in Figure 1B, a clear indication of compositional differences was seen on the surface of the C17_1400_3h sample. Through EDS analysis, five areas were selected and the composition of each spectrum (element fraction given in wt%), was recorded and is shown as an inset in Figure 1. Spectrum 1 revealed that a high concentration of oxygen is present in the matrix of the film, while Spectra 2–5 are carbon-rich and oxygen-deficient. Nitrogen is also present within the formed segregation which can originate from the annealing atmosphere.

The sp^{2-h}ybridized carbon was shown to be present in both the SiOC matrix as well as in the oxygen-depleted segregations and was extensively studied by means of Raman spectroscopy. Raman analysis has been identified as a suitable non-destructive characterization technique for carbon and carbon-based materials where every band of the spectrum corresponds to a specific vibrational frequency of a molecular bond. In particular, carbon materials are typically characterized by three major bands in the Raman spectrum, namely the G-band, the D-band, and the 2D-band. The G-band is denoted as the characteristic band of graphene at 1582 cm^{-1}, which is a result of the only Raman active E_{2g} mode at the Γ point. The E_{2g} mode is doubly degenerate optical vibration where carbon atoms move in graphene planes.[26–28] In a graphitic material, the three-dimensional lattice built from layers of graphene, the zone centers are given by $\Gamma^{graphite} = 2A_{2u} + 2B_{2g} + 2E_{1u} + 2E_{2g}$. This results in two Raman-active modes at the Γ point at 1582 cm^{-1} and at 44 cm^{-1}. The other prominent peaks on the Raman spectrum belong to the disorder-induced bands within the material. D-band on the other hand is the double-resonant Raman process caused by hybridized vibrational mode at the edges of graphene.[29] The second-order peak, the 2D-band (also called D* or G′), is a result of the longitudinal optical branches of graphite in an over bent state. Detailed work on the assignment of

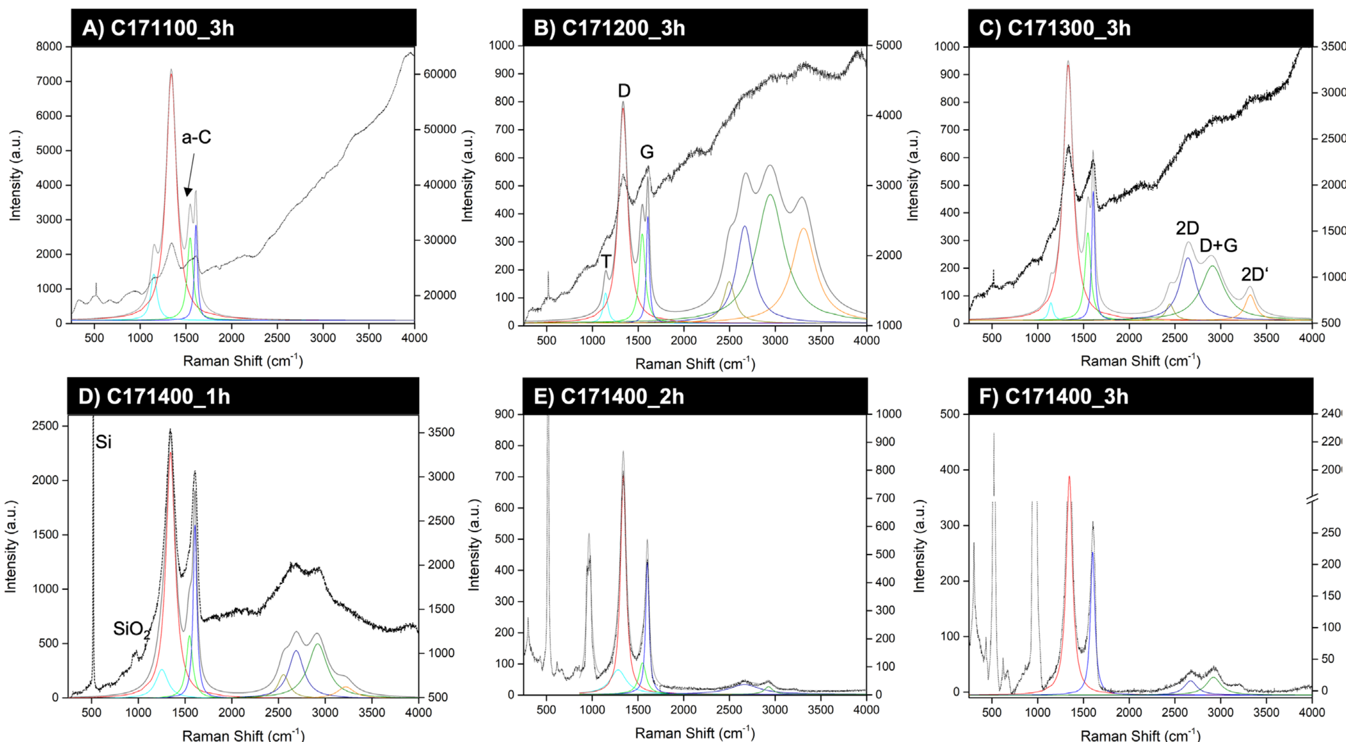

FIGURE 2 Lorentzian fitting of the Raman spectra of the matrix of the SiOC samples annealed at different temperatures and dwelling times. The untreated spectra are shown in black.

these bands has been made to extract indications about the quality and microstructure of carbon-based materials, including crystallinity and level of disorder revealed by the peak positions, peak shapes, and peak intensities.[30–33] Larouche et al. expanded the work by considering the tortuosity of carbon domains within the material and defining a new parameter, L_{eq} (see Equation (4)) by multiplying the tortuosity ratio with the lateral crystal size, L_a [34] (see Equation (1)). The works of Cançado et al. on quantifying defects have been the basis of the present study to calculate the defect density, n_D, and the distance between defects, L_D[30,31] (see Equations (2) and (3)).

$$L_a = \left(2.4 \times 10^{-10}\right) \lambda_L^4 \left(\frac{A_D}{A_G}\right)^{-1} \tag{1}$$

$$L_D^2 = 1.8\ x\ 10^{-9}\ \lambda_L^4 \frac{A_G}{A_D} \tag{2}$$

$$n_D = \frac{2.4\ x\ 10^{22} A_D}{\lambda_L^4 \qquad A_G} \tag{3}$$

$$L_{eq} = 77.0648 \frac{A_{2D}}{A_D.} \tag{4}$$

Looking at Figure 2, the untreated spectra in black exhibit high fluorescence background for the samples annealed at temperatures below 1400°C. The broad region concealing the second-order Raman region from 2400 cm^{-1} indicates the amorphous state of the samples. At 1400°C, increasing the dwelling time promotes better crystallinity in the samples while the peaks of Si and the silica coming from the substrate also become more pronounced. This can be related to the decreasing thickness of the film as the annealing temperature and dwelling time increase, which is indeed clear from the cross-sections of the samples shown in Figure 3. Using the area under the curve of each peak taken using the Lorentz fitting, the graphitization indices of the sp^{2-h}ybridized carbon phase in the studied samples were assessed with the help of Equations (1)–(4) and are listed in Table 1. An improvement in the ratio between the D- and G- bands can be seen as the temperature and dwelling times increase. This is further supported by the increasing of the lateral crystallite size L_a, which improved by four times as the temperature increased from 1100°C to 1400°C. On the other hand, a decrease of the value of L_{eq} with increasing temperature is seen for the SiOC-based amorphous matrix of the film. Zooming into the values calculated from C17_1300_3h and C17_1400_1h samples, the L_a and the L_{eq} of both the matrix and the oxygen-depleted segregations are comparable in magnitudes. As the annealing temperature of the thin film increases, it is shown that the size of the carbon domains in the segregated areas increases faster than that of the sp2-hybridized carbon phase present in the amorphous matrix. This is in agreement with a previous study, in which was

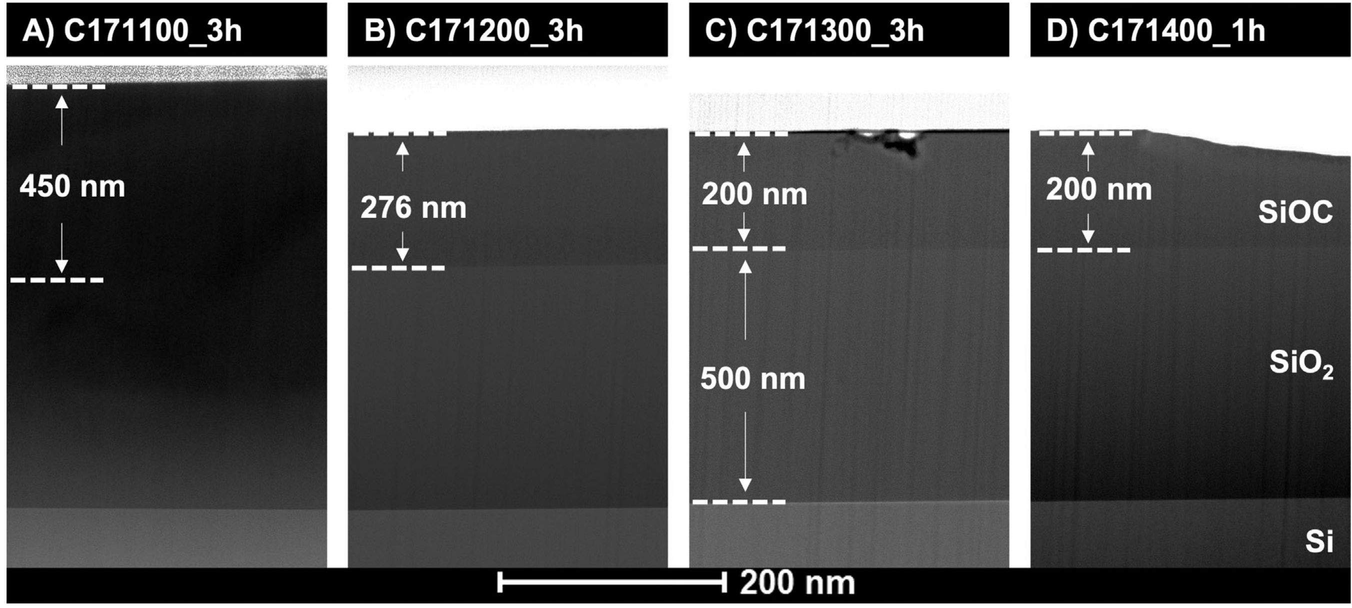

FIGURE 3 Cross-section of the matrices of SiOC film samples annealed at (A) 1100°C for 3 h, (B) 1200°C for 3 h, (C) 1300°C for 3 h, and (D) 1400°C for 1 h

TABLE 1 Graphitization indices of SiOC thin-film samples annealed at different temperatures and dwelling times. Indices were calculated using the Raman spectra using Equations (1), (2), (3) and (4)

Sample		A_D	A_G	A_{2D}	A_D/A_G	L_a (nm)	L_D (nm)	n_D ($\times$ 1012 cm^{-3})	L_{eq} (nm)
Matrix	C17_1100_3h	70.58	8.13	—	8.68	1.93	3.91	2.98	—
	C17_1200_3h	18.35	2.99	15.07	6.14	2.73	4.65	2.11	63.31
	C17_1300_3h	41.30	6.25	16.29	6.61	2.53	4.48	2.27	30.40
	C17_1400_1h	38.49	11.05	12.27	3.48	4.81	6.17	1.20	24.57
	C17_1400_2h	33.64	12.67	7.76	2.65	6.31	7.07	0.91	17.78
	C17_1400_3h	30.30	14.32	4.94	2.12	7.92	7.92	0.73	12.56
Precipitate	C17_1300_3h	41.30	6.25	16.29	6.61	2.53	4.48	2.27	30.40
	C17_1400_1h	30.76	8.51	8.45	3.62	4.63	6.06	1.24	21.17
	C17_1400_2h	36.99	11.34	18.41	3.26	5.13	6.38	1.12	38.35
	C17_1400_3h	18.30	15.21	18.22	1.20	13.93	10.50	4.14	76.74

also shown that the sp2-carbon in the segregations of the SiOC thin films is higher graphitized than the sp2-carbon from the amorphous matrix.[25]

The SiOC thin films on Si substrate were prepared for TEM and EELS analyses by preparing the cross-section via the FIB technique. Lamellae were taken along the matrices of the film, while additional lamellae were prepared for samples where oxygen-depleted segregations were evident. Displayed in Figure 3 are the cross-sections of samples annealed from 1100–1300°C for 3 h and the sample annealed at 1400°C for 1 h. The interfaces between the Si substrate, the SiO_2 passivation layer, and the SiOC film are clearly exposed after annealing at 1200°C. This method exposed the true thickness of the SiOC film at ≈200 nm. In the sample annealed at 1100°C, the amount of oxygen in the SiOC film gradually increases as it approaches the interface with the SiO_x passivation layer as shown in Figure S1. As the temperature increases, the thickness of the SiOC film decreases from 450 nm in the sample prepared at 1100°C to ≈200 nm in the sample annealed at 1400°C. At the same time, the oxygen-depleted segregations appear within the film. Interestingly, C17_1400_1h showed the development of a sinkhole, or a depression, leading to the segregations at the center, also shown in Figure 7A. The formation of the segregation started to manifest after annealing at 1300°C for 3 h.

EDS profiles of the cross-sections presented in Figure 3 are extracted to determine the diffusivity of carbon between the SiOC thin film and the SiO_x layers depicted in Figure 4. Using the Fick's second law of diffusion, the carbon diffusion constant (D_C) was estimated using Equation (5), where c_{max} and c_{min} are the initial concentrations

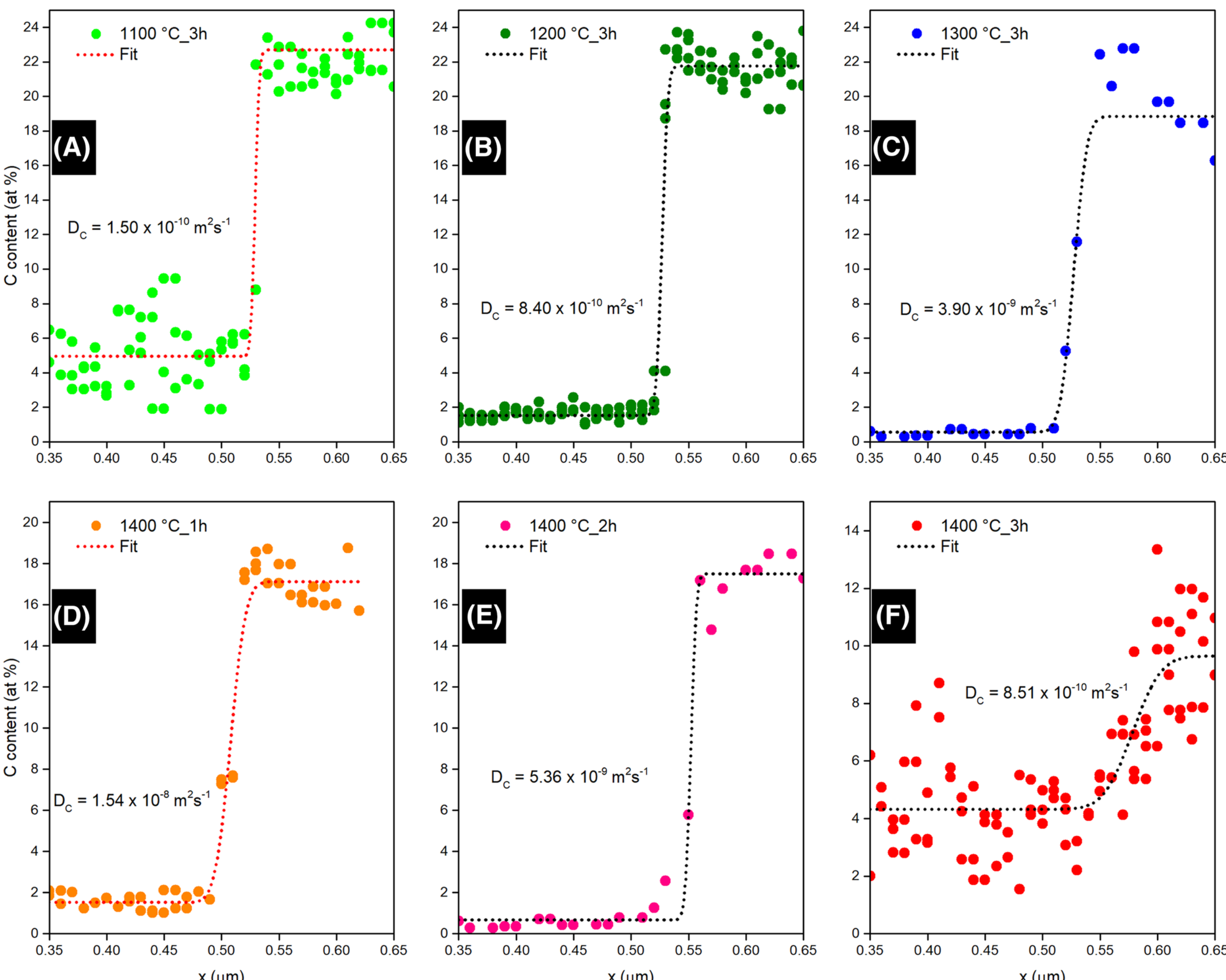

FIGURE 4 (A–C) Carbon profiles from EDS analysis and calculated coefficients of diffusion for SiOC thin film samples annealed at different temperatures, 1100–1300°C, at 3 h dwelling time. (D–F) Carbon profiles of isothermally annealed samples at 1400°C at different dwelling times, 1–3 h

at the interface between the SiOC film and the SiO_x passivation layer, x_0 corresponds to the inflection point of the profile, and t is annealing dwell time.

$$y\ (x,t) = \frac{c_{max} + c_{min}}{2} + \frac{c_{max} - c_{min}}{2} \mathrm{erf}\left(\frac{x - x_0}{2\sqrt{D_C t}}\right) \tag{5}$$

$$D_C = D_0 exp\left(-\frac{Q_d}{RT}\right) \tag{6}$$

Figure 4A–C displays the resulting carbon distribution after 3 h of annealing at temperatures 1100–1300°C, wherein the carbon concentration on the SiOC layer is sustained at ≈22 at%. In Figure 4D–F, isothermal annealing is performed at 1400°C at different dwelling times, 1–3 h. The resulting diffusion coefficients for the isothermally annealed samples exhibited an inverse proportionality with increasing dwelling time. The diffusion coefficient at 1400_3h sample is one magnitude lower than those for the other two samples annealed at 1400°C. This can be attributed to the low carbon concentration gradient between the film and SiO_x layer which is a result of the growth of C-rich segregations which are more prominent after 3 h of annealing at 1400°C. To keep the carbon concentration at an akin level, the 1400_1h sample is used to compare the diffusion coefficients of carbon at different temperatures.

Using the Arrhenius relation in Equation (6), wherein D_0 is the pre-exponential factor, Q_d is the activation energy, and R is the gas constant (8.31 J mol^{-1} K^{-1}), an exponential relationship of the diffusivity with temperature is observed in Figure 5A. The natural logarithm of the calculated D_C is

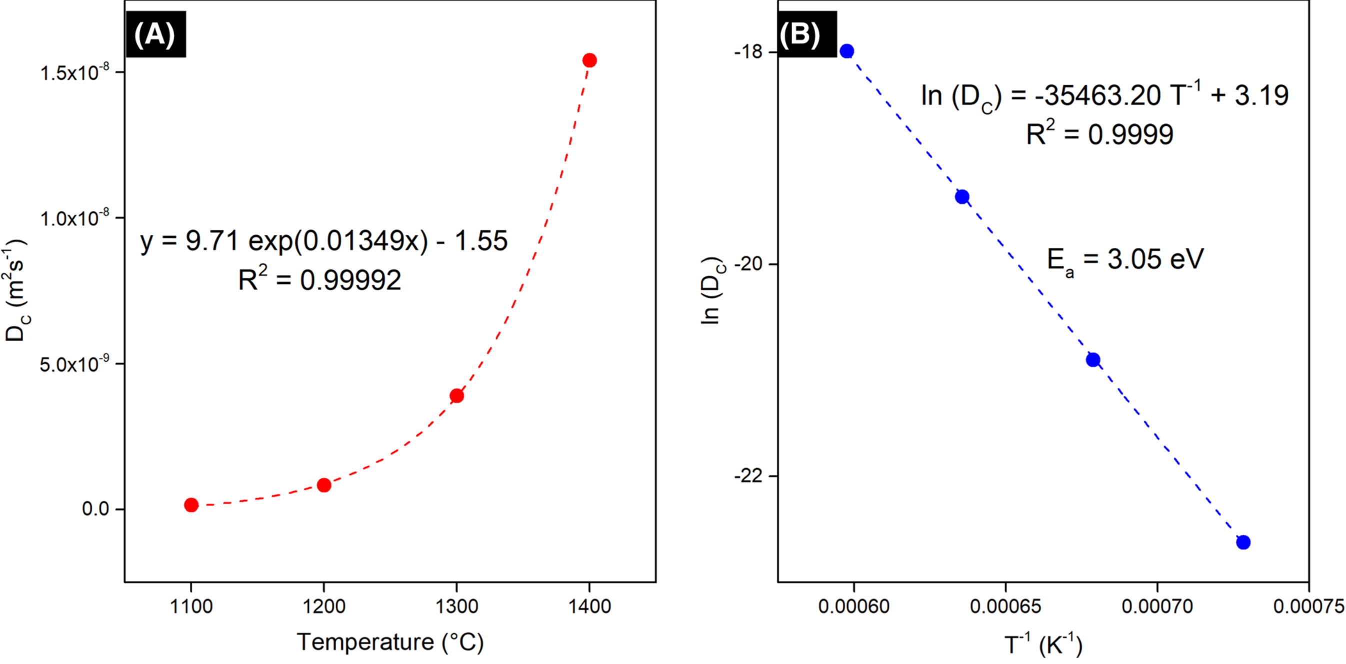

FIGURE 5 Diffusion coefficients of carbon obtained from EDS analysis of carbon profiles of SiOC thin film samples annealed at different isothermal temperatures (A) and the corresponding Arrhenius plot thereof (B)

then plotted against the inverse of temperature to extract the activation energy of the diffusing species which is shown in Figure 5B. The activation energy is extracted from the slope of the line of the Arrhenius plot resulting in 3.05 eV with an excellent fit of 99.99% and D_0 equal to 3.19. The calculated activation energy is comparable to the value of Shimoo et al.,[35] E_a^C = 3.74 eV, obtained from the reduction of SiO_2 with graphite leading to the formation of SiC and SiO as reduction products. In comparison, looking at the potential diffusivity of the three elements present in SiOC, the calculated E_a^C (3.05 eV) of carbon to silica is lower than the activation energy required to facilitate self-diffusion of Si to SiO_2 (E_a^{Si} = 4.56 eV)[35–37] but larger than the activation energy required to diffuse oxygen to silica (E_a^O = 2.54 eV).[38,39] Increasing the annealing temperature also promotes free carbon segregation which also increases the C/SiO_2 mixture ratio leading to a significant increase in the production of SiC. Consequently, with more time for annealing, the concentration of carbon left on the SiOC matrix diminishes slowing down the diffusivity of carbon which is evident in Figure 4D–F.

The EELS map and selected area electron diffraction (SAED) pattern of the graphitic carbon domains are presented in Figure 6. The Si $L_{2,3}$ edge, which is highly visible in all the spectra can be divided into the energy loss near edge structure (ELNES) at 120 eV with an onset at 104 eV, and the extended energy loss fine structure (EXELFS) at 150 eV which is superimposed with the L_1 edge.[40–43] The broadened peak at 120 eV is a result of the amorphous O-Si-C units within the region with the residual peak at 115 eV from the Si-O-Si bonds.[41,43] The absence of a sharp peak at 108 eV confirms the absence of SiO_2 within the C-rich area of the segregation.[40,42] Moreover, at the midpart of the map (black area), the C K-edge is predominantly composed of broad π^* peaks at 285 eV, which diminishes toward the gray area of the map with the rise of the σ^* peak ≈300 eV which suggests the existence of a mixture of sp2 and sp3 carbons.[19,41,44,45] The white region on the map exhibited peaks of N K-edge at 400 eV which supports the presence of Si_3N_4 within the segregation. In Figure 6B, the HRTEM image of the C-rich area along the (0003) basal plane exhibited the hexagonal rings of carbon structure with bent areas indicated by the white dashed lines. In conjunction with the Raman results in Table 1, these results support the tortuous nature of the carbon domains present in the film.

Two models to structurally describe the architecture of amorphous silicon oxycarbide have been proposed by Widgeon et al.[1] and Saha et al., [46] respectively, focusing on the SiC_nO_{4-n}-based glassy network and the sp2-carbon phase. The work of Widgeon et al. described the structure of SiOC to follow a Swiss-cheese morphology composed of a fractal network and "voids." The fractal network has the SiC_nO_{4-n} composition while the sp2-hybridized carbons are found within its voids. As deduced from Raman analysis, C17_1100_3h sample is in agreement with the model of Widgeon et al. with ~2 nm free carbon domains, although this is not easy to envision based on the SEM

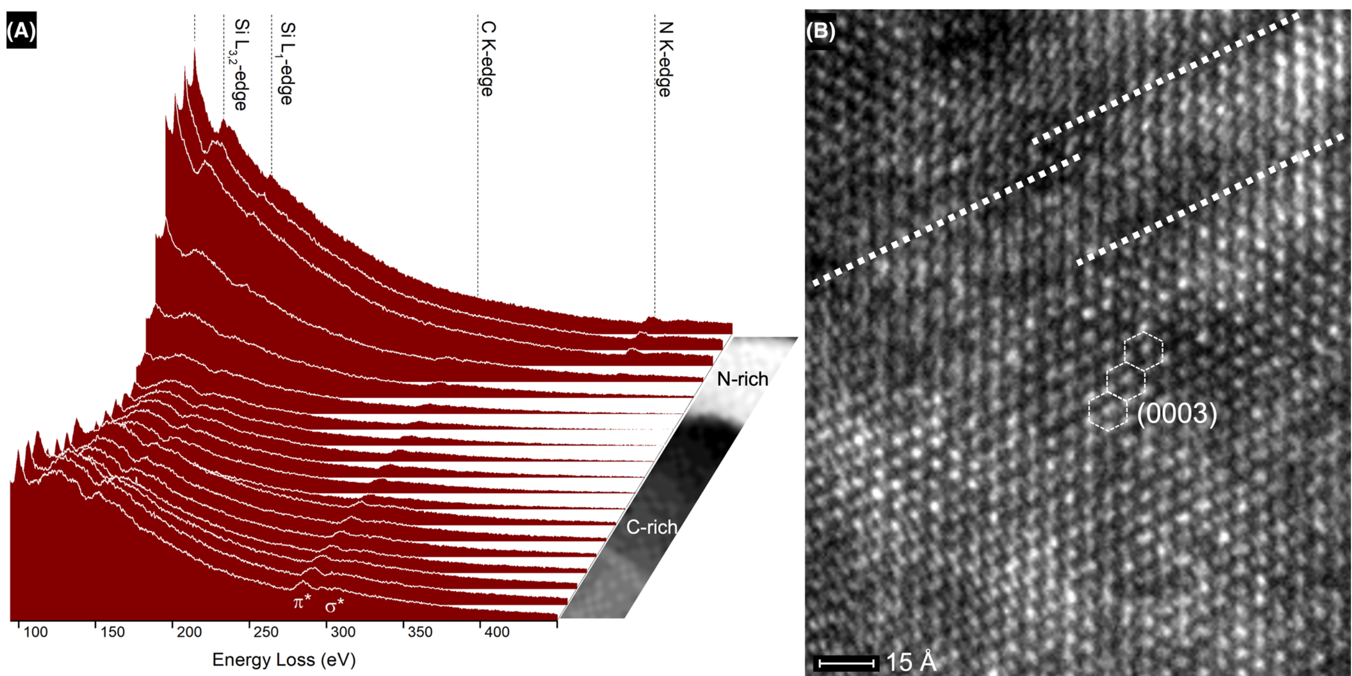

FIGURE 6 (A) EELS spectra of C17_1400_3h sample taken within the segregation region (C/SiC/N). (B) HAADF pattern of graphitic carbon taken along the (0003) plane. Dashed lines indicate the curved sections of the graphitic carbon formed within the segregation

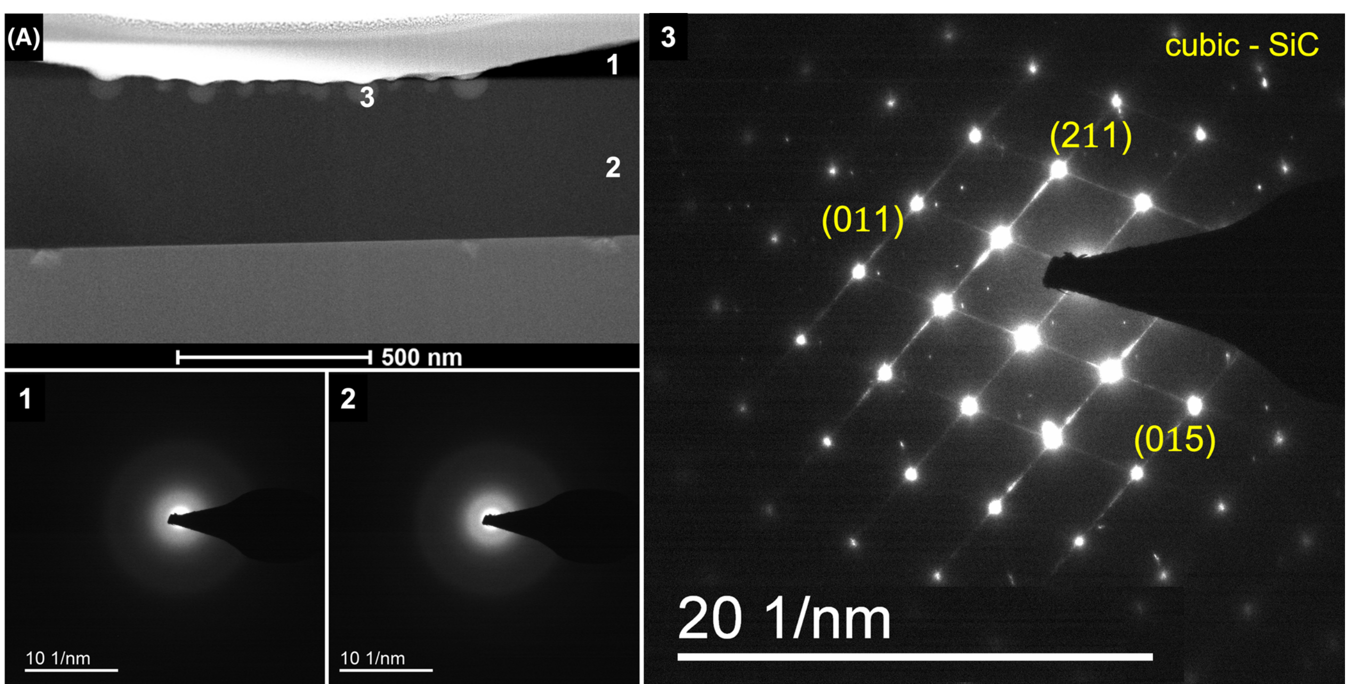

FIGURE 7 TEM image of C17_1400_1h sample with an evident thickness. SAED patterns of (1) SiOC film and (2) SiO2 layer remained in amorphous state while (3) stacking faults of SiC are found on the thickness-depleted area of the SiOC film.

image in Figure 1B. Relating to Figure 1B, the microstructure of the thin film synthesized in the present work at 1400°C agrees well with the model of Widgeon et al. on a microscale. It is considered that the formation of sp2-hybridized carbon serves as the main driving force for the generation of the carbon-rich segregations manifested on the thin film microstructure. The diffusivity suggests that increasing the annealing temperature promotes the

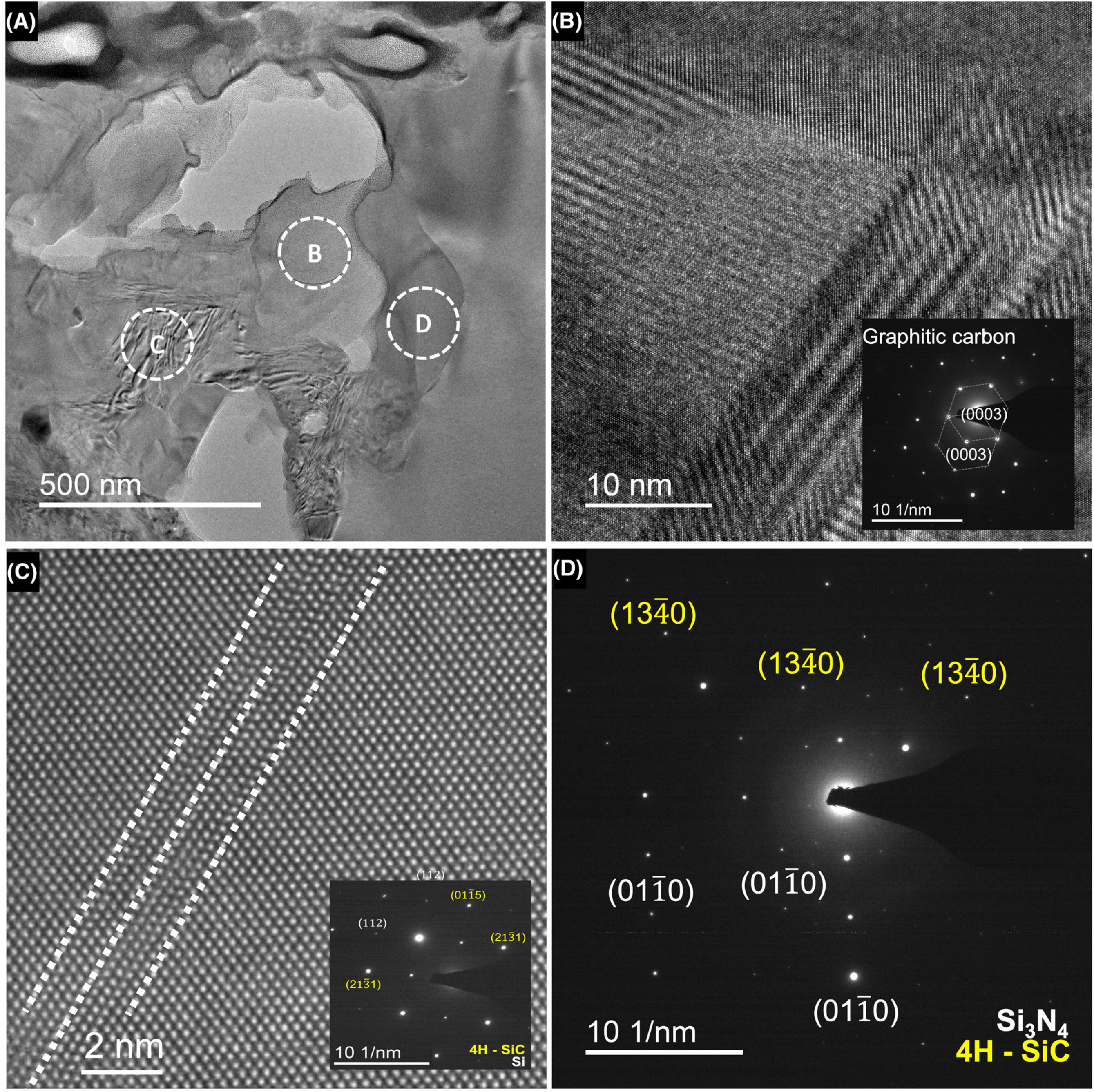

FIGURE 8 TEM image and SAED pattern of the carbon-rich area of the C17_1400_3h sample. (A) TEM image of C17_1400_3h sample segregation with equivalent SAED patterns. (B) Graphitic carbon; (C) 4H-SiC-rich region; (D) β-Si3N4-rich region

formation of SiC_nO_{4-n} structural units, which facilitates a migration path for the free carbons. With the benefit of the SiO_2 layer from the silicon substrate, after annealing at 1400°C for 1 h, diffusion of the carbon is highly favored leading to the formation of the microscale carbon-rich segregations denoted by the thickness depletion in Figure 7. The SAED pattern (3) confirms the presence of stacking faults of cubic-SiC on the interface of the SiOC film and the SiO_2 layer, while the rest of the SiOC film remains in an amorphous state (Figure 7_SAED Pattern 1). SAED Pattern 2 denotes the SiO_2 layer.

After 3 h of annealing at 1400°C, the segregation grows further down into the SiO_2 layer without reaching the Si substrate. In Figure 8, the segregation area is revealed to be composed of dense areas containing sp2-hybridized carbon domains, 4H-SiC, and β-Si_3N_4, which are presented with

corresponding SAED patterns. The formation of Si_3N_4 is reasonable and is a consequence of the reaction of N_2 gas with the in situ formed $SiO_{4-x}C_x$. The reaction has a minimal contribution during the thermal decomposition of SiOC/Si/SiC and is more favored at temperature between 1400 and 1600°C.[47] It is obvious from the SAED patterns that multiple crystalline phases exist in the segregation. On the TEM image, it is apparent that 4H-SiC and β-Si_3N_4 exist as fragments distributed in the area of the segregation.

4 | CONCLUSIONS

In the present study involving several annealing temperatures and dwelling times, the SiOC thin-film displays two distinct phases of segregated round-shaped structures homogenously distributed in a matrix. These two phases are differentiated by the amount of carbon and oxygen contents making the segregation C-rich and O-depleted, whereas the matrix is O-rich. Through Raman analysis, non-destructive characterization of the carbon domains with the SiOC film is carried out revealing the domain of sp^2-hybridized carbons present on both the matrix and the segregations. Through this work, a clear manifestation of carbon domains is demonstrated, which correspondingly facilitates the formation of SiC via diffusion. Finally, increasing the annealing temperature demonstrated a positive trend in the growth mechanism of the microscale segregation composed of SiC, Si_3N_4, and graphitic carbon domains, which is confirmatory of the 2-level hierarchical microstructure of the SiOC film on a silicon substrate. The diffusion coefficient of carbon to silica showed a direct proportionality to increasing temperature and an Arrhenius relation resulting in activation energy of 3.05 eV.

AUTHOR CONTRIBUTIONS

Conceptualization: Emmanuel III Ricohermoso and Emanuel Ionescu; methodology, software, formal analysis, investigation, resources, and data curation: Emmanuel III Ricohermoso, Maxime Vallet, Eva Heripre, and Susana Solano-Arana; writing—original draft preparation: Emmanuel III Ricohermoso; writing—review and editing: Emanuel Ionescu and Ralf Riedel; visualization: Emmanuel III Ricohermoso; supervision: Emanuel Ionescu; project administration: Emmanuel III Ricohermoso, Maxime Vallet, and Emanuel Ionescu; funding acquisition: Emanuel Ionescu and Ralf Riedel. All authors have read and agreed to the published version of the manuscript.

ACKNOWLEDGMENTS

The authors gratefully acknowledge funding from the German Science Foundation (DFG Germany)—grant no. 411658150 (microstructured C/SiCX (X = O,N)-based high-temperature strain gauge). Additionally, Emanuel Ionescu acknowledges funding from DFG within the Heisenberg program (IO 64/1). The authors would also like to thank Dr. Maxime Vallet for his assistance for the TEM measurements.

Open access funding enabled and organized by Projekt DEAL.

CONFLICT OF INTEREST

The authors declare no conflict of interest.

ORCID

Emmanuel III Ricohermoso https://orcid.org/0000-0002-4093-4751
Ralf Riedel https://orcid.org/0000-0001-6888-7208
Emanuel Ionescu https://orcid.org/0000-0002-3266-3031

REFERENCES

1. Widgeon SJ, Sen S, Mera G, Ionescu E, Riedel R, Navrotsky A. 29Si and 13C solid-state NMR spectroscopic study of nanometer-scale structure and mass fractal characteristics of amorphous polymer derived silicon oxycarbide ceramics. Chem Mater. 2010;22(23):6221–8.
2. Ionescu E, Mera G, Riedel R. Polymer-derived ceramics: materials design towards applications at ultrahigh-temperatures and in extreme environments. In: Nanotechnology: Concepts, methodologies, tools, and applications. IGI Global; 2014. p. 1108–39.
3. Mera G, Navrotsky A, Sen S, Kleebe HJ, Riedel R. Polymer-derived SiCN and SiOC ceramics – structure and energetics at the nanoscale. J Mater Chem A. 2013;1(12):3826–36.
4. Mera G, Gallei M, Bernard S, Ionescu E. Ceramic nanocomposites from tailor-made preceramic polymers. Nanomaterials (Basel). 2015;5(2):468–540.
5. Babonneau F, Soraru GD, D'Andrea G, Dire S, Bois L. Silicon oxycarbide glasses from sol-gel precursors. MRS Online Proceedings Library (OPL). 1992;271:789.
6. Kalfat R, Babonneau F, Gharbi N, Zarrouk H. 29 Si MAS NMR investigation of the pyrolysis process of cross-linked polysiloxanes prepared from polymethylhydrosiloxane. J Mater Chem. 1996;6(10):1673–8.
7. Trimmel G, Badheka R, Babonneau F, Latournerie J, Dempsey P. Solid state NMR and TG/MS study on the transformation of methyl groups during pyrolysis of preceramic precursors to SiOC glasses - ProQuest. J Sol-Gel Sci Technol. 2003;26(1–3):279–83.
8. Rosenburg F, Balke B, Nicoloso N, Riedel R, Ionescu E. Effect of the content and ordering of the sp2 free carbon phase on the charge carrier transport in polymer-derived silicon oxycarbides. Molecules. 2020;25(24):5919.
9. Weinmann M, Ionescu E, Riedel R, Aldinger F. Chapter 11.1.10 - Precursor-Derived Ceramics*. In: Somiya S, editor. Handbook of advanced ceramics. 2nd ed. Oxford: Academic Press; 2013. p. 1025–101.
10. Ionescu E, Kleebe HJ, Riedel R. Silicon-containing polymer-derived ceramic nanocomposites (PDC-NCs): preparative approaches and properties. Chem Soc Rev. 2012;41(15):5032–52.

11. Felix Rosenburg, Emanuel Ionescu, Norbert Nicoloso, Ralf Riedel. High-temperature Raman spectroscopy of nano-crystalline carbon in silicon oxycarbide. Materials. 2018;11(1):93.
12. Roth F, Waleska P, Hess C, Ionescu E, Nicoloso N. UV Raman spectroscopy of segregated carbon in silicon oxycarbides. J Ceram Soc Japan. 2016;124(10):1042–5.
13. Colombo P, Mera G, Riedel R, Sorarù GD. Polymer-derived ceramics: 40 years of research and innovation in advanced ceramics. J Am Ceram Soc. 2010;93(7):1805–37.
14. Riedel R, Mera G, Hauser R, Klonczynski A. Silicon-based polymer-derived ceramics: synthesis properties and applications-a review: dedicated to Prof. Dr. Fritz Aldinger on the occasion of his 65th birthday. Nippon Seramikkusu Kyokai Gakujutsu Ronbunshi. 2006;114(1330):425–44.
15. Kleebe HJ, Turquat C, Sorarù GD. Phase separation in an SiCO glass studied by transmission electron microscopy and electron energy-loss spectroscopy. J Am Ceram Soc. 2001;84(5):1073–80.
16. Chomel AD, Dempsey P, Latournerie J, Hourlier-Bahloul D, Jayasooriya UA. Gel to glass transformation of methyltriethoxysilane: a silicon oxycarbide glass precursor investigated using vibrational spectroscopy. Chem Mater. 2005;17(17):4468–73.
17. Sorarù GD, D'Andrea G, Glisenti A. XPS characterization of gel-derived silicon oxycarbide glasses. Mater Lett. 1996;27(1):1–5.
18. Sorarù GD. Silicon oxycarbide glasses from gels: Code: H1. J Sol-Gel Sci Technol. 1994;2(1–3):843–8.
19. Giuliano G, Hans-Joachim K, D BY, Florence B. Evolution of C-rich SiOC ceramics Part II. Characterization by high lateral resolution techniques: electron energy-loss spectroscopy, high-resolution TEM and energy-filtered TEM. Int J Mater Res. 2006;97(6):710–20.
20. Sorarù GD, Modena S, Guadagnino E, Colombo P, Egan J, Pantano C. Chemical durability of silicon oxycarbide glasses. J Am Ceram Soc. 2002;85(6):1529–36.
21. Bois L, Maquet J, Babonneau F, Bahloul D. Structural characterization of sol-gel derived oxycarbide glasses. 2. Study of the thermal stability of the silicon oxycarbide phase. Chem Mater. 1995;7(5):975–81.
22. Bréquel H, Parmentier J, Walter S, Badheka R, Trimmel G, Masse S, et al. Systematic structural characterization of the high-temperature behavior of nearly stoichiometric silicon oxycarbide glasses. Chem Mater. 2004;16(13):2585–98.
23. Saha A, Raj R. Crystallization maps for SiCO amorphous ceramics. J American Ceramic Society. 2007;90(2):578–83.
24. Ricohermoso E, Klug F, Schlaak H, Riedel R, Ionescu E. Electrically conductive silicon oxycarbide thin films prepared from preceramic polymers. Int J Appl Ceram Technol. 2021;19(1):149–64.
25. Ricohermoso E, Klug F, Schlaak H, Riedel R, Ionescu E. Compressive thermal stress and microstructure-driven charge carrier transport in silicon oxycarbide thin films. J Eur Ceram Soc. 2021;41(13):6377–84.
26. Reich S, Thomsen C. Raman spectroscopy of graphite. Phil Trans R Soc A: Math, Phys Eng Sci. 2004;362(1824):2271–88.
27. Kostić R, Mirić M, Radić T, Radović M, Gajić R, Popović ZV. Optical characterization of graphene and highly oriented pyrolytic graphite. Acta Phys Pol A. 2009;116(4):718–21.
28. Rousseau DL, Bauman RP, Porto SPS. Normal mode determination in crystals. J Raman Spectrosc. 1981;10(1):253–90.
29. Saito R, Jorio A, Souza Filho AG, Dresselhaus G, Dresselhaus MS, Pimenta MA. Probing phonon dispersion relations of graphite by double resonance Raman scattering. Phys Rev Lett. 2002;88(2):027401.
30. Cançado LG, Takai K, Enoki T, Endo M, Kim YA, Mizusaki H, et al. General equation for the determination of the crystallite size La of nanographite by Raman spectroscopy. Appl Phys Lett. 2006;88(16):163106.
31. Cançado LG, Jorio A, Ferreira EHM, Stavale F, Achete CA, Capaz RB, et al. Quantifying defects in graphene via Raman spectroscopy at different excitation energies. Nano Lett. 2011;11(8):3190–6.
32. Bokobza L, Bruneel JL, Couzi M. Raman spectra of carbon-based materials (from graphite to carbon black) and of some silicone composites. C. 2015;1(1):77–94.
33. Baranov AV, Bekhterev AN, Bobovich YaS, Petrov VI. Interpretation of certain characteristics in Raman spectra of graphite and glassy carbon. Opt Spectrosc. 1987;62:612–6.
34. Larouche N, Stansfield BL. Classifying nanostructured carbons using graphitic indices derived from Raman spectra. Carbon. 2010;48(3):620–9.
35. Shimoo T, Mizutaki F, Ando S, Kimura H. Kinetics of reduction of silica with graphite. J Jpn Inst Met. 1988;52(10):945–53.
36. Estreicher SK, Backlund DJ, Carbogno C, Scheffler M. Activation energies for diffusion of defects in silicon: the role of the exchange-correlation functional. Angew Chem Int Ed. 2011;50(43):10221–5.
37. Bracht H. Self- and foreign-atom diffusion in semiconductor isotope heterostructures. I. Continuum theoretical calculations. Phys Rev B. 2007;75(3):035210.
38. di Ventra M, Pantelides ST. Oxygen stability, diffusion, and precipitation in SiC: implications for thin-film oxidation. Journal of Elec Materi. 2000;29(3):353–8.
39. Gösele U, Tan TY. Oxygen diffusion and thermal donor formation in silicon. Appl Phys A. 1982;28(2):79–92.
40. Wang YY, Chan SF, Jin Q, Zhuang K, Choi JK. A method of using Si L-edge for O/Si and N/Si quantitative ratio analysis by electron energy loss spectroscopy (EELS). Micron. 2021;146:103065.
41. Schneider R, Woltersdorf J, Lichtenberger O. Phase identification in composite materials by EELS fine-structure analysis. J Microsc. 1996;183(1):39–44.
42. Garvie L, Buseck P. Bonding in silicates: Investigation of the Si L2,3 edge by parallel electron energy-loss spectroscopy. Am Mineral. 1999;84:946–64.
43. Pippel E, Lichtenberger O, Woltersdorf J. Identification of silicon oxycarbide bonding in Si-C-O-glasses by EELS. J Mater Sci Lett. 2000;19:2059–60.
44. Edalati K, Daio T, Ikoma Y, Arita M, Horita Z. Graphite to diamond-like carbon phase transformation by high-pressure torsion. Appl Phys Lett. 2013;103(3):034108.
45. Ponsonnet L, Donnet C, Varlot K, Martin JM, Grill A, Patel V. EELS analysis of hydrogenated diamond-like carbon films. Thin Solid Films. 1998;319(1):97–100.
46. Saha A, Raj R, Williamson DL. A model for the nanodomains in polymer-derived SiCO. J Am Ceram Soc. 2006;89(7):2188–95.

47. Osip H, Czosnek C, Janik JF, Marchewka J, Sitarz M. Amorphous silicon oxynitride-based powders produced by spray pyrolysis from liquid organosilicon compounds. Materials (Basel). 2021;14(2):386.

SUPPORTING INFORMATION

Additional supporting information can be found online in the Supporting Information section at the end of this article.

How to cite this article: Ricohermoso E, Heripre E, Solano-Arana S, Riedel R, Ionescu E. Hierarchical microstructure growth in a precursor-derived SiOC thin film prepared on silicon substrate. Int J Appl Ceram Technol. 2022;1–12. https://doi.org/10.1111/ijac.14185